A study of four problems in nonlinear vibrations *via* the method of multiple scales

A Thesis
Submitted for the Degree of
Doctor of Philosophy
in the Faculty of Engineering

By
K. Nandakumar

Department of Mechanical Engineering
Indian Institute of Science
Bangalore - 560 012
India

August 2009

Dedicated to the lotus feet of
Lord Sri Krishna of Guruvayoor
Lord Vithoba and Rakhumai of Pandharpur
Lord Jagannatha, Balabhadra and Subhadra of Puri

Abstract

This thesis involves the study of four problems in the area of nonlinear vibrations, using the asymptotic method of multiple scales (MMS). Accordingly, it consists of four sequentially arranged parts.

In the first part of this thesis we study some nonlinear dynamics related to the amplitude control of a lightly damped, resonantly forced, harmonic oscillator. The slow flow equations governing the evolution of amplitude and phase of the controlled system are derived using the MMS. Upon choice of a suitable control law, the dynamics is represented by three coupled, nonlinear ordinary differential equations involving a scalar free parameter. Preliminary study of this system using the bifurcation analysis package MATCONT reveals the presence of Hopf bifurcations, pitchfork bifurcations, and limit cycles which seem to approach a homoclinic orbit.

However, close approach to homoclinic orbit is not attained using MATCONT due to an inherent limitation of time domain-based continuation algorithms. To continue the limit cycles closer to the homoclinic point, a new algorithm is proposed. The proposed algorithm works in phase space with an ordered set of points on the limit cycle, along with spline interpolation. The algorithm incorporates variable stretching of arclength based on local curvature, through the use of an auxiliary index-based variable. Several numerical examples are presented showing favorable comparisons with MATCONT near saddle homoclinic points. The algorithm is also formulated with infinitesimal parameter increments resulting in ordinary differential equations, which gives some advantages like the ability to handle fold points of periodic solution branches upon suitable re-parametrization. Extensions to higher dimensions are outlined as well.

With the new algorithm, we revisit the amplitude control system and continue the limit cycles much closer to the homoclinic point. We also provide some independent semi-analytical estimates of the homoclinic point, and mention an atypical property of the homoclinic orbit.

In the second part of this thesis we analytically study the classical van der Pol oscillator, but with an added fractional damping term. We use the MMS near the Hopf bifurcation point. Systems with $\mathcal{O}(1)$ fractional terms, such as the one studied here, have hitherto been largely treated numerically after suitable approximations of the fractional order operator in the frequency domain. Analytical progress has been restricted to systems with small fractional terms. Here, the fractional term is approximated by a recently proposed Galerkin-based discretization scheme resulting in a set of ODEs. These ODEs are then treated by the MMS, at parameter values close to the Hopf bifurcation. The resulting slow flow provides good approximations to the full numerical solutions. The system is also studied under weak resonant forcing. Quasiperiodicity, weak phase locking, and entrainment are observed. An interesting observation in this work is that although the Galerkin approximation nominally leaves several long time scales in the dynamics, useful MMS approximations of the fractional damping term are nevertheless obtained for relatively large deviations from the nominal bifurcation point.

In the third part of this thesis, we study a well known tool vibration model in the large delay regime using the MMS. Systems with small delayed terms have been studied extensively as perturbations of harmonic oscillators. Systems with $\mathcal{O}(1)$ delayed terms, but near Hopf points, have also been studied by the method of multiple scales. However, studies on systems with large delays are few in number. By "large" we mean here that the delay is much larger than the time scale of typical cutting tool oscillations. The MMS upto second order, recently developed for such large-delay systems, is applied. The second order analysis is shown to be more accurate than first order. Numerical integration of the MMS slow flow is much faster than for the original equation, yet shows excellent accuracy. A key point is that although certain parameters are treated as small (or, reciprocally, large), the analysis is not restricted to infinitesimal distances from the Hopf bifurcation. In the present analysis, infinite dimensional dynamics is retained in the slow flow, while the more usual center manifold reduction gives a planar phase space. Lower-dimensional dynamical features, such as Hopf bifurcations and families of periodic solutions, are also captured by the MMS. The strong sensitivity of the slow modulation dynamics to small changes in parameter values, peculiar to such systems with large delays, is seen clearly.

In the last part of this thesis, we study the weakly nonlinear whirl of an asymmetric, overhung rotor near its gravity critical speed using a well known two-degree of freedom model. Gravity critical speeds of rotors have hitherto been studied using linear analysis, and ascribed to rotor stiffness asymmetry. Here we present a weakly nonlinear study of this phenomenon. Nonlinearities arise from finite displacements, and the rotor's static lateral deflection under gravity is taken as small. Assuming small asymmetry and damping, slow flow equations for modulations of whirl amplitudes are developed using the MMS. Inertia asymmetry appears only at second order. More interestingly, even without stiffness asymmetry, the gravity-induced resonance survives through geometric nonlinearities. The gravity resonant forcing does not influence the resonant mode at leading order, unlike typical resonant oscillations. Nevertheless, the usual phenomena of resonances, namely saddle-node bifurcations, jump phenomena and hysteresis, are all observed. An unanticipated periodic solution branch is found. In the three dimensional space of two modal coefficients and a detuning parameter, the full set of periodic solutions is found to be an imperfect version of three mutually intersecting curves: a straight line, a parabola, and an ellipse.

To summarize, the first and fourth problems, while involving routine MMS, involve new applications with rich dynamics. The second problem demonstrated a semi-analytical approach *via* the MMS to study a fractional order system. Finally, the third problem studied a known application in a hitherto less-explored parameter regime through an atypical MMS procedure. In this way, a variety of problems that showcase the utility of the MMS have been studied in this thesis.

Acknowledgements

I thank my advisor Prof. Anindya Chatterjee for his constant guidance, encouragement and support throughout my doctoral studies. My association with him for the past several years, both as a graduate student and a doctoral student, has been immensely beneficial to me. His technical expertise has helped me at several crucial junctures. I have learnt the science of nonlinear dynamics from scratch under his able guidance. Our technical interactions involve multiple time scales. He generated ideas on a fast time scale, which I understood, assimilated and worked out on a slow time scale! My association with him has left an indelible change in the way I think about technical matters.

I thank Prof. E. J. Doedel for his timely help in sending hard copies of several papers which were very useful in the work on continuation of limit cycles. I thank Prof. J. A. T. Machado for his prompt help in sending me papers regarding fractional calculus.

I thank the Indian Institute of Science for providing an excellent academic environment, good library, computer facilities, financial aid, hostel, mess facilities, and overall support during my doctoral days.

I have been associated with the *Dynamics lab* during my masters and doctoral studies. During this time, I have enjoyed spending many many hours with the lab members discussing technical, as well as non-technical matters, which have directly and indirectly helped me in my research work. I will cherish memories of the time we spent here. Some

of the lab members have provided direct technical support related to this thesis, and I will acknowledge them specifically in the appropriate chapters of this thesis. Apart from the lab members, I thank my friends Sachin, Pandey, Sai-ji, Gupta-ji, Abhijit, Venkatesh, Ramkumar and Premkumar for their companionship. I thank the *Marathi gang*, one and all, for all the fun we have had. Special thanks to Manthram, Sandhya and Mukhil kutty. Meeting them during weekends gave me lot of enthusiasm and energy to work.

I thank Prasanna, Jaishankar, Murthy mama, Sriram, and Chandru for the bhajans and spiritual discussions which gave me peace of mind and helped me in my research work.

Last, but definitely not the least, I owe a lot to my family members. Without the sacrifices of my appa and amma, I cannot imagine the completion of this work. All these years, they have made countless compromises and managed all the family affairs to ensure that my studies progressed smoothly. I also thank my sisters and their families for their constant help and encouragement. I finally thank all my other close relatives for their affection and support.

Contents

List of Figures

List of Tables

Chapter 1

Overview and main contributions of the thesis

This thesis deals with the study of four problems in the area of nonlinear vibrations. The theme common to these problems is that they are all amenable to analysis using the asymptotic method of multiple scales [1]. The actual applications of the MMS to these problems, while not fundamentally novel, are not always quite routine.

In this chapter we begin with a brief introduction to this classical method of multiple scales (MMS). We then briefly mention the nature of the problems studied in this thesis using this method, and highlight our main contributions.

1.1 Method of Multiple Scales (MMS)

1.1.1 Motivation

The method of multiple scales is a classical singular perturbation method used to study systems involving distinct phenomena operating at disparate length/time scales. There are several excellent textbooks devoted to the development and application of this method to various physical systems. In what follows we explain, using some common examples, the domain of applicability of the method.

Nature and engineering are abundant with phenomena involving disparate time and/or length scales. A limited sample includes *slow damping* of vibrations of a simple pendulum oscillating in quiescent air, beating (slow amplitude modulation) of two *weakly-coupled* oscillators, *boundary layer* phenomena of fluids, and *slowly evolving damage* in a machine component. In all of these phenomena, there are at least two mechanisms which operate on distinctly disparate time/length scales. For example, in the case of the weakly damped simple pendulum, the pendulum executes *many* complete cycles of oscillation before its amplitude diminishes to, say, half of its initial value. Thus there is a fast time scale in which the system oscillates and a slow time scale in which the amplitude decays. In the case of accumulating damage in a machine component, it may tolerate many loading cycles before it fractures. There is some underlying defect which slowly evolves during the service of the component and leads to failure. In the case of flow of fluids over solid boundaries, there is a very small region adjoining the solid boundary where the fluid moves slowly and viscous forces predominate. Outside this *thin* region, the flow is predominantly inviscid. This is an example of a case with disparate *length scales.*

In this thesis, we restrict ourselves to the case of phenomena with disparate *time scales*, which is more relevant to the study of vibrations. By treating one of these scales as fast, we create a hierarchy of time scales on which the various processes operate. Once this identification of disparate time scales is made, the physical problem can be treated asymptotically using a well established multiple scales procedure.

1.1.2 Literature review

There exists an extensive literature on the method of multiple scales and the related method of averaging. The literature includes several popular textbooks, review articles, and papers describing the application of MMS to various systems. We shall review some of them here.

According to Nayfeh [1], there exist at least two versions of the method of multiple scales. One goes by the name of many-variable expansion, also called the derivative-expansion procedure. In this thesis, we adopt this first version. The second version goes by the name of two-variable expansion procedure [2]. In Chapter 6 of [1], the author begins with the development of these two versions in their basic forms and applies them to study several problems ranging from the simplest case of the harmonic oscillator with weak linear damping to systems as complicated as a weakly nonlinear partial differential equation modeling wave-wave interaction. Subsequently, the author presents generalizations of these two versions to deal with more complicated situations such as systems with variable coefficients.

The book by Nayfeh and Mook [3] addresses several problems arising in weakly nonlinear vibrations through the MMS. The range of applications studied there include free, forced, self-excited and parametrically excited vibrations of single and multi-degree of freedom systems, and continuous systems. Extensive references to the relevant literature are provided.

Application of the MMS to structural mechanics has been addressed in the book by Pai and Nayfeh [4]. Starting from one dimensional systems such as strings and cables, the book provides a thorough study of beams, membranes, plates, shells and composite structures. An extensive list of references has also been provided.

The book by Kevorkian and Cole [2] is more mathematically oriented. The class of problems studied there include boundary layer flow of viscous fluids, nonlinear oscillations of single and multi degree of freedom systems, passage through resonance problems, and some problems in shallow water waves and gas dynamics modeled by weakly nonlinear partial differential equations.

In addition to the abovementioned textbooks and many more (see, for e.g., [5, 6, 7]), there are several review articles on the general method itself as well as its application to several problems. We discuss them briefly here.

In a recent review article, Cartmell [8] discusses the origins, strengths, weaknesses, and the range of applicability of the method of multiple scales in the context of weakly nonlinear oscillators. The article examines various practical aspects of the method such as the role of term-ordering, non-dimensionalization and time scaling, series truncation, inclusion and exclusion of higher order nonlinearities, and typical problems in handling secular terms. The article also provides an extensive list of references.

In a critique [9], Nayfeh addresses the inconsistencies [10, 11] in the application of the MMS to higher orders and treatment of the resulting slow flow. These issues were also discussed in [8]. Similar studies for periodic motions of delayed systems can be found in [12]. Review articles on application of the MMS to specific areas of vibrations, such as modal interactions [13], machining dynamics [14] and many more, are available in the literature.

Apart from these text books, review articles and critiques, there are several research papers showcasing the application of the MMS to the study of various vibration related problems. An incomplete list includes problems related to wheel shimmy [15, 16], rotordynamics [17, 18], delayed systems [14, 19, 20], fractional order systems [21], strongly nonlinear oscillations [22, 23] and hysteretic systems [24]. Approximate realizations of the asymptotic calculation are discussed in [23, 25].

With the above brief introduction to the MMS, we now proceed to outline the problems studied in this thesis using this method.

1.2 Problems studied in this thesis

In what follows, we briefly present the nature of the four problems studied in this thesis. Each of these problems involves the application of the MMS at varying levels of sophistication. While some involve a straightforward application of the method to study the resulting dynamics, some others involve atypical steps in either the preparation of the system to apply the MMS or in the MMS procedure itself.

Amplitude control of a resonantly forced, weakly damped, harmonic oscillator

This study spans Chapters 2 through 4.

In this problem, we study some nonlinear dynamics related to the amplitude control of a weakly damped, harmonic oscillator subjected to weak control forcing. It is more usual to study the dynamics of the oscillator subjected to a *given* forcing. Here, however, we are interested in the dynamics of the system subjected to a suitably *chosen* control law to achieve a *desired* amplitude envelope.

The slow flow equations governing the evolution of the amplitude and phase of the oscillator are derived using a routine application of the MMS. Subsequently, a control law based on the speed-gradient algorithm [26, 27] is adopted. With this choice of control forcing, the dynamics is represented by a system of three coupled, nonlinear ordinary differential equations. The resulting system involves a non-analytic nonlinearity and a scalar free parameter. A preliminary numerical study of this system, aided by the time domain-based bifurcation package MATCONT [28, 29], reveals Hopf bifurcations, pitchfork bifurcations, and the presence of three limit cycles which seem to approach a homoclinic point upon variation of the control parameter. The presence of the non-analytic nonlinearity makes this homoclinic point atypical. A semi-analytical estimate of this atypical homoclinic parameter value is obtained. The initial MATCONT simulations could not get quite close to this estimated homoclinic point.

To approach the homoclinic points more closely, we present a new phase space-based algorithm for continuation of limit cycles using splines. The proposed algorithm works in phase space with an ordered set of points on the limit cycle, along with spline interpolation. The algorithm is applied to several popular systems involving homoclinic orbits with favorable results.

MMS *via* discretization of a fractionally damped van der Pol oscillator

In this second problem, the system of interest is still a single degree of freedom oscillator, but with self-excitation and fractional order damping. The presence of fractional damping introduces infinite dimensionality and makes the study interesting. This study is presented in Chapter 5.

Here, we use the MMS to analytically study the classical van der Pol oscillator with an added fractional order damping term, near the Hopf bifurcation point. Systems with $\mathcal{O}(1)$ fractional terms, such as this problem, have hitherto been largely treated numerically, after suitable approximations of the fractional order operator in the frequency domain. Here we take a semi-analytical route to study this system. We first approximate the fractional order term using a recently proposed Galerkin scheme [30] resulting in a set of ODEs. Subsequently, we restrict attention close to a Hopf bifurcation and study the near-Hopf dynamics using the MMS on the system of ODEs. The resulting MMS slow flow provides good approximations to the full numerical solutions. We also study the system under weak resonant forcing. The usual phenomena of quasiperiodicity, weak phase locking, and entrainment are all observed. An interesting observation in this work is that although the Galerkin approximation nominally leaves several long time scales in the dynamics, useful approximations are nevertheless obtained by the asymptotic method of multiple scales even for reasonably large departures from the Hopf bifurcation value.

Infinite dimensional slow modulation of cutting tool vibrations

This problem too is concerned with a single degree of freedom oscillator, but with infinite dimensional dynamics introduced through the presence of time delays. This study consists of Chapter 6.

Here we apply the MMS upto second order, as developed in [31], to a well known model of regenerative cutting vibrations in the large delay regime. While $\mathcal{O}(1)$ delays in machine tool vibrations have been extensively studied, here we are interested in large delays. By “large” we mean the delay is much larger than the time scale of typical cutting tool oscillations. Our second order analysis is found to be more accurate than the first order analysis. Unlike usual studies based on center manifold reductions, our MMS analysis is *not* restricted to near-Hopf situations and hence helpful to study a much wider parameter regime. The advantage of the present analysis is that infinite dimensional dynamics is retained in the slow flow, while the more usual center manifold reduction gives a planar phase space. Lower-dimensional dynamical features, such as Hopf bifurcations and families of periodic solutions, are also captured by the MMS. The large delay introduces sensitive dependence on small changes in parameters, which are well captured by the MMS approximations. Overall, a new and useful characterization of the nonlinear dynamics is obtained for a hitherto less-explored parameter regime.

Nonlinear secondary whirl of an overhung rotor

In this problem, as opposed to the first three problems, we study a two degree of freedom model [32] for a slightly asymmetric, horizontal, perfectly balanced, overhung rotor near its gravity critical speed. This study spans Chapters 7 through 9. We mention here that this work on overhung rotor also appears in [33].

We study an idealized asymmetric *nonlinear* overhung rotor model of [32], spinning close to its gravity critical speed. Nonlinearities arise from finite displacements, and the rotor's static lateral deflection under gravity is taken as small. Assuming small asymmetry and damping, slow modulations of whirl amplitudes are studied using the MMS. Inertia asymmetry has a second order effect on the gravity resonance. More interestingly, nonlinearities sustain the gravity resonance phenomenon even for a *symmetric* rotor. The resonant forcing from gravity has to be retained at leading order unlike usual studies on weakly nonlinear oscillations where the resonant forcing is taken to be weak. The usual phenomena of resonances, namely saddle-node bifurcations, jump phenomena and hysteresis, are all observed. An unanticipated periodic solution branch is found. In the three dimensional space of two modal coefficients and a detuning parameter, the full set of periodic solutions is found to be an imperfect version of three mutually intersecting curves: a straight line, a parabola, and an ellipse.

At the end of these four independent studies, we finally present some conclusions and pointers to future work in Chapter 10.

Chapter 2

Amplitude control of a resonantly forced, lightly damped, harmonic oscillator

In this chapter, we start the first part of this thesis namely the amplitude control of a resonantly forced, lightly damped, harmonic oscillator. More usually, studies are conducted for a given forcing. Here, however, we are interested in the dynamics of the system subjected to a suitably *chosen* control law to obtain a desired slowly varying amplitude envelope. Routine application of the MMS yields the slow flow equations for the amplitude and phase of the oscillator. The control forcing is then chosen based on the well known speed-gradient algorithm [26, 27]. The resulting dynamics is represented by a system of three coupled nonlinear ordinary differential equations. Preliminary numerical study of this system, aided by the bifurcation analysis package MATCONT, is presented which reveals among other things the interesting situation of three limit cycles apparently approaching homoclinic orbits. We also highlight the limitations of such packages in continuing limit cycles close to homoclinic points.

We mention that the discrete algorithm developed in connection with this problem appears in [34].

We now begin with a description of the system.

2.1 System

Our system (see Fig. 2.1) is a lightly damped harmonic oscillator with a frequency close to 1. The oscillator is subjected to weak resonant forcing as $f(t) = u(t)\sin(t)$, where $u(t)$ is a small and slowly varying function of time. The response is expected to be of the form $A\sin(t+\phi)$, where the amplitude A and the phase ϕ are expected to be slowly varying functions of time. Now, we wish to choose the control input $u(t)$ such that the amplitude of the response follows a given amplitude envelope. To that end, we first derive the slow flow equations of the system using the method of multiple scales.

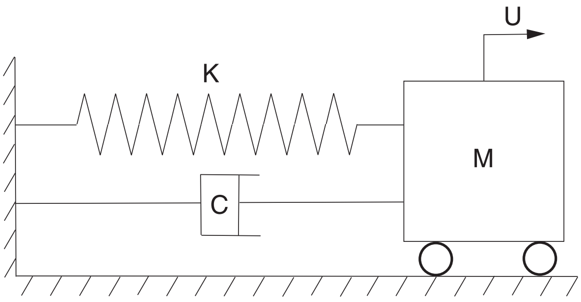

Figure 2.1: Simple harmonic oscillator.

2.2 Slow flow *via* the method of multiple scales

Consider the oscillator of Fig. 2.1. The governing equation of motion, after suitable scaling, is

$$\ddot{x} + \epsilon\, c\, \dot{x} + (1 + \epsilon\, \Delta)\, x = \epsilon\, U(\epsilon t)\, \sin(t), \tag{2.1}$$

where $0 < \epsilon \ll 1$, c is the damping coefficient, U is a slowly varying forcing function, and Δ represents the detuning from resonance. We derive the first order slow flow equations governing the evolution of the amplitude and the phase of the response using the MMS. The application of the MMS for this system is routine [1, 2, 3]. However, as we shall see, the resulting dynamics is interesting.

We begin by defining multiple time scales: $T_0 = t, \quad T_1 = \epsilon t, \quad T_2 = \epsilon^2 t, \cdots$. The solution is then assumed as a new function X of the multiple time scales as

$$x(t) = X(T_0, T_1, T_2, \cdots)\,. \tag{2.2}$$

The representation of the solution as in Eq. 2.2 is intuitively appealing and explicitly asserts that the solution is dependent on several independent time scales over which the various physical mechanisms act. For our case, the time scale $T_0 = t$ is associated with the normal oscillations at a frequency close to unity, and the slow time scale $T_1 = \epsilon t$ is associated with longer durations over which the forcing and damping act to produce significant changes in the response. With this definition of time scales, we write $U(\epsilon t) = U(T_1)$ in Eq. 2.1.

The derivatives are treated according to

$$\frac{d}{dt} = \frac{\partial}{\partial T_0} + \epsilon \frac{\partial}{\partial T_1} + \epsilon^2 \frac{\partial}{\partial T_2} + \cdots\,. \tag{2.3}$$

Henceforth for this system, we will conduct a first order analysis only. In addition, the solution itself is expanded in a power series in ϵ as

$$X(T_0, T_1) = X_0(T_0, T_1) + \epsilon X_1(T_0, T_1) + \cdots\,. \tag{2.4}$$

Here it is assumed that X_0 and X_1 are $\mathcal{O}(1)$ quantities.

Substituting Eq. 2.4 in Eq. 2.1 and using Eq. 2.3, at $\mathcal{O}(1)$ we have

$$\frac{\partial^2 X_0}{\partial^2 T_0^2} + X_0 = 0\,, \tag{2.5}$$

where, for simplicity of notation, we have suppressed the dependencies of X_0 on the independent variables.

The solution of Eq. 2.5 is

$$X_0(T_0, T_1) = A(T_1) \sin\left(T_0 + \phi(T_1)\right), \tag{2.6}$$

where A and ϕ are the amplitude and phase of the oscillations respectively. Note that since Eq. 2.5 is a *partial differential equation* in T_0, its solution contains arbitrary functions of the independent variables other than T_0. Thus in Eq. 2.6, we have taken the amplitude A and phase ϕ as functions of T_1.

Substituting Eq. 2.6 in Eq. 2.1, we get at $\mathcal{O}(\epsilon)$:

$$\begin{aligned}\frac{\partial^2 X_1}{\partial^2 T_0^2} + X_1 \;=\; & \left(-U + A\Delta\cos(\phi) - cA\sin(\phi) - 2\frac{d\phi}{dT_1} A\cos(\phi) - 2\frac{dA}{dT_1}\sin(\phi)\right)\sin(T_0) + \\ & \left(cA\cos(\phi) + A\Delta\sin(\phi) - 2\frac{d\phi}{dT_1}A\sin(\phi) + 2\frac{dA}{dT_1}\cos(\phi)\right)\cos(T_0)\,. \qquad (2.7)\end{aligned}$$

Now the right hand side of Eq. 2.7 contains resonant forcing. To ensure that we get a bounded solution for X_1 consistent with the assumptions of Eq. 2.4, we set the coefficients of these harmonic forcing terms to zero. This step is popularly known as removal of secular terms.

Thus setting the coefficients of $\cos(T_0)$ and $\sin(T_0)$ to zero and solving the resulting set of linear algebraic equations, we arrive at the slow flow

$$\frac{dA}{dT_1} = -\frac{cA}{2} - \frac{U\sin(\phi)}{2}\,, \qquad (2.8)$$

$$\frac{d\phi}{dT_1} = \frac{\Delta}{2} - \frac{U\cos(\phi)}{2A}\,. \qquad (2.9)$$

Equations 2.8 and 2.9 govern the slow evolution of amplitude and phase of the response. For a *given* U, it is straightforward to determine the response by integrating Eqs. 2.8 and 2.9 (numerically if necessary).

Here, however, we are interested in *determining* the control input U that is required to asymptotically track a specified time profile, $\hat{A}$, of the amplitude. To that end, we adopt the control law:

$$\frac{dU}{dT_1} = \frac{K\,(A-\hat{A})\,\sin\phi}{2}\,, \qquad (2.10)$$

where K is a user-specified control gain. The above control law is based on the well-known speed-gradient algorithm [26, 27]. Note that our aim here is not to critique the control law, but to investigate the resulting dynamics.

On scaling time as $\tau = \frac{T_1}{2}$ and denoting τ-derivatives using overdots, Eqs. 2.8 and 2.10 become

$$\dot{A} = -c\,A - U\,\sin\phi\,, \qquad (2.11)$$

$$\dot{\phi} = \Delta - \frac{U\,\cos\phi}{A}\,, \qquad (2.12)$$

$$\dot{U} = K\,\sin\phi(A-\hat{A})\,. \qquad (2.13)$$

Rewriting Eqs. 2.11 through 2.13 in Cartesian coordinates using $x = A\,\cos\phi$ (note that this x is different from that of Eqs. 2.1 and 2.2), $y = A\,\sin\phi$ and $z = U$, and (arbitrary choices) setting $\hat{A} = 3$, $c = 1$ and $\Delta = 3$, we have

$$\begin{aligned} \dot{x} &= -x - 3\,y\,, && (2.14)\\ \dot{y} &= 3\,x - y - z\,, && (2.15)\\ \dot{z} &= K\,y\left(1 - \frac{3}{\sqrt{x^2+y^2}}\right)\,. && (2.16) \end{aligned}$$

2.3 Study of Eqs. 2.14 through 2.16

From now on, we focus on the study of Eqs. 2.14 through 2.16. The system has a non-analytic nonlinearity, and the origin is not a fixed point. The system involves a single, scalar parameter K. We will focus on the periodic solutions of this system and their continuation with respect to the system parameter K.

Periodic orbits

Equations 2.14 through 2.16 possess two equilibria at $\left(\frac{-9}{\sqrt{10}}, \frac{3}{\sqrt{10}}, \frac{-30}{\sqrt{10}}\right)$ and $\left(\frac{9}{\sqrt{10}}, \frac{-3}{\sqrt{10}}, \frac{30}{\sqrt{10}}\right)$ for any K. At $K = 25$, there is a subcritical Hopf bifurcation and two small, unstable limit cycles are born around these two equilibria.

For a range of $K < 25$, these two unstable limit cycles exist near these equilibria. There also exists a large (i.e., distinct from the two small ones born about equilibrium points), stable limit cycle for these K values. For $K > 25$, the large limit cycle exists but the small ones do not. As K decreases from 25, these limit cycles evolve. In particular, the two small limit cycles grow in size and approach the large limit cycle. A plot of these large and small limit cycles at $K = 17.14$ is provided in Figs. 2.2 and 2.3. A 3D plot is provided in Fig. 2.2, and we plot the $X - Y$ projection of the 3D plot in Fig. 2.3. There is at least one symmetry-breaking pitchfork bifurcation of the large limit cycle (at $K \approx 15.15$), with subsequent bifurcations of the resulting limit cycles as well, but we do not report on them here and focus on the numerical continuation of the primary solution branch.

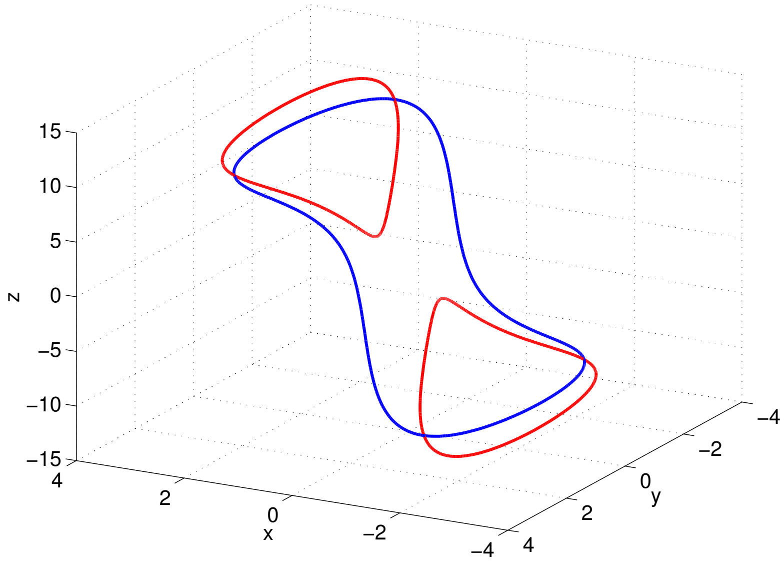

Figure 2.2: Left: 3-D plot of large and small limit cycles of Eqs. 2.14 through 2.16 for $K = 17.14$.

We initially performed continuation of these limit cycles using the popular bifurcation analysis package MATCONT [28, 29], before developing our continuation algorithm. In MATCONT simulations, the small orbit could be continued upto $K = 13.8740$, while the large orbit could be continued upto $K = 13.9326$. Continuation subsequently became difficult due to the highly unstable nature of these limit cycles. It is possible that some combination of skill and determination may coax MATCONT, which allows choice of some free parameters, to go somewhat closer. In this context, we document some of our experiences with MATCONT in Tables 2.1 and 2.2.

The small and large limit cycles, from MATCONT simulations, at $K = 13.9412$ are shown in Fig. 2.4. It is clear from Fig. 2.4 that as K decreases, the large and the small orbits approach each other, and we expect that at some critical value of K these three cycles merge with each other at a homoclinic point and disappear. Due to the non-analytic nonlinearity and hence the lack of a genuine equilibrium at the origin, an estimate of this homoclinic parameter value cannot be obtained using standard methods [35, 36, 37, 38, 39, 40]. A semi-analytical estimate of the same will be provided in Chapter 4.

For now, it appears from our results that a time-domain collocation based software

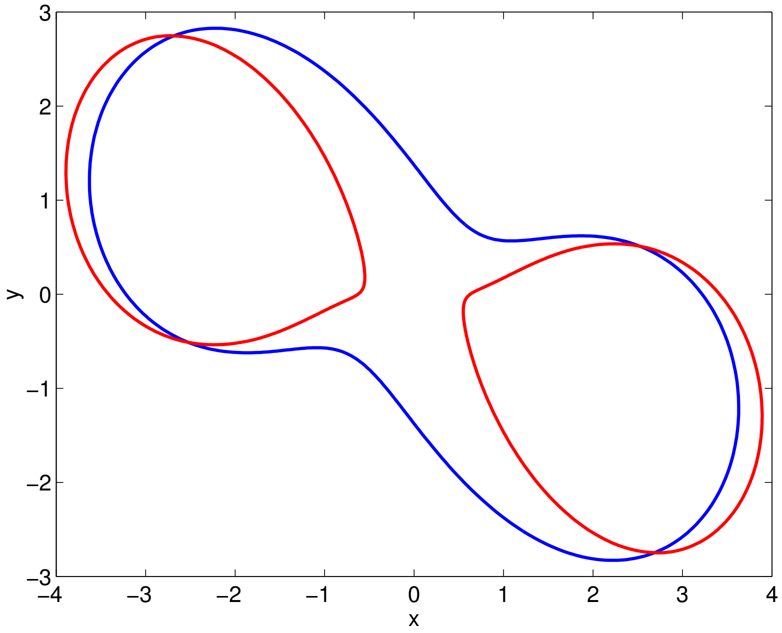

Figure 2.3: $X - Y$ projection of large and small limit cycles of Eqs. 2.14 through 2.16 for $K = 17.14$.

NTST	NCOL	min. step size	max. step size	Tol.	min. K attained
40	4	$1e-5$	0.1	$1e-8$	13.9412
30	4	$1e-5$	0.1	$1e-6$	13.9465
20	4	$1e-5$	0.1	$1e-6$	13.9408
60	4	$1e-12$	0.1	$1e-6$	13.9326
100	4	$1e-12$	0.1	$1e-8$	13.9549
200	6	$1e-5$	0.1	$1e-8$	13.9775

Table 2.1: MATCONT results for continuation of large, symmetric orbit of Eqs. 2.14 through 2.16. In this and all tables that follow, "Tol." refers to the error tolerance setting used in MATCONT.

such as MATCONT, though generally versatile and powerful, is presently unable to get very close to this homoclinic point in a reliable fashion: increasing the number of subin-

NTST	NCOL	min. step size	max. step size	Tol.	min. K attained
20	4	$1e-5$	0.1	$1e-6$	13.8740
30	4	$1e-5$	0.1	$1e-6$	14.2471
40	4	$1e-5$	0.1	$1e-6$	14.3225
60	4	$1e-5$	0.1	$1e-6$	14.3294
100	4	$1e-5$	0.1	$1e-6$	14.3247
200	4	$1e-5$	0.1	$1e-6$	14.3226
200	6	$1e-8$	0.2	$1e-8$	14.3299
60	7	$1e-5$	0.1	$1e-8$	14.2763

Table 2.2: MATCONT results for continuation of small, asymmetric orbit of Eqs. 2.14 through 2.16.

tervals “NTST” and the number of collocation points “NCOL” therein does not produce monotonically closer approach to the homoclinic point.

In the next section, we discuss the possible reasons for the failure of MATCONT and a possible remedy to the situation.

2.4 Need for a better continuation algorithm

In bifurcation analysis packages like MATCONT, limit cycles are computed by solving a boundary value problem in the time domain [41, 42]. The limit cycle, which is a periodic solution in the time domain, is sought as a solution of a boundary value problem with periodic conditions at the end points of the unknown time period interval. The solution of this boundary value problem is then determined by a collocation method. While this strategy to compute limit cycles is versatile and successful in most cases, it may be troublesome in cases of limit cycles approaching homoclinic orbits.

For a limit cycle approaching a homoclinic orbit, a large fraction of the total time

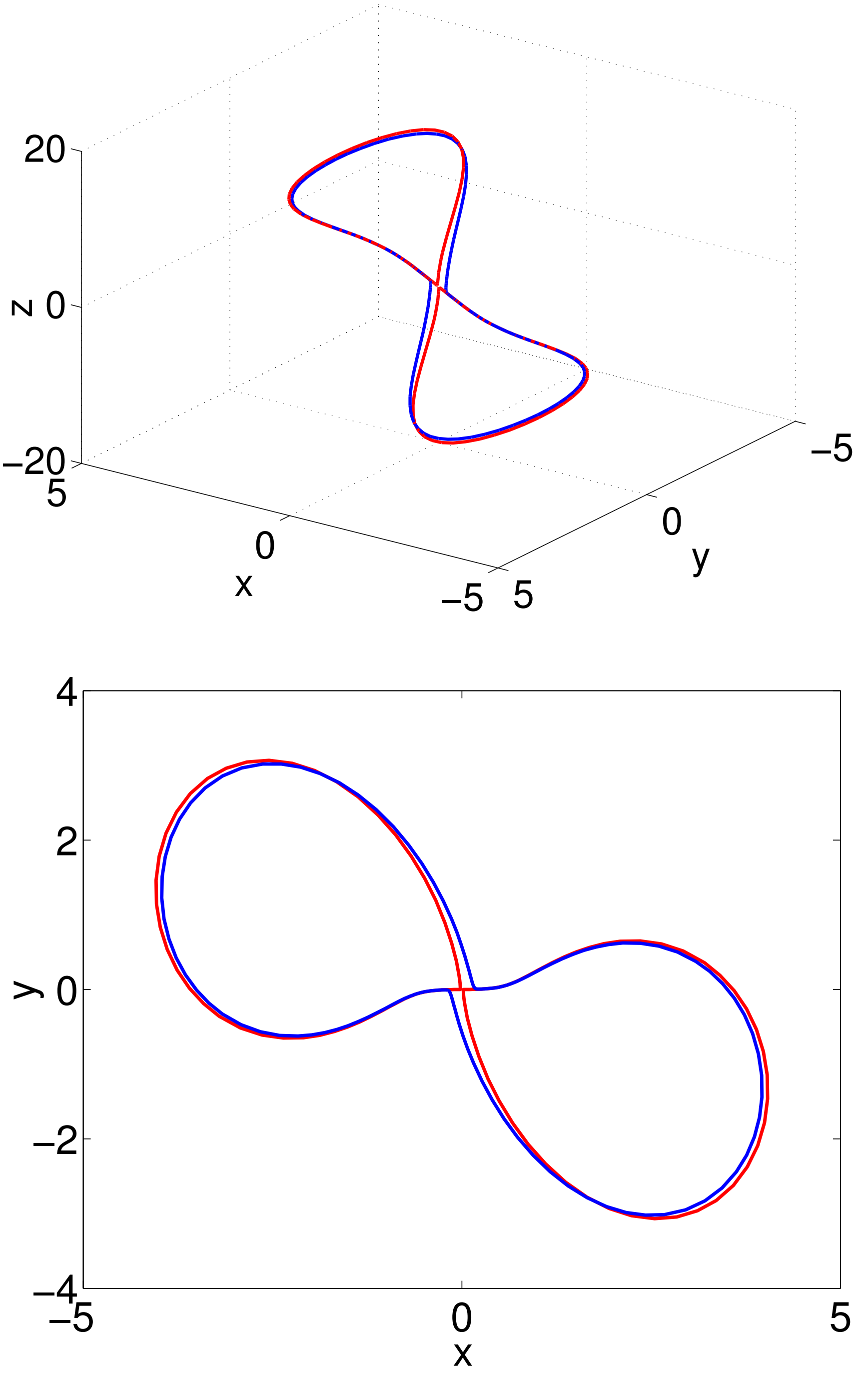

Figure 2.4: MATCONT plots of large and small orbits of Eqs. 2.14 through 2.16 for $K = 13.9412$. Top: 3-D plot. Bottom: limit cycle projected onto $X - Y$ plane.

period of the solution is spent in traversing a short length of the trajectory in phase space near the fixed point, while the rest of the length of the trajectory is traversed in a much smaller fraction of the total time period. Thus the near-homoclinic orbits in phase space represent *near-discontinuous* solutions in the time domain, and hence time domain-based methods, such as in MATCONT, have to tackle a discontinuity while approximating these near-homoclinic limit cycles. On the other hand, in phase space such near-homoclinic orbits represent kink-like situations which are easier to handle than the discontinuities in time domain. Also, the arclength of the limit cycle remains finite as the limit cycle becomes near-homoclinic, while the time period of the limit cycle grows unbounded, leading to numerical difficulties.

Thus, phase space-based algorithms may perform better in continuation of limit cycles close to homoclinic orbits. We present one such algorithm in the next chapter and explain the similarities and differences between our algorithm and other contemporary phase space-based algorithms [43, 44, 45].

With the newly developed algorithm, we will revisit Eqs. 2.14 through 2.16 in Chapter 4 and obtain much closer approaches to the homoclinic point than that attained by MATCONT.

Chapter 3

A new phase space-based limit cycle continuation algorithm

Motivated by the need to continue the limit cycles of the system studied in Chapter 2 close to the homoclinic point, here we develop a new phase space-based algorithm for continuation of limit cycles in autonomous systems involving a scalar free parameter. The algorithm is first presented in a three dimensional setting. Subsequently, the procedure to compute auxiliary quantities such as time period and Floquet multipliers of the limit cycle are outlined. We apply the proposed algorithm to continue limit cycles in several popular systems, with favorable results. We then reformulate our algorithm using infinitesimal parameter increments to obtain ordinary differential equations (ODEs). This ODE formulation enables us to exploit the advantages offered by commercial ODE solvers, such as adaptive step-sizing capabilities and the ease of data storage provided. The ODE formulation, upon suitable reparametrization, is also shown to continue limit cycle solution branches past fold points, which is a useful feature in bifurcation analyses. Finally, we outline the extension of the proposed algorithm to dimensions greater than three.

We now begin with a brief introduction to our algorithm as well as a survey of the relevant literature.

3.1 Introduction

Systems of ODEs often exhibit limit cycles in certain parameter regimes. As parameters are varied, these limit cycles can undergo a variety of bifurcations (see, e.g., [46, 47, 48]). Among these, the creation of homoclinic connections is to some extent a motivation for this work. We present here a method for numerical continuation of limit cycles wherein we work directly in the phase space and drop explicit consideration of the underlying time. The method seems to have advantages over the usual time-based strategies when the limit cycle approaches a saddle homoclinic point. Compared to other approaches to continuation of limit cycles using geometrical ideas in phase space where the limit cycle is viewed as a curve (a geometrical object), here we represent the limit cycle using a simpler geometrical object, namely a finite, ordered set of discrete points in phase space.

There presently exist powerful and versatile software packages that perform, among other things, continuation of limit cycles in parameter space; these include LOCBIF [49], AUTO [50], and MATCONT [28, 29]. Specifically for continuation of limit cycles, these packages retain the independent variable (time), rescale it to unit length (using the as yet unknown time period of the cycle), and use some form of either shooting or collocation [41, 42, 51, 52, 53].

One problem with explicitly retaining the time is that as the limit cycle approaches a hyperbolic fixed point, the flow slows down. Consequently, all the variation within the limit cycle gets compressed into a small proportion of the overall time interval, leading to numerically troublesome near-discontinuous trajectories.

Continuation of limit cycles in phase space, parametrized by arclength, has also been developed (see, e.g., [43, 44, 45]). In this approach, the limit cycle is viewed as a geometric object, namely a closed curve, and the natural parametrization of arclength is adopted. Subsequently, solution and continuation proceeds with the usual collocation based methods.

Here, we align with [43] in viewing the limit cycle as a geometric object, but computationally work with a finite, ordered set of discrete points in phase space as opposed to a curve; and we put forward equations governing the evolution of these points in phase space as a parameter is varied. The independent variable in our approach is an artificial continuous variable which takes on consecutive integral values at successive discrete points representing the limit cycle. This index-based variable implies an underlying variable stretching of the arclength coordinate, but requires no explicit knowledge thereof; it gives us flexibility in setting up equations for continuation of limit cycles as a parameter is varied, as will be seen below.

Thus, we differ from the explicit time-based approaches in reducing discontinuities to corners as saddle homoclinic points are approached; and we differ from the arclength-based approaches [43, 44, 45] in both our implicit rescaling and conceptually finite dimensional strategy. In our numerical examples below, we will focus on continuation close to saddle homoclinic points, and compare results from our algorithm with a popular time-domain based approach, which (in contrast with, say, [43]) is both readily available in the form of functional software and serves as a benchmark.

The algorithm developed and demonstrated in this preliminary work is limited to autonomous systems; is presently unable to address issues involving higher codimension bifurcations [54, 55, 56, 40]. Our algorithm is most useful in the (possibly unanticipated) approach to a saddle homoclinic bifurcation[1]; and may eventually serve as an extra option for an analyst using a package such as mentioned above.

In what follows we will describe the proposed algorithm in some detail, and then consider some numerical examples. For these problems, our algorithm does very well. Comparisons with MATCONT are favorable.

We emphasize that wherever we compare our results with MATCONT below, we focus on but one feature of MATCONT; and our intention is to compare our phase space-based approach with the time-based collocation methods popularly employed in several commercial packages, of which MATCONT is just one example. We mention that henceforth in this chapter and elsewhere in this thesis, wherever we refer to homoclinic points, we mean saddle homoclinic points with all leading eigenvalues being real.

---

[1] Near a saddle-focus with leading complex eigenvalues infinitely many fold points exist along the cycle branch [57], and hence our algorithm fails near such points.

3.2 Algorithm

Our algorithm takes several points in phase space that lie on the limit cycle for a given parameter value; and then for a nearby parameter value seeks nearby points in phase space, subject to conditions discussed below, to approximate the limit cycle. All interpolation between points is done using splines in phase space; the index i of each point along the curve is treated as a discrete value of a continuous underlying variable also called i, which is the independent variable in the splines. There is no preferred directionality along the limit cycle, and stability of the limit cycle is irrelevant.

Consider a system of parameterized ODEs

$$\dot{X} = F(X, \lambda), \tag{3.1}$$

where X is the state vector and λ is a scalar free parameter. For simplicity, we first consider the case when X is 2- or 3- dimensional. Extension to higher dimensions is presented in section 3.8.

We assume that we have a starting limit cycle solution, for some λ, obtained by any method. We choose n points on the limit cycle in phase space as shown schematically in Fig. 3.1. The position vectors of the points are $X_1, X_2, \ldots, X_n$. Let the parameter be varied from λ to $\lambda + \Delta\,\lambda$. The corresponding increments of the position vectors, $\Delta\,X_1, \ldots, \Delta\,X_n$, are to be determined. Our strategy, as is usual, is to construct a vector $g(y)$, where y and g are m-dimensional (for suitable m), and numerically seek a solution to the vector equation $g(y) = 0$. The construction of $g(y)$ is described below.

Consider the discrete indices $I = \{1, 2, 3, \ldots, n\}$ labeling the points $\{X_1 + \Delta\,X_1, \ldots, X_n + \Delta\,X_n\}$. We approximate the limit cycle by treating i as a continuous variable, which takes values between 1 and $n+1$; and by interpolating the individual components of X_i using cubic splines. In the spline fit we use *periodic* end conditions: this is possible, e.g., through a built-in function in MATLAB, after augmenting the list of points by one (setting $X_{n+1} = X_1$).

We need to determine n vector increments for n points. This amounts to $3\,n$ scalar unknowns in a 3D setting, for which we need $3\,n$ scalar equations (the 2D case is easier). In phase-space based approaches (see, for example, [58]) where the limit cycle is viewed as

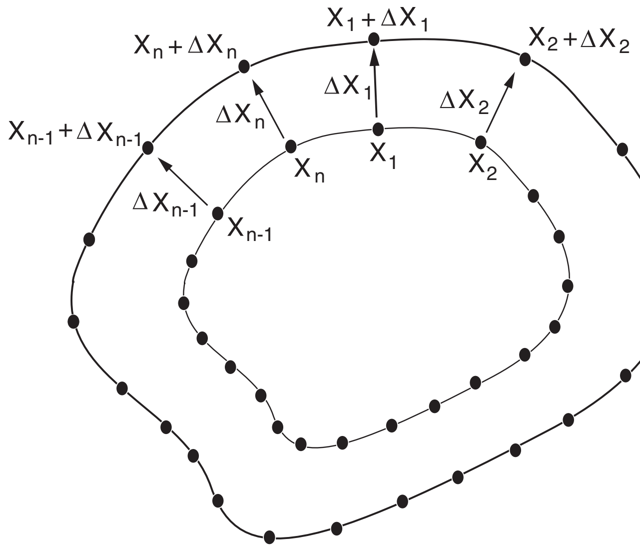

Figure 3.1: A schematic of the limit cycle and increments in position vectors.

a closed curve, the flow field ($F(X, \lambda)$) at each point is constrained to be along the local tangent to the limit cycle. In a 3-dimensional setting, this constraint yields 2 conditions at each point, while the remaining condition is provided by enforcement of the parametrized differential equation along the tangential direction.

The equations we will formulate below have some similarities with the above approach in that we too explicitly enforce the flow to be parallel to the local tangent to the limit cycle at n points. However, we *do not* explicitly parametrize the limit cycle in the tangential direction, and use other conditions as will be explained below.

We now proceed to set forth $3\,n$ equations governing the increments of the position vectors of the points.

1. The first of these $3n$ equations is special, in that it incorporates a phase condition (see, for example, [59]) to ensure uniqueness. Here, we incorporate the classical Poincaré phase condition. Note that there are other, perhaps numerically more convenient, phase conditions employed elsewhere (see, for example, [38]). We let ΔX_1 be normal to the flow field direction at X_1. This is achieved by

$$\langle \Delta X_1, F(X_1, \lambda) \rangle = 0, \tag{3.2}$$

where $\langle ., . \rangle$ is the Euclidean inner product. A similarly motivated phase condition that involves an integral or average leads to greater computational complexity that is avoided here.

2. Let ΔS_i be the change in length of the ith segment of the limit cycle. More precisely,

$$\Delta S_i = \|(X_{i+1} + \Delta X_{i+1}) - (X_i + \Delta X_i)\| - \|X_{i+1} - X_i\|,$$

where $i = 1, 2, \ldots, n$, and $\|.\|$ is the Euclidean norm.

Further, let κ denote the curvature at the midpoint of a segment. That is (see [60]),

$$\kappa_i = \frac{\|X'_{i+1/2} \times X''_{i+1/2}\|}{\|X'_{i+1/2}\|^3},$$

where the derivatives required above are evaluated using the spline interpolant (Matlab returns the required polynomial coefficients). Note that the primes here, as well as in our formulation that follows, denote derivatives with respect to the index variable i. We then adopt the $n - 1$ dimensionless scalar equations

$$\Delta S_i \, (\bar{\kappa} + \kappa_i) = \Delta S_{i+1} \, (\bar{\kappa} + \kappa_{i+1}), \quad i = 1, 2, \ldots, n-1. \tag{3.3}$$

where $\bar{\kappa}$ is the mean curvature over all i.

The above condition is somewhat arbitrary, but may be motivated as follows. First, we wish to have some control over the evolving distribution of points on the periodic orbit; and plan to achieve this by imposing conditions either on arclength or changes thereof. Second, we wish to write dimensionless equations; and so curvature is used to introduce another length scale in addition to arclength. Note that in the proposed condition (Eq. 3.3), ΔS_i can be positive or negative; but the sign must be the same for all i. When the overall length of the periodic orbit in phase space increases (or decreases), each ΔS_i will be positive (respectively, negative). However, the change in length will be smaller in places where the curvature is higher, forcing the points to spread out in portions of relatively low curvature.

We try to elaborate more here. We recall that our approach here is to represent the limit cycle (which is a closed curve) by a finite set of points and put forth conditions governing the positions of these points. Firstly, we have to ensure that the points do sit on the new limit cycle corresponding to the new parameter value. This is assured by the tangent constraints that will be explianed soon below. After positioning the points *on* the limit cycle, we still have the freedom to distribute the points *along* the limit cycle. Here, an analogy of the limit cycle to a rigid wire and the points to be beads along the wire may be helpful. We exploit this freedom to pack these points more closely in regions where the limit cycle has greater curvature. This will help us capture sharp regions of the limit cycle well. We anticipate such sharp regions in near-homoclinic orbits. Note also that freedom in this context is just another name for indeterminacy in that these conditions, or any other suitable arbitrary condition governing the distribution of points, fix the positions of the points on the limit cycle. The $n-1$ added conditions incorporated through Eq. 3.3 thus serve two purposes:

(a) Remove indeterminacy, and

(b) Control the relative spreading out of points, keeping arclength changes small in regions of high curvature and large in regions of low curvature.

The presence of mean curvature $\bar{\kappa}$ in Eq. 3.3 plays a stabilizing role by avoiding excessive stretching of segments with low curvature. It may be possible in future work to develop more sophisticated criteria which *increase* the density of points in regions of high curvature, but we have avoided this issue here for simplicity.

We now have n equations, and need $2n$ more.

3. The actual flow should be directed along the limit cycle, and this will give us $2n$ equations. Note that this is equivalent to Eq. 2 of [58].

   Derivatives of interpolants tend to be least accurate at interpolation points. Accordingly, taking derivatives of $X + \Delta X$ (from the spline interpolant), we will require that

$$X'_{i+1/2} + \Delta X'_{i+1/2}$$

   and

$$F(X_{i+1/2} + \Delta X_{i+1/2}, \lambda + \Delta\lambda)$$

   are *parallel*.

   Specifically, letting[2]

$$\overrightarrow{A_i} = (X_{i+1/2} + \Delta X_{i+1/2})' = X'_{i+1/2} + \Delta X'_{i+1/2},$$

---

[2] The interpolant of the sum is the sum of the interpolants.

and letting

$$\overrightarrow{B_i} = \frac{F(X_{i+1/2} + \Delta X_{i+1/2}, \lambda + \Delta\lambda)}{\|F(X_{i+1/2} + \Delta X_{i+1/2}, \lambda + \Delta\lambda)\|},$$

we form the cross-product of $\overrightarrow{A_i}$ and $\overrightarrow{B_i}$ as

$$\overrightarrow{C_i} = \overrightarrow{A_i} \times \overrightarrow{B_i}.$$

We wish to enforce $\overrightarrow{C_i} = 0$.

In three dimensions[3], we use the principal normal along the known limit cycle [60],

$$\overrightarrow{P_i} = \frac{X'_{i+1/2} \times (X''_{i+1/2} \times X'_{i+1/2})}{\|X'_{i+1/2}\|^4},$$

and the binormal

$$\overrightarrow{Q_i} = \frac{X'_{i+1/2}}{\|X'_{i+1/2}\|} \times \frac{\overrightarrow{P_i}}{\|\overrightarrow{P_i}\|},$$

where $X'_{i+1/2}$ is understood to be a vector in 3D. Then we write two scalar equations for each interval:

$$\left\langle \overrightarrow{C_i}\,, \frac{\overrightarrow{P_i}}{\|\overrightarrow{P_i}\|} \right\rangle = 0, \quad i = 1, \ldots, n, \tag{3.4}$$

and

$$\langle \overrightarrow{C_i}\,, \overrightarrow{Q_i} \rangle = 0, \quad i = 1, \ldots, n. \tag{3.5}$$

Equations (3.4) and (3.5), evaluated for each segment, together provide $2\,n$ scalar equations, bringing the total to the required $3n$.

The above equations, given X_i, λ and $\Delta\lambda$, are to be solved iteratively for the unknown increments ΔX_i, $i = 1, \ldots, n$. This completes the continuation strategy. After finding the limit cycle, we can estimate the time period of the limit cycle solution using numerical integration. Floquet multipliers can also be estimated. These procedures will be described here below. As indicated earlier, however, the strength of the method seems to lie in approaching homoclinic points.

---

[3] In two dimensions, $\overrightarrow{C_i}$ has only one nontrivial component, $A_{i1}B_{i2} - A_{i2}B_{i1}$, which we set to zero. This gives n equations, one for each interval; and we have all the equations we need.

3.2.1 Time period computation

The time period computation proceeds by adding up the times taken for a phase point to traverse each of the individual segments of the computed limit cycle curve. That is,

$$T = \sum_{i=1}^{n-1} \int_{X_i}^{X_{i+1}} \frac{ds}{V} + \int_{X_n}^{X_1} \frac{ds}{V},$$

where each path-dependent integral is evaluated along the (spline-interpolated) limit cycle, and V is the variable speed of the phase point along the limit cycle (i.e, the magnitude of the vector field). Rewriting the above in terms of the index-based variable used in our work,

$$T = \sum_{i=1}^{n-1} \int_{j=i}^{j=i+1} \frac{\|X'\|\,dj}{\|F(X,\lambda)\|} + \int_{j=n}^{j=n+1} \frac{\|X'\|\,dj}{\|F(X,\lambda)\|},$$

where $j \in [i, i+1]$ is a continuous variable of integration and $X_{n+1} = X_1$ by periodicity. We have evaluated the above integrals using the elementary midpoint rule, because hundreds of points on the limit cycle are available.

3.2.2 Floquet multiplier computation

Consider the variational equation associated with the limit cycle solution $x(t)$ of Eq. 3.1

$$\dot{y} = \left.\frac{\partial F(X,\lambda)}{\partial X}\right|_{X=x(t)} y. \tag{3.6}$$

We wish to compute the monodromy matrix associated with Eq. 3.6 using the spline-interpolated limit cycle points. To that end, we rewrite Eq. 3.6 in terms of the index-based variable j as

$$y' = J\,y,$$

where the Jacobian

$$J = \frac{\|X'\|}{\|F(X(j),\lambda)\|} \left.\frac{\partial F(X(j),\lambda)}{\partial X}\right|_{X=x(j)},$$

primes denote derivatives with respect to j, and X is taken as a function of j. Let J_i denote the Jacobian at $X_{i+1/2}$ evaluated using the spline-interpolant. For a sufficiently refined mesh (i.e., when many points are used on the limit cycle), the constant J_i can be used in place of the variable J over the interval $[i, i+1]$. We then have, over the interval $[i, i+1]$, the approximate solution

$$y(i+1) = e^{J_i}\, y(i).$$

Then

$$y(T) = y(n+1) = \left(e^{J_n} \dots e^{J_1}\right) y(1),$$

and the desired Floquet multipliers are the eigenvalues of

$$M = e^{J_n} \dots e^{J_1}.$$

3.3 Numerical examples

We now apply the above developed algorithm to four popular examples. Of these, three involve approach to homoclinic points and one is a more routine example. In all these cases, the algorithm is shown to perform as good or better than MATCONT.

3.3.1 The Lorenz system

We next consider the well-known Lorenz system with popular parameter values,

$$\begin{aligned} \dot{x} &= 10\,(y - x), & (3.7)\\ \dot{y} &= \rho\, x - y - z\, x, & (3.8)\\ \dot{z} &= x\, y - 8\, z/3. & (3.9) \end{aligned}$$

Of particular interest here is the homoclinic bifurcation at $\rho \approx 13.9265$ [61, 62].

Tight estimates of the homoclinic parameter value are obtained in the literature [63, 64]. Here we are interested in applying our algorithm to continue the relevant limit cycle(s) as close to the homoclinic point as possible. In MATCONT, we could proceed upto about $\rho = 13.9820$. Using our algorithm with 500 points starting at $\rho = 15$, we reached $\rho = 13.92678$. In other words, our algorithm got closer by two orders of magnitude (again, more determined or expert use of MATCONT may reduce this difference; but see Table 3.1). Some relevant results are plotted in Figs. 3.2 through 3.3.

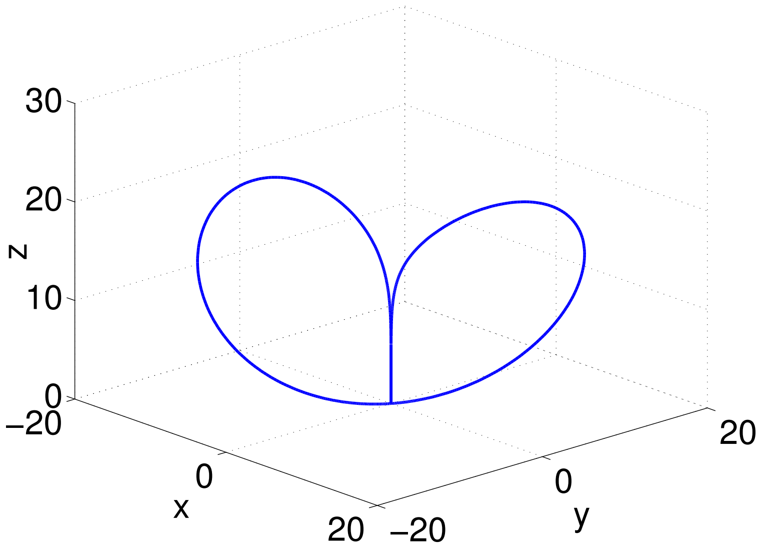

Figure 3.2: Limit cycle solutions (there are two cycles plotted) of Eqs. 3.7 through 3.9 from our algorithm for $\rho = 13.92678$.

NTST	NCOL	min. step size	max. step size	Tol.	min. ρ attained
20	4	$1e-5$	0.1	$1e-6$	14.025229
50	4	$1e-5$	0.1	$1e-6$	14.088939
20	4	$1e-12$	0.01	$1e-8$	14.028721
30	4	$1e-12$	0.01	$1e-8$	14.021818
60	4	$1e-12$	0.01	$1e-8$	14.085116
20	4	$1e-12$	0.01	$1e-6$	14.028467
20	4	$1e-12$	0.1	$1e-8$	13.982035
50	4	$1e-12$	0.1	$1e-8$	14.124387

Table 3.1: MATCONT results for limit cycle of Eqs. 3.7 through 3.9.

3.3.2 Chua's circuit

We next consider the Chua's circuit [65] equations

$$\dot{x} = \alpha\,(y - x^3/16 + x/6), \tag{3.10}$$

$$\dot{y} = x - y + z, \tag{3.11}$$

$$\dot{z} = -\beta\,y. \tag{3.12}$$

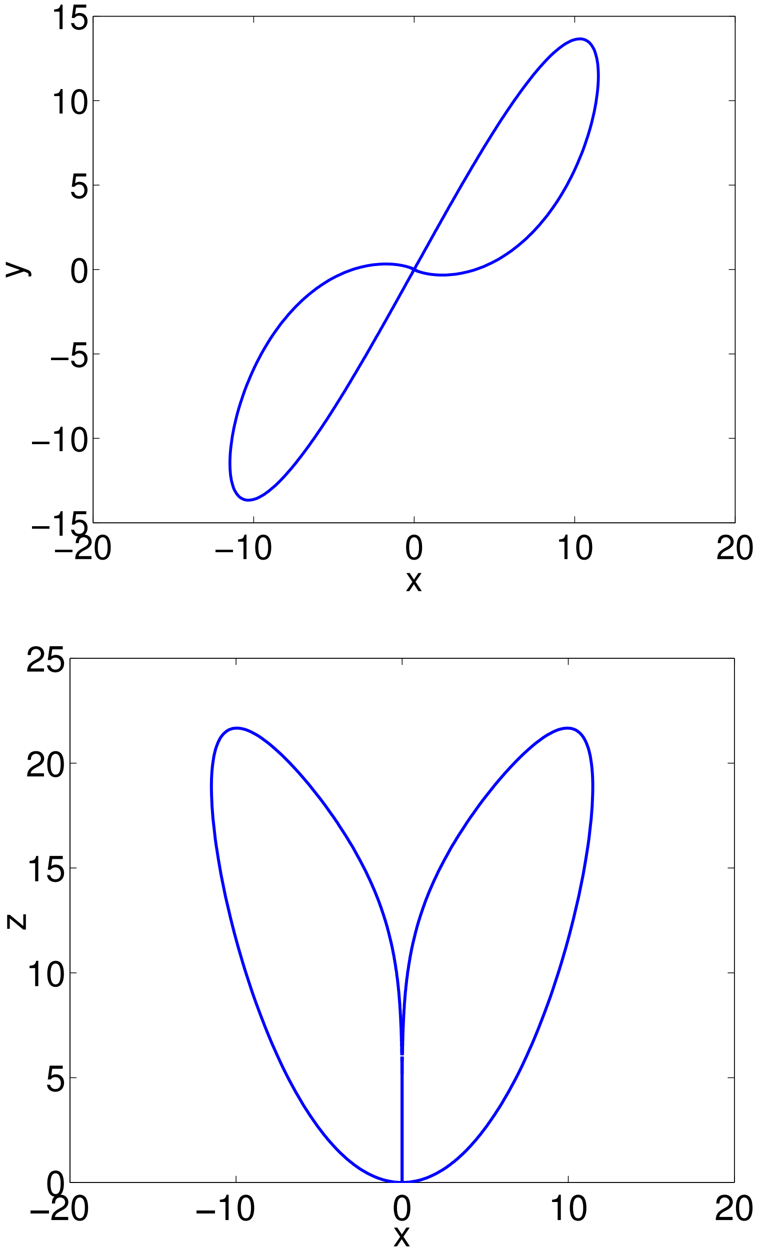

Figure 3.3: 2-D view of limit cycle of Eqs. 3.7 through 3.9 obtained from our algorithm for $\rho = 13.92678$. Top: $X - Y$ projection. Bottom: $X - Z$ projection.

The system has three fixed points, at $(0, 0, 0)$, $\left(\sqrt{\frac{8}{3}}, 0, -\sqrt{\frac{8}{3}}\right)$ and $\left(-\sqrt{\frac{8}{3}}, 0, \sqrt{\frac{8}{3}}\right)$. In [65], the system was studied for $\beta = 14$, $\beta = 1.4$ and $\beta = 0.5$.

For $\beta = 0.5$, a homoclinic bifurcation is reported at $\alpha = 0.576$ in [65]; unfortunately, no more significant digits are reported. For this same value, $\beta = 0.5$, we numerically continued the limit cycles using MATCONT and our algorithm.

NTST	NCOL	min. step size	max. step size	Tol.	min. α attained
20	4	$1e-12$	0.005	$1e-8$	0.58101094
50	4	$1e-12$	0.005	$1e-8$	0.58333874
60	4	$1e-12$	0.005	$1e-8$	0.58452656
20	4	$1e-5$	0.1	$1e-6$	0.58246042
30	4	$1e-5$	0.1	$1e-6$	0.58329184
50	4	$1e-5$	0.1	$1e-6$	0.58301373

Table 3.2: MATCONT results for limit cycle of Eqs. 3.10 through 3.12.

In MATCONT, we continued the unstable limit cycle starting from $\alpha = 0.62132034$ and could reach $\alpha = 0.58101094$ (see Table 3.2).

With our algorithm, we started with a 400-point limit cycle at $\alpha = 0.615$ and reached $\alpha = 0.57656854$. The limit cycles obtained at $\alpha = 0.57656854$ are presented in Figs. 3.4 through 3.5. In this problem, we reached the homoclinic point accurate upto about half of the last significant digit reported in [65], while MATCONT stopped at a distance of about 0.005.

3.3.3 Examples where MATCONT does as well or better

3.3.3.1 A 2-D example from Strogatz

We study the following system from [66]:

$$\begin{aligned} \dot{x} &= y, && (3.13) \\ \dot{y} &= -\mu\, y + x - x^2 + x\, y. && (3.14) \end{aligned}$$

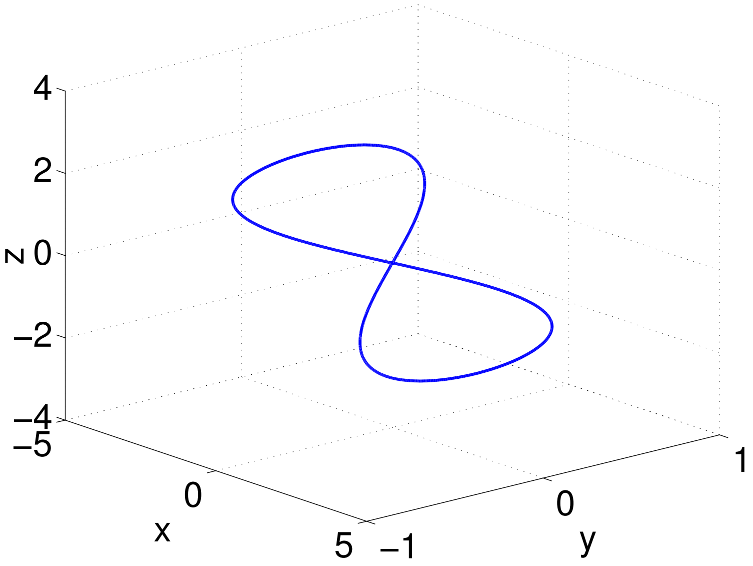

Figure 3.4: Limit cycle solution of Eqs. 3.10 through 3.12 from our algorithm for $\alpha = 0.57656854$.

The above system has two equilibria $(0, 0)$ and $(1, 0)$. As μ decreases from above unity, at $\mu = 1$ a stable limit cycle is born around $(1, 0)$ in a supercritical Hopf bifurcation; this limit cycle grows and becomes a homoclinic orbit at $\mu \approx 0.8645$ (these 4 significant digits are reported in [66]).

We started our algorithm with a limit cycle for $\mu = 0.95$ obtained by a shooting method, and used 500 points. We managed, with some manual intervention in parameter step choices, to proceed upto $\mu \approx 0.864547$. Results are shown in Fig. 3.6 (top), where our final solution as well as several intermediate limit cycles are plotted. The time period computed from our algorithm is plotted in Fig. 3.6 (bottom). For this problem, MATCONT went to 0.864545 (perhaps better, but not by much).

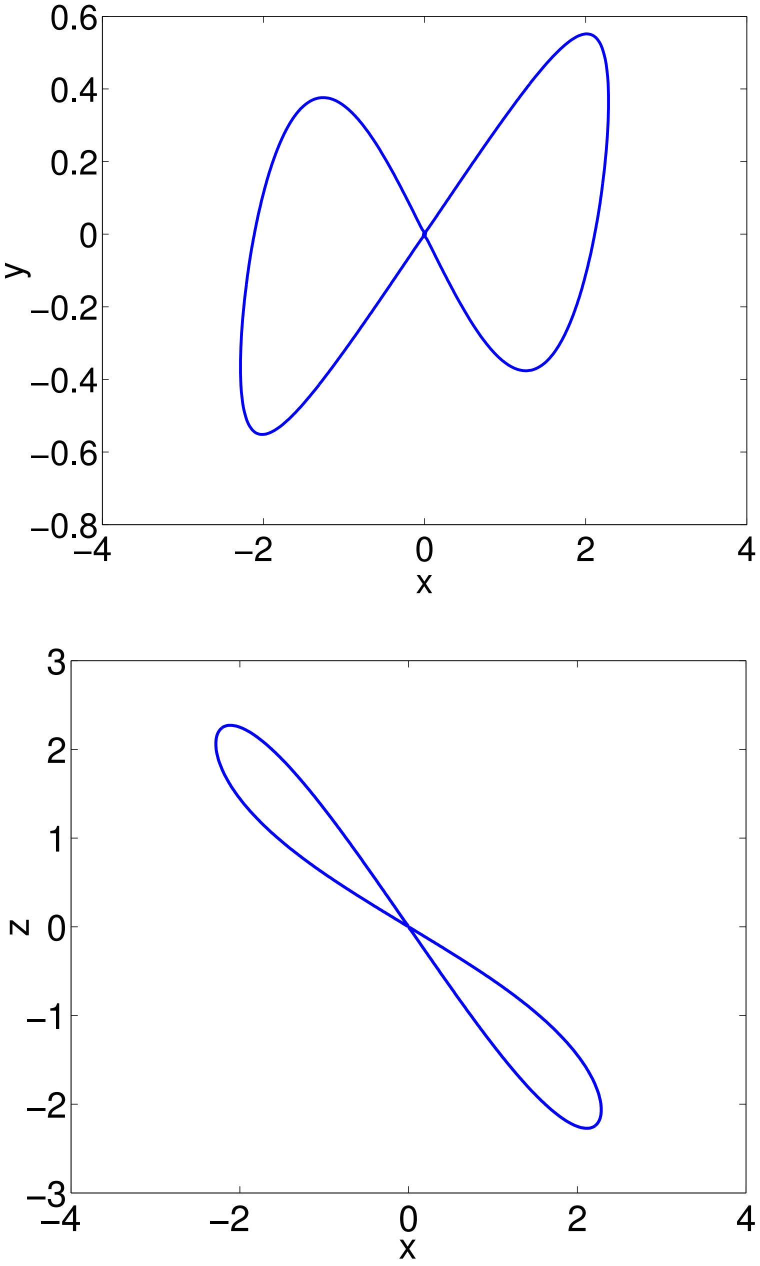

Figure 3.5: 2-D view of limit cycle of Eqs. 3.10 through 3.12 obtained from our algorithm for $\alpha = 0.57656854$. Top: $X - Y$ projection. Bottom: $X - Z$ projection.

3.3.3.2 The van der Pol oscillator

We now apply our algorithm to the van der Pol oscillator

$$\dot{x} = y, \tag{3.15}$$

$$\dot{y} = -\mu\, y(x^2 - 1) - x. \tag{3.16}$$

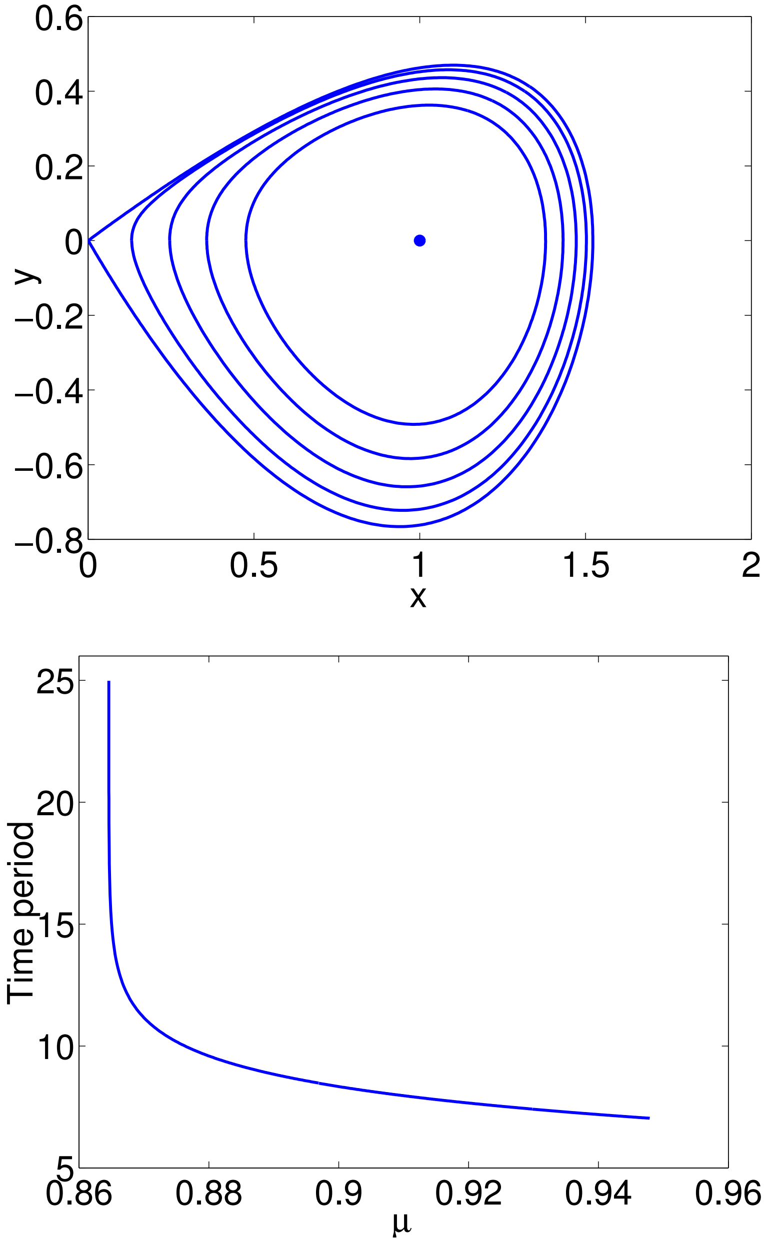

Figure 3.6: Top: limit cycles of Eqs. 3.13 and 3.14 obtained from our algorithm from $\mu = 0.95$ to $\mu = 0.864547$. Bottom: plot of time period of limit cycle of Eqs. 3.13 and 3.14 as a function of μ computed from our algorithm.

We will perform continuation for large μ. Here, no homoclinic points are involved. For this example, our algorithm needed a large number of points on the limit cycle to progress to high values of μ (e.g., with 2000 points we went to 21.23), while MATCONT proceeded to above 40 after some trial and error with simulation parameter choices (see Table 3.3), which indicates that the maximum attained with our level of expertise with MATCONT is partly a matter of persistence and luck). Thus, MATCONT surely has its strengths; and our algorithm seems to have its primary advantage in continuing limit cycles very close to homoclinic points. A plot of the limit cycle obtained from our algorithm at $\mu \approx 21.23$ is shown in Fig. 3.7(top).

NTST	NCOL	min. step size	max. step size	Tol.	max. μ attained
20	4	$1e-5$	0.1	$1e-6$	7.745
20	4	$1e-12$	0.1	$1e-6$	9.079
40	4	$1e-5$	0.1	$1e-6$	2.983
40	4	$1e-12$	0.01	$1e-6$	3.808
60	4	$1e-5$	0.1	$1e-6$	12.42
60	2	$1e-5$	0.1	$1e-6$	9.846
40	4	$1e-9$	0.1	$1e-8$	11.54
100	4	$1e-12$	0.01	$1e-8$	41.12

Table 3.3: MATCONT results for limit cycle of Eqs. 3.15 and 3.16.

We believe that MATCONT does better with the van der Pol oscillator because, for large μ, there is essentially a pair of discontinuities in the solution when viewed as a function of time; in contrast, for this system with large μ, in phase space the limit cycle curve stretches out without bound in the y direction, causing the finite number of points used (500, 1000 or 2000, as the case may be) to eventually be insufficient. There are also some oscillations, limited to a few points as is typical of spline interpolation, observed in the van der Pol limit cycle for large μ (see Fig. 3.7).

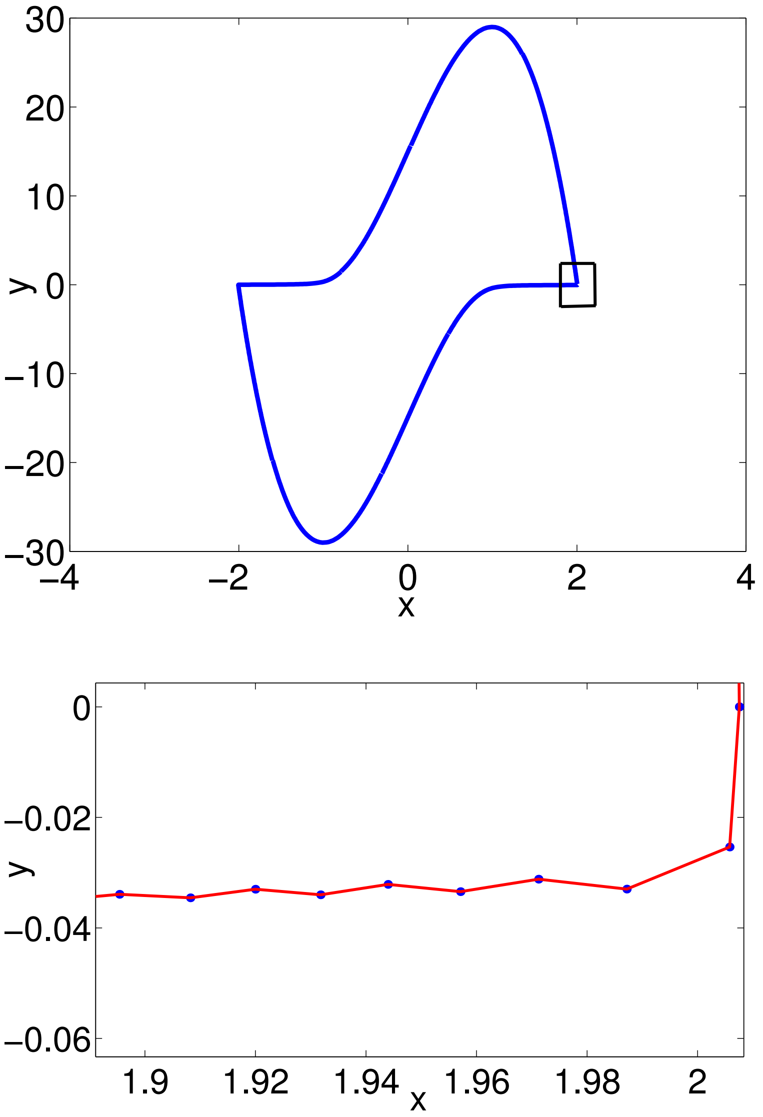

Figure 3.7: Top: limit cycle of Eqs. 3.15 and 3.16 obtained from our algorithm for $\mu = 21.23$. Bottom: zoomed portion of limit cycle showing the oscillatory behavior in the transition regions.

3.4 Convergence: some numerical results

In this section, we define two easily computed error measures and use them to empirically demonstrate the convergence of our results with increasing n.

Consider an n-point approximation of the limit cycle obtained from our algorithm for some particular parameter value. At each point on the limit cycle (see Fig. 3.8), let θ be the angle between the unit tangent vector obtained from the spline interpolant and that from the flow. Since our algorithm enforces parallelism between the unit tangent vectors only at the midpoint of each segment (in i-coordinates), the angle θ does not vanish at all points. At any point of the limit cycle we take $1 - \cos\theta$ as the "angle-error" due to the approximation. Note that this quantity vanishes pointwise in the limit as the length of the largest interval in phase space goes to zero with $n \to \infty$; and that for small angular deviations $1 - \cos\theta \approx \frac{\theta^2}{2}$, thus representing squared angular deviation.

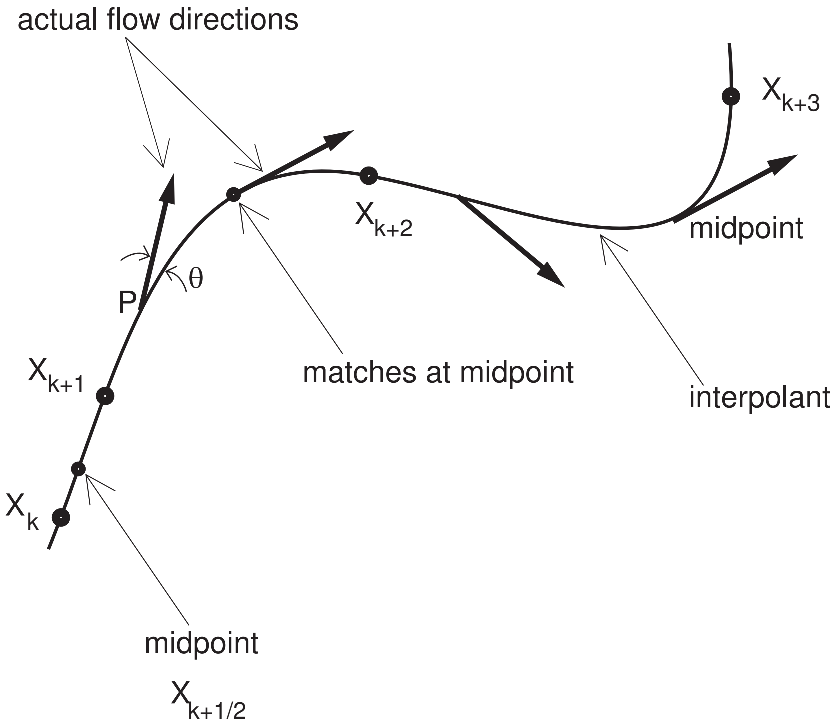

Figure 3.8: Schematic showing deviation of flow from the tangent to the interpolant at a typical point P.

We can sum up the angle-errors at each point of the limit cycle to obtain a global angle-error measure, $E(n)$, for the n-point limit cycle approximation. More precisely we have

$$E(n) = \oint (1 - \cos\theta) ds, \tag{3.17}$$

where ds is the elemental arclength (in phase space) and the integral is evaluated over the

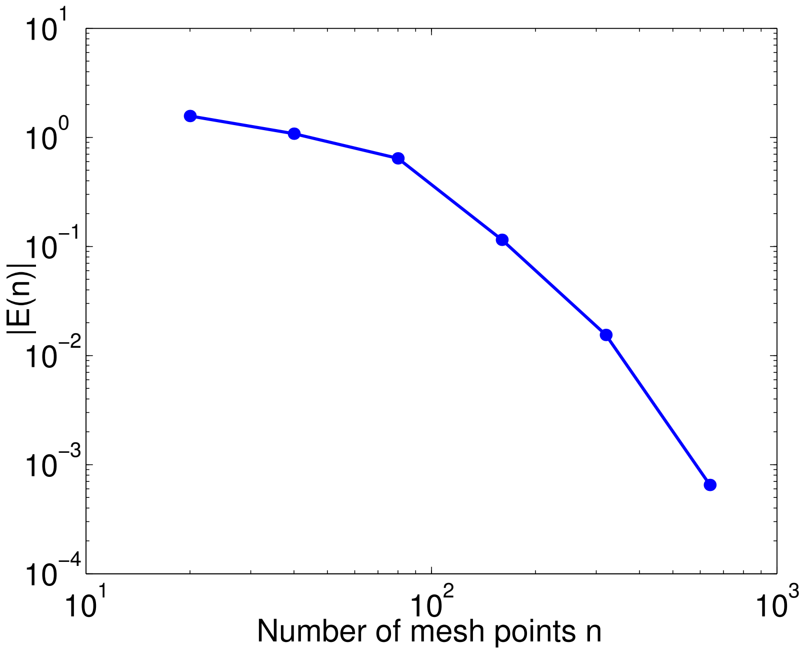

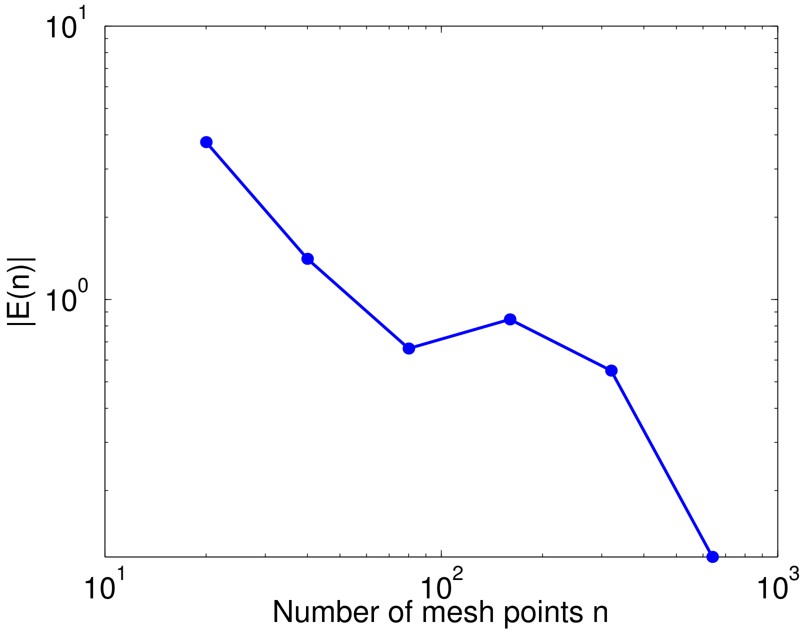

Figure 3.9: Top: convergence results based on angle error measure of Eq. 3.18 for the limit cycle of Eqs. 3.15 and 3.16 at $\mu = 5$. Bottom: results for $\mu = 10.0049$. The dots are computed points; the interpolation is for easier visibility only.

limit cycle. In practice, we evaluate Eq. 3.17 as

$$E(n) = \int_{i=1}^{i=n+1} (1 - \cos\theta) \|X'\| \, di, \tag{3.18}$$

where

$$\cos\theta = \left\langle \frac{X'}{\|X'\|}, \frac{F(X,\lambda)}{\|F(X,\lambda)\|} \right\rangle .$$

As the number of points increases, we expect this error to decrease asymptotically to zero as the tangent vector from the spline interpolant and that from the flow align with each other everywhere on the limit cycle.

We now present convergence results based on the global angle-error measure for the van der Pol oscillator of Eqs. 3.15 and 3.16. We obtained approximations to the limit cycle at $\mu = 5$ and $\mu = 10.0049$ using $n = 20, 40, 80, \ldots, 640$ points. For each n, we compute the total angle error given by Eq. 3.18. The results are plotted in Fig. 3.9. Convergence, though strongly indicated, does not follow a clear power law, probably because of the adaptive redistribution of points along the limit cycle based on our curvature-based criterion of Eq. 3.3.

As another indicator of convergence of our approximations with increasing number of mesh points, we compute the arclength of the limit cycle for each n as

$$S(n) = \int_{i=1}^{i=n+1} \|X'\| \, di. \tag{3.19}$$

We expect that as $n \to \infty$, the arclength computed from the spline interpolant converges to the exact arclength of the limit cycle.

We compute the arclengths for the limit cycles of Eqs. 3.15 and 3.16 at $\mu = 5$ and $\mu = 10.0049$ for $n = 20, 40, 80, \ldots, 640$ points. For plotting purposes, we take the arclength of the 640 point mesh as “exact” and deem the difference between this “exact” value and the arclength at any smaller n as the “arclength error” at that particular n. Results are shown in Fig. 3.10, which again indicates convergence, but not according to some simple power law, presumably for the reason mentioned above.

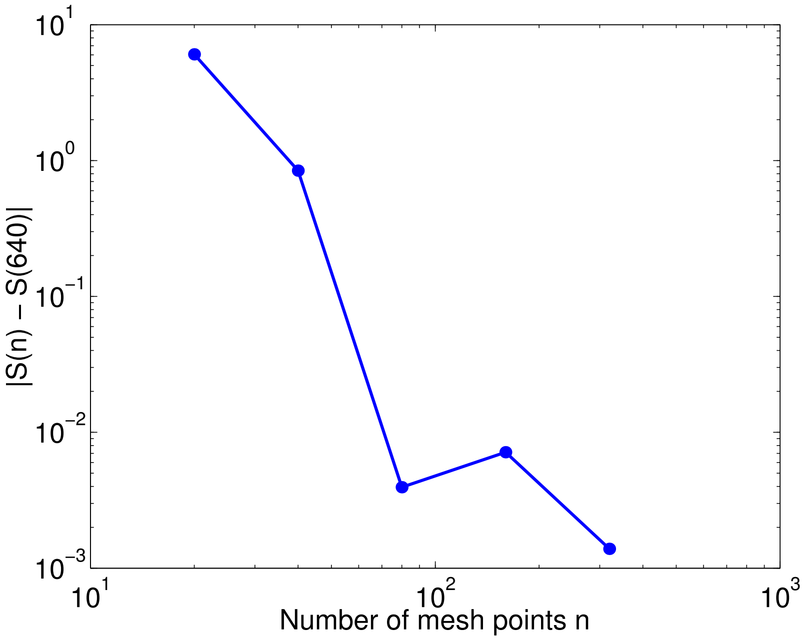

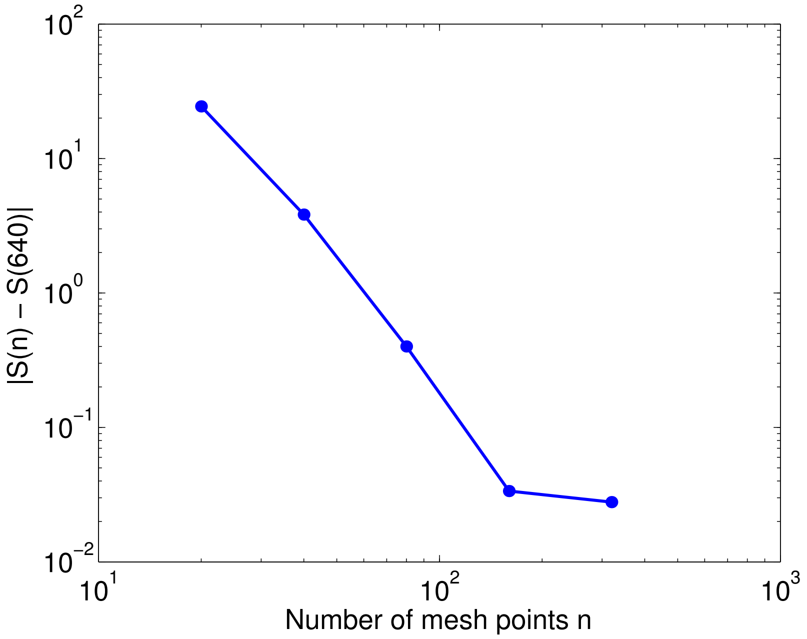

Figure 3.10: Top: arc length error plots for the limit cycle of Eqs. 3.15 and 3.16 at $\mu = 5$. Bottom: results for $\mu = 10.0049$. The dots are computed points; the interpolation is for easier visibility only.

3.5 Shortcomings of the finite parameter increment approach

Thus far, we have presented a new phase space-based algorithm to continue limit cycles. We have demonstrated the usefulness of our algorithm through several examples. The performance of our algorithm, however, can be improved on the following counts:

1. The continuation strategy of section 3.2 involved finite parameter increments. This discrete strategy yields algebraic governing equations for the increments of the points on the limit cycle. In this strategy, there is arbitrariness in the choice of parameter increments, and thus we do not have fine control on our approach to homoclinic points. This problem could be remedied by reformulating our algorithm with infinitesimal parameter increments, thereby obtaining ODEs instead of algebraic equations. ODEs enable us to exploit the capabilities of powerful numerical integration solvers, such as adaptive step sizing, to approach homoclinic points more closely.
2. The existing continuation strategy also has the obvious disadvantage of being unable to pass fold points. This is illustrated in Fig. 3.11, where the solution branch folds back. Thus for an incremented parameter past the fold point, the algorithm would fail to find a solution. This could be remedied by the well known arclength reparametrization technique [68].

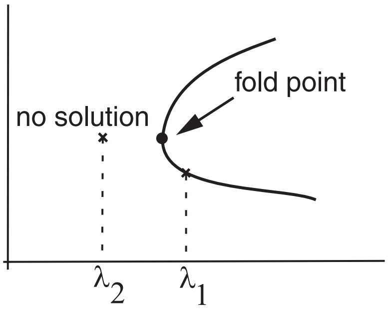

Figure 3.11: A schematic showing failure of the parameter increment strategy in continuing past a fold point.

3. Also, our algorithm is currently applicable to dimensions not greater than three. Extension of the algorithm to higher dimensions is straightforward and would improve the versatility of the algorithm.

We address the above three improvements in the forthcoming sections of this chapter.

3.6 Our algorithm: ODE formulation

The finite parameter increment continuation strategy, presented earlier in this chapter, is known in the literature as natural parameter continuation [51]. Here we reformulate our algorithm by considering infinitesimal parameter increments thereby transitioning from algebraic equations to ODEs. Such ODE-based approaches, known in the literature as parametric differentiation techniques ([67, 68]), are sometimes used as tangent predictors for subsequent Newton-Raphson correction iterations [68]; for simplicity, we do not undertake such subsequent corrections in this study.

The ODE formulation of this chapter has been presented in [69]

We start our ODE formulation with the phase condition of Eq. 3.2, which for an infinitesimal parameter increment, becomes

$$\left\langle \frac{dX_1(\lambda)}{d\lambda}, F(X_1(\lambda), \lambda) \right\rangle = 0. \tag{3.20}$$

The curvature-based constraint of Eq. 3.3, in the infinitesimal parameter increment limit, becomes

$$\frac{dS_i}{d\lambda}\,(\bar{\kappa} + \kappa_i) = \frac{dS_{i+1}}{d\lambda}\,(\bar{\kappa} + \kappa_{i+1}), \quad i = 1, 2, \ldots, n-1, \tag{3.21}$$

where the derivatives are given more explicitly as

$$\frac{dS_i}{d\lambda} = \frac{\left\langle (X_i(\lambda) - X_{i+1}(\lambda)), \left(\frac{dX_i(\lambda)}{d\lambda} - \frac{dX_{i+1}(\lambda)}{d\lambda} \right) \right\rangle}{\|X_{i+1}(\lambda) - X_i(\lambda)\|}.$$

Note that since our curvature computations are based on the limit cycle for the current parameter value, there are no derivatives of curvatures (with respect to λ) involved in our equations.

We now have n equations.

To obtain $2\,n$ more equations, we now consider Eqs. 3.4 and 3.5. Consider the i-th segment of the limit cycle for a parameter value λ. Let the tangent vector computed from the spline interpolant at the midpoint be $X'_{i+1/2}(\lambda)$, and let the unit vector from the flow be $\overrightarrow{N}(X_{i+1/2}(\lambda),\lambda) = \dfrac{F(X_{i+1/2},\lambda)}{\|F(X_{i+1/2},\lambda)\|}$. At an incremented parameter value $\lambda+\Delta\lambda$, these equations read as

$$\left\langle \left(X'_{i+1/2}(\lambda+\Delta\lambda) \times \overrightarrow{N}(X_{i+1/2}(\lambda+\Delta\lambda),\lambda+\Delta\lambda) \right), \frac{\overrightarrow{P_i}}{\|\overrightarrow{P_i}\|} \right\rangle = 0, \quad i = 1,\ldots,n, \tag{3.22}$$

and

$$\left\langle \left(X'_{i+1/2}(\lambda+\Delta\lambda) \times \overrightarrow{N}(X_{i+1/2}(\lambda+\Delta\lambda),\lambda+\Delta\lambda) \right), \overrightarrow{Q_i} \right\rangle = 0, \quad i = 1,\ldots,n, \tag{3.23}$$

where $\dfrac{\overrightarrow{P_i}}{\|\overrightarrow{P_i}\|}$ and $\overrightarrow{Q_i}$ are the principal normal and binormal vectors respectively at the midpoint of the segment.

We expand the left hand sides of the above equations upto first order infinitesimals in λ. In particular, for Eq. (3.22), after suppressing dependencies on independent variables, we have

$$\begin{aligned} &\left\langle X'_{i+1/2} \times \left(\frac{\partial \overrightarrow{N}}{\partial X} \frac{dX_{i+1/2}}{d\lambda} \right), \frac{\overrightarrow{P_i}}{\|\overrightarrow{P_i}\|} \right\rangle + \left\langle X'_{i+1/2} \times \frac{\partial \overrightarrow{N}}{\partial \lambda}, \frac{\overrightarrow{P_i}}{\|\overrightarrow{P_i}\|} \right\rangle + \\ &\qquad \left\langle \frac{dX'_{i+1/2}}{d\lambda} \times \overrightarrow{N}, \frac{\overrightarrow{P_i}}{\|\overrightarrow{P_i}\|} \right\rangle = 0, \quad i = 1,\ldots,n, \end{aligned} \tag{3.24}$$

where all quantities are evaluated at $(X_{i+1/2},\lambda)$.

In the above equation, we need to express quantities such as $\dfrac{dX_{i+1/2}}{d\lambda}$ and $\dfrac{dX'_{i+1/2}}{d\lambda}$ in terms of our primary dependent variables X_i and their derivatives $\dfrac{dX_i}{d\lambda}$. To that end, we proceed as follows. Since the cubic spline interpolant is a linear function of X_i, we have

$$Y_{1/2} = \left\{\begin{array}{c} X_{1+1/2} \\ X_{2+1/2} \\ \cdot \\ \cdot \\ \cdot \\ X_{n+1/2} \end{array}\right\} = R \left\{\begin{array}{c} X_1 \\ X_2 \\ \cdot \\ \cdot \\ \cdot \\ X_n \end{array}\right\} = R\,Y, \quad Y'_{1/2} = \left\{\begin{array}{c} X'_{1+1/2} \\ X'_{2+1/2} \\ \cdot \\ \cdot \\ \cdot \\ X'_{n+1/2} \end{array}\right\} = S \left\{\begin{array}{c} X_1 \\ X_2 \\ \cdot \\ \cdot \\ \cdot \\ X_n \end{array}\right\} = S\,Y, \tag{3.25}$$

where for the 3 dimensional case with n points the size of the constant matrices R and S is $3\,n \times 3\,n$. Thus we have $\dfrac{dY_{1/2}}{d\lambda} = R\,\dfrac{dY}{d\lambda}$, $\dfrac{dY'_{1/2}}{d\lambda} = S\,\dfrac{dY}{d\lambda}$. Utilizing the above relations in Eqs. 3.24 and repeating the procedure for n segments we obtain n equations. Similar computations using Eq. (3.23) yield n more equations.

The final set of ODEs, after some re-arrangement, can be compactly written as

$$P(Y(\lambda), \lambda)\,\frac{dY}{d\lambda} = Q(Y(\lambda), \lambda)\,, \tag{3.26}$$

where Y is as defined in Eq. (3.25), P is a $3\,n \times 3\,n$ matrix and Q is a $n \times 1$ vector. We could write the above equation as

$$\frac{dY}{d\lambda} = P^{-1}Q, \tag{3.27}$$

which represents the continuous version of our discrete formulation of section 3.2. Numerical integration of Eq. (3.27) will fail at a fold point where P becomes singular. In the literature, several alternate approaches such as arclength continuation have been reported [51, 68].

We adopt the arclength approach here, wherein we consider Y as well as the parameter λ as functions of the arclength, s, along the branch, whence Eq. (3.26) becomes

$$P(Y(s), \lambda(s))\,\frac{dY}{ds} - Q(Y(s), \lambda(s))\frac{d\lambda}{ds} = 0. \tag{3.28}$$

We have $3\,n$ equations for $3\,n + 1$ unknowns namely, $\dfrac{dY}{ds}$ and $\dfrac{d\lambda}{ds}$. Hence we add an additional condition [51] as

$$\left\langle M_0, \frac{dY}{ds} \right\rangle + N_0\,\frac{d\lambda}{ds} > 0, \tag{3.29}$$

where $\begin{bmatrix} M_0 \\ N_0 \end{bmatrix}$ denotes the unit tangent vector computed at the previous integration step. For sufficiently small integration step size, this condition preserves the orientation of the continuation branch [51]. We finally normalize the arclength derivatives as follows:

$$\left\langle \frac{dY}{ds}, \frac{dY}{ds} \right\rangle + \left(\frac{d\lambda}{ds} \right)^2 = 1. \tag{3.30}$$

The intention is to solve Eqs. 3.28 and 3.30, subject to the inequality (3.29). In practice, this is done by replacing the " > 0" in Eq. (3.29) with " $= 1$" and solving it along with Eq. (3.28), with subsequent scalar normalization of the solution to satisfy Eq. (3.30). We adopt the above strategy so as to avoid solving the nonlinear system of equations Eqs. 3.28 and 3.30. Also, as stated earlier, inclusion of Eq. 3.29 preserves the orientation of the continuation branch [51].

3.7 Application of ODE formulation: a fold bifurcation

We now present an example involving a fold bifurcation showcasing the capabilities of the above described formulation.

We consider the equations for Chua's circuit as presented in [65]

$$\begin{aligned} \dot{x} &= \alpha\,(y - x^3/16 + x/6), && (3.31) \\ \dot{y} &= x - y + z, && (3.32) \\ \dot{z} &= -\beta\, y, && (3.33) \end{aligned}$$

for $\beta = 1.4$.

In [65] it is reported that for $\beta = 1.4$ a pair of unstable limit cycles are born around the two equilibria $\left(\sqrt{\frac{8}{3}}, 0, -\sqrt{\frac{8}{3}}\right)$ and $\left(-\sqrt{\frac{8}{3}}, 0, \sqrt{\frac{8}{3}}\right)$ in a sub-critical Hopf bifurcation at $\alpha = 1.423$ (our more accurate estimate below is 1.424). On decreasing α, these limit cycles merge with two co-existing stable limit cycles at $\alpha = 1.418$ (our estimate: 1.4177) in a fold bifurcation. On following the solution branch beyond the fold point, with increasing α, these two stable limit cycles approach each other and finally merge into a single limit cycle at $\alpha = 1.431$ in a homoclinic bifurcation.

We start with a 400-point unstable limit cycle at $\alpha = 1.4240$ and continue it past the fold point upto near homoclinic orbit. The fold point according to our approach is at $\alpha = 1.4177$ and the final value of α reached by us is 1.4316. We compute the time period of the limit cycle solutions along the branch and plot them in Fig. 3.12. The plot reveals the fold point at $\alpha \approx 1.418$ as well as the unlimited growth of time period near the homoclinic point at $\alpha \approx 1.431$. We also plot the stable and unstable orbits at different values of α in Fig. 3.13.

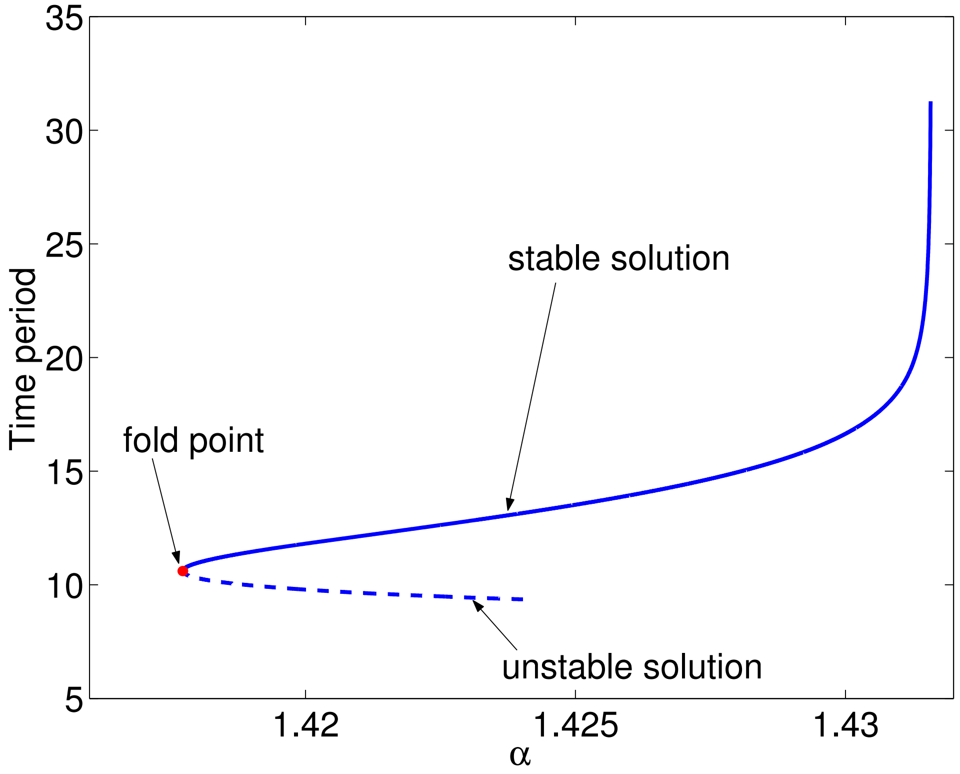

Figure 3.12: A plot of time period of the limit cycle solutions of Eqs. 3.31 through 3.33 for $\beta = 1.4$ revealing the fold bifurcation at $\alpha \approx 1.4177$.

3.8 Our algorithm: extension to higher dimensions

In section 3.2, we have presented our algorithm in a three dimensional setting. However, the algorithm can be easily extended to dimensions greater than three as will be shown

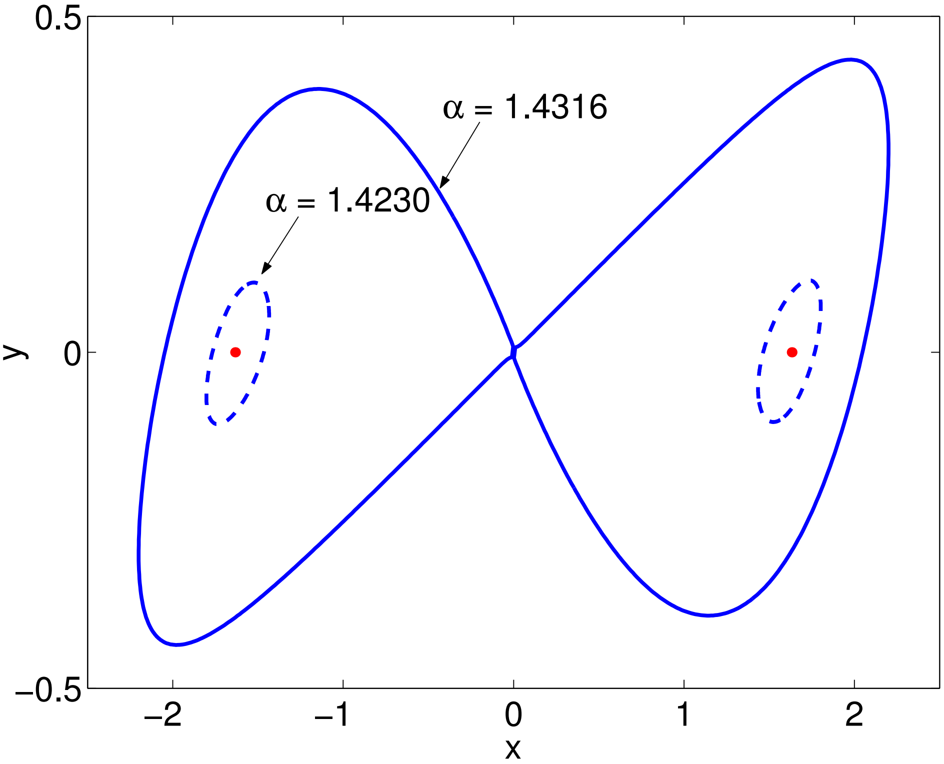

Figure 3.13: $X-Y$ plot of the unstable orbit at $\alpha = 1.4230$ which undergoes fold bifurcation and grows into a near-homoclinic stable orbit at $\alpha = 1.4316$. Also plotted is this near-homoclinic orbit at $\alpha = 1.4316$.

below.

Consider $\dot{X} = F(X, \lambda)$, with X now being p-dimensional and $p > 3$. Let this system possess a limit cycle solution in p-dimensional space. We wish to continue this limit cycle by varying λ.

We have n points in our limit cycle approximation and hence we need $p\,n$ equations. Of these, n equations are obtained from the phase condition and curvature-stretch conditions exactly similar to Eqs. 3.2 through 3.3. In higher dimensions, the first generalized curvature is obtained using the following formula [70, 71]

$$\kappa_i = \frac{\langle e_1', e_2 \rangle}{\|X_{i+1/2}'\|}\,,$$

where primes denote derivatives with respect to the parametrizing index variable and

$$e_1 = \frac{X'_{i+1/2}}{\|X'_{i+1/2}\|},$$

$$e_2 = \frac{(X''_{i+1/2} - \langle X''_{i+1/2}, e_1\rangle\, e_1)}{\|X''_{i+1/2} - \langle X''_{i+1/2}, e_1\rangle\, e_1\|}.$$

The remaining $(p-1)\,n$ equations are obtained by requiring that the actual flow be directed along the limit cycle (see [58] for similar conditions).

Specifically, for the i-th segment, we find a set of $p-1$ vectors, say $\{v_1, v_2, \ldots, v_{p-1}\}$ which are mutually orthogonal as well as orthogonal to the flow direction

$$\frac{F(X_{i+1/2} + \Delta X_{i+1/2}, \lambda + \Delta\lambda)}{\|F(X_{i+1/2} + \Delta X_{i+1/2}, \lambda + \Delta\lambda)\|}.$$

In MATLAB, such a set $\{v_1, v_2, \ldots, v_{p-1}\}$ can be easily obtained (numerically) by the *null* command in each Newton-Raphson iteration.

We also compute the tangent vector from our spline interpolant as

$$\overrightarrow{A_i} = (X_{i+1/2} + \Delta X_{i+1/2})' = X'_{i+1/2} + \Delta X'_{i+1/2}.$$

For the i-th segment we obtain $p-1$ equations by enforcing that $\overrightarrow{A_i}$ be orthogonal to the set $\{v_1, v_2, \ldots, v_{p-1}\}$. More precisely, we require that

$$\langle \overrightarrow{A_i}, v_j\rangle = 0, \quad j = 1, 2, \ldots, p-1.$$

Repeating the procedure for the n segments we obtain the required $(p-1)\,n$ equations.

We now study a 4-dimensional system using our algorithm and compare our results with MATCONT. Consider the following system of two weakly coupled van der Pol oscillators studied by [72]

$$\ddot{p} + p + \epsilon\,\dot{p}\,(p^2 - 1) + \epsilon\,\alpha\,(p - r) = 0, \tag{3.34}$$

$$\ddot{r} + (1 + \epsilon\,\Delta)\,r + \epsilon\,\dot{r}\,(r^2 - 1) - \epsilon\,\alpha\,(p - r) = 0, \tag{3.35}$$

where $0 < \epsilon \ll 1$, Δ represents detuning and α denotes the strength of coupling. As shown in [72], for a certain range of α and Δ, strongly phase-locked (periodic) limit cycle solutions exist for the above system.

Rewriting the above system in state space form we have

$$\begin{aligned}
\dot{p} &= q, && (3.36)\\
\dot{q} &= -p - \epsilon\, q\,(p^2-1) - \epsilon\,\alpha\,(p-r), && (3.37)\\
\dot{r} &= s, && (3.38)\\
\dot{s} &= -(1+\epsilon\,\Delta)\,r - \epsilon\, s\,(r^2-1) + \epsilon\,\alpha\,(p-r). && (3.39)
\end{aligned}$$

We used $\epsilon = 0.01$ and $\Delta = 1$ in our simulations. We started with a 300-point limit cycle approximation at $\alpha = 1.01$ and continued the strongly phase-locked limit cycle solution for increasing values of α. The results from our algorithm are plotted along with those from MATCONT for $\alpha = 4.27$ in Fig. 3.14 and 3.15. Agreement is good. This demonstrates the use of our algorithm in continuing limit cycles in dimensions more than three.

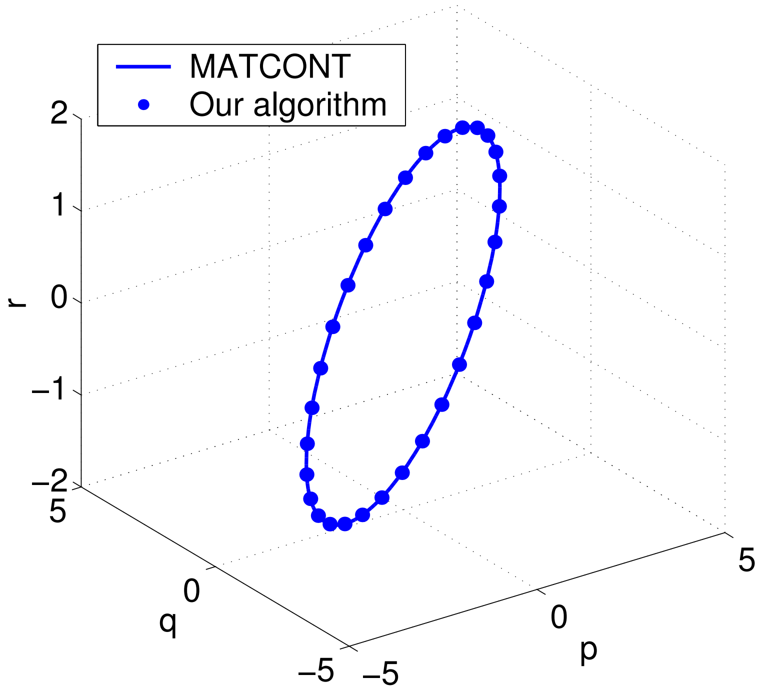

Figure 3.14: Limit cycle of Eqs. 3.36 through 3.39 for $\alpha = 4.27$: projection onto $p-q-r$ space.

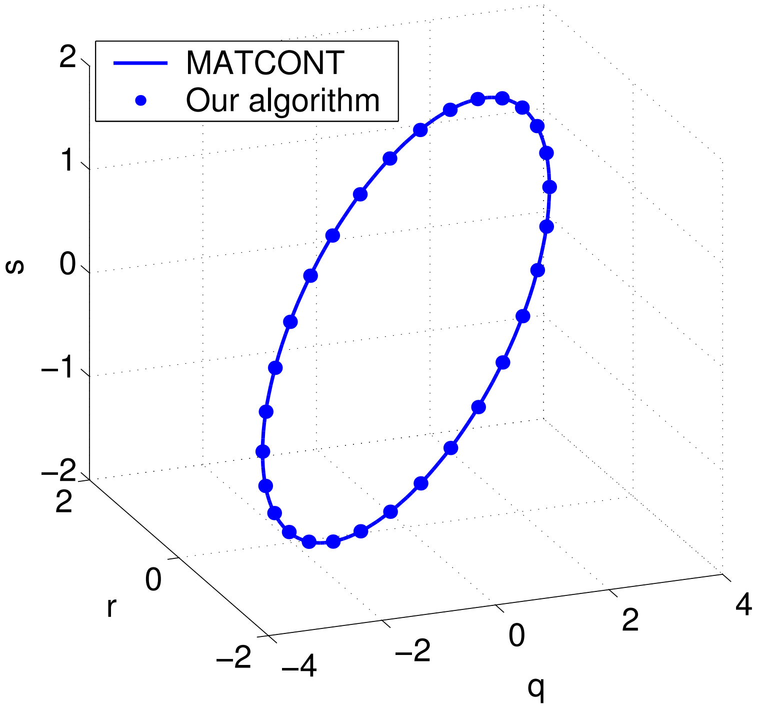

Figure 3.15: Limit cycle of Eqs. 3.36 through 3.39 for $\alpha = 4.27$: projection onto $q-r-s$ space.

3.9 Closing remarks

We have presented an algorithm for continuation of limit cycles occuring in parameterized systems of autonomous ODEs. The algorithm approximates the limit cycle using a number of points in phase space, and interpolates between them using an artificial index-based variable and cubic splines. The approach seems useful, in particular, close to homoclinic points. The algorithm is initially presented in a 3D setting, with a finite parameter increment continuation strategy. Subsequently, we have reformulated the algorithm using infinitesimal parameter increments yielding ODEs. This reformulation is applied to situations involving fold bifurcations. Finally, extension of the algorithm to higher dimensions is outlined (only in the discrete form, so far).

The algorithm in its present form is unable to detect higher co-dimension singularities along branches of limit cycles, which can be handled by packages like MATCONT.

Also, the algorithm is currently unable to address homoclinic orbits involving saddle-foci and the associated spiral orbits.

Future work may alleviate some of these apparent shortcomings. In particular, other interpolation schemes might be used in place of splines; and Eq. 3.3, which is the most flexible part of the algorithm, might be replaced with something that is found to be better.

Despite the said shortcomings, in our view, the algorithm already offers one extra alternative to an analyst, and could be added to the suite of algorithms already incorporated into packages like MATCONT.

Recall that the development of the algorithm was motivated by the need to continue the limit cycles close to the homoclinic point of the amplitude control problem of Chapter 2. With the new algorithm in place, we revisit the amplitude control problem of Chapter 2 in Chapter 4.

Chapter 4

Return to amplitude control: Results

In Chapter 2, we started the study related to the amplitude control of a lightly damped, resonantly forced oscillator. In the course of this study, we faced the need for continuing limit cycles close to a homoclinic point. Motivated by this need, we developed and presented a new phase space-based algorithm in Chapter 3. The algorithm was applied to several problems. Encouraged by its success, in this chapter we apply the algorithm to the system studied in Chapter 2.

4.1 Amplitude control problem of Chapter 2

Recall that the system studied in Chapter 2 was

$$\dot{x} = -x - 3\,y\,, \tag{4.1}$$

$$\dot{y} = 3\,x - y - z\,, \tag{4.2}$$

$$\dot{z} = K\,y\left(1 - \frac{3}{\sqrt{x^2+y^2}}\right)\,. \tag{4.3}$$

In Chapter 2, we had continued the large and small limit cycles of the above system using MATCONT. Based on the plots of these orbits in Fig. 2.4, we hypothesized that these large and small limit cycles will approach each other and get destroyed in a homoclinic bifurcation. However, we do not yet know the critical value of K at which the homoclinic bifurcation occurs. If the origin had been a genuine equilibrium point of the above system, an estimate of the homoclinic point could have been obtained by standard methods (see, for e.g., [35, 36, 37, 38, 39, 40]). Here, however, the origin is not an equilibrium point. In such an atypical situation, what is this critical value of K at which the limit cycles merge and disappear?

4.2 Semi-analytical estimate of homoclinic point

In order to gain better understanding of the near-origin dynamics of Eqs. 4.1 through 4.3, we first consider the regularized system

$$\begin{aligned} \dot{x} &= -x - 3\,y & (4.4)\\ \dot{y} &= 3\,x - y - z & (4.5)\\ \dot{z} &= K\,y\left(1 - \frac{3}{\sqrt{\alpha + x^2 + y^2}}\right), & (4.6)\end{aligned}$$

where $0 < \alpha \ll 1$.

With $\alpha > 0$, the system has an equilibrium at the origin. The other two equilibria referred to in section 2.3 persist near their $\alpha = 0$ locations. For $\alpha = 1e{-}5$, we find the three equilibria at $(0,0,0)$, $(2.846, -.9487, 9.487)$ and $(-2.846, .9487, -9.487)$. The eigenvalues, for $K = 14$, at the origin are

$$\lambda_1 = -1.0007,\ \lambda_2 = -115.65,\ \lambda_3 = 114.65,$$

and the corresponding eigenvectors are

$$V_1 = \begin{bmatrix} .99955e-2 \\ .22617e-5 \\ .29986e-1 \end{bmatrix},$$

$$V_2 = \begin{bmatrix} -.17205e-3 \\ -.65750e-2 \\ -.75432 \end{bmatrix},$$

$$V_3 = \begin{bmatrix} -.17140e-3 \\ .66072e-2 \\ -.76462 \end{bmatrix}.$$

The origin is a saddle with V_1 and V_2 being the stable eigenvectors and V_3 being the unstable eigenvector.

As α is decreased further (numerical results not presented here), we observe that the z component of the approach direction vector V_1 becomes three times the x component. This observation will be utilized later when we present results from our algorithm. We also observe that λ_2 and λ_3 become large, approximately equal in magnitude, and opposite in sign; and that V_2 and V_3 become closer to parallel, while their z components become much larger than their y components, which in turn become much larger than their x components.

With these observations we revisit Eqs. 4.1 through 4.3, and seek a power series solution which leaves the origin at $t = 0$, given by

$$x(t) = \sum_{m=3}^{N} a_m t^m , \tag{4.7}$$

$$y(t) = \sum_{m=2}^{N} b_m t^m , \tag{4.8}$$

$$z(t) = \sum_{m=1}^{N} c_i t^m . \tag{4.9}$$

We substitute Eqs. 4.7 through 4.9 in Eqs. 4.1 through 4.3 and solve for the unknown coefficients a_i, b_i and c_i to obtain

$$x(t) = -3\,K\,t^3/2 + 3\,K\,t^4/4 + \ldots \tag{4.10}$$

$$y(t) = 3\,K\,t^2/2 - \,K\,t^3/2 + (-9\,K/8 - \,K^2/8)\,t^4 + \ldots \tag{4.11}$$

$$z(t) = -3\,K\,t + (K^2/2 + K/2)\,t^3 - \,K\,(1 + K)\,t^4/8 + \ldots \tag{4.12}$$

For a chosen value of K, we first compute the initial conditions x, y, z for numerical integration by evaluating Eqs. 4.10 through 4.12 at $t = 0.002$. We then integrate Eqs. 4.1 through 4.3 with these initial conditions and error tolerances of $1e - 13$ in MATLAB's function "ode45". We plot the norm of the numerical solution, $\sqrt{x(t)^2 + y(t)^2 + z(t)^2}$, for various K values, against time in Fig. 4.1. For K close to the homoclinic point value, the computed solution returns close to the origin. As depicted in Fig. 4.1, we find $K = 13.82786$ is a good estimate of the homoclinic point (the last digit may be unreliable). For $K = 13.827$, in contrast, the trajectory goes more quickly to one of the two fixed points.

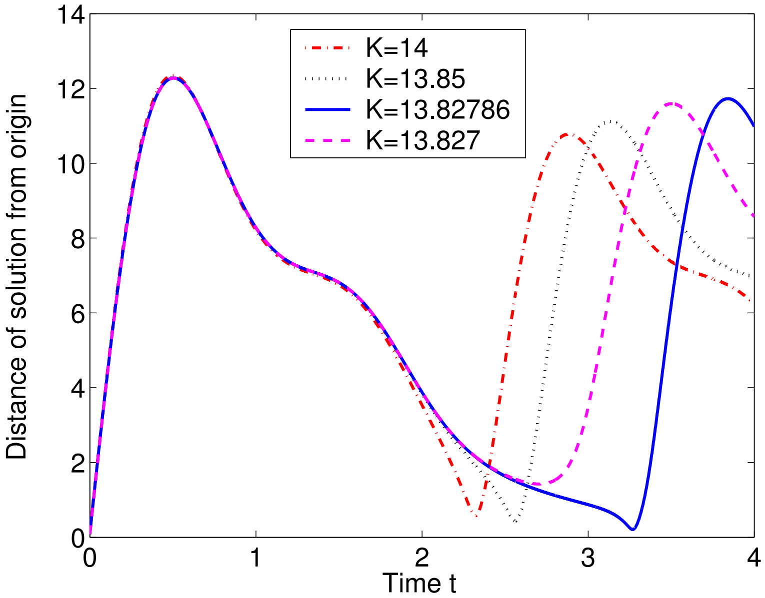

Figure 4.1: Return to the homoclinic point. For $K = 13.82786$, the closest approach to the origin is acceptably small.

We repeated the above numerical experiments by evaluating Eqs. 4.10 through 4.12 at $t = 0.001$ instead of 0.002. Here too, we found $K \approx 13.82786$, with the last digit probably unreliable.

Having obtained an estimate of the homoclinic parameter value, we proceed to continue the limit cycles using the algorithm of Chapter 3.

4.3 Results from our algorithm

We now perform limit cycle continuation of the small and large orbits using our algorithm and demonstrate its efficacy in coming close to the above determined homoclinic point. We first present results based on the finite parameter increment strategy. Later on, we will present results based on the ODE formulation. For the small orbit, we started with a limit cycle solution at $K = 16$. We had 500 points in our starting limit cycle. We successfully continued the small, asymmetric limit cycle upto $K = 13.83356$. For comparison, we plot

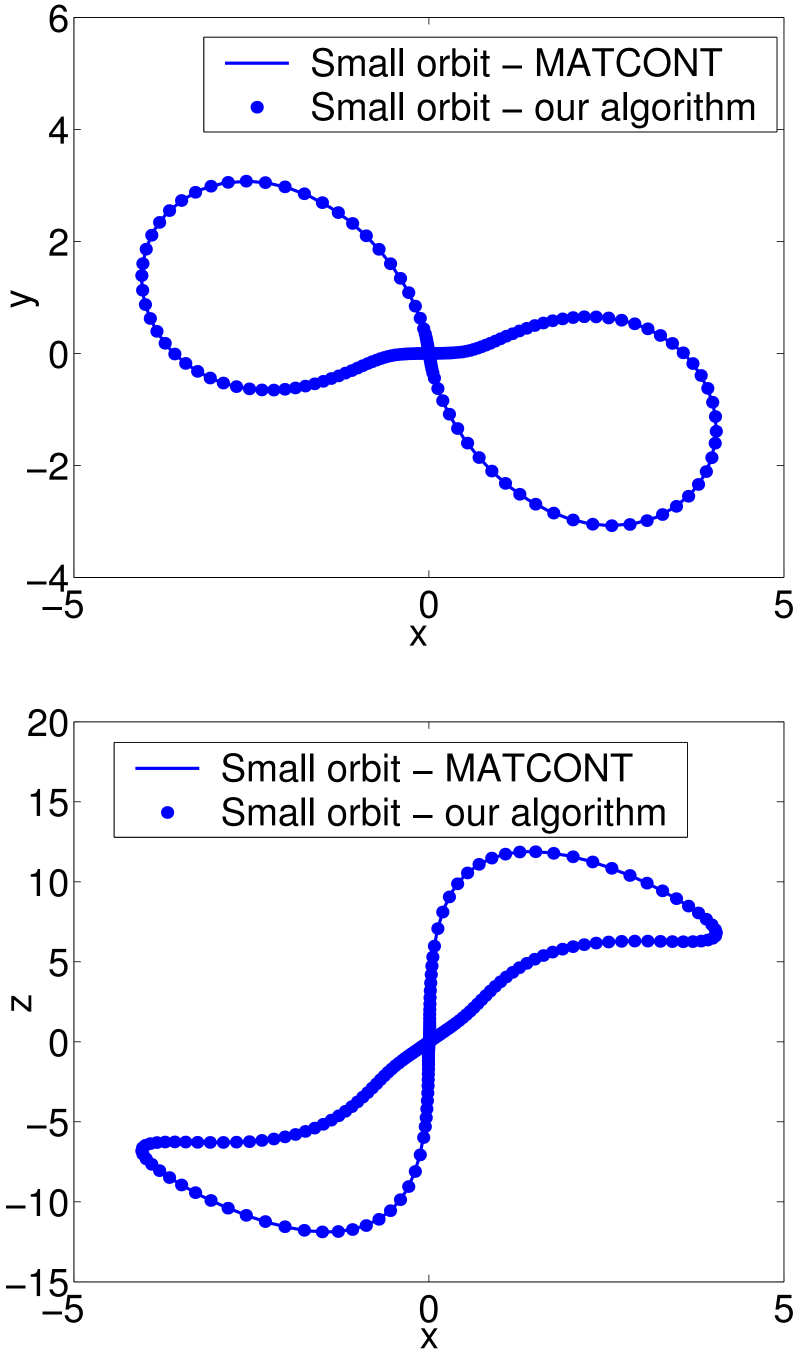

Figure 4.2: Comparison of limit cycles of Eqs. 4.1 through 4.3 for $K = 13.8740$ obtained from our algorithm and MATCONT. Top: $X - Y$ projection. Bottom: $X - Z$ projection.

the two small limit cycles obtained using our algorithm at $K = 13.8740$, along with those from MATCONT, in Fig. 4.2. We have plotted fewer than 500 points for visual clarity. Agreement is good. Note, however, that our terminal value of 13.83356 differs from the limiting value of 13.82786 by 0.0055; in contrast, MATCONT's terminal value of 13.8740 differs by about 0.041, which is about 7 times larger.

For the large orbit, we started with a limit cycle at $K = 15.5$. There were 600 points in the starting solution. We were able to proceed till $K \approx 13.83140$. This value of K differs from the limiting value by about 0.0035. In contrast, MATCONT's termination at 13.9326 differs from the limiting value by about 0.105, which is about 30 times larger.

For completeness, we plot the small and large limit cycles obtained using our algorithm for $K = 13.8335$ in Fig. 4.3. The large limit cycle is now visually indistinguishable from the two small ones, both being quite close to homoclinic.

We also plot the projection of the two small limit cycles onto the X-Z plane in Fig. 4.4. Also plotted is the $z = 3\,x$ line near the origin; the limit cycle proceeds almost along this line along one segment of the loop; this numerical/graphical observation is related to the components of the eigenvector V_1 as explained in section 4.2.

The time periods for the small and large orbits computed from our algorithm, as described in Chapter 3, are plotted in Fig. 4.5, along with the same quantities estimated by MATCONT. The largest Floquet multiplier for the two orbits from our algorithm, as described in Chapter 3, are plotted along with results from MATCONT in Fig. 4.6. Agreement is good. The computation of the other two multipliers had visible difficulties, both with our algorithm and MATCONT. For example, one Floquet multiplier is theoretically equal to unity for any limit cycle (i.e., for all K); the corresponding numerical values obtained from our algorithm and MATCONT are plotted side by side in Fig. 4.7, and show spurious oscillations. However, since it is well known that accurate computation of Floquet multipliers of disparate magnitudes is difficult [41], we do not investigate these Floquet multipliers further.

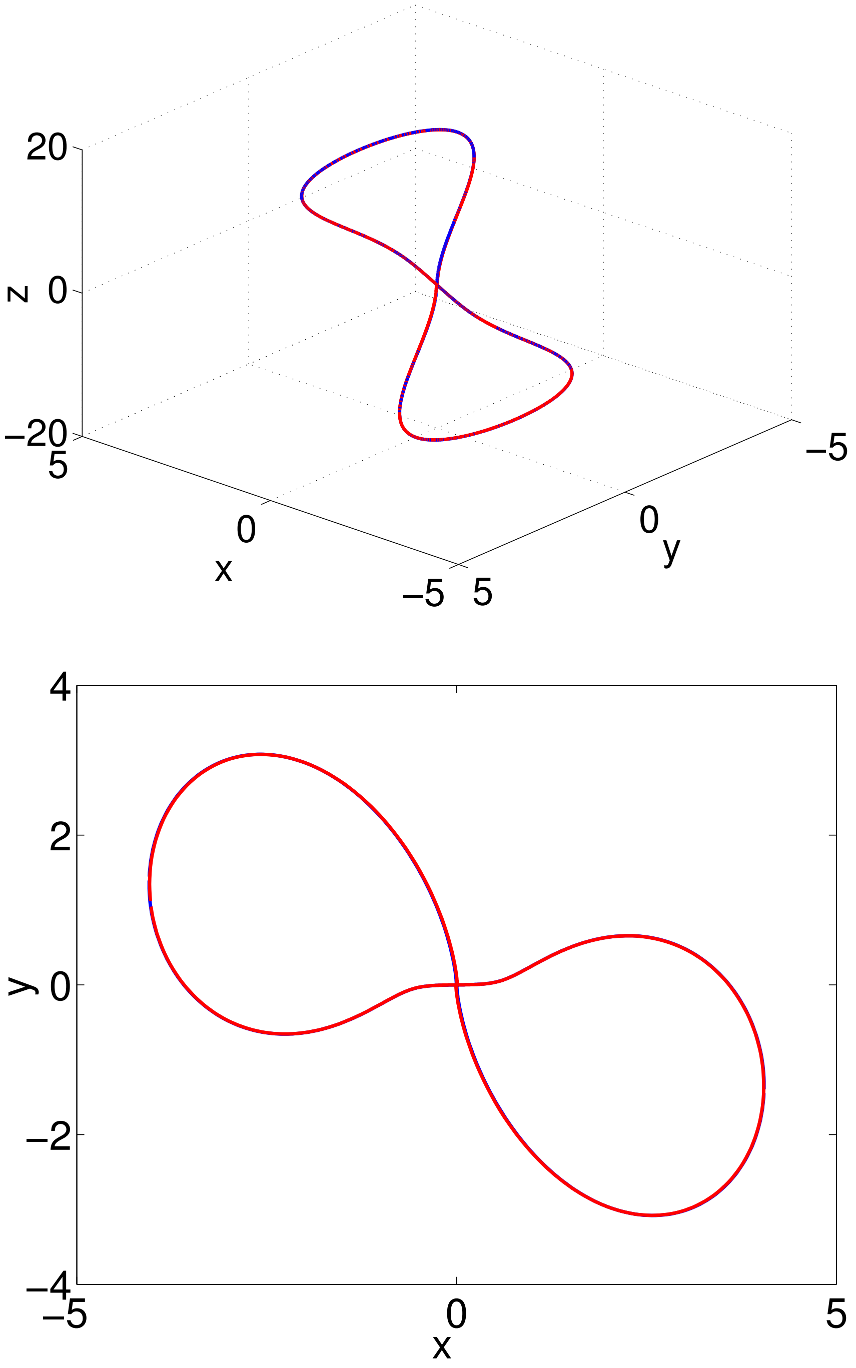

Figure 4.3: The large and small orbits of Eqs. 4.1 through 4.3 from our algorithm for $K = 13.8335$; the plots are visually indistinguishable. Top: 3-D. Bottom: $X-Y$ projection.

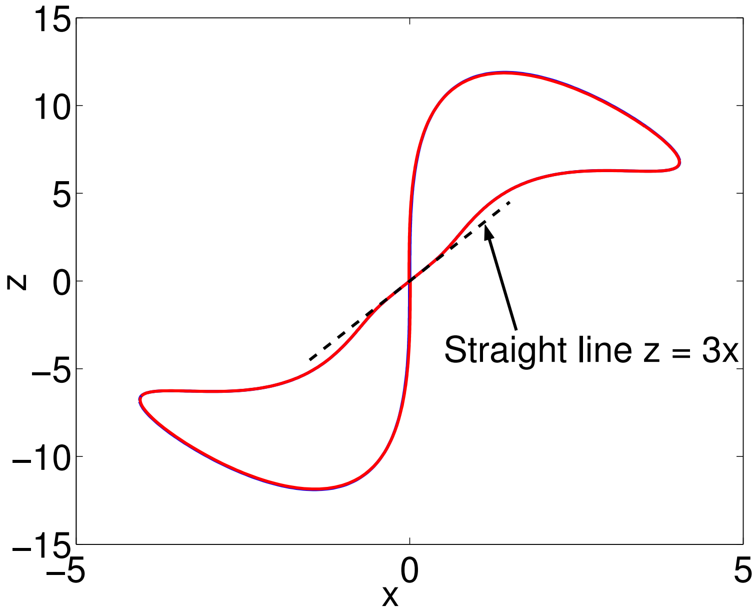

Figure 4.4: $X - Z$ projection of the large and small orbits of Eqs. 4.1 through 4.3 from our algorithm for $K = 13.8335$ revealing the asymptotic approach directions.

4.3.1 Further comments on implementation

The increments in K (here, the increments were negative) were decided adaptively based on the number of Newton-Raphson iterations needed for the previous parameter increment. If the number of iterations exceeded a threshold (we have used several choices like 5, 7, 10, etc.), the parameter increment was reduced to 70% of the previous value. To reduce the number of function evaluations, a modified Newton-Raphson method was used in some cases (the Jacobian matrix calculated during the first iteration was used unchanged in subsequent iterations). However, the iteration termination criterion was held constant at $1e - 9$, and so these procedural tricks have no influence on the reported final results.

Apart from the 500 point-mesh for the small limit cycle, for which we present results here, we also tried 50, 100, 300 and 800 points: in all cases, we reached comparable K values. With more points, the accuracy of indirectly computed quantities such as time period was higher.

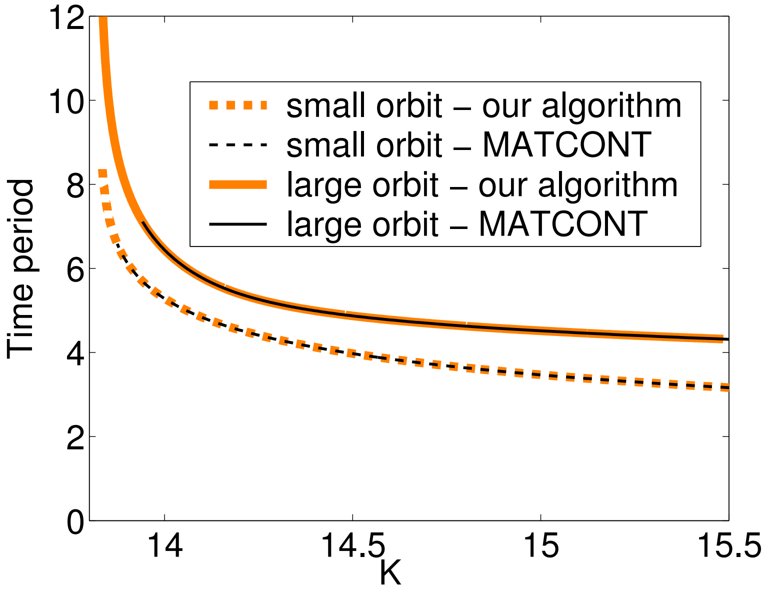

Figure 4.5: Time period of large and small limit cycles of Eqs. 4.1 through 4.3 computed from our algorithm along with those from MATCONT.

Overall, performance of the algorithm was robust.

Note that the above strategy for deciding the step size is avoided with the ODE formulation of section 3.6.

4.3.2 Results from ODE formulation

We also applied the ODE formulation of section 3.6 in continuing the limit cycles of Eqs. 4.1 through 4.3. We could continue the small, asymmetric limit cycle upto $K = 13.8281$, which is much closer to the estimated homoclinic point $K \approx 13.8278$ than the best results of section 4.3. The large, symmetric limit cycle could be continued till $K = 13.8282$, which is also very good. The number of mesh points and other details remain the same as in section 4.3.

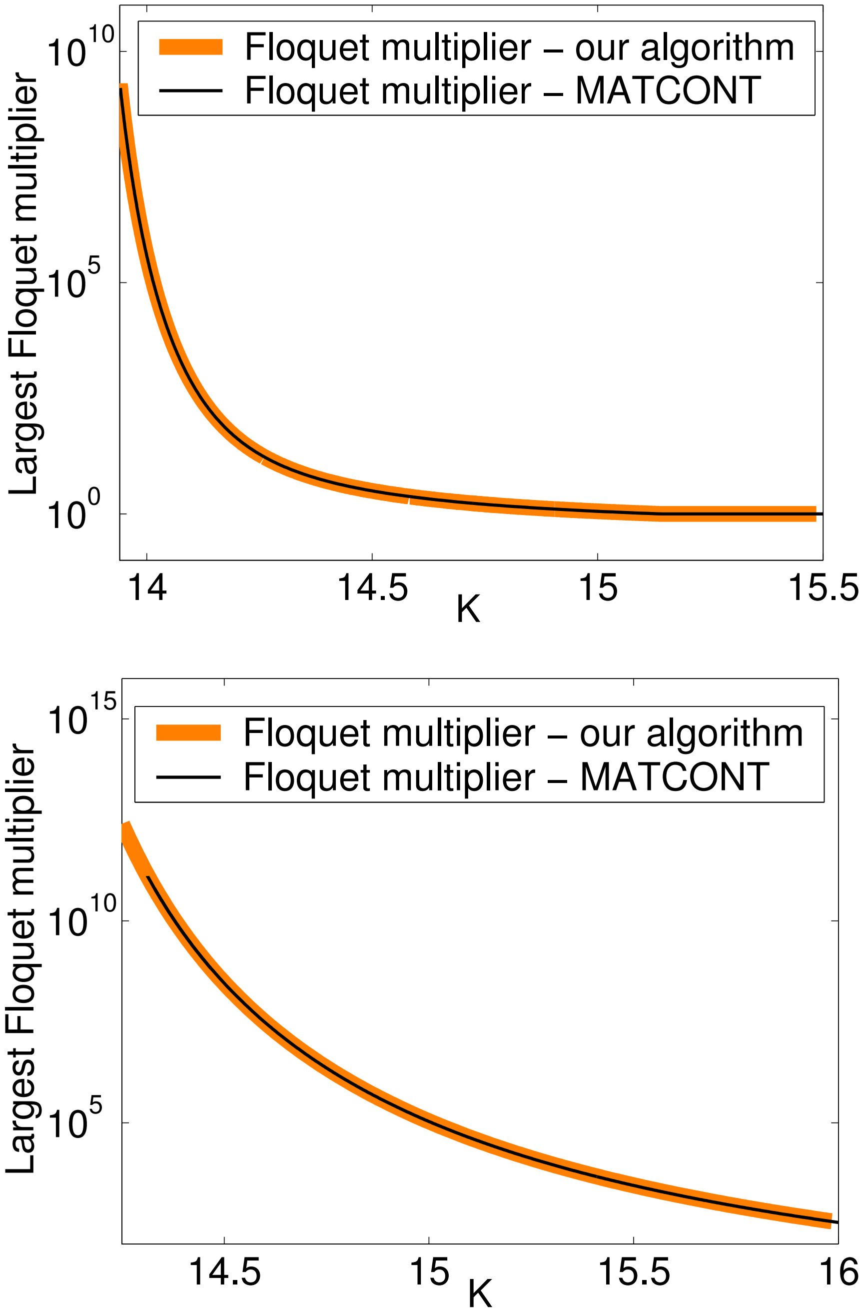

Figure 4.6: Largest Floquet multiplier of limit cycles of Eqs. 4.1 through 4.3 from our algorithm and MATCONT. Top: large, symmetric orbit. Bottom: small, asymmetric orbit.

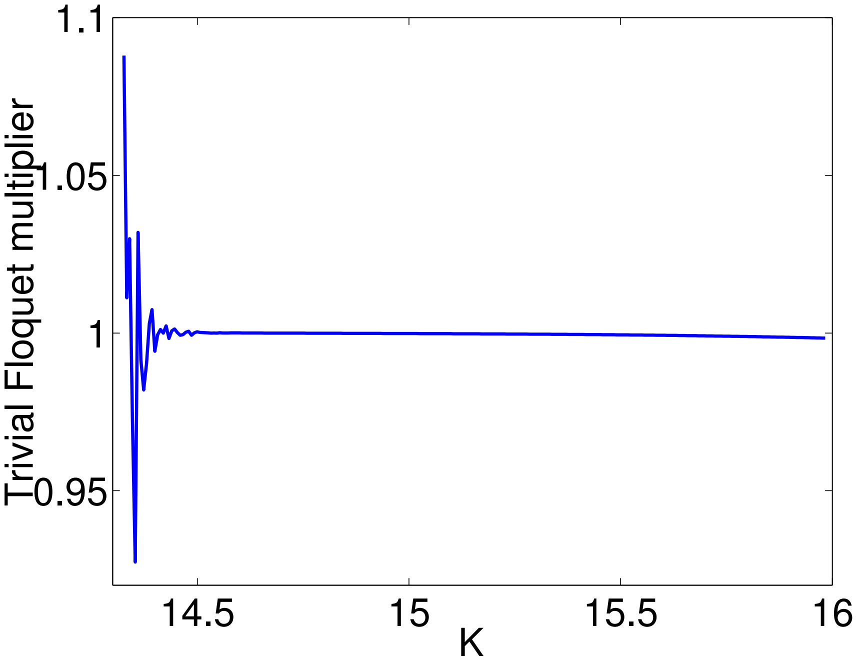

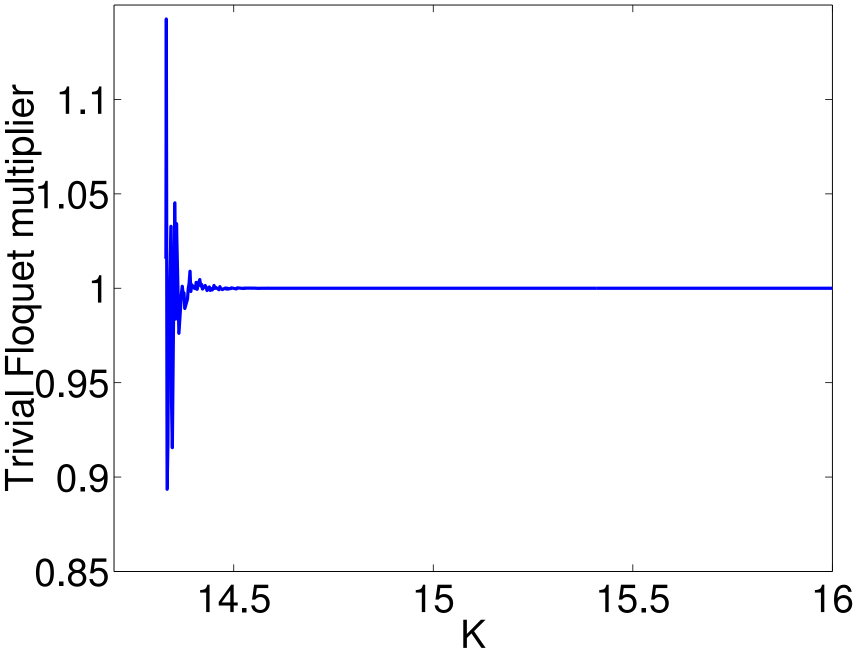

Figure 4.7: Top: Floquet multiplier along the small orbit of Eqs. 4.1 through 4.3 from our algorithm. Bottom: Floquet multiplier along the small orbit from MATCONT.

4.4 Closing remarks

We conclude the study of the first problem of this thesis with a few closing remarks. In this problem, we studied some nonlinear dynamics related to the amplitude control of a lightly damped, resonantly forced, harmonic oscillator. In the course of this study, we encountered an interesting computational problem of continuing limit cycles close to homoclinic points. To that end, we developed a new phase space-based algorithm for limit cycle continuation. The algorithm seems to be particularly useful for continuing limit cycles near homoclinic points. Later, we revisited the amplitude control problem and successfully applied the proposed algorithm to continue the limit cycles of our system of interest quite close to the semi-analytically estimated homoclinic point.

We now move on to the second problem studied in this thesis in the next chapter.

Chapter 5

MMS *via* discretization of a fractionally damped van der Pol oscillator

In this chapter, we present the second problem studied in this thesis.

Here, we study the classical van der Pol oscillator with an added fractional damping term. The system is near Hopf bifurcation. The presence of fractional damping introduces infinite dimensionality and makes the study interesting. Systems with $\mathcal{O}(1)$ fractional terms, such as the one studied in this work, have hitherto been largely treated numerically, after suitable approximations of the fractional order operator in the frequency domain. Analytical progress has been restricted to systems with small fractional terms. In this work, the fractional term is approximated by a recently proposed Galerkin-based discretization scheme [30] resulting in a set of ODEs. A distinguishing feature of this scheme is that, while most existing methods to treat fractional order systems provide approximations to *specific solutions* of the original system for specified initial conditions, the discretization scheme used here approximates the *original system* itself by providing *another system* of ODEs, whose solutions approximate those of the original system. These ODEs are then amenable to usual treatment by the method of multiple scales, provided only that we are close to the bifurcation point. The resulting slow flow provides good approximations to the full numerical solutions, as will be demonstrated in this chapter.

5.1 Introduction

In this work, we adopt the Riemann-Liouville definition definition of the fractional derivative with $x(0) = 0$ [30, 73], which is

$$D^{\alpha}[x(t)] = \frac{1}{\Gamma(1-\alpha)} \int_0^t \frac{\dot{x}(\tau)}{(t-\tau)^{\alpha}} d\tau \,. \tag{5.1}$$

Fractional order derivatives arise in the modeling of chemical [74, 75], biological [76], economic [77] and engineering systems. Engineering applications include viscoelastic damping models [78, 79, 80, 81] and fractional order controllers [82, 83] (see also [84, 85]). The nonlinear dynamics literature contains studies of the fractional order counterparts of the traditional Duffing oscillator [86], Mathieu equation [87], van der Pol oscillator [88, 89, 90, 91], coupled oscillators [92, 93], Chua's circuit [94] and other systems. In most of these studies, the fractional order operator is approximated in the frequency domain [95, 96, 97, 98] to yield a system of ODEs in the time domain, and the resulting approximate system is studied using simulations, phase portraits, Poincaré maps and bifurcation diagrams. Analytical treatment of transient dynamics of nonlinear systems with $\mathcal{O}(1)$ fractional derivative terms has not been attempted. In this work, we make a semi-analytical contribution in this direction.

We study the dynamics of a fractional van der Pol oscillator (fractional order derivatives will be discussed further below) of the form

$$\ddot{x} + \beta\, D^{\alpha}[x(t)] + \mu\, \dot{x}\, (x^2 - 1) + x = 0 \,, \tag{5.2}$$

with parameters β and μ not individually small; for β sufficiently large with μ fixed, the origin is stable, while for μ sufficiently large with β fixed, the origin is unstable and a stable limit cycle exists. We will consider β and μ values that are near the Hopf bifurcation curve. We will also study the case of light resonant forcing. A key point here is that our approach is semi-analytical, with an initial numerical discretization of the fractional derivative operator, followed by analytical treatment using the MMS.

Unlike other studies of fractional van der Pol oscillators (see, e.g., [88, 90, 91]) which discretize the fractional order operator using frequency domain ideas, we utilize a recently proposed Galerkin projection-based discretization scheme [30]. This scheme has been shown to provide useful numerical approximations for several fractional order systems [99, 100, 101], and is simple to use provided 3 matrices have been computed (we provide these matrices for $\alpha = 1/2$ and $\alpha = 1/3$ in appendices B and C respectively). A distinguishing feature of this scheme, as mentioned above, is that the Galerkin scheme provides an approximation to the *original system* itself by providing *another* dynamic system. Subsequent analysis could in principle proceed using *any* useful method: we use the MMS. Note that this approach of approximating an infinite dimensional system by a finite dimensional one through Galerkin projections is often done in the case of partial differential equations modeling several physical systems (see, for e.g., [4]). However, use of such an approach to subsequently analytically study fractional order systems is new.

Note that our system of Eq. 5.2, as well as our approach to approximate the fractional derivative, differ from [91], wherein the highest derivative is of fractional order; our system is also different from [89] wherein the damping is purely fractional; finally note that, *after* discretization using a scheme known to be accurate, our subsequent treatment is analytical (MMS).

We emphasize that the method of averaging and the MMS have both been applied, without numerical discretization, to fractional order ODEs [21, 102, 103, 104, 105, 106] and PDEs [107] where the fractional damping term was small. In contrast, we study the system near a Hopf bifurcation, but at a point where the fractional derivative term is *not* small. Direct MMS treatment of the fractional derivative operator in such cases has not been done anywhere so far to the best of our knowledge, and is not attempted here, either. Even the MMS treatment of an approximating system, such as we do here, is a new contribution to the study of fractionally damped systems.

We proceed by using the Galerkin scheme [30] to approximate the fractional order operator. The approximation scheme of [30] yields two $n \times n$ matrices $\mathbf{A}_\alpha$, $\mathbf{B}_\alpha$ and an $n \times 1$ matrix $\mathbf{c}_\alpha$ (see appendices B and C), which depend on the order of the fractional term α as denoted by the subscripts, as well as a user-specified frequency range.

The solution of the original Eq. 5.2 is approximated by the solution of the following coupled system of ODEs.

$$\begin{aligned} \ddot{x} + \frac{\beta}{\Gamma(1+\alpha)\Gamma(1-\alpha)}\,\mathbf{c}_\alpha^T\mathbf{a} + \mu\,\dot{x}\,(x^2-1) + x &= 0\,, && (5.3)\\ \mathbf{A}_\alpha\dot{\mathbf{a}} + \mathbf{B}_\alpha\mathbf{a} &= \mathbf{c}_\alpha\dot{x}\,, && (5.4) \end{aligned}$$

where the superscript T denotes matrix transpose. The initial conditions for Eqs. 5.3 and 5.4 are taken as $\mathbf{a}(0) = \mathbf{0}$, and $x(0) = 0$ by assumption (for simplicity only: nonzero initial conditions can be accommodated using the Caputo derivative [108]).

5.2 The unforced system

We consider the van der Pol oscillator

$$\ddot{x} + \beta\, D^{\alpha}[x(t)] + \mu\, \dot{x}\,(x^2 - 1) + x = 0\,. \tag{5.5}$$

We consider the case of $\alpha = \frac{1}{2}$ in detail below, and briefly present results for the case of $\alpha = \frac{1}{3}$ later. Thus,

$$\ddot{x} + \beta\, D^{\frac{1}{2}}[x(t)] + \mu\, \dot{x}\,(x^2 - 1) + x = 0\,. \tag{5.6}$$

5.2.1 Hopf bifurcation point

For $\beta = 0$, we have the usual van der Pol oscillator for which the trivial solution $x(t) \equiv 0$ loses stability through a Hopf bifurcation at $\mu = 0$. For $\mu < 0$, the origin is stable. For $\mu > 0$, the origin is unstable and surrounded by a stable limit cycle.

For $\beta > 0$, the presence of fractional damping stabilizes the origin and postpones the onset of Hopf bifurcation. At the Hopf point, we anticipate harmonic solutions of a particular frequency. We explicitly seek the possibility of such a solution by substituting $x = e^{i\,\omega t}$, for a constant ω, in Eq. 5.6. We get (using Eq. 5.1)

$$\left(-\omega^2 + \beta\, \mathrm{erf}(\sqrt{i\omega t})\sqrt{i\omega} - i\mu\omega + 1\right) e^{i\omega t} = 0\,, \tag{5.7}$$

where erf(.) is the error function. Now, $e^{i\omega t} \neq 0$. Thus for a periodic solution we require

$$-\omega^2 + \beta\, \mathrm{erf}(\sqrt{i\omega t})\sqrt{i\omega} - i\mu\omega + 1 = 0\,, \tag{5.8}$$

For a harmonic solution[1], we let $t \to \infty$ in the above equation, noting $\mathrm{erf}(\sqrt{i\omega t}) \to 1$. Thus, we obtain the Hopf bifurcation equation as

$$-\omega^2 + \beta\sqrt{i\omega} - i\mu\omega + 1 = 0\,. \tag{5.9}$$

---

[1] Methods like harmonic balance on fractional system involve similar steps and arrive at similar results (see Eq. 12 of [109]). See also Eq. 15 of [21], and also Eq. 15 of[105]

Note that Eq. 5.9 is *not* the characteristic equation of the linearization of Eq. 5.6 in the sense that the general solution of Eq. 5.6 is not of the form e^{st}, as would be in the case of ordinary differential equations yielding the complete set of complementary solutions. However, a Hopf bifurcation point is, nevertheless, determined by Eq. 5.9.

Separating real and imaginary parts of Eq. 5.9 gives

$$\begin{aligned} -\omega^2 + 1 + \frac{\beta\sqrt{\omega}}{\sqrt{2}} &= 0\,, & (5.10)\\ \frac{\beta\sqrt{\omega}}{\sqrt{2}} - \mu\,\omega &= 0\,. & (5.11)\end{aligned}$$

Eliminating ω between Eqs. 5.10 and 5.11 and simplifying, we obtain

$$\beta = \sqrt{\mu^3 + \mu^2\sqrt{\mu^2+4}}\,. \tag{5.12}$$

Equation 5.12 marks the locus of Hopf bifurcation points in the $\beta - \mu$ plane. For $0 < \mu \ll 1$, Eq. 5.12 becomes

$$\beta \approx \sqrt{2}\,\mu\,, \tag{5.13}$$

The small-μ limit result of Eq. 5.13 could also be obtained by the method of averaging, following [103] by treating β and μ as small after linearizing Eq. 5.6. Thus, setting $\mu = \epsilon\,\bar{\mu}$ and $\bar{\beta} = \epsilon\,\bar{\beta}$, where $0 < \epsilon \ll 1$, the slow flow governing the evolution of amplitude R is found to be (details not presented)

$$\frac{dR}{dt} = \epsilon\,R\left(\frac{\bar{\mu}}{2} - \frac{\bar{\beta}}{2\sqrt{2}}\right)\,,$$

Setting the coefficient of R in the right hand side of the slow flow to zero, we verify Eq. 5.13.

5.2.2 Conversion to ODEs

We now proceed with the Galerkin approximation of the fractional derivative of Eq. 5.6 using Eqs. 5.3 and 5.4. For $\alpha = \frac{1}{2}$, these equations yield

$$\ddot{x} + \frac{2}{\pi}\,\beta\,\mathbf{c}_{1/2}^T\mathbf{a} + \mu\,\dot{x}\,(x^2-1) + x = 0\,, \tag{5.14}$$

$$\mathbf{A}_{1/2}\dot{\mathbf{a}} + \mathbf{B}_{1/2}\mathbf{a} = \mathbf{c}_{1/2}\dot{x}\,. \tag{5.15}$$

The matrices $\mathbf{A}_{1/2}$, $\mathbf{B}_{1/2}$ and $\mathbf{c}_{1/2}$ (for[2] $n = 15$) are provided in appendix B. Henceforth, in this chapter we drop the dependencies of the matrices on α and simply write $\mathbf{A}$, $\mathbf{B}$ and $\mathbf{c}$, while they actually refer to $\mathbf{A}_{1/2}$, $\mathbf{B}_{1/2}$ and $\mathbf{c}_{1/2}$.

Rewriting Eqs. 5.14 and 5.15 in state space form, we have

$$\dot{\mathbf{x}} = \mathbf{M}\mathbf{x} + \mathbf{N}\,, \tag{5.16}$$

where the state vector $\mathbf{x} = \begin{Bmatrix} x \\ \dot{x} \\ \mathbf{a} \end{Bmatrix}$, the 17×17 matrix $\mathbf{M} = \begin{bmatrix} 0 & 1 & \mathbf{0}^T \\ -1 & \mu & -\frac{2}{\pi}\,\beta\,\mathbf{c}^T \\ \mathbf{0} & \mathbf{A}^{-1}\,\mathbf{c} & -\mathbf{A}^{-1}\mathbf{B} \end{bmatrix}$, the vector $\mathbf{N} = \begin{Bmatrix} 0 \\ -\mu\,\dot{x}\,x^2 \\ \mathbf{0} \end{Bmatrix}$, the boldface $\mathbf{0}$ is a 15×1 null vector, and 0 is just the scalar zero.

Linearization of Eq. 5.16 yields $\dot{\mathbf{x}} = \mathbf{M}\mathbf{x}$, which yields the eigenvalue problem

$$|\mathbf{M} - \lambda\mathbf{I}| = 0\,, \tag{5.17}$$

where $\mathbf{I}$ is the identity matrix. Substituting $\lambda = i\,\omega$ in the above equation and separating real and imaginary parts yields two long equations in β, μ and ω (not given here). These equations are numerically solved for μ and ω over a range of β, and the resulting solutions are plotted along with Eq. 5.12 as well as the small-μ approximation of Eq. 5.13 in Fig. 5.1. It is clear that Eqs. 5.12 and 5.17 give overlapping results in Fig. 5.1. We separately plot the difference in μ, as predicted by Eq. 5.12 and by the Galerkin method, in Fig. 5.2. The agreement seen in Fig. 5.1 and implied by 5.2 suggests the correctness of Eq. 5.12 as well as the accuracy of the Galerkin approximation (Eqs. 5.14 and 5.15).

In Fig. 5.1, the region below the curve represents stable parameter values, while the region above the curve represents unstable points. For a fixed β, as we increase μ, the system undergoes a Hopf bifurcation as the curve is crossed. Subsequently the origin is unstable and the near-Hopf point dynamics is governed by nonlinearities. In what follows we analyze Eqs. 5.14 and 5.15, using the MMS, for a fixed value of β; and for μ near the corresponding Hopf bifurcation point.

---

[2] The approximation could be refined by taking larger n, but we do not do that here.

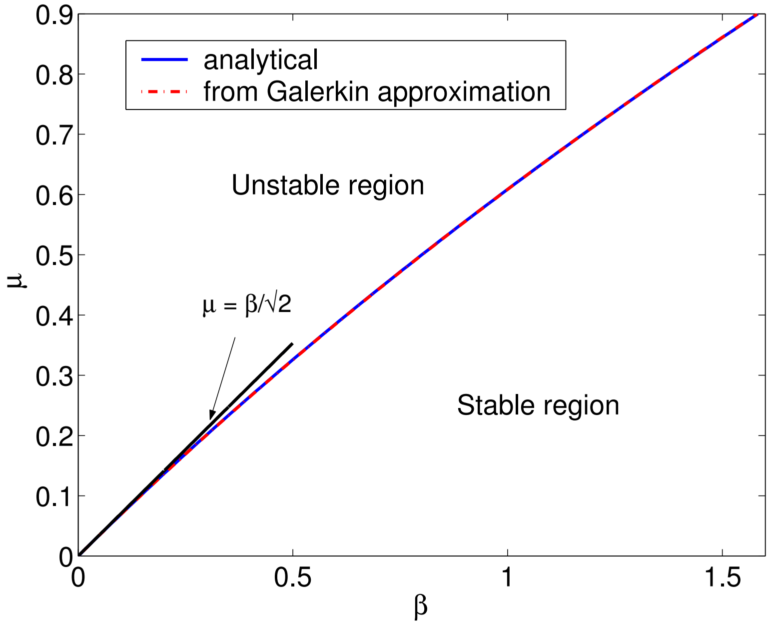

Figure 5.1: Locus of Hopf bifurcation points obtained from Eqs. 5.12 and 5.17, along with the small-μ approximation of Eq. 5.13. Excellent agreement is seen between predictions of Eqs. 5.12 and 5.17.

5.3 MMS analysis

From this point onwards, we are using the MMS to examine the system of Eqs. 5.14 and 5.15. The fractional derivative has been discretized accurately and is no longer dealt with in a direct manner.

We fix $\beta = 1$. The Hopf point[3] is $(\bar{\mu}, \beta) = (0.60856, 1)$ (from Eq. 5.17). The purely imaginary eigenvalues of $\mathbf{M}$ at the Hopf bifurcation point are $\lambda = \pm 1.3494i$. Apart from these imaginary eigenvalues, there are 15 other eigenvalues which are all negative. A numerical examination of these eigenvalues raises an interesting but peripheral question, which we will discuss in appendix E. We now proceed with the MMS analysis.

---

[3] All results in this chapter are reported with five displayed significant digits, although we have performed our calculations with 40 digits of precision in the package MAPLE.

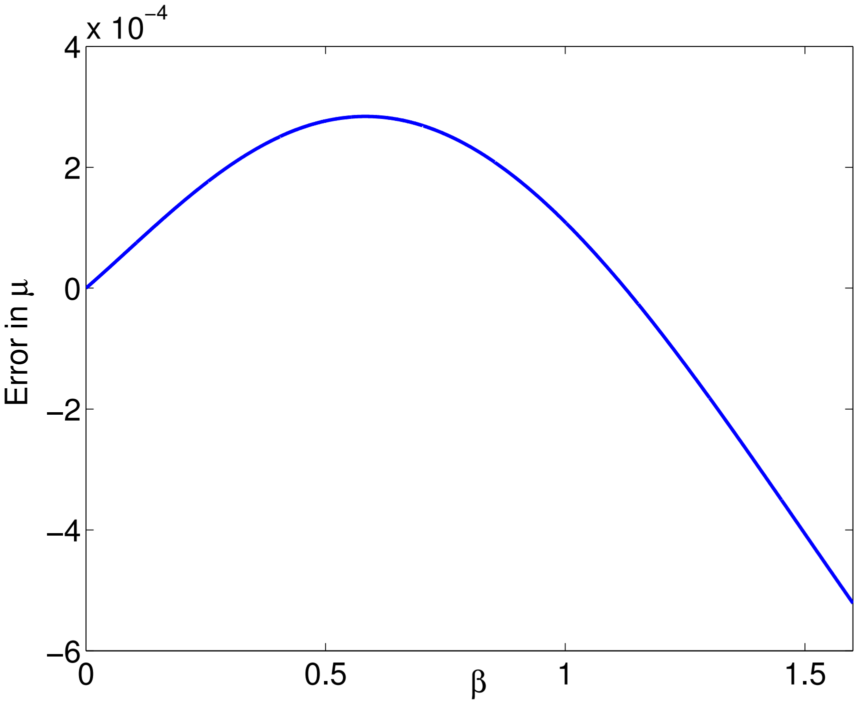

Figure 5.2: A plot of the difference in μ as computed from Eqs. 5.12 and 5.17.

5.3.1 Scaling

To facilitate the application of the MMS, we introduce detuning near $\bar{\mu}$ and adopt the following new scaling variables

$$\mu = \bar{\mu}(1+\epsilon),\ \mathbf{x} = \sqrt{\epsilon}\mathbf{y}$$

where $0 < \epsilon \ll 1$, where $\mathbf{y} = \left\{ \begin{array}{c} y \\ \dot{y} \\ \mathbf{b} \end{array} \right\}$. Here $\bar{\mu}$ and $\mathbf{y}$ are $\mathcal{O}(1)$ quantities.

Substitution of the above in Eq. 5.16 and simplifying, we get

$$\dot{\mathbf{y}} = \mathbf{P}\mathbf{y} + \epsilon\mathbf{Q}_1 + \mathcal{O}(\epsilon^2)\,, \tag{5.18}$$

where $\mathbf{P} = \begin{bmatrix} 0 & 1 & \mathbf{0}^T \\ -1 & \bar{\mu} & -\frac{2}{\pi}\,\mathbf{c}^T \\ \mathbf{0} & \mathbf{A}^{-1}\,\mathbf{c} & -\mathbf{A}^{-1}\mathbf{B} \end{bmatrix}$, and $\mathbf{Q}_1 = \left\{ \begin{array}{c} 0 \\ -\bar{\mu}\,\dot{y}\,y^2 + \bar{\mu}\,\dot{y} \\ \mathbf{0} \end{array} \right\}$. Note that $\mathbf{P}$ is just the matrix $\mathbf{M}$ (Eq. 5.16) evaluated at the Hopf point $(\bar{\mu}, \beta) = (0.60856, 1)$. We now proceed with the application of the MMS to Eq. 5.18.

5.3.2 MMS

We introduce fast and slow time scales $T_0 = t$ and $T_1 = \epsilon t$ respectively, and write

$$\mathbf{y} = \mathbf{y}_0(T_0, T_1) + \epsilon \mathbf{y}_1(T_0, T_1) + \cdots . \tag{5.19}$$

Substitution of Eq. 5.19 in Eq. 5.18, we obtain at $\mathcal{O}(1)$:

$$\frac{\partial \mathbf{y}_0}{\partial T_0} = \mathbf{P}\mathbf{y}_0 . \tag{5.20}$$

Note that the system Eq. 5.20 is at Hopf bifurcation. We take the solution of Eq. 5.20 as

$$\mathbf{y}_0(T_0, T_1) = (r(T_1) + is(T_1))\,\mathbf{u}\,e^{i\omega T_0} + (r(T_1) - is(T_1))\,\bar{\mathbf{u}}\,e^{-i\omega T_0} , \tag{5.21}$$

where the real-valued functions $r(T_1)$ and $s(T_1)$ are to be determined from calculations at subsequent orders; $\omega = 1.3494$ (from the purely imaginary eigenvalue of $\mathbf{P}$); $\mathbf{u}$ is the right eigenvector of $\mathbf{P}$ corresponding to the eigenvalue $\lambda = 1.3494\,i$, and $\bar{\mathbf{u}}$ is the complex conjugate of $\mathbf{u}$. Decaying components along all other eigenvectors of $\mathbf{P}$ are dropped from the solution of Eq. 5.20. As discussed in a different context in [20], dropping the decaying exponentials gives us the dynamics on the center manifold.

In Eq. 5.21, we have normalized the eigenvector such that the first element of $\mathbf{u}$ is unity. This is done because the first component of the state vector is the dynamical quantity of primary interest to us. Our slow flow equations below will correspond to this particular normalization.

Proceeding to the next order, at $\mathcal{O}(\epsilon)$ we have

$$\frac{\partial \mathbf{y}_1}{\partial T_0} - \mathbf{P}\mathbf{y}_1 = -\frac{\partial \mathbf{y}_0}{\partial T_1} + \mathbf{Q}_1(\mathbf{y}_0) . \tag{5.22}$$

Substituting the leading order solution Eq. 5.21 in the right hand side of Eq. 5.22 we obtain

$$\frac{\partial \mathbf{y}_1}{\partial T_0} - \mathbf{P}\mathbf{y}_1 = \mathbf{v}(T_1)e^{i\omega T_0} + \bar{\mathbf{v}}(T_1)e^{-i\omega T_0} + \mathbf{w}(T_1)e^{3i\omega T_0} + \bar{\mathbf{w}}(T_1)e^{-3i\omega T_0} , \tag{5.23}$$

where overbars denote complex conjugates, and where $\mathbf{v}$ and $\mathbf{w}$ involve complicated expressions (not presented) in terms of r, s, and their partial derivatives with respect to T_1.

In Eq. 5.23, we encounter forcing in resonance with the eigenvalues $\pm i\omega$. To eliminate secular terms, we must ensure that $\mathbf{v}$ is orthogonal to the left eigenvector of $\mathbf{P}$ corresponding to the eigenvalue $i\omega$ [110], with the corresponding condition for $\bar{\mathbf{v}}$ being then automatically satisfied. Thus, the solvability conditions may be written compactly as

$$\mathbf{v}^T\mathbf{g} = 0\,, \tag{5.24}$$

where $\mathbf{g}$ is the left eigenvector of $\mathbf{P}$ corresponding to the eigenvalue $i\omega$. We have normalized $\mathbf{g}$ such that its first element is unity, though it is not essential here. Separating real and imaginary parts of Eq. 5.24 yields, after some elementary manipulations, the slow flow equations:

$$\frac{\partial r}{\partial T_1} = 0.33748\,r + 0.042409\,s - 0.33748\,r^3 - 0.042409\,r^2\,s - 0.33748\,r\,s^2 - 0.042409\,s^3\,, \tag{5.25}$$

$$\frac{\partial s}{\partial T_1} = -0.042409\,r + 0.33748\,s + 0.042409\,r^3 - 0.33748\,r^2\,s + 0.042409\,r\,s^2 - 0.33748\,s^3\,, \tag{5.26}$$

where we have dropped dependencies of r and s on T_1 for brevity.

5.3.3 Numerical results

We now present some numerical results to demonstrate the utility of the slow flow equations. We choose $\epsilon = 0.01$ and we take $\mathbf{y}(0) = \left\{\begin{array}{ccc} 0 & 1 & \mathbf{0} \end{array}\right\}^T$ which, for $\epsilon = 0.01$, corresponds to $\mathbf{x}(0) = \left\{\begin{array}{ccc} 0 & 0.1 & \mathbf{0} \end{array}\right\}^T$. The initial conditions on r and s are then determined from Eq. 5.21 as $r(0) + i\,s(0) = \dfrac{\mathbf{g}^T\,\mathbf{y}(0)}{\mathbf{g}^T\,\mathbf{u}} = -0.051642 - 0.41096i$.

With the above initial conditions, Eqs. 5.25 and 5.26 are integrated to obtain the evolution of r and s. The final solution is computed as

$$\mathbf{x}(t) = 2\sqrt{\epsilon}\,\mathrm{Re}\left(\left(r(T_1) + is(T_1)\right)\mathbf{u}\,e^{i\omega t}\right)\,, \tag{5.27}$$

where Re(.) represents the real part of the quantity in the parenthesis. Also for direct comparison, Eqs. 5.14 and 5.15 were integrated with the initial conditions $\mathbf{x}(0)$, using $\beta = 1$ and $\mu = \bar{\mu}(1+\epsilon) = 0.61464$ (compare with $\bar{\mu} = 0.60856$).

The first component of the solution vector $x(t)$, from direct integration, is plotted along with the amplitude of the MMS approximations in Fig. 5.3. A portion of the complete solution $x(t)$ computed from the MMS approximations is plotted along with that from direct numerical integration in Fig. 5.4. The agreement is good to plotting accuracy.

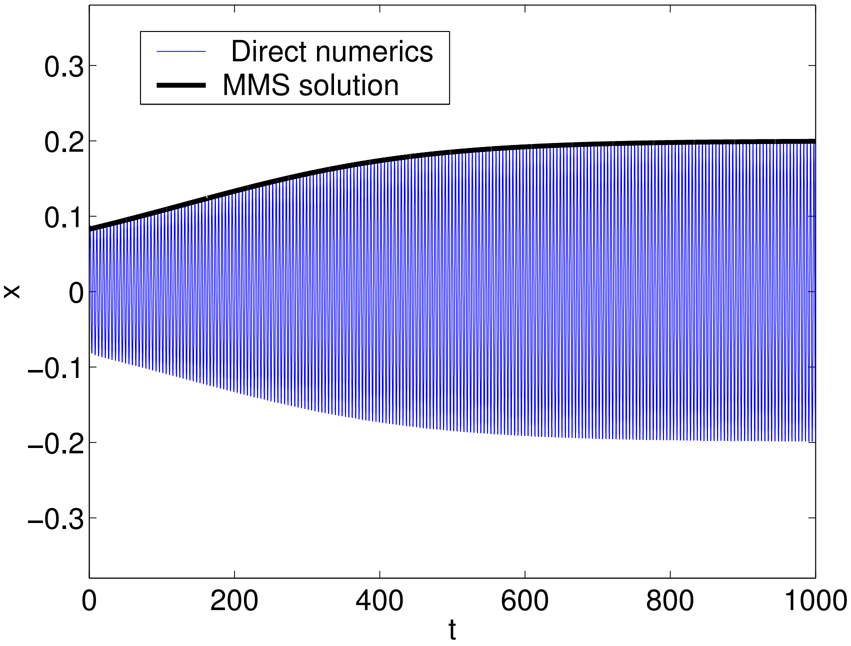

Figure 5.3: Plots of solutions obtained by direct numerical integration of Eqs. 5.14 and 5.15 and amplitudes from the MMS slow flow Eqs. 5.25 and 5.26. Parameters and initial conditions: $\epsilon = 0.01$, $\beta = 1$, $\mu = 0.61464$, $\bar{\mu} = 0.60856$; $\dot{x}(0) = 0.1$, all other state variables have zero initial conditions; $r(0)$ and $s(0)$ taken as explained in main text. Plot shows solution settling down to a limit cycle oscillation.

In another simulation, we took $\epsilon = 0.01$ and $\mathbf{x}(0) = \left\{ \begin{array}{ccc} 0 & 0.5 & \mathbf{0} \end{array} \right\}^T$. The results, in Figs. 5.5 and 5.6, show good agreement.

In another example, we took a somewhat larger value of the parameter as $\epsilon = 0.06$, with $\mathbf{x}(0) = \left\{ \begin{array}{ccc} 0 & 0.2 & \mathbf{0} \end{array} \right\}^T$. The results in Fig. 5.7 show good agreement.

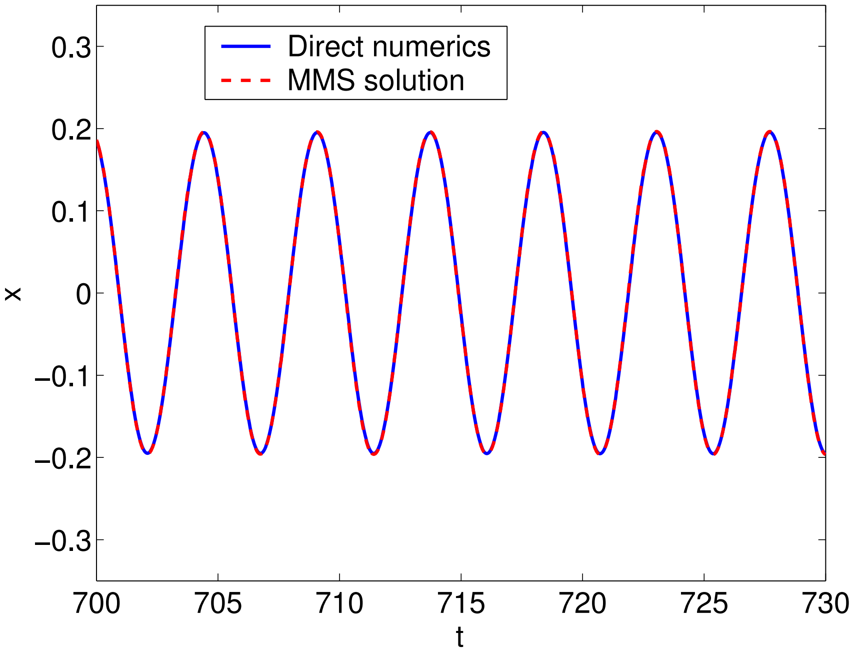

Figure 5.4: A portion of the solution of Fig. 5.3; also plotted is the full solution from the MMS slow flow. Agreement of the MMS solution with full numerics is good.

5.3.4 Results for $\alpha = \frac{1}{3}$

In the previous section, we have demonstrated the application of the MMS on a fractional van der Pol oscillator taking $\alpha = \frac{1}{2}$. However, the method is general and can be used for any α. Only the matrices **A**, **B** and **c** change; these are provided in appendix C. Here we briefly present the results for the following equation:

$$\ddot{x} + \beta\, D^{\frac{1}{3}}[x(t)] + \mu\, \dot{x}\, (x^2 - 1) + x = 0\,. \tag{5.28}$$

We take $\beta = 1.2$ and the Hopf bifurcation parameters (from the Galerkin approximation) are $(\bar{\mu}, \beta) = (0.46229, 1.2)$. Proceeding as before, the final slow flow equations are:

$$\frac{\partial r}{\partial T_1} = 0.25090\, r + 0.028488\, s - 0.25090\, r^3 - 0.028488\, r^2\, s - 0.25090\, r\, s^2 - 0.028488\, s^3\,, \tag{5.29}$$

$$\frac{\partial s}{\partial T_1} = -0.028488\, r + 0.25090\, s + 0.028488\, r^3 - 0.25090\, r^2\, s + 0.028488\, r\, s^2 - 0.25090\, s^3\,. \tag{5.30}$$

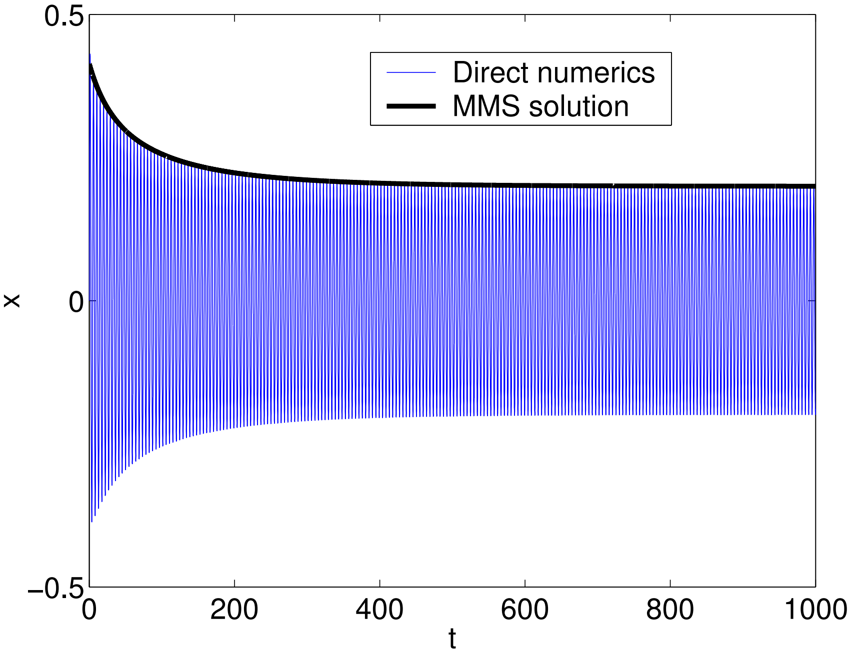

Figure 5.5: Plots of solutions obtained by direct numerical integration of Eqs. 5.14 and 5.15 and the MMS slow flow Eqs. 5.25 and 5.26. Parameters and initial conditions: $\epsilon = 0.01$, $\beta = 1$, $\mu = 0.61464$, $\bar{\mu} = 0.60856$; $\dot{x}(0) = 0.5$, all other state variables have zero initial conditions; $r(0)$ and $s(0)$ taken as explained in main text. Plot shows solution settling down to a limit cycle oscillation.

In a simulation, we took $\epsilon = 0.03$ and $\mathbf{x}(0) = \left\{ \begin{array}{ccc} 0 & 0.05 & \mathbf{0} \end{array} \right\}^T$, with $\mathbf{0}$ being the 15×1 null vector. The results are plotted in Fig. 5.8 and 5.9, showing good agreement.

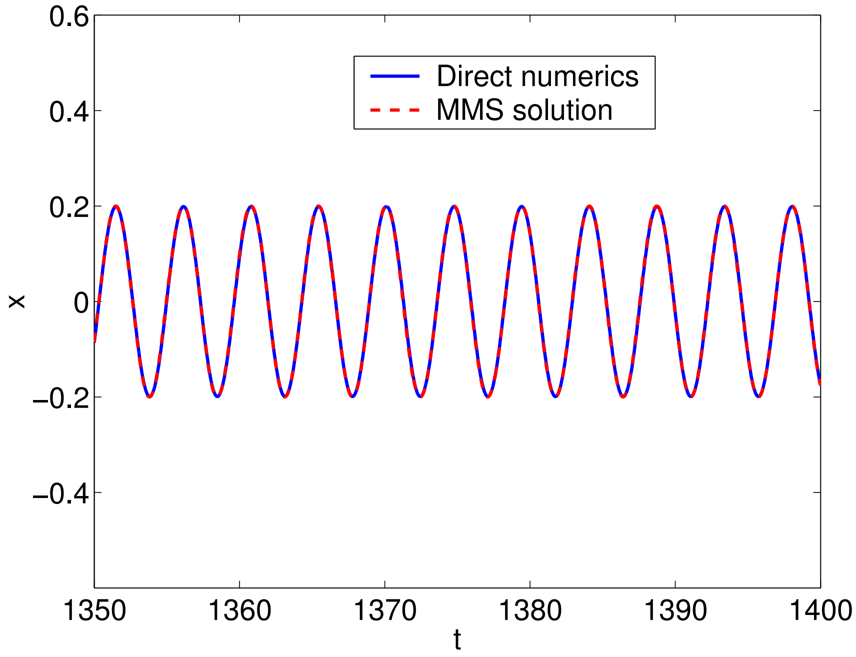

Figure 5.6: A portion of the solution of Fig. 5.5; also plotted is the full solution from the MMS slow flow. Agreement of the MMS solution with full numerics is good (visually indistinguishable).

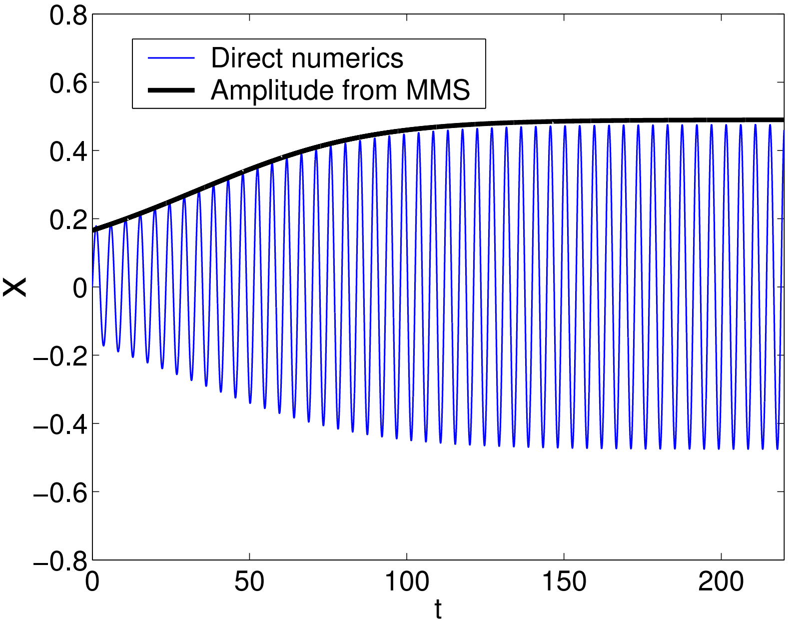

Figure 5.7: Plot of solutions obtained by direct numerical integration of Eqs. 5.14 and 5.15 and the amplitude of the solution from the MMS slow flow Eqs. 5.25 and 5.26. Parameters and initial conditions: $\epsilon = 0.06$, $\beta = 1$, $\mu = 0.64507$, $\bar{\mu} = 0.60856$; $\dot{x}(0) = 0.2$, all other state variables have zero initial conditions; $r(0)$ and $s(0)$ taken as explained in main text. Plot shows solution settling down to a limit cycle oscillation.

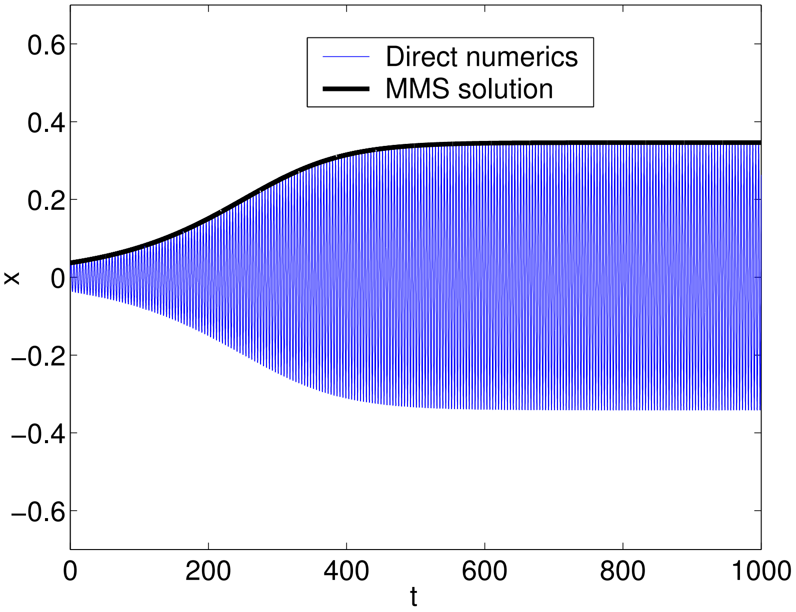

Figure 5.8: Solutions from direct numerical integration and Eqs. 5.29 and 5.30. Here: $\epsilon = 0.03$, $\beta = 1.2$, $\mu = 0.47616$, $\bar{\mu} = 0.46229$; $\dot{x}(0) = 0.05$, $x(0) = 0$, and $\mathbf{a}(0) = \mathbf{0}$; $r(0)$ and $s(0)$ taken as explained in main text. Agreement is excellent.

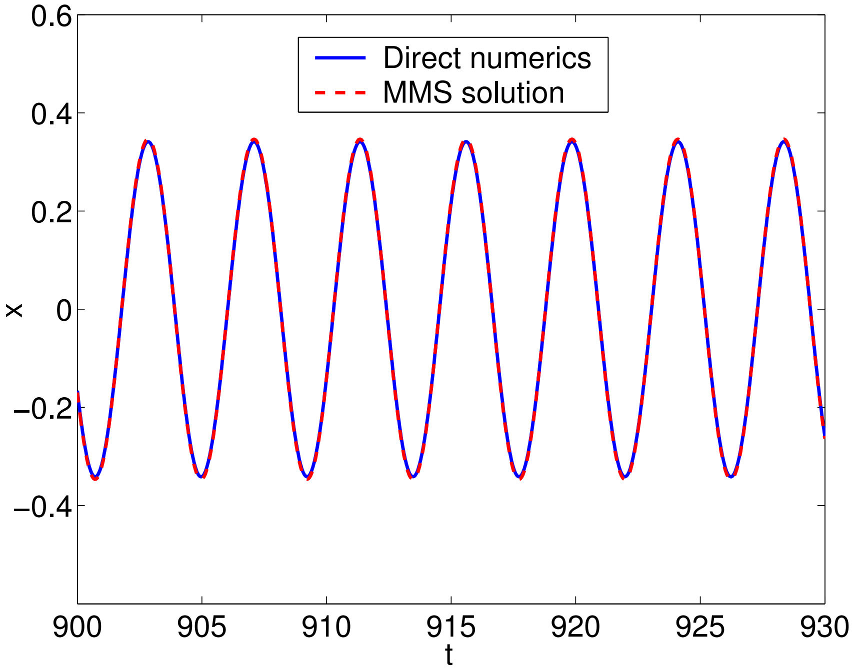

Figure 5.9: A portion of the solution of Fig. 5.8; also plotted is the full solution from the MMS slow flow. Agreement is good.

5.4 Dynamics under resonant forcing

5.4.1 Scaling and the MMS

We now add resonant forcing to the system studied earlier. We consider

$$\ddot{x} + \frac{2}{\pi}\,\beta\,\mathbf{c}^T\mathbf{a} + \mu\,\dot{x}\,(x^2-1) + x = F\cos(\Omega\,t), \tag{5.31}$$

$$\mathbf{A}\dot{\mathbf{a}} + \mathbf{B}\mathbf{a} = \mathbf{c}\dot{x}\,. \tag{5.32}$$

As before we set $\beta = 1$. The system undergoes Hopf bifurcation at $\bar{\mu} = 0.60856$. The corresponding bifurcating eigenvalue is $\pm i\omega_0 = 1.3494\,i$. Scaling time as $\tau = \Omega\,t$, Eqs. 5.31 and 5.32 become

$$x'' + \frac{2}{\pi\,\Omega^2}\,\mathbf{c}^T\mathbf{a} + \frac{\mu}{\Omega}\,x'\,(x^2-1) + \frac{x}{\Omega^2} = \frac{F}{\Omega^2}\cos(\tau), \tag{5.33}$$

$$\mathbf{A}\mathbf{a}' + \frac{1}{\Omega}\mathbf{B}\mathbf{a} = \mathbf{c}x'\,, \tag{5.34}$$

where primes denote differentiation with respect to scaled time. Corresponding to the scaled time, we redefine the state vector as $\mathbf{x} = \left\{\begin{array}{c} x \\ x' \\ \mathbf{a} \end{array}\right\}$.

For small departures of μ from $\bar{\mu}$, we expect the limit cycle frequency to be close to $\omega_0 = 1.3494$, and we want to force the system resonantly. With the above observations, we introduce the following new scaling variables:

$$\mathbf{x} = \sqrt{\epsilon}\mathbf{y}\,, \mu = \bar{\mu}(1+\epsilon)\,, \Omega = \omega_0(1+\epsilon\,\Delta)\,, F = \epsilon\,\sqrt{\epsilon}H\,,$$

where $0 < \epsilon \ll 1$, $\mathbf{y} = \left\{\begin{array}{c} y \\ y' \\ \mathbf{b} \end{array}\right\}$, $\omega_0 = 1.3494$, and $\bar{\mu}$, $\mathbf{y}$, ω_0, H and Δ are $\mathcal{O}(1)$.

With the above scaling, Eq. 5.33 becomes

$$y'' + \frac{2}{\pi\,\omega_0^2}\,\mathbf{c}^T\mathbf{b} - \frac{\bar{\mu}}{\omega_0}\,y' + \frac{y}{\omega_0^2} = \epsilon\left(\frac{4\,\Delta\,\mathbf{c}^T\mathbf{b}}{\omega_0^2\,\pi} + \frac{2\,\Delta\,y}{\omega_0^2} - \frac{\bar{\mu}\,y'\,y^2}{\omega_0} - \frac{\bar{\mu}\,\Delta\,y'}{\omega_0} + \frac{\bar{\mu}\,y'}{\omega_0} + \frac{H\,\cos\tau}{\omega_0^2}\right). \tag{5.35}$$

Also, Eq. 5.34 becomes

$$\mathbf{A}\,\mathbf{b}' + \frac{1}{\omega_0}\mathbf{B}\mathbf{b} = \mathbf{c}y' + \epsilon\frac{\Delta}{\omega_0}\mathbf{B}\mathbf{b}\,. \tag{5.36}$$

Rewriting Eqs. 5.35 and 5.36 in state space form we get

$$\mathbf{y}' = \mathbf{R}\mathbf{y} + \epsilon\,\mathbf{S}_1 + \mathcal{O}(\epsilon^2)\,, \tag{5.37}$$

where

$$\mathbf{R} = \begin{bmatrix} 0 & 1 & \mathbf{0}^T \\ -\frac{1}{\omega_0^2} & \frac{\bar{\mu}}{\omega_0} & -\frac{2}{\pi\,\omega_0^2}\,\mathbf{c}^T \\ \mathbf{0} & \mathbf{A}^{-1}\,\mathbf{c} & -\frac{1}{\omega_0}\mathbf{A}^{-1}\mathbf{B} \end{bmatrix},$$

and

$$\mathbf{S}_1 = \left\{ \begin{array}{c} 0 \\ \frac{4\,\Delta\,\mathbf{c}^T\mathbf{b}}{\omega_0^2\,\pi} + \frac{2\,\Delta\,y}{\omega_0^2} - \frac{\bar{\mu}\,y'\,y^2}{\omega_0} - \frac{\bar{\mu}\,\Delta\,y'}{\omega_0} + \frac{\bar{\mu}\,y'}{\omega_0} + \frac{H\,\cos\tau}{\omega_0^2} \\ \frac{\Delta}{\omega_0}\mathbf{A}^{-1}\mathbf{B}\mathbf{b} \end{array} \right\},$$

The eigenvalues of the matrix $\mathbf{R}$ are listed in appendix D, where we will discuss an interesting time scale related issue for this system. Here, the key point is that two eigenvalues are $\pm i$ since we are now using scaled time τ for our derivatives; and all other eigenvalues are real and negative.

MMS for Eq. 5.37 proceeds in the same way as before except that now the time scales are $T_0 = \tau$, $T_1 = \epsilon\,\tau$ etc. The leading order solution is taken as

$$\mathbf{y}_0(T_0, T_1) = (r(T_1) + is(T_1))\,\mathbf{u}_1\,e^{iT_0} + (r(T_1) - is(T_1))\,\bar{\mathbf{u}}_1\,e^{-iT_0}\,, \tag{5.38}$$

where $\mathbf{u}_1$ is the right eigenvector of the matrix $\mathbf{R}$ corresponding to the eigenvalue i, normalized such that its first element is unity; and $\bar{\mathbf{u}}_1$ is the complex conjugate of $\mathbf{u}_1$.

Proceeding as before, the slow flow governing the evolution of r and s are

$$\begin{aligned}\frac{\partial r}{\partial T_1} &= -0.019135\,H + 0.25009\,r + 0.031427\,s + \Delta\,s - 0.25009\,r^3 - 0.031427\,r^2\,s - \\ &\quad 0.25009\,r\,s^2 - 0.031427\,s^3\,,\end{aligned} \tag{5.39}$$

$$\begin{aligned}\frac{\partial s}{\partial T_1} &= -0.15227\,H - 0.031427\,r + 0.25009\,s - \Delta\,r + 0.031427\,r^3 - 0.25009\,r^2\,s + \\ &\quad 0.031427\,r\,s^2 - 0.25009\,s^3\,.\end{aligned} \tag{5.40}$$

5.4.2 Numerical results

For the van der Pol oscillator forced near resonance, at a given level of detuning, for smaller forcing magnitudes, quasiperiodic behavior is expected. Increased forcing magnitude is expected to entrain the oscillator to the forcing frequency.

We demonstrate these behaviors through numerical simulations below. For $\epsilon = 0.01$, we fixed the detuning at $\Delta = 0.5$ and the forcing magnitude $H = 1$. Thus $\mu = \bar{\mu}(1 + \epsilon) = 0.61464$ and $F = \epsilon\sqrt{\epsilon}H = 0.001$. Equations 5.33 and 5.34 are integrated for these parameter values and zero initial conditions. Also, the slow flow equations Eqs. 5.39 and 5.40 are integrated for these parameter values and the final solution is obtained as explained earlier. The full solution from numerical integration along with the amplitude from the MMS approximation is plotted in Fig. 5.10. A zoomed portion thereof is plotted in Fig. 5.11. The agreement between the MMS results and direct numerical treatment is good. It is clear that for this particular forcing magnitude, the system exhibits quasiperiodic behavior. Next, keeping all other parameters fixed at their earlier values, we increase the forcing magnitude to $H = 5$. The results are plotted in Figs. 5.12 and 5.13, and show entrainment. In both cases, the MMS gives a good approximation.

5.4.3 Phase drift, weak phase locking, and entrainment

From the results presented in Figs. 5.10 through 5.13, it is seen that the behavior of the forced, fractionally damped van der Pol oscillator is qualitatively similar to the ordinary forced van der Pol oscillator. In particular, it is seen that for a fixed detuning (with increase in forcing magnitude), the oscillator transitions gradually from phase drift to weak phase locking to entrainment . These results are well established for the usual forced van der Pol oscillator [3, 111, 112, 5].

For completeness, we briefly present some numerical results illustrating this transition. Our treatment of the slow flow closely follows [112]. Of the many standard texts dealing with the forced van der Pol oscillator, we compare our treatment with that in [111]. Both [112] and [111] derive similar slow flow equations. Subsequently, [111] deals with polar coordinates and derives expressions for curves in the parameter plane demarcating regions of phase drift and entrainment. The treatment in [112] is more graphical and insightful

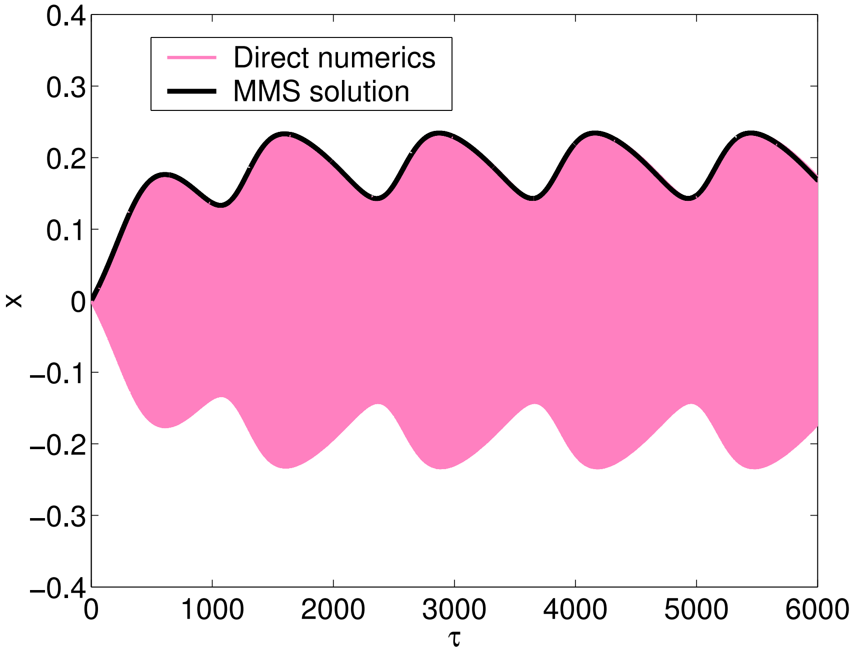

Figure 5.10: Plots of solutions obtained by direct numerical integration of Eqs. 5.33 and 5.34 and the amplitude from the MMS slow flow Eqs. 5.39 and 5.40. Parameters and initial conditions: $\epsilon = 0.01$, $\beta = 1$, $\mu = 0.61464$, $\bar{\mu} = 0.60856$, $\Delta = 0.5$, $\Omega = 1.3562$, $\omega_0 = 1.3494$, $H = 1$, $F = 0.001$; Zero initial conditions on all state variables; $r(0)$ and $s(0)$ taken as explained in main text. Plot shows quasiperiodic motion.

and, through a series of phase portraits, illustrates the transition from phase drift through weak phase locking to entrainment.

Recall that the MMS solution upto leading order is

$$x = 2\,(r(T_1)\,\phi - s(T_1)\,\psi)\,\cos T_0 - 2\,(r(T_1)\,\psi + s(T_1)\,\phi)\,\sin T_0\,, \tag{5.41}$$

where ϕ and ψ are the real and imaginary parts of the first component of the eigenvector $\mathbf{u}_1$ of Eq. 5.38.

We now introduce the following new set of variables

$$\rho = 2\,(r(T_1)\,\phi - s(T_1)\,\psi)\,, \quad \sigma = -2\,(r(T_1)\,\psi + s(T_1)\,\phi)\,.$$

In particular, because of the way we have normalized the eigenvector (see section 5.3) $\phi = 1$

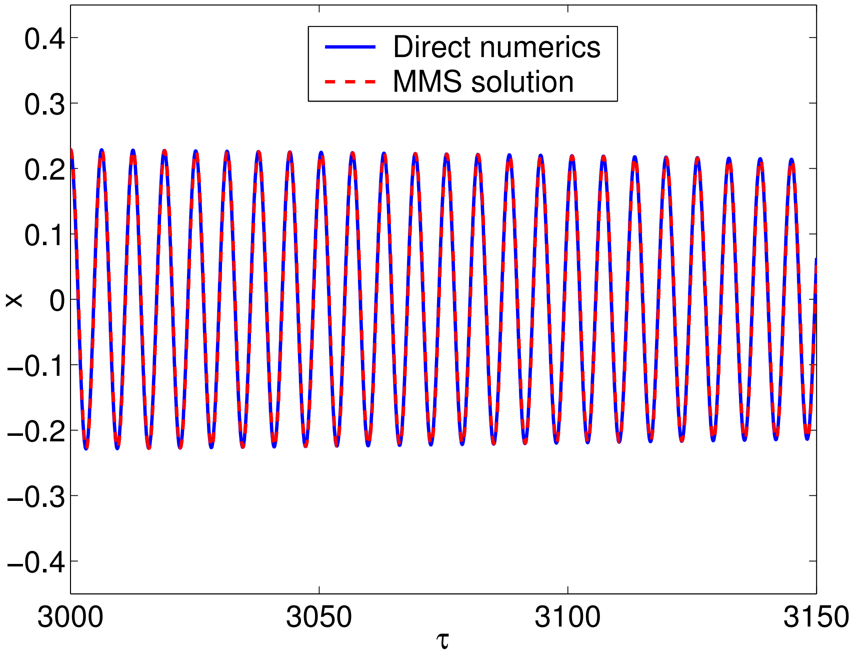

Figure 5.11: A portion of the solution of Fig. 5.10; also plotted is the full solution from the MMS slow flow. Agreement of the MMS solution with full numerics is good.

and $\psi = 0$, giving

$$\rho = 2\,r(T_1)\,, \quad \sigma = -2\,s(T_1)\,.$$

Regardless of our normalization, Eq. 5.41 becomes

$$x = \rho\,\cos T_0 + \sigma\,\sin T_0\,, \tag{5.42}$$

and Eqs. 5.39 and 5.40 become

$$\frac{\partial\rho}{\partial T_1} = -0.038270\,H + 0.25009\,\rho - 0.031427\,\sigma - \Delta\,\sigma - 0.062524\,\rho^3 + 0.0078569\,\rho^2\,\sigma - 0.062524\,\rho\,\sigma^2 + 0.0078569\,\sigma^3\,, \tag{5.43}$$

$$\frac{\partial\sigma}{\partial T_1} = 0.30455\,H + 0.031427\,\rho + 0.25009\,\sigma + \Delta\,\rho - 0.0078569\,\rho^3 - 0.062524\,\rho^2\,\sigma - 0.0078569\,\rho\,\sigma^2 - 0.062524\,\sigma^3\,. \tag{5.44}$$

Fixed points of Eqs. 5.43 and 5.44 result in periodic solutions of x according to Eq. 5.42, while periodic solutions of Eqs. 5.43 and 5.44 (closed curves in $\rho-\sigma$ phase plane), represent phase-changing, quasiperiodic solutions of x according to Eq. 5.42.

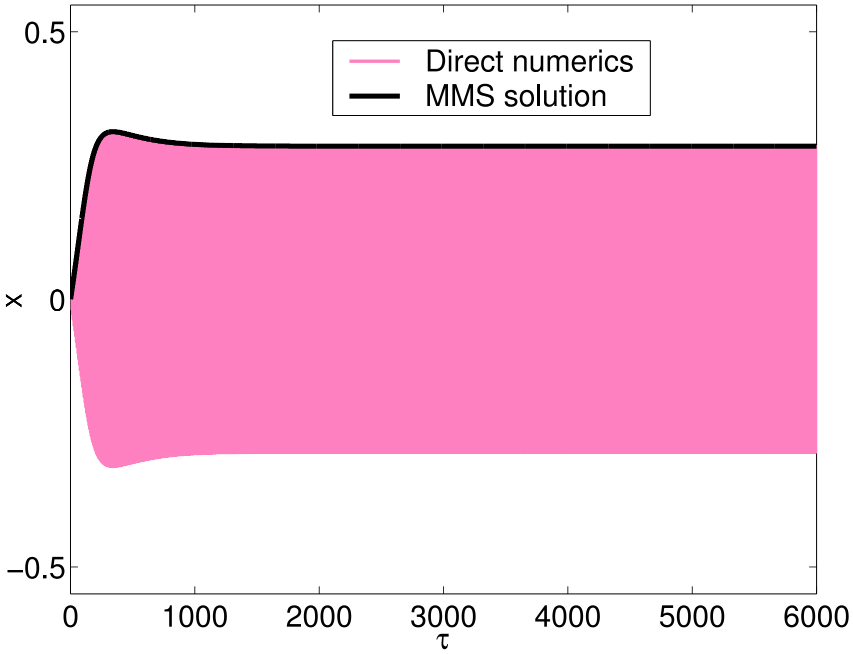

Figure 5.12: Plots of solutions obtained by direct numerical integration of Eqs. 5.33 and 5.34 and the amplitude of the MMS slow flow Eqs. 5.39 and 5.40. Parameters and initial conditions: $\epsilon = 0.01$, $\beta = 1$, $\mu = 0.61464$, $\bar{\mu} = 0.60856$, $\Delta = 0.5$, $\Omega = 1.3562$, $\omega_0 = 1.3494$, $H = 5$, $F = 0.005$; Zero initial conditions on all state variables; $r(0)$ and $s(0)$ taken as explained in main text. Plot shows entrainment.

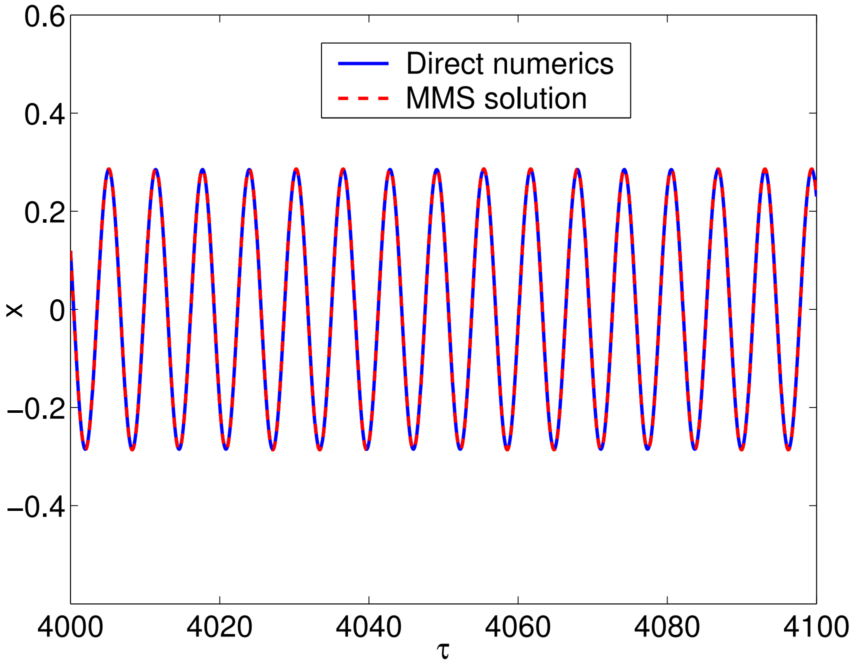

Figure 5.13: A portion of the solution of Fig. 5.12; also plotted is the full solution from the MMS slow flow. Agreement of the MMS solution with full numerics is good.

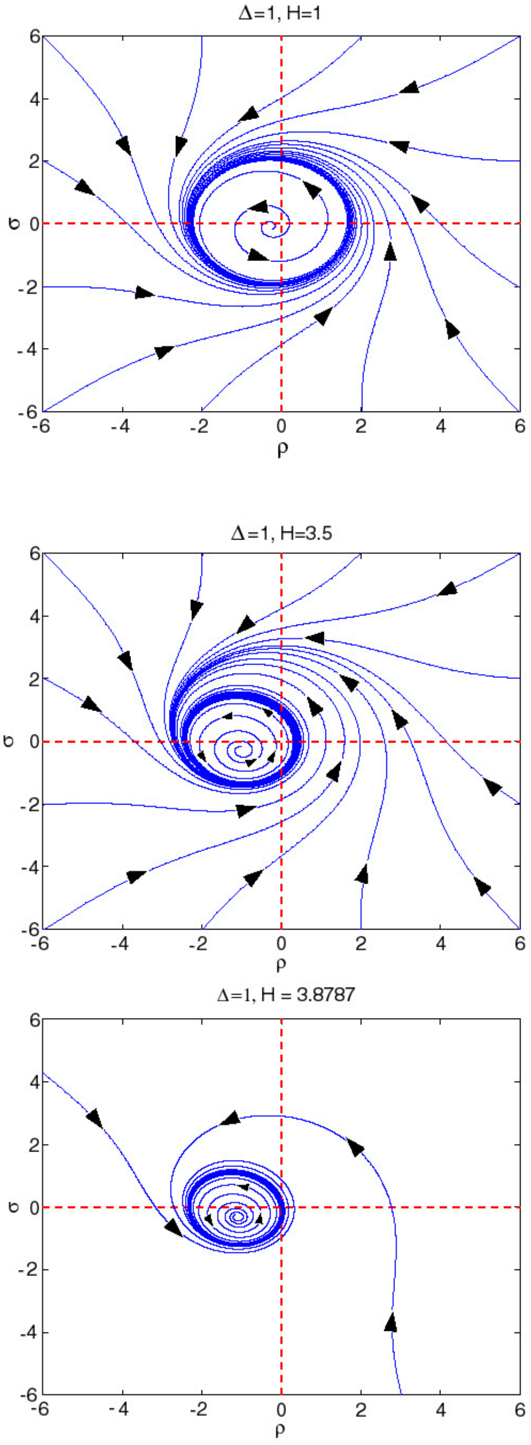

Figure 5.14: Sequence of phase portraits of Eqs. 5.43 and 5.44 for fixed Δ and increasing H; First and second plots: limit cycle encircling origin denotes stable, phase-drifting solution. Third plot: critical limit cycle passing through the origin denoting transition from phase drifting to weak phase locking.

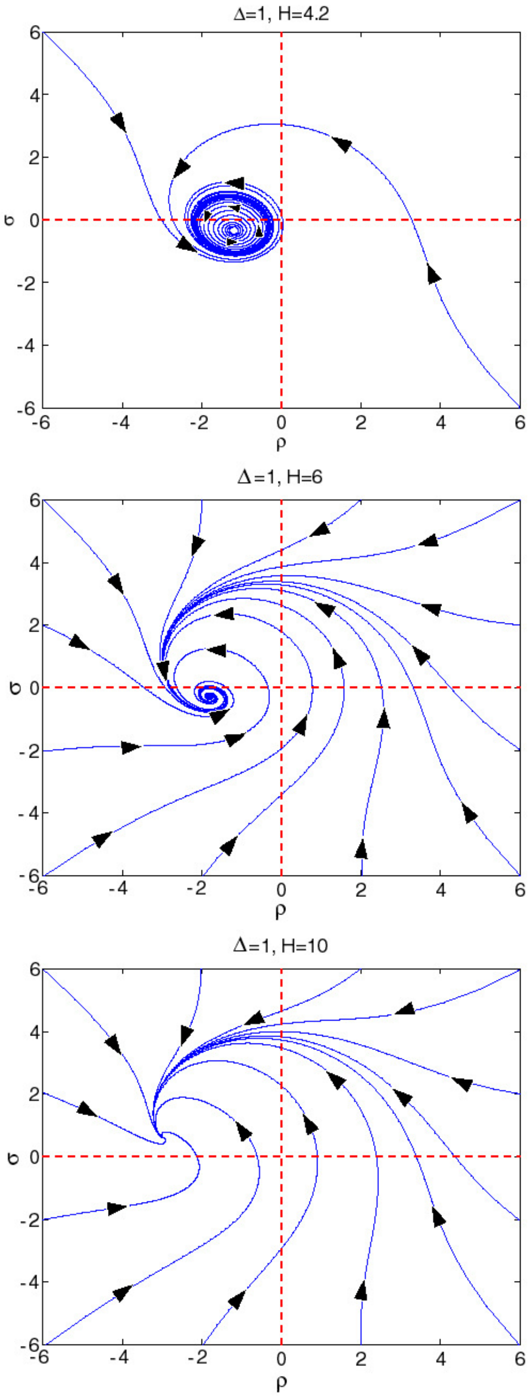

Figure 5.15: Continuation of the phase portraits of Fig. 5.14. First plot: limit cycle *not* encircling the origin representing weak phase-locking. Second plot: entrained solution represented by the stable focus. Third plot: entrained solution represented by the stable node.

We now consider a series of phase portraits in the $\rho - \sigma$ plane, for a fixed value of $\Delta = 1$ and steadily increasing forcing magnitude H. Note that the $\rho - \sigma$ plane is more commonly known as the van der Pol plane [5]. For $H = 1$, there is an unstable fixed point near the origin surrounded by a stable limit cycle that encircles the origin. Thus the steady state behavior, represented by the limit cycle, is a phase-drifting quasiperiodic solution. As we increase H further, the limit cycle shrinks in size and simultaneously drifts away from the origin. For H as high as 3.5 the limit cycle still encircles the origin (see second plot of Fig. 5.14), thus implying a continuously drifting phase situation. These situations are plotted in the first two phase portraits of Fig. 5.14.

At $H \approx 3.8787$ (see third plot of Fig. 5.14), the limit cycle passes through the origin. This value of H marks the transition of the steady state from a phase-drifting case to a weakly phase-locked case. For still greater H, the limit cycle no more encloses the origin. However for a range of H above this critical value of 3.8787, the weakly phase locked solution persists while the limit cycle gradually diminishes in size in the $\rho - \sigma$ plane (see first plot in Fig. 5.15). For sufficiently large H the limit cycle shrinks to a point and disappears, leaving a stable fixed point which represents the phase-locked or entrained solution. The second and third plots in Fig. 5.15 represent this situation of entrainment. In the second plot of Fig. 5.15, the fixed point is a stable focus, while in the third plot, which represents a higher H than the second plot, the fixed point is a stable node.

5.5 Closing remarks

In this chapter, we have studied the free and forced vibrations of the classical van der Pol oscillator with an added fractional order damping term. The fractional term is approximated by a set of ODEs through a recently presented Galerkin-based discretization scheme. The Galerkin approach offers easy amenability to analytical treatment of the approximated system. The resulting ODEs of our approximation have been studied using the MMS near Hopf bifurcations. Good agreements with numerics have been obtained.

Since the Galerkin scheme has been shown [30, 99, 100, 101] to be useful in solving a variety of fractional order equations, future work may involve analytically studying systems such as van der Pol oscillators whose highest derivative is of fractional order, fractional

Lorenz system, fractional Chua's circuit etc. Such systems have hitherto been studied largely numerically.

Acknowledgements

I thank Satwinder Jit Singh for the detailed discussions he had with me on several aspects of fractional calculus. I also thank him for providing me with the matrices presented in appendices B and C.

Chapter 6

Infinite dimensional slow modulation of cutting tool vibrations

Starting with the study of a resonantly forced oscillator in Chapter 2, we moved on to the study of a fractionally damped, van der Pol oscillator in Chapter 5. Although the fractional damping added infinite dimensionality to the system, the fractional damping term was approximated by a Galerkin scheme resulting in a finite set of ODEs. We also restricted our attention to a point close to Hopf bifurcation. Thus the final MMS slow flow was finite dimensional. In contrast, the study to be presented in this chapter involves a slow flow which is itself *infinite dimensional*. This study will constitute the third part of the thesis. The problem studied in this chapter concerns the dynamics of a time-delayed model for machine tool vibrations.

In particular, we apply the method of multiple scales (MMS) to a well known model of regenerative cutting vibrations in the large delay regime. By "large" we mean the delay is much larger than the time scale of typical cutting tool oscillations. In the literature, oscillators with small delayed terms have been treated conveniently as slight perturbations of the harmonic oscillator [113, 114, 115]. In these cases, one needs to solve an ODE at each order. Oscillators with $\mathcal{O}(1)$ delayed terms, but near Hopf bifurcation point, have again been treated by the MMS and center manifold reductions (see, for e. g., [20]). In this case, one needs to solve a linear Delay Differential Equation (DDE) at a Hopf point, at each order. However, studies on oscillators with *large delay* are few in number [31, 116, 117, 118, 119]. This chapter presents one such study. The MMS upto second order, recently developed for such large-delay systems [31], is applied here to study tool dynamics in the large delay regime.

We mention that the work presented in this chapter has been largely presented in [120].

6.1 Introduction

Delayed dynamics arises in models of diverse phenomena [116, 121, 122, 123, 124, 125, 126] including metal cutting [127, 128, 129, 130]. Delays appear in cutting dynamics because tool vibrations leave behind a wavy cut surface that affects cutting forces on the next pass; this phenomenon (see Fig. 6.1) is called the regenerative effect [127].

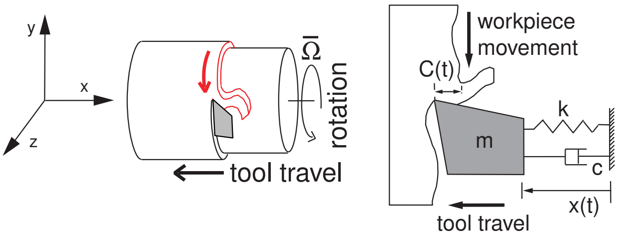

Figure 6.1: Typical turning operation. Left: overall view. Right: zoomed view indicating wavy surfaces and SDOF model.

The literature on machine tool vibrations is large (see, e.g., [130], [131, 132, 133, 134, 135, 136, 137, 138, 139, 140, 141, 142, 143]). Our interest here is in studying new aspects of a well-known model for vibrations during turning operations.

In particular, we study the regime of light cuts on objects of large diameter (necessitating slower spindle speeds, because for maintaining the same cutting speed, doubling the diameter requires halving the spindle speed), such that the time of one revolution is large, and the cutting force is small. The tool dynamics thus involves a large delay compared to the time scale of tool oscillations (see, e.g., discussion in [31]).

To emphasize and also clarify the above point, we note that “large” or “small” are meaningful only in comparison with some other quantity. For example, if the tool vibration frequency is 400 Hz, while the workpiece rotation speed is 1200 RPM (i.e., 20 Hz), then the delay is large for our purposes (20 cycles of oscillation) although for many *technological* issues not related to this analysis, a speed of 1200 RPM may not be considered low.

A consequence of the large delay is that the slow *modulation* dynamics of the tool vibration is itself governed, within the method of multiple scales (MMS) approximation, by a delay differential equation where the delay is $\mathcal{O}(1)$ (numerical integration is thereby speeded up dramatically).

Usual treatments of the model we consider here involve center manifold reductions that treat the distance from bifurcation as small, and all other parameters (including the delay) as $\mathcal{O}(1)$, leading usually to a 2D slow flow. The reader is referred to [144] for a comparative study of the application of method of multiple scales vis-à-vis the center manifold reduction approach in analyzing delayed systems near Hopf bifurcations.

The crucial distinction between such near-Hopf bifurcation analysis and ours is that we are in a sense further away from the bifurcation point so that we can better resolve the effects of *disparate* sizes of other parameters (e.g., smallness of chip width versus largeness of time delay). The key dynamic phenomena we can capture using this approach lie in the infinite dimensional nature of the slow modulation of tool vibrations, something that is not captured by center manifold reductions or other analyses based on infinitesimal distance from bifurcation with other physical parameters held fixed.

Our analysis uses the MMS, specialized for this problem, as developed in [31]; as discussed there, application of the method to second order involves some technical issues, which occur here as well. We mention that the MMS had been applied upto first order to equations with large delay in [116], though the focus there was on periodic and quasi-periodic solutions. Similar studies on two other problems were performed in [117], where transient dynamics was also studied. Here, we develop the slow flow upto second order, and numerically examine some transient dynamics as well, to demonstrate the validity of the infinite dimensional slow modulation dynamics predicted by the second order MMS.

In the context of the present study involving phenomena of disparate time scales, we note that [145] and [146] study machine tool vibration chatter control using high-frequency excitations. While both our study and theirs involve disparate time scales, our model focuses on the regime where the tool vibration frequency is much *larger* than the spindle spin speed resulting in large delays, while in their models the tool vibration frequency is much *smaller* than the high frequency control excitations. Moreover, while our study involves a DDE with a large delay, theirs involve ODEs because the regenerative effect is dropped. However, in a broader context, these papers are examples of the many different approaches adopted for studying the technologically important problem of metal cutting dynamics.

6.2 Single degree of freedom model

We briefly discuss the derivation of the well known tool vibration model that we study here. A more detailed presentation can be found in [131]. Consider a typical turning operation as shown in Fig. 6.1. Let the nominal chip thickness corresponding to steady-state cutting be f_0 and let $x(t)$ be the displacement from the nominal thickness position. The instantaneous chip thickness is $f = f_0 + x(t) - x\left(t - \frac{2\pi}{\Omega}\right)$, where Ω is the angular velocity of the work piece. Dynamic equilibrium of the tool gives

$$\ddot{x} + 2\zeta\,\omega_n\,\dot{x} + \omega_n^2\,x = -\frac{1}{m}\Delta F_x,$$

where $\omega_n = \sqrt{\frac{k}{m}}$ is the tool natural frequency, ζ is the damping ratio, m is the mass of the tool, and ΔF_x is the additional chip force. We have (expanding Taylor's power law, see [131]), $\Delta F_x = F_x(f) - F_x(f_0) \approx K\,w\left(\frac{3}{4}\,f_0^{\frac{-1}{4}}\,\Delta\,f - \frac{3}{32}\,f_0^{\frac{-5}{4}}\,\Delta\,f^2 + \frac{5}{128}\,f_0^{\frac{-9}{4}}\,\Delta\,f^3\right)$, where $\Delta\,f = f - f_0$ is the additional chip thickness, K is a constant and w is the chip width. Upon substitution of the above in tool vibration equation and suitable non-dimensionalization (see [131]) we have

$$\ddot{x} + 2\,\zeta\,\dot{x} + (1+p)\;x - p\,x(t-\mu) = \frac{3\,p}{10}\left\{(x - x(t-\mu))^2 - (x - x(t-\mu))^3\right\}, \qquad (6.1)$$

where x is the non-dimensional tool displacement from the mean position (corresponding to nominal chip thickness), p is a non-dimensional bifurcation parameter proportional to chip width, and $\mu = \dfrac{2\,\pi\omega_n}{\Omega}$ is the non-dimensional delay. We are interested in large μ, as mentioned above.

We mention that a more general model than Eq. 6.1 (including structural as well as cutting force nonlinearities) was originally proposed in [132] and has been extensively studied in several papers (e.g., [130, 133, 134, 135]). Stépán [136] discusses a number of models which include additional damping terms, distributed delays, etc. Multi-degree of freedom models (e.g., [137, 138, 139]), and stochastic models (e.g., [140, 141]) have also been studied.

In this work, however, we focus on the non-trivial dynamics created by a large delay in Eq. 6.1; and we will use the second order MMS, as developed in [31], for our study.

6.2.1 Stability chart

Linear analysis of Eq. 6.1 gives stability charts demarcating stable and unstable parameter regimes (here p and $\frac{\Omega}{\omega_n}$), for any ζ held fixed. Such a chart is shown in Fig. 6.2 (see [131, 133, 142]). On the stability boundary, the equilibrium at zero undergoes a subcritical Hopf bifurcation [131, 133, 142]. Adjacent lobes meet at double Hopf points [143]. Stability is ensured for all cutting speeds below the threshold chip width p_{min}.

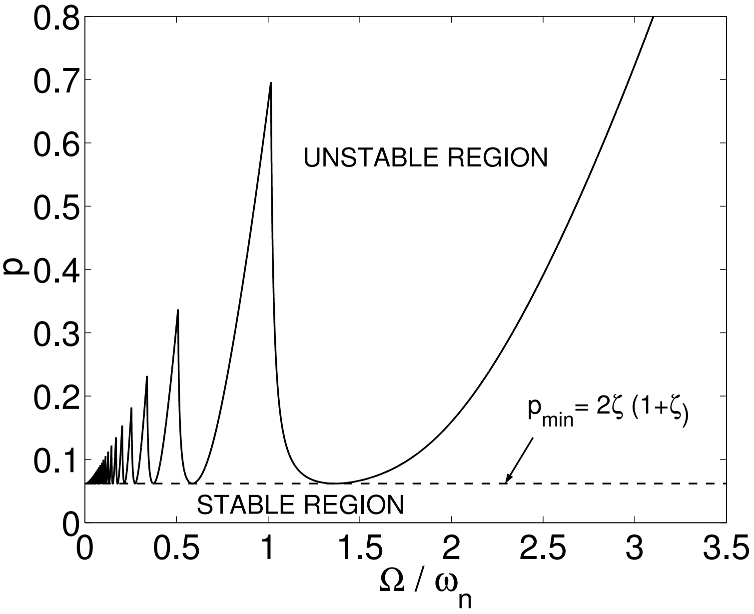

Figure 6.2: Stability chart for linearized version of Eq. 6.1 with $\zeta = 0.03$.

6.2.2 Dimensionality

Several authors have analytically studied Hopf bifurcations of delayed systems. Lindstedt's method, which ignores transient dynamics, is used in [147, 148]. Center manifold reductions, used in [131, 141, 142, 149], project the infinite dimensional system onto a plane and study the dynamics thereon. Direct MMS by-passing center manifold reduction was used in [20], and also used near a double Hopf point of the present model in [143]. A comparison of the MMS and center manifold approaches near Hopf bifurcations in delayed systems is presented in [144].

Dynamics on the center manifold (whether explicitly obtained as such or not) is simple due to lower dimensionality. Near-origin solutions are limited to monotonic growth or decay (perhaps approaching limit cycles) when the center manifold is planar; somewhat more complicated dynamics is possible on 4-dimensional center manifolds near double Hopf points. The center manifold approach is, however, confined close to Hopf points. In contrast, we consider a large delay regime where the slow modulation dynamics is in principle infinite dimensional even under the MMS approximation.

6.2.3 Large delay regime

As discussed earlier, large delays correspond to low values of $\dfrac{\Omega}{\omega_n}$ in Fig. 6.2. In the large delay regime in Fig. 6.2 (low $\frac{\Omega}{\omega_n}$), the stability lobes get narrower and crowd together closely. This makes the dynamics sensitive to small changes in parameters like chip width p and spindle speed Ω, motivating our study of Eq. 6.1 for large values of $\dfrac{2\,\pi\omega_n}{\Omega}$.

We start by scaling various terms in Eq. 6.1. It is observed in the "large delay" regime of Fig. 6.2 that the chip width p, damping ζ and the non-dimensional speed $\dfrac{\Omega}{\omega_n}$ are of the same order of smallness. Hence, we scale parameters as:

$$\frac{\Omega}{\omega_n} = \epsilon, \quad 2\,\zeta = \epsilon\,\alpha, \quad p = \epsilon\,\beta, \tag{6.2}$$

where $0 < \epsilon \ll 1$, and α and β are $\mathcal{O}(1)$ quantities. We also write

$$\lambda = -\frac{3\,\beta}{10}. \tag{6.3}$$

Note that λ is not an independent physical parameter, but retaining it independently is convenient, e.g., in removing nonlinear terms by artificially setting it to zero if needed. Thus, Eq. 6.1 becomes

$$\ddot{x} + x + \epsilon \left\{ \alpha\, \dot{x} + \beta\, (x - x(t-\mu)) + \lambda\, (x - x(t-\mu))^2 - \lambda\, (x - x(t-\mu))^3 \right\} = 0, \qquad (6.4)$$

where $\mu = \dfrac{\tau}{\epsilon} = \dfrac{2\,\pi}{\epsilon}$ is the non-dimensional large delay. Note that in the development of the MMS the delay τ is a free parameter and hence has been retained symbolically below, although $\tau = 2\,\pi$ is fixed for our problem.

6.3 Multiple scales for large delay

Second order MMS for oscillators with large delay was developed in [31], which we follow. We introduce multiple time scales: $T_0 = t, T_1 = \epsilon\, t, T_2 = \epsilon^2\, t$. We then assume $x(t) = X(T_0, T_1, T_2)$, where

$$X(T_0, T_1, T_2) \;=\; X_0(T_0, T_1, T_2) + \epsilon\, X_1(T_0, T_1, T_2) + \epsilon^2 X_2(T_0, T_1, T_2) + \ldots \qquad (6.5)$$

in which the X_i are to be determined. We substitute Eq. 6.5 in Eq. 6.4 and expand in powers of ϵ. During this expansion procedure, the delay terms are treated as explained in [31]. In particular, the large delay term $\dfrac{\tau}{\epsilon}$ is labeled as τ_1 and treated independent of ϵ in the expansions, as explained and justified there.

At leading order we have

$$\frac{\partial^2}{\partial {T_0}^2} X_0(T_0, T_1, T_2) + X_0(T_0, T_1, T_2) = 0, \qquad (6.6)$$

whose solution is $X_0 = A(T_1, T_2)\sin(T_0 + \phi(T_1, T_2))$. We now adopt the following notation for brevity.

$$A \equiv A(T_1, T_2),\; \phi \equiv \phi(T_1, T_2), \qquad (6.7)$$

$$A_\tau \equiv A(T_1 - \tau, T_2),\; A_{2\,\tau} \equiv A(T_1 - 2\,\tau, T_2), \qquad (6.8)$$

$$\phi_\tau \equiv \phi(T_1 - \tau, T_2),\; \phi_{2\,\tau} \equiv \phi(T_1 - 2\,\tau, T_2), \qquad (6.9)$$

$$A_1 \equiv \frac{\partial\, A}{\partial T_1},\; A_{11} \equiv \frac{\partial^2\, A}{\partial T_1^2},\; A_2 \equiv \frac{\partial\, A}{\partial T_2}, \qquad (6.10)$$

$$\phi_1 \equiv \frac{\partial\, \phi}{\partial T_1},\; \phi_{11} \equiv \frac{\partial^2\, \phi}{\partial T_1^2},\; \phi_2 \equiv \frac{\partial\, \phi}{\partial T_2}. \qquad (6.11)$$

Substituting the above in the $\mathcal{O}(\epsilon)$ equation and eliminating secular terms yields the first order slow flow. Following [31], we replace τ_1 in the equations by the quantity

$$z(\tau,\epsilon) = 2\,\pi \left(\frac{\tau}{2\,\pi\,\epsilon} \bmod 1\right).$$

Note that z is periodic in $\frac{1}{\epsilon}$. The first order slow flow is

$$\begin{aligned} A_1 &= -\frac{1}{2}\,\alpha\,A + \frac{3}{8}\,\lambda\,{A_\tau}^3 \sin(\psi) - \frac{1}{2}\,\beta\,A_\tau \sin(\psi) - \frac{3}{8}\,\lambda\,A{A_\tau}^2 \sin(2\,\psi) + \\ &\quad \frac{3}{8}\,\lambda\,A^2 A_\tau \sin(\psi) \end{aligned} \tag{6.12}$$

$$\begin{aligned} \phi_1 &= -\frac{3\,\lambda\,{A_\tau}^2}{4} - \frac{\beta\,A_\tau \cos(\psi)}{2\,A} + \frac{9\,\lambda\,A\,A_\tau \cos(\psi)}{8} - \frac{3\,\lambda\,{A_\tau}^2 \cos(2\,\psi)}{8} - \frac{3\,\lambda\,A^2}{8} + \\ &\quad \frac{\beta}{2} + \frac{3\,\lambda\,{A_\tau}^3 \cos(\psi)}{8\,A}, \end{aligned} \tag{6.13}$$

where $\psi = \phi + z - \phi_\tau$; and $\lambda = -\dfrac{3\,\beta}{10}$ as mentioned earlier.

We see that the slow flow itself is a delay differential equation; however the original delay was τ/ϵ, and now the delay is merely τ, numerically easier to handle for the same required accuracy level. The slow modulation dynamics remains infinite dimensional. Moreover, sensitive dependence on the small parameter ϵ is retained in the leading order slow flow through z, something not encountered in routine applications of the MMS.

We now proceed to second order which, we will see, is needed to capture the qualitative dynamics correctly. At second order, we encounter retarded functional partial differential equations, as explained in [31]; however, as also explained there, the difficulty can be side-stepped at second order, and we do the same here. The second order expressions are long and are given in the appendix A(they were retained in all numerical solutions presented here). The final slow flow is given below:

$$A^{'} = A_1 + \epsilon\,A_2, \tag{6.14}$$

$$\phi^{'} = \phi_1 + \epsilon\,\phi_2, \tag{6.15}$$

where the primes denote derivative with respect to slow time $\epsilon\,t$, A_1 and ϕ_1 are given in the first order slow flow equations Eqs. 6.12 and 6.13, and A_2 and ϕ_2 are second order corrections. It is interesting to note that for the second order slow flow, the delay is 2τ as opposed to τ for the first order slow flow.

6.4 Results: MMS *vs.* Numerics

We now present some numerical results for Eq. 6.4 and compare the predictions from the slow flow yielded by the MMS.

6.4.1 First *vs.* Second order

We first examine stability charts for the linearized MMS equations ($\lambda = 0$ in Eq. 6.4), for first and second order, and compare with results of Fig. 6.2 in Fig. 6.3 below.

We first describe the procedure to obtain stability chart from the slow flow. We first consider the first order case. We start with Eqs. 6.12 and 6.13. We artificially set $\lambda = 0$ to obtain the linear system and then look for periodic solutions by requiring

$$A_1 = 0, \;\; A_\tau = A, \tag{6.16}$$

$$\phi_1 = \left(\frac{\omega - 1}{\epsilon}\right), \tag{6.17}$$

$$\psi = \frac{\omega\tau}{\epsilon}. \tag{6.18}$$

where ω is the angular frequency of the periodic solution (in the T_0 time scale). Note that, by definition, the angular frequency ω is the total time derivative of the phase of the solution. Thus

$$\omega = \frac{d}{dt}(T_0 + \phi(T_1, T_2))\,.$$

Using the definition of the various time scales in the above expression and remembering that $\phi_1 \equiv \frac{\partial \phi}{\partial T_1}$, we get

$$\omega = 1 + \epsilon\phi_1\,,$$

whence we get Eq. 6.17.

Now from Eq. 6.15 upto $\mathcal{O}(\epsilon)$ we get

$$\phi' = \phi_1$$

which for the periodic solution case becomes (using Eq. 6.17 and subsequent integration),

$$\phi = \left(\frac{\omega - 1}{\epsilon}\right) T_1 + \nu$$

with ν being an arbitrary constant. Thus

$$\phi_\tau = \left(\frac{\omega - 1}{\epsilon}\right)(T_1 - \tau) + \nu$$

and therefore $\psi = \phi + z - \phi_\tau$ becomes (remembering that $z = \frac{\tau}{\epsilon}$)

$$\psi = \frac{\omega\tau}{\epsilon}\,.$$

Thus using Eqs. 6.16 through 6.18, Eqs. 6.12 and 6.13 become respectively (using Eq. 6.2)

$$p\,\sin(\psi) + 2\zeta = 0, \tag{6.19}$$

$$\omega - 1 = \frac{p}{2}\left(1 - \cos(\psi)\right). \tag{6.20}$$

Note that physical damping ζ is fixed at a particular value (here 0.03) and the delay parameter $\tau = 2\,\pi$ for our analysis.

Solving for ψ and p from the above equations and using Eq. 6.18, we get

$$p = \left(\frac{(\omega - 1)^2 + \zeta^2}{\omega - 1}\right), \tag{6.21}$$

$$\epsilon = \left(\frac{\omega\,\tau}{2\,m\,\pi + \arcsin\left(\frac{-2\,\zeta\,(\omega-1)}{(\omega-1)^2+\zeta^2}\right)}\right), \tag{6.22}$$

where m is a positive integer.

We now have expressions for the stability boundary curves in the $p - \epsilon$ plane parameterized by ω. Each value of m in Eq. 6.22 gives rise to one of the lobes observed in Fig. 6.3. Each lobe is truncated at the points of intersection with adjacent lobes. The points of intersection are determined using a Newton-Raphson technique.

For the second order case, we have the quantity

$$\gamma = \phi + 2\,z - \phi_{2\,\tau},$$

which, under the requirements of a periodic solution at the stability boundary, becomes

$$\gamma = 2\,\psi = \frac{2\omega\,\tau}{\epsilon}.$$

The above derivation follows exactly the same steps as those leading to Eq. 6.18.

Following a similar, but algebraically slightly more involved, procedure as for the first order, we can arrive at the stability boundary curves parameterized by ω.

The stability charts obtained from the first and second order slow flow as described above are plotted together with that of Fig. 6.2 in Fig. 6.3.

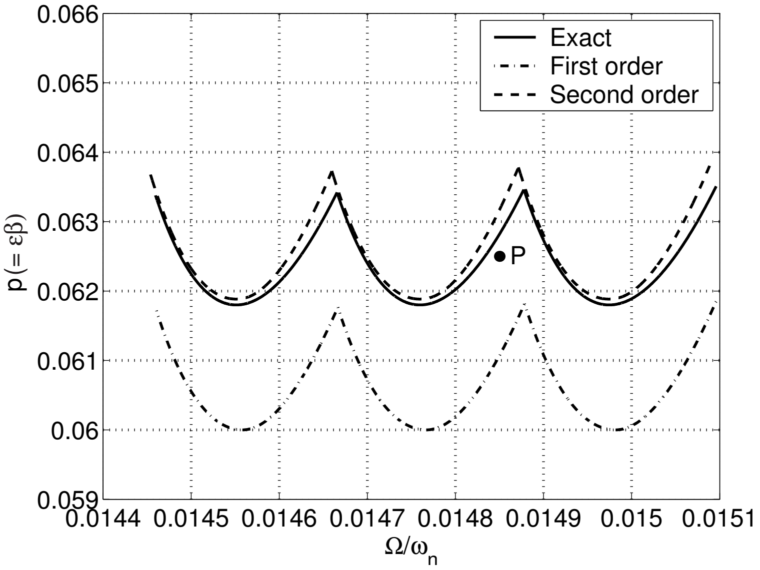

Figure 6.3: Comparison of stability charts generated by first and second order slow flow (damping parameter $\zeta = 0.03$).

The stability boundaries from second order MMS are significantly more accurate than those from first order analysis. The average distance between the stability boundaries predicted from the two orders (first and second) is comparable to the range of variations in the stability boundary itself.

We choose a parameter set (point P in Fig. 6.3) and compare the results of the direct numerical solution with the first and second order MMS in Fig. 6.4. All further numerical results in this chapter use the second order MMS.

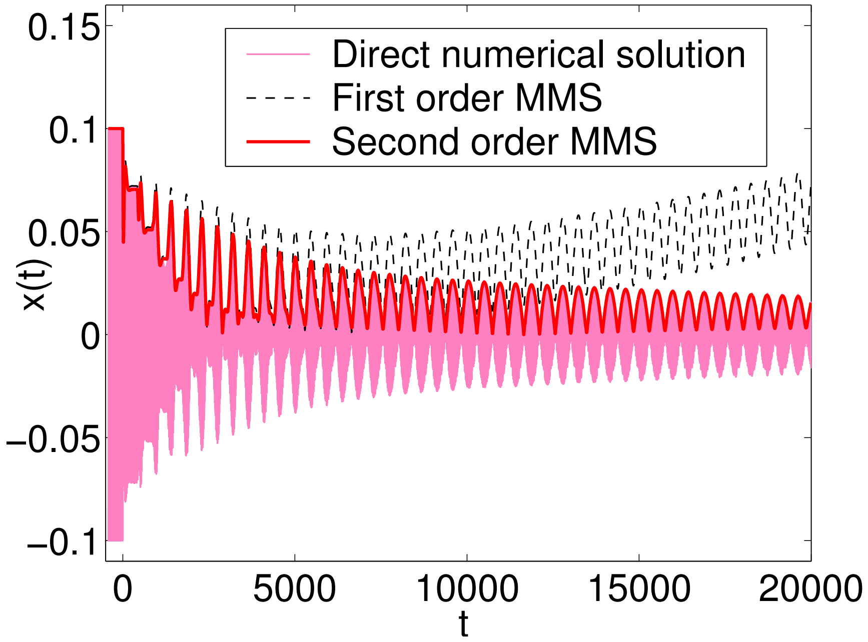

Figure 6.4: Numerical solution of original DDE Eq. 6.4 and numerical solution of first and second order slow flow equations. Parameter values used: $\zeta = 0.03$, $\epsilon = 0.01485$, $p = 0.0625$, $\tau = 2\,\pi$. Corresponding scaled parameters: $\alpha = 4.0404$, $\beta = 4.2087$. Initial conditions used: $x(t) = 0.1\,\sin t$, $\dot{x}(t) = 0.1\,\cos(t)$ for $t \in [-\frac{\tau}{\epsilon}, 0]$ and $A(\eta) = 0.1$ and $\phi(\eta) = 0$ for $\eta \in [-2\,\tau, 0]$.

6.4.2 Sensitivity to ϵ

As stated earlier, the results are sensitive to changes in ϵ, hence parameter values. For example, consider the zoomed stability chart for $\zeta = 0.03$ shown in Fig. 6.5. We choose two points R and Q for our study, as shown in the figure. Point R lies in unstable regime, whereas point Q lies in the stable regime. For these points we integrate Eq. 6.4 numerically using MATLAB's DDE23 routine. The slow flow equations are also integrated using the same (DDE23) routine. Results are shown in Fig. 6.6, and the agreement is close enough to be visually near-indistinguishable. In particular, though the change in ϵ is small, the qualitative dynamics is different in the two cases. Finally, the non-monotonic variation in the amplitude is something beyond, at least, a 2-dimensional center manifold reduction.

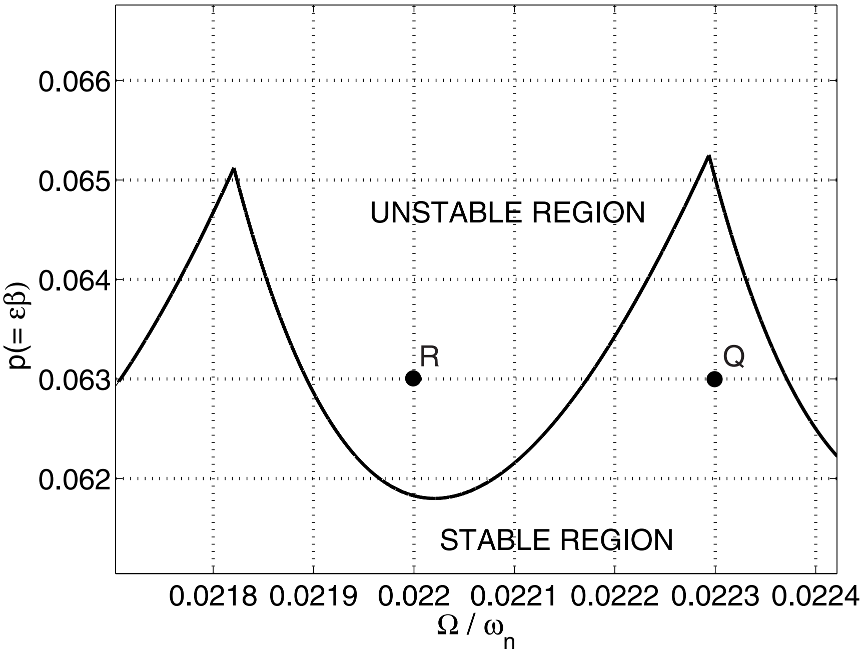

Figure 6.5: Stability chart with parameter choices R and Q in unstable and stable regimes respectively (damping parameter used was $\zeta = 0.03$).

The computational advantage of the MMS slow flow lies in that the full simulation of Eq. 6.4 took 11 minutes while the MMS slow flow was integrated in 13 seconds on the same computer for the same specified error tolerance (10^{-7}).

6.4.3 Other initial function choices

For another point in stable regime, we used a sinusoid with linearly decreasing amplitude as initial function and compared the results with that of slow flow equations in Fig. 6.7. The match is excellent (visually near-indistinguishable). Although the solution is decaying on average, decay is not monotonic as it would be on a center manifold.

Since the bifurcation is sub-critical (e.g., [131]), larger initial conditions lead to growth here, even though other, smaller, initial conditions lead to decay. These growing and decaying solutions coexist, which is common for nonlinear systems. To see this, for the same parameter values, we use an initial function somewhat larger than before (see

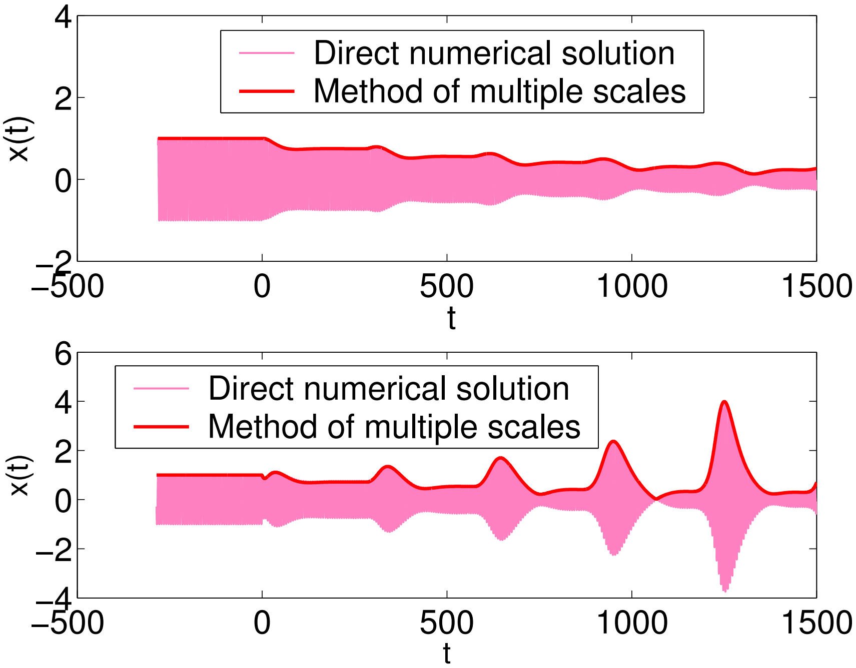

Figure 6.6: Top: Numerical solution of original DDE Eq. 6.4 and numerical solution of slow flow Eqs. 6.14 and 6.15 corresponding to point Q of Fig. 6.5. Parameter values for point Q: $\zeta = 0.03$, $\epsilon = 0.0223$, $p = 0.063$, $\tau = 2\,\pi$. Corresponding scaled parameters: $\alpha = 2.6906$, $\beta = 2.8251$. Initial conditions: $x(t) = \sin(t)$, $\dot{x}(t) = \cos(t)$ for $t \in [-\frac{\tau}{\epsilon}, 0]$ and $A(\eta) = 1$ and $\phi(\eta) = 0$ for $\eta \in [-2\,\tau, 0]$. Bottom: same as Top, except that we consider point R instead of Q, with $\epsilon = 0.022$ instead of 0.0223. Corresponding scaled parameters: $\alpha = 2.7273$, $\beta = 2.8636$.

Fig. 6.8). The match is good for moderate amplitudes, though poorer where the nonlinear terms are no longer comparable to the linear term, something implicitly assumed in the MMS expansion.

As pointed out earlier, our analysis is applicable to a wider range of chip width p values as compared to a center manifold calculation which is based on infinitesimal closeness to the Hopf bifurcation value of p^* (say). We choose a value of p which is far removed from the critical value and compare the slow flow results with direct numerical solution of Eq. 6.4 in Fig. 6.9. The match is good (to the extent of being visually near-indistinguishable), as expected, even for p values distant from the bifurcation value p^* with $p - p^* = \mathcal{O}(p^*)$.

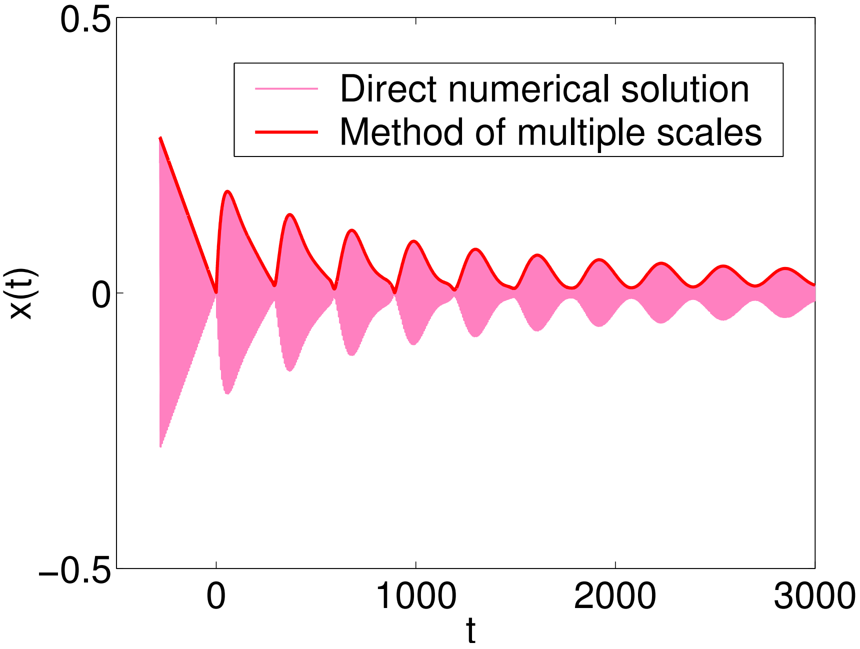

Figure 6.7: Numerical solution of original DDE Eq. 6.4 and numerical solution of slow flow Eqs. 6.14 and 6.15. Parameter values used: $\zeta = 0.03$, $\epsilon = 0.0223$, $p = 0.0612$, $\tau = 2\,\pi$. Corresponding scaled parameters: $\alpha = 2.6906$, $\beta = 2.7444$. Initial conditions used: $x(t) = (0.001 - 0.001\,t)\,\sin t$, $\dot{x}(t) = (0.001 - 0.001\,t)\cos(t) - 0.001\,\sin(t)$ for $t \in [-\frac{\tau}{\epsilon}, 0]$ and $A(\eta) = 0.001 - 0.001\,\frac{\eta}{\epsilon}$ and $\phi(\eta) = 0$ for $\eta \in [-2\,\tau, 0]$.

6.4.4 Other results

The MMS can also elucidate local features of the bifurcation, such as variation of the limit cycle amplitude with chip width p. In Fig. 6.10, we plot the limit cycle amplitude for $\epsilon = 0.0452$ for Eq. 6.4 (using DDE BIFTOOL [150]). Also plotted is the limit cycle amplitude obtained from the MMS with fixed ϵ using arclength-based continuation. The match is good overall. The Hopf bifurcation, from the second order MMS, is at a slightly larger p than for the original DDE, consistent with the small mismatch in Fig. 6.3.

In some prior studies of tool vibration models [134, 135, 117, 151], secondary bifurcations leading to quasi-periodic and chaotic solutions were reported for models with significant structural nonlinearities (e.g., cubic restoring forces). In other work, it has been

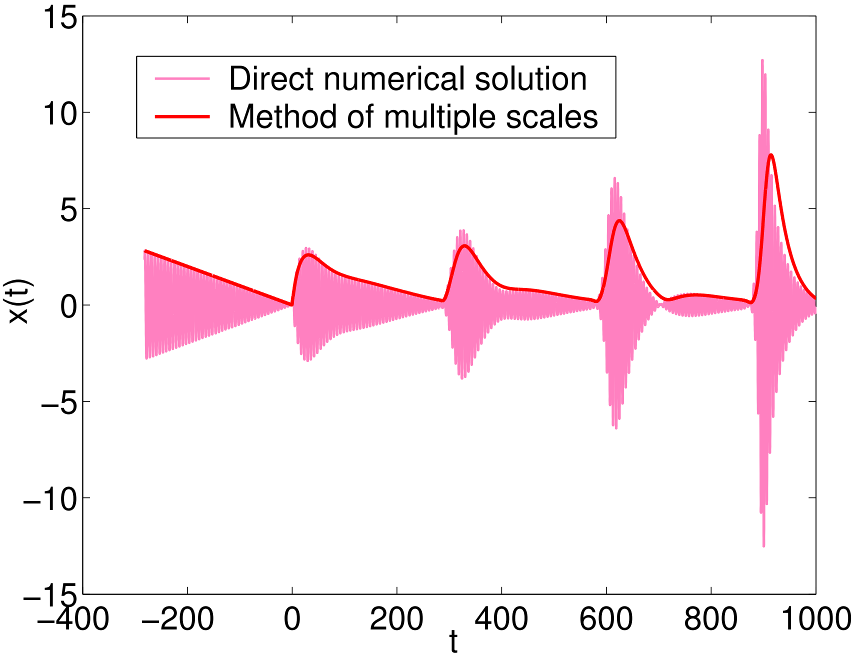

Figure 6.8: Numerical solution of original DDE Eq. 6.4 and numerical solution of slow flow Eqs. 6.14 and 6.15. Parameter values: $\zeta = 0.03$, $\epsilon = 0.0223$, $p = 0.0612$, $\tau = 2\,\pi$. Corresponding scaled parameters: $\alpha = 2.6906$, $\beta = 2.7444$. Initial conditions: $x(t) = (0.001 - 0.01\,t)\,\sin t$, $\dot{x}(t) = (0.001 - 0.01\,t)\cos(t) - 0.01\,\sin(t)$ for $t \in [-\frac{\tau}{\epsilon}, 0]$ and $A(\eta) = 0.001 - 0.01\,\frac{\eta}{\epsilon}$ and $\phi(\eta) = 0$ for $\eta \in [-2\,\tau, 0]$. The key point is that at $t = 0$, the amplitude is small; but the large delay allows earlier and larger values to play a role, showing that the amplitude modulation dynamics does involve delays, unlike in a 2-dimensional center manifold calculation.

pointed out that loss of contact between tool and workpiece (self-interrupted cutting) may provide a nonlinear effect stronger than structural nonlinearity [152]. The present model, lacking structural nonlinearities, does not exhibit such secondary bifurcations; however, a user must keep in mind that large-amplitude solutions predicted by this model are inaccurate beyond the point of contact loss.

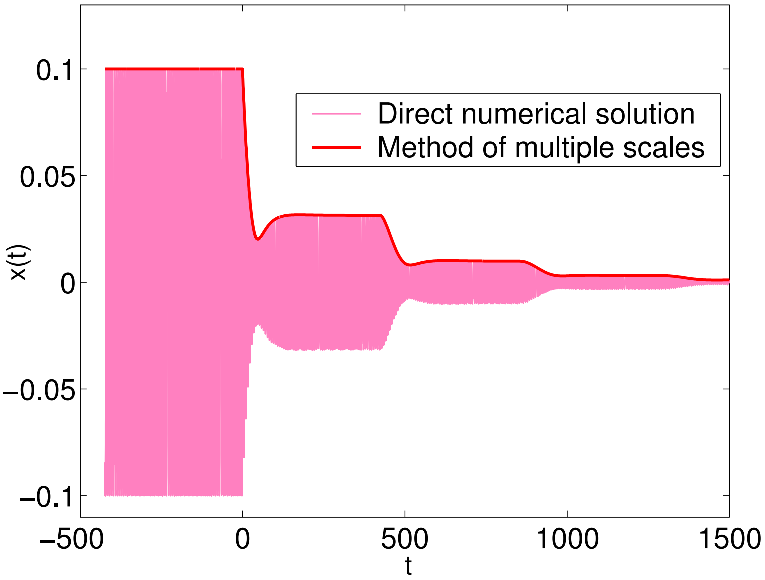

Figure 6.9: Numerical solution of original DDE Eq. 6.4 and numerical solution of slow flow Eqs. 6.14 and 6.15. Parameter values used: $\zeta = 0.03$, $\epsilon = 0.01485$, $p = 0.02$, $\tau = 2\,\pi$. Corresponding scaled parameters: $\alpha = 4.0404$, $\beta = 1.3468$. Initial conditions used: $x(t) = 0.1\,\sin(t)$, $\dot{x}(t) = 0.1\,\cos(t)$ for $t \in [-\frac{\tau}{\epsilon}, 0]$ and $A(\eta) = 0.1$ and $\phi(\eta) = 0$ for $\eta \in [-2\,\tau, 0]$.

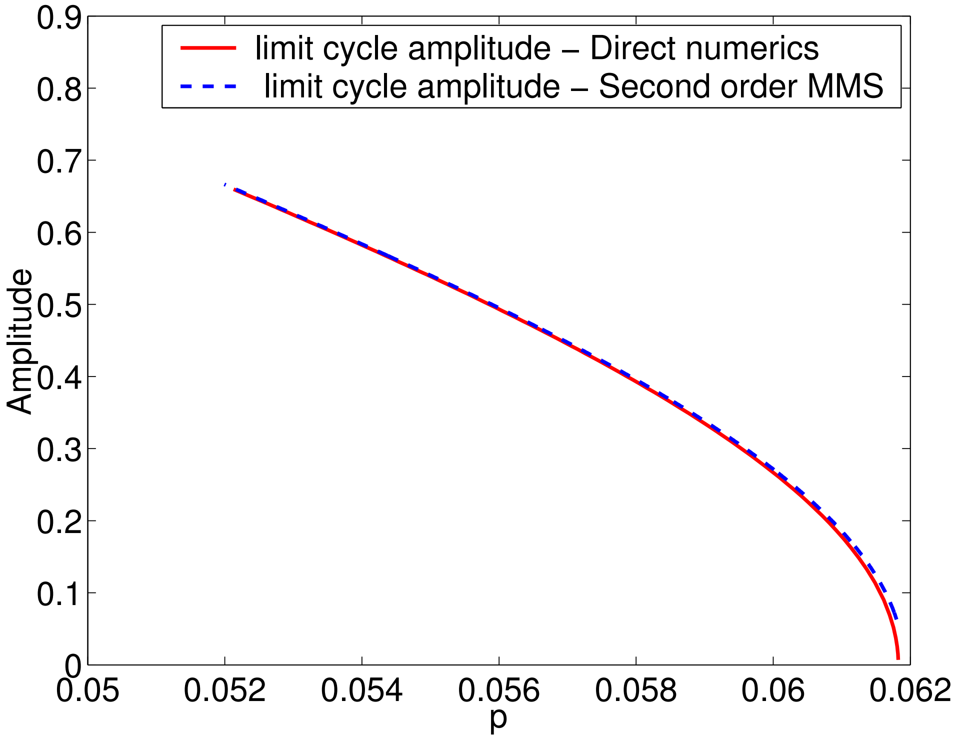

Figure 6.10: Comparison of limit cycle amplitude as a function of chip width, based on direct continuation study of Eq. 6.4 and second order slow flow. Parameters used were $\epsilon = 0.0452$ and $\zeta = 0.03$.

6.5 Closing remarks

We conclude the study of the third problem of this thesis with some closing remarks.

The aim of this work was twofold. The first was to demonstrate that there is a reasonable parameter regime for a well studied cutting model where the recently developed second order MMS with large delays could be used fruitfully. The second was to use this MMS to capture and exhibit dynamics that is outside the scope of the more popularly used center manifold reduction near the stability boundaries; in particular, our analysis holds at small but non-infinitesimal distances from the stability boundary, where the dynamics has visible higher dimensional behavior than captured by center manifold reductions. A few aspects of the MMS results are worth emphasizing again because of their relative novelty in such settings. First, the slow flow remains strongly sensitive to ϵ and contains an $\mathcal{O}(1)$ delay (as opposed to the original large delay). Second, the second order MMS, while more accurate than first order MMS, has a delay that is double that in the first order case. Third, the slow flow can in principle be used for possibly similar systems to study phenomena well beyond the center manifold reduction, such as bifurcating quasiperiodic oscillations in the modulation dynamics (see [117]), though such phenomena were not observed in the specific system studied here.

In closing, we mention one caveat relevant to the MMS. The original system has many fast-decaying solutions very different from the slowly-modulated solutions assumed by the MMS. In numerical comparisons, therefore, initial conditions chosen must reasonably fit the “slowly modulated” description, as in the examples above. This issue is discussed in [31], and in a related context in appendix A of [103].

In this study, we have treated the MMS slow flow largely numerically. Future work may involve more detailed analytical examination of the infinite dimensional slow flow. Another interesting question that could be addressed in future is the determination of the basin of attraction of the origin, in a parameter regime where the origin is known to be stable. The infinite dimensionality of the slow flow makes this question difficult. However, this question might be of practical relevance as it would enable us to determine operating conditions such that excessive tool vibrations are avoided.

Finally, apart from this tool delay application, the analysis procedure could be applied in future to other engineering applications with large delays.

Acknowledgements

I thank Pankaj Wahi for the detailed discussions that he had with me which gave direction to this work. He is a co-author on [120].

Chapter 7

Nonlinear secondary whirl of an overhung rotor

Thus far in this thesis, we have only studied single degree of freedom systems, albeit with increasing complexity. Now, we move on to study a two degree of freedom system. Here we study the nonlinear whirling of a well-known [32] two-degree of freedom model of an overhung rotor spinning close to its gravity critical speed.

This last problem spans Chapters 7 through 9. In the present chapter, we explain the significance of this study, present a brief review of the literature, derive the equations of motion of the system, and set up expressions for the gravity critical speed. Subsequent chapters will present the MMS analysis of the equations of motion derived here.

7.1 Introduction and literature review

Rotors are important components in several engineering applications, and rotor dynamics constitutes an independent field of study. Rotor instabilities and whirl include a range of phenomena too diverse to discuss here in detail.

In particular *asymmetric rotors* exhibit interesting phenomena such as unstable speed ranges between critical speeds (e.g., [153, 154, 155, 156]), gravity critical speeds

([157, 158, 159]), and nonlinearity-induced additional resonances (e.g., [160, 161, 162, 163, 164, 165]). In addition, stator asymmetry can create new instabilities while modifying ones existing due to rotor asymmetry (e.g., [166, 167, 168, 169]). An excellent overview of nonlinear phenomena in rotordynamics is provided in [170].

Here, we focus on gravity-induced resonances in perfectly balanced overhung rotors, sometimes called Stodola-Green rotors [171]. Gravity-induced resonances occur in slightly asymmetric rotors at about half of the mean flexural critical speed [153]. The relevant literature primarily identifies these gravity critical speeds ([157, 167, 172]), with subsequent linear analyses under various idealizations: Jeffcot rotor models on rigid bearings [157, 171, 173, 174], Jeffcot rotors on flexible pedestals [175], Euler-Bernoulli beam models [176, 177] and three dimensional (3D) finite element (FE) models [178]. Experimental results on horizontal cantilever shafts were reported, e.g., by [179], and on a simply supported shaft with a centrally-mounted wheel were reported by [180].

Studies of nonlinear behavior near gravity critical speeds of overhung rotors are, somewhat surprisingly, absent from the literature. Two exceptions are [161], [181], but they study shafts supported at both ends. [161] studied internal resonances in an asymmetric shaft with a centrally mounted disc near both the primary and gravity critical speeds; bearing clearances introduced nonlinearities. [181] studied the $1 : -1$ internal resonance (between forward and backward whirl modes) in a simply supported, slender, asymmetric shaft near both the primary as well as secondary critical speeds; note that the resonance effectively presupposes small gyroscopic effects. In contrast, we study an overhung rotor with significant gyroscopic effects and non-infinitesimal deflections. We use the method of multiple scales (see [110]) and references therein) up to second order, with some problem-specific adaptation, while [161, 181] use the method of averaging up to first order.

In this work, we study the idealized overhung rotor model of [32]. In that work, linear equations were written, gravity was ignored, and a linear stability analysis pointed out, e.g., the unstable gap between primary whirl speeds. Here, we write nonlinear equations for finite displacements. Linearization yields the correct gravity critical speed. Subsequently, for spin near the gravity critical speed, we use the method of multiple scales (MMS) for a detailed study. We remark that the model studied here, if fabricated exactly, might have low practical utility (in addition to nonlinear effects we will ignore here). Overhung rotors where the end-loaded shaft passes through a bearing are far more common. However, models for such rotors would require at least two more degrees of freedom, and so we have focussed here on the simplest possible overhung rotor model from the literature.

7.2 System description

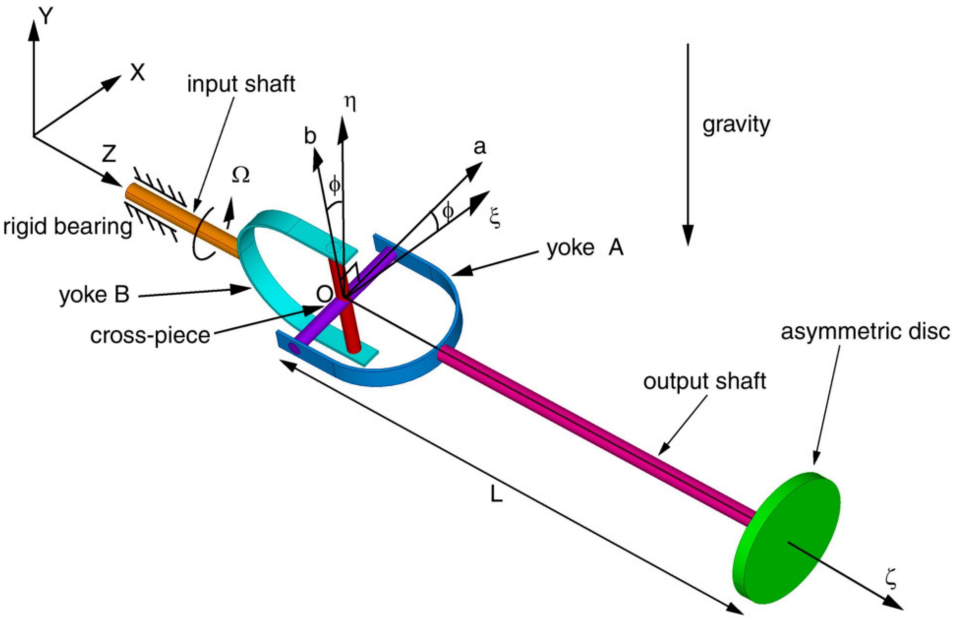

Figure 7.1: Schematic of overhung rotor model of [32].

The rotor model of [32] is shown in Fig. 7.1. Let XYZ represent the inertial coordinate system, with unit vectors $\mathbf{i}$, $\mathbf{j}$ and $\mathbf{k}$. Gravity acts along $-\mathbf{j}$ as shown. The horizontal input shaft spins at a constant rate Ω about $\mathbf{k}$, and in turn spins the nominally-horizontal, overhung output shaft through a massless universal joint made of two yokes and a cross-piece with center O, as shown. The output shaft is rigid, and massless but for the disc of mass M at its end. The disc, the output shaft and yoke A are collectively called “the rotor,” and its length is L.

The rotor has two rotational degrees of freedom. Let unit vectors $\mathbf{a}$ and $\mathbf{b}$ be defined as shown in Fig. 7.1. Let $\bar{\theta}_a$ and $\bar{\theta}_b$ be the rotations about $\mathbf{a}$ and $\mathbf{b}$. These rotations are resisted by torsion springs of stiffnesses K_a and K_b respectively. We assume $K_a \geq K_b$.

Weak torsional dashpots in parallel with the torsion springs provide energy dissipation.

For kinetic energy calculations we will use the rotor's moment of inertia matrix about point O. Let the principal axes of that matrix be ξ-η-ζ with I_ξ, I_η being the diametral, and I_ζ being the polar, moments of inertia respectively. For an asymmetric rotor, $I_\xi \neq I_\eta$. We assume $I_\xi \geq I_\eta$. When $\bar{\theta}_a = \bar{\theta}_b = 0$, the inertia axes ξ-η make an angle ϕ with the stiffness axes **a**-**b** (see figure).

7.3 Equations of motion

Linearized equations of motion derived by Lagrange's method utilizing body-fixed axes ($\xi\eta\zeta$) were presented in [32]. Here, our derivation of the nonlinear equations of motion begins with lab-fixed coordinates XYZ, and our representation of rotation matrices mimics that in [182]. In particular, we will make repeated use of an axis-angle formula as described below.

We choose and hold a single set of coordinate axes (XYZ) fixed, so that vectors are equivalent to their matrices of components. Now, on rotating any rigid body through an angle ψ about a unit vector $\mathbf{n}$, any vector $\mathbf{r}$ embedded in the body is transformed (rotated) to the vector $\mathbf{r}'$ given by $\mathbf{r}' = \mathbf{R}(\mathbf{n},\psi)\mathbf{r}$, where

$$\mathbf{R}(\mathbf{n},\psi) = \cos\psi\,\mathbf{I} + (1-\cos\psi)\,\mathbf{n}\,\mathbf{n}^t + \sin\psi\,\mathbf{S}(\mathbf{n}),$$

where in turn the t-superscript denotes matrix transpose and $\mathbf{S}(\mathbf{n})$ is the skew-symmetric cross-product matrix.[1] More explicitly,

$$\mathbf{S}(\mathbf{n}) = \begin{bmatrix} 0 & -n_3 & n_2 \\ n_3 & 0 & -n_1 \\ -n_2 & n_1 & 0 \end{bmatrix},$$

and n_1, n_2 and n_3 are the components of $\mathbf{n}$ in the fixed inertial axes we use for the entire calculation ($\mathbf{n}$ is called the *axial vector* of $\mathbf{S}(\mathbf{n})$ above). To avoid possible confusion, we emphasize that our formula differs from that describing transformation of vector components in the case where the body is held fixed while coordinate axes are rotated. All rotations

---

[1] $\mathbf{S}(\mathbf{n})\,\mathbf{u} = \mathbf{n}\times\mathbf{u}$ for all $\mathbf{n}$ and $\mathbf{u}$.

of all bodies will be viewed as successive rotations of the above form; angular velocities of bodies will be extracted from time derivatives of rotation matrices; moment of inertia matrix calculations will also use these same rotation matrices; and when the system kinetic and potential energies are known, it remains to model the dissipation and then Lagrange's equations can be written routinely. We explain these details here below.

We now proceed to obtain an expression for the kinetic energy. Note that point O is fixed in inertial space at all times. It is also fixed in the rotor. We use the angles $\bar{\theta}_a$ and $\bar{\theta}_b$, as described above, as generalized coordinates. In the reference configuration, the **a**-**b** axes are coincident with our inertial X-Y axes, i.e., in the reference configuration, $\mathbf{a} = \mathbf{i}$ and $\mathbf{b} = \mathbf{j}$.

The rotor's orientation at any arbitrary time t is described using a 3-2-1 Euler angle sequence. First, the rotor is rotated (by the input shaft) about Z through an angle $\Omega\,t$. Then the rotor is rotated through an angle $\bar{\theta}_b$ about the Z-rotated **b** axis. Finally, the rotor is rotated through an angle $\bar{\theta}_a$ about the first Z-rotated and then **b**-rotated **a** axis. The individual matrices for the above three rotations are, respectively,

$$\begin{aligned} \mathbf{R}_1 &= \mathbf{R}(\mathbf{k}, \Omega\,t), \\ \mathbf{R}_2 &= \mathbf{R}(\mathbf{R}_1\mathbf{j}, \bar{\theta}_b), \\ \mathbf{R}_3 &= \mathbf{R}(\mathbf{R}_2\,\mathbf{R}_1\mathbf{i}, \bar{\theta}_a), \end{aligned}$$

which we have computed symbolically using MAPLE. The final rotation matrix is

$$\mathbf{R}_{net} = \mathbf{R}_3\,\mathbf{R}_2\,\mathbf{R}_1.$$

The angular velocity of the rotor is then the axial vector of the skew-symmetric matrix $\dot{\mathbf{R}}_{net}\,\mathbf{R}_{net}^t$, where the overdot denotes a time derivative. The angular velocity components are found, using MAPLE, to be[2]

$$\omega = \left\{ \begin{array}{c} \omega_X \\ \omega_Y \\ \omega_Z \end{array} \right\} = \left\{ \begin{array}{c} \dot{\bar{\theta}}_a \cos(\Omega\,t)\,\cos\bar{\theta}_b - \dot{\bar{\theta}}_b \sin(\Omega\,t) \\ \dot{\bar{\theta}}_b \cos(\Omega\,t) + \dot{\bar{\theta}}_a \sin(\Omega\,t)\,\cos\bar{\theta}_b \\ \Omega - \dot{\bar{\theta}}_a \sin\bar{\theta}_b \end{array} \right\}.$$

The moment of inertia tensor of the rotor about O expressed in the body-fixed principal

---

[2] The angular velocity components along body-fixed principal axes were separately computed as a check, and agreed with those reported in Eq. 5 of [32]. However, we will uniformly use the XYZ axes only.

axes is

$$\mathbf{I}_{\xi\eta\zeta} = \begin{bmatrix} I_\xi & 0 & 0 \\ 0 & I_\eta & 0 \\ 0 & 0 & I_\zeta \end{bmatrix}.$$

Thus, the moment of inertia matrix about the inertial axes is given by[3]

$$\mathbf{I}_{XYZ} = \mathbf{R}_{net}\,\mathbf{R}_\phi\,\mathbf{I}_{\xi\eta\zeta}\,\mathbf{R}_\phi^t\,\mathbf{R}_{net}^t,$$

where

$$\mathbf{R}_\phi = \mathbf{R}(\mathbf{k}, -\phi) = \begin{bmatrix} \cos\phi & \sin\phi & 0 \\ -\sin\phi & \cos\phi & 0 \\ 0 & 0 & 1 \end{bmatrix}.$$

Finally, the kinetic energy is given by (detailed expression not reproduced here)

$$T = \frac{1}{2}\,\omega^t\,\mathbf{I}_{XYZ}\,\omega. \tag{7.1}$$

The potential energy arises from the torsion springs and gravity and is given by

$$\begin{aligned} V &= \frac{1}{2}\,K_a\,\bar{\theta}_a^2 + \frac{1}{2}\,K_b\,\bar{\theta}_b^2 + M g\,L\,(\mathbf{R}_{net}\mathbf{k})\cdot\mathbf{j} & (7.2) \\ &= \frac{1}{2}\,K_a\,\bar{\theta}_a^2 + \frac{1}{2}\,K_b\,\bar{\theta}_b^2 + M g\,L\,\sin(\Omega\,t)\,\cos\bar{\theta}_a\,\sin\bar{\theta}_b - \\ &\quad M g\,L\,\cos(\Omega\,t)\,\sin\bar{\theta}_a, & (7.3) \end{aligned}$$

where $\mathbf{R}_{net}$ is the net rotation matrix and g is the acceleration due to gravity.

We now turn to dissipation, which we model through viscous, torsional damping at the pivots in the universal joint. The generalized dissipation forces for $\bar{\theta}_a$ and $\bar{\theta}_b$, denoted by $\mathcal{F}_a$ and $\mathcal{F}_b$ are respectively

$$\mathcal{F}_a = -c\,\dot{\bar{\theta}}_a\,, \quad \mathcal{F}_b = -c\,\dot{\bar{\theta}}_b\,,$$

where c is a common coefficient.

---

[3] Note again that our rotation matrices correspond to rotated bodies with axes held fixed. This puts the transposed multiplying matrices on the right hand side, instead of on the left hand side as occurs for formulas based on rotated coordinate systems.

Finally, the Lagrangian is $\mathcal{L} = T - V$, and Lagrange's equations are

$$\frac{d}{dt}\left(\frac{\partial \mathcal{L}}{\partial \dot{\bar{\theta}}_a}\right) - \left(\frac{\partial \mathcal{L}}{\partial \bar{\theta}_a}\right) = -c\,\dot{\bar{\theta}}_a\,, \tag{7.4}$$

$$\frac{d}{dt}\left(\frac{\partial \mathcal{L}}{\partial \dot{\bar{\theta}}_b}\right) - \left(\frac{\partial \mathcal{L}}{\partial \bar{\theta}_b}\right) = -c\,\dot{\bar{\theta}}_b\,. \tag{7.5}$$

The full expressions, obtained using the symbolic algebra package MAPLE, are long and not reproduced here.

7.4 Linearization

We introduce the following symbols for ease of presentation:

$$I_m = \left(\frac{I_\xi + I_\eta}{2}\right), \quad I_d = \left(\frac{I_\xi - I_\eta}{2}\right), \quad K_m = \left(\frac{K_a + K_b}{2}\right), \quad K_d = \left(\frac{K_a - K_b}{2}\right).$$

Thus, I_m represents the mean diametral mass moment of inertia, while I_d represents inertia asymmetry; and K_m represents the mean stiffness, while K_d represents stiffness asymmetry. Using the above, linearization of Eqs. 7.4 and 7.5 yields

$$\mathbf{A}\ddot{\bar{\Theta}} + (\mathbf{B} + \mathbf{E})\dot{\bar{\Theta}} + \mathbf{C}\bar{\boldsymbol{\Theta}} = \mathbf{F}, \tag{7.6}$$

where $\bar{\boldsymbol{\Theta}} = \begin{Bmatrix} \bar{\theta}_a \\ \bar{\theta}_b \end{Bmatrix}$, $\mathbf{F} = \begin{Bmatrix} M\,g\,L\,\cos(\Omega\,t) \\ -M\,g\,L\,\sin(\Omega\,t) \end{Bmatrix}$, and the coefficient matrices

$$\mathbf{A} = \begin{bmatrix} I_m + I_d\,\cos 2\phi & -I_d\,\sin 2\phi \\ -I_d\,\sin 2\phi & I_m - I_d\,\cos 2\phi \end{bmatrix}, \quad \mathbf{B} = \Omega\,(I_\zeta - 2I_m)\begin{bmatrix} 0 & 1 \\ -1 & 0 \end{bmatrix},$$

$$\mathbf{C} = \begin{bmatrix} \Omega^2\,(I_\zeta - I_m + I_d\,C_{2\phi}) + K_m + K_d & -\Omega^2\,I_d\,S_{2\phi} \\ -\Omega^2\,I_d\,S_{2\phi} & \Omega^2\,(I_\zeta - I_m - I_d\,C_{2\phi}) + K_m - K_d \end{bmatrix},$$

where $C_{2\phi}$ and $S_{2\phi}$ denote $\cos 2\phi$ and $\sin 2\phi$, respectively; and $\mathbf{E}$ is simply c times the 2×2 identity matrix. Note that $\mathbf{A}$ is the inertia matrix, $\mathbf{B}$ adds gyroscopic terms, $\mathbf{E}$ adds damping, and $\mathbf{C}$ is an effective stiffness matrix. However, if we ignore gravity and seek synchronous whirl solutions, then we must use $\det(\mathbf{C}) = 0$, showing that some gyroscopic *effects* are included in $\mathbf{C}$ as well.

That **C** includes some gyroscopic terms is not well understood by all, and confuses some readers; a few lines of further explanation are therefore provided here. The equations of motion for the overhung rotor are written using co-ordinates measured in a rotating frame (θ_a and θ_b). At the synchronous critical speed, the rotor appears stationary in the rotating frame. This amounts to setting the derivatives of all order of θ_a and θ_b to zero. Thus we are left with $\mathbf{C}\bar{\boldsymbol{\Theta}} = \mathbf{0}$. For a non-trivial $\bar{\boldsymbol{\Theta}}$, we require $\det(\mathbf{C}) = 0$. This gives the correct expression for the synchronous whirl speed. However, we know that for the overhung rotor, the synchronous whirl speed is significantly influenced by the gyroscopic forces. Thus an accurate determination of the critical speed using $\det(\mathbf{C}) = 0$, implies that the matrix **C**, although apparently representing the stiffness matrix, effectively includes the gyroscopic effects. For continuum rotors (bottles, funnels etc.), the form and nature of gyroscopic terms are not obvious from the equations of equilibrium of a continuum point. Accurate determination of critical speeds of such rotors involves identification of terms at the continuum level which cause the macroscopically manifested gyroscopic effects. This problem of determination of critical speeds of continuum rotors is addressed in more detail in [183].

Moving on, following [32], we introduce

$$\epsilon_i = \frac{I_d}{I_m}, \quad \epsilon_s = \frac{K_d}{K_m}, \quad J = \frac{I_\zeta}{I_m}, \quad \tau = \Omega\, t, \quad \sigma = \frac{\Omega}{\sqrt{K_m/I_m}}\,,$$

where ϵ_i and ϵ_s are non-dimensional inertia and stiffness asymmetries, respectively, J represents the source of gyroscopic effects if any, τ is non-dimensional time and σ is non-dimensional spin speed. Note that $0 \le \epsilon_i < 1$, $0 \le \epsilon_s < 1$, $0 < J < 2$ and $0 \le \phi \le \frac{\pi}{2}$. At the extremes, which we avoid, $J = 0$ for a point mass at the shaft tip, while $J = 2$ for a centrally-pivoted zero-thickness disc (i.e., $L = 0$).

Substituting the above definitions in Eq. 7.6 and simplifying, we have

$$\bar{\mathbf{A}}\bar{\boldsymbol{\Theta}}'' + (\bar{\mathbf{B}} + \bar{\mathbf{E}})\bar{\boldsymbol{\Theta}}' + \bar{\mathbf{C}}\bar{\boldsymbol{\Theta}} = \bar{\mathbf{F}}, \tag{7.7}$$

where primes denote derivatives with respect to τ,

$$\bar{\mathbf{A}} = \begin{bmatrix} 1+\epsilon_i\cos 2\phi & -\epsilon_i\sin 2\phi \\ -\epsilon_i\sin 2\phi & 1-\epsilon_i\cos 2\phi \end{bmatrix}, \quad \bar{\mathbf{B}} = (J-2)\begin{bmatrix} 0 & 1 \\ -1 & 0 \end{bmatrix},$$

$$\bar{\mathbf{C}} = \begin{bmatrix} J-1+\epsilon_i\cos 2\phi + (1+\epsilon_s)/\sigma^2 & -\epsilon_i\sin 2\phi \\ -\epsilon_i\sin 2\phi & J-1-\epsilon_i\cos 2\phi + (1-\epsilon_s)/\sigma^2 \end{bmatrix},$$

$$\bar{\mathbf{E}} = \frac{c}{\sigma\sqrt{K_m I_m}} \begin{bmatrix} 1 & 0 \\ 0 & 1 \end{bmatrix}, \text{ and } \bar{\mathbf{F}} = \frac{M\,g\,L}{K_m \sigma^2} \begin{Bmatrix} \cos\tau \\ -\sin\tau \end{Bmatrix}.$$

7.5 Undamped gravity critical speed

We initially ignore the damping and consider the homogeneous equation

$$\bar{\mathbf{A}}\bar{\mathbf{\Theta}}'' + \bar{\mathbf{B}}\bar{\mathbf{\Theta}}' + \bar{\mathbf{C}}\bar{\mathbf{\Theta}} = \mathbf{0}\,. \tag{7.8}$$

The characteristic equation of Eq. 7.8 is of the form $\alpha\,\lambda^4 - 2\,\beta\,\lambda^2 + \gamma = 0$, where the α, β and γ we obtain (we have checked) match [32]. Synchronous whirl corresponds to $\lambda = 0$. However, here we are interested in gravity critical speeds. According to [167] and [172], for an asymmetric two degree of freedom rotor, there are four natural frequencies for each spin speed. At the gravity critical speed, one of these frequencies vanishes, whence constant gravity can excite the corresponding mode. That same condition corresponds to $\lambda = 1$ in our treatment because our generalized coordinates are defined in a rotating system. Setting $\lambda = 1$ in the above characteristic equation and solving for Ω, we obtain

$$\Omega_{gc} = \sqrt{\frac{K_m}{I_m}}\sqrt{\frac{1-\epsilon_s^2}{4-2J}}\,. \tag{7.9}$$

If stiffness asymmetry and J are *both* small, $\Omega_{gc} \approx \frac{1}{2}\sqrt{\frac{K_m}{I_m}}$, as has been noted by many others. Also, inertia asymmetry and the angle ϕ have no effect on the gravity critical speed (as stated by [153]). In our nonlinear analysis, however, inertia asymmetry will have a weak (second order) effect.

7.6 Closing remarks

In this starting chapter on the study of gravity critical speeds of rotors, we have presented the equations of motion of an asymmetric, overhung rotor in the presence of gravity. Subsequently, we have linearized the equations of motion and derived the expression for the gravity critical speed through an eigenvalue analysis. In the next chapter, we will conduct an MMS analysis assuming operation close to the gravity critical speed and considering small nonlinearities, weak asymmetries and small damping.

Chapter 8

MMS slow flow: Analysis of primary resonant solutions

In this chapter we conduct a second order MMS analysis on the equations of motion of the overhung rotor derived in the previous chapter, after suitable scaling. We will treat the asymmetries as small and include nonlinearities arising from large displacements. The second order slow flow is shown to provide good approximations. We shall subsequently analyze the first order slow flow and study the role of various parameters such as inertia and stiffness asymmetry as well as the gyroscopic effects in the gravity resonance phenomena. We shall also comment on the persistence of weak resonances even in the *absence* of asymmetries.

We first begin with the MMS procedure.

8.1 Method of multiple scales

We first identify the small parameter to be used in the subsequent MMS expansions. Recall that in the right hand side of Eq. 7.7, the expression for the forcing term, $\bar{\mathbf{F}}$, contained the parameter $\dfrac{M\,g\,L}{K_m}$, which represents the static angular deflection of the rotor under self-weight, which is typically small; we will use this parameter in our multiple scales expansion. Now, Lagrange's Eqs. 7.4 and 7.5 involve trigonometric terms. We will expand them in power series (upto fifth power). To deem the asymmetries and damping as small, and also to stay close to the gravity critical speed, we further define

$$\sqrt{\nu} = \frac{M\,g\,L}{K_m}, \quad \bar{\theta}_a = \sqrt{\nu}\,\theta_a\,, \quad \bar{\theta}_b = \sqrt{\nu}\,\theta_b, \quad \epsilon_i = \nu\,\delta,$$

$$\epsilon_s = \nu\,\kappa, \quad c = \nu\,\mu\,\sqrt{K_m\,I_m}, \quad \sigma = \frac{1}{\sqrt{4-2J}} + \nu\,\Delta\,,$$

where $0 < \nu \ll 1$; where θ_a, θ_b, κ, δ, μ and Δ are $\mathcal{O}(1)$ quantities; and where Δ represents detuning or deviation from the leading order expression for gravity critical speed. Note that asymmetries, as well as damping, have been taken to be one order smaller than the static deflection of the rotor.

A consequence of such scaling is that, unlike typical near-resonance analyses of weakly nonlinear oscillators (see pp. 163-173 of [3]), the forcing from gravity will appear at leading order itself in the analysis below. Technically, this is possible without blowup of terms because the resonant forcing does not directly excite the corresponding resonant mode in this two d.o.f. system. Physically and intuitively, the near axisymmetric nature of the rotor diminishes the magnitude of the response, thus allowing the rotor to tolerate relatively larger forcing.

Expanding for small $\sqrt{\nu}$ and then dividing through by $\sqrt{\nu}$, and on replacing primes by overdots to better match the convention for time derivatives (understanding that overdots now signify τ-derivatives), we finally have

$$\mathbf{P}\ddot{\boldsymbol{\Theta}} + \mathbf{Q}\dot{\boldsymbol{\Theta}} + \mathbf{R}\boldsymbol{\Theta} = \mathbf{f} + \nu\mu\mathbf{D}\dot{\boldsymbol{\Theta}} + \nu(\mathbf{N_1} + \mathbf{N_2}) + \nu^2\mathbf{N_3}\,. \tag{8.1}$$

where $\boldsymbol{\Theta} = \left\{ \begin{array}{c} \theta_a \\ \theta_b \end{array} \right\}$, $\mathbf{f} = (4-2J)\left\{ \begin{array}{c} \cos\tau \\ -\sin\tau \end{array} \right\}$, and the coefficient matrices

$$\mathbf{P} \;=\; \begin{bmatrix} 1 & 0 \\ 0 & 1 \end{bmatrix}, \quad \mathbf{Q} \;=\; (J-2)\begin{bmatrix} 0 & 1 \\ -1 & 0 \end{bmatrix},$$

$$\mathbf{R} \;=\; \begin{bmatrix} 3-J & 0 \\ 0 & 3-J \end{bmatrix}, \quad \text{and } \mathbf{D} \;=\; -\sqrt{4-2J}\begin{bmatrix} 1 & 0 \\ 0 & 1 \end{bmatrix}.$$

The term $\mathbf{N_1} = \{N_{11}, N_{12}\}^t$ contains harmonic forcing terms and terms linear in the generalized coordinates and their derivatives; these terms, though linear, represent small effects (as denoted by the ν premultiplier). The term $\mathbf{N_2} = \{N_{21}, N_{22}\}^t$ contains cubic nonlinearities (such as θ_a^3 and $\dot{\theta}_b\theta_a^2$), as well as quadratically nonlinear parametric forcing terms (such as $\theta_a\theta_b \sin\tau$ and $\theta_a^2 \cos\tau$). Finally, the term $\mathbf{N_3} = \{N_{31}, N_{32}\}^t$ contains a combination of forcing, linear and nonlinear terms upto fifth order. Detailed expressions for these terms are provided in appendix F. materials.

We now proceed to apply the method of multiple scales (MMS) to Eq. 8.1, and begin with a first order analysis.

We first rewrite the equations in state space form as

$$\dot{\mathbf{X}} = \mathbf{M}\mathbf{X} + \mathbf{G}(\tau) + \nu\mathbf{H}(\mathbf{X},\tau) + \nu^2\mathbf{W}(\mathbf{X},\tau)\,, \tag{8.2}$$

where the state vector $\mathbf{X} = \left\{\begin{array}{c}\theta_a\\ \dot{\theta}_a\\ \theta_b\\ \dot{\theta}_b\end{array}\right\}$,

$$\mathbf{M} = \begin{bmatrix} 0 & 1 & 0 & 0\\ J-3 & 0 & 0 & 2-J\\ 0 & 0 & 0 & 1\\ 0 & J-2 & J-3 & 0 \end{bmatrix}, \quad \mathbf{G}(\tau) = (4-2J)\left\{\begin{array}{c}0\\ \cos\tau\\ 0\\ -\sin\tau\end{array}\right\},$$

and $\mathbf{H}$ and $\mathbf{W}$ incorporate asymmetry, detuning, damping and nonlinearities.

We introduce multiple time scales: $T_0 = \tau$, $T_1 = \nu\tau$, $T_2 = \nu^2\tau, \cdots$ and write

$$\mathbf{X} = \mathbf{X}_0(T_0,T_1,T_2,\cdots) + \nu\mathbf{X}_1(T_0,T_1,T_2,\cdots) + \nu^2\mathbf{X}_2(T_0,T_1,T_2,\cdots) + \cdots\,. \tag{8.3}$$

Substituting Eq. 8.3 in Eq. 8.2 and taking time derivatives as is usual for the MMS, we have at $\mathcal{O}(1)$:

$$\frac{\partial\mathbf{X}_0}{\partial T_0} = \mathbf{M}\mathbf{X}_0 + (2-J)\left\{\begin{array}{c}0\\ 1\\ 0\\ i\end{array}\right\}e^{iT_0} + (2-J)\left\{\begin{array}{c}0\\ 1\\ 0\\ -i\end{array}\right\}e^{-iT_0}\,, \tag{8.4}$$

where $\mathbf{G}(\tau)$ has been written using complex exponential notation.

Now the eigenvalues of $\mathbf{M}$ are: $i, -i, i(J-3), -i(J-3)$, with $J \neq 2$. Thus, the harmonic forcing could *potentially* excite unbounded responses along eigenvectors corresponding to the eigenvalues $\pm i$. It turns out that it does not. This issue is a key aspect of the present analysis. In view of its importance here, we pause to consider a general system

$$\dot{\mathbf{x}} = \mathbf{A}\mathbf{x} + \mathbf{u}e^{\lambda t}.$$

If λ is *not* an eigenvalue of $\mathbf{A}$, then there is a solution of the form $\mathbf{x} = \mathbf{b}e^{\lambda t}$, found easily by solving $(\mathbf{A} - \lambda\,\mathbf{I})\mathbf{b} = -\mathbf{u}$, where $\mathbf{I}$ is the identity matrix and $\mathbf{A} - \lambda\,\mathbf{I}$ is not singular because λ is not an eigenvalue. In contrast, if λ is in fact an eigenvalue of $\mathbf{A}$, then the coefficient matrix is singular and there is in general no bounded solution for $\mathbf{b}$. In the *special case* where $\mathbf{u}$ lies in the column space of $\mathbf{A} - \lambda\,\mathbf{I}$, or equivalently, when $\mathbf{u}$ is orthogonal to the left null vector of $\mathbf{A} - \lambda\,\mathbf{I}$, then there are bounded but nonunique solutions for $\mathbf{b}$. The nonuniqueness consists of an arbitrary scalar multiple of the *right* null vector of $\mathbf{A} - \lambda\,\mathbf{I}$. In our MMS analysis, the situation is the last one, with bounded but nonunique solutions at first order.

Thus, the solution for $\mathbf{X}_0$ is bounded and nonunique. Intuitively, since the gravity resonance is mainly due to asymmetries which are absent at this order, we expect no unbounded solutions here. The lack of immediately unbounded solutions resembles, for example, the dynamics of a straight rod excited torsionally at a bending natural frequency. In this way, our system differs from usual resonantly forced, weakly nonlinear oscillators where no primary-resonance forcing can be sustained at leading order.

Proceeding with our analysis, the solution of Eq. 8.4 contains a complementary solution and a particular integral. The particular integral, as discussed above, is non-unique. Moreover, the non-unique portion can be absorbed into the complementary solution involving the eigenvalues $\pm\, i$. Thus the solution of Eq. 8.4 is

$$\begin{aligned}\mathbf{X}_0(T_0,T_1,T_2) \;=\;& (c_1(T_1,T_2)+ic_2(T_1,T_2))\left\{\begin{array}{c}1\\ i\\ -i\\ 1\end{array}\right\}e^{iT_0} + \left\{\begin{array}{c}1\\ i\\ 0\\ 0\end{array}\right\}e^{iT_0} + \\ & (c_1(T_1,T_2)-ic_2(T_1,T_2))\left\{\begin{array}{c}1\\ -i\\ i\\ 1\end{array}\right\}e^{-iT_0} + \left\{\begin{array}{c}1\\ -i\\ 0\\ 0\end{array}\right\}e^{-iT_0}. \qquad (8.5)\end{aligned}$$

We have not included the contribution of the eigenvalue $i(J-3)$ in the complementary solution as it is neither resonantly forced (since $J \neq 2$), nor involved in any internal resonances (as we have verified; details not presented here), and hence will be eventually damped out. The real-valued functions $c_1(T_1, T_2)$ and $c_2(T_1, T_2)$ are to be determined from calculations at subsequent orders.

Proceeding to the next order, at $\mathcal{O}(\nu)$ we have

$$\frac{\partial \mathbf{X}_1}{\partial T_0} - \mathbf{M}\mathbf{X}_1 = -\frac{\partial \mathbf{X}_0}{\partial T_1} + \mathbf{H}(\mathbf{X}_0, T_0). \tag{8.6}$$

Substituting Eq. 8.5 in the right hand side of Eq. 8.6, we have

$$\frac{\partial \mathbf{X}_1}{\partial T_0} - \mathbf{M}\mathbf{X}_1 = \mathbf{U}(T_1, T_2)e^{iT_0} + \bar{\mathbf{U}}(T_1, T_2)e^{-iT_0} + \mathbf{V}(T_1, T_2)e^{3iT_0} + \bar{\mathbf{V}}(T_1, T_2)e^{-3iT_0}\,, \tag{8.7}$$

where overbars denote complex conjugates, and where $\mathbf{U}$ and $\mathbf{V}$ involve complicated expressions (not presented) in terms of c_1, c_2, their partial derivatives with respect to T_1, along with system parameters.

In Eq. 8.7, as before, we encounter forcing in resonance with the eigenvalues $\pm\, i$. To eliminate secular terms, we must ensure (as discussed above) that $\mathbf{U}$ is orthogonal to the left eigenvector of $\mathbf{M}$ corresponding to the eigenvalue i (see also, e.g., [110]), with a corresponding condition for $\bar{\mathbf{U}}$ being then identically satisfied. Thus, the solvability conditions may be written compactly as

$$\mathbf{U}^t(T_1, T_2) \left\{ \begin{array}{c} -i \\ \frac{1}{J-3} \\ 1 \\ \frac{i}{J-3} \end{array} \right\} = 0. \tag{8.8}$$

Separating the real and imaginary parts of Eq. 8.8, we obtain after elementary manipulations the slow flow equations (dependencies on T_1 and T_2 suppressed for simplicity)

$$\begin{aligned} \frac{\partial c_1}{\partial T_1} \;=\; \frac{1}{2J-8} \Big(& 16\, c_2 + 24\, c_2^3 + 24\, c_2 c_1 + 8\sqrt{4-2\,J}\Delta\, J\, c_2 - 13\, J\, c_2 + 24\, c_1^2 c_2 - \\ & 22\, J\, c_1^2 c_2 - 24\, J\, c_2 c_1 - 16\sqrt{4-2\,J}\Delta\, c_2 + 2\sqrt{4-2\,J}\mu\, c_1 + \\ & \sqrt{4-2\,J}\mu - 22\, J\, c_2^3 \Big)\,, \end{aligned} \tag{8.9}$$

$$\begin{aligned}\frac{\partial c_2}{\partial T_1} = \frac{1}{2J-8}\Big(&-6-4\,\kappa+5\,J+12\,J\,c_2^2-24\,c_2^2c_1+23\,J\,c_1+36\,J\,c_1^2+22\,J\,c_2^2c_1+\\ &8\,\sqrt{4-2\,J}\Delta-36\,c_1^2-12\,c_2^2-24\,c_1^3+22\,J\,c_1^3-24\,c_1+2\,\kappa\,J+\\ &16\,\sqrt{4-2\,J}\Delta\,c_1-4\,\sqrt{4-2\,J}\Delta\,J+2\,\sqrt{4-2\,J}\mu\,c_2-\\ &8\,\sqrt{4-2\,J}\Delta\,J\,c_1\Big)\,. \end{aligned} \tag{8.10}$$

The above equations govern, upto first order, the evolution of whirling solution amplitudes. We mention here that we have in fact proceeded to the next order (after solving Eq. 8.7) and obtained expressions for $\dfrac{\partial c_1}{\partial T_2}$ and $\dfrac{\partial c_2}{\partial T_2}$. The second order slow flow contains the inertia asymmetry parameter which is absent at first order; and provide better approximations than the first order. Details are presented in appendix G.

8.2 Initial results

The fixed points of the slow flow equations (Eqs. 8.9 and 8.10, if working with first order) represent periodic solutions of Eq. 8.2. These slow flow equations will, by and large, be treated numerically below. Note that numerical treatment of the slow flow is much faster than direct numerical treatment of the original Eq. 8.2. We will use only the first order slow flow for the most part, because it suffices for the qualitative dynamics we examine; for some parameter values, however, second order equations do give greater accuracy, as we will illustrate below.

Before a detailed study of the slow flow, some preliminary numerical results are plotted in Fig. 8.1. From the fixed points of the first order slow flow, Eqs. 8.9 and 8.10, the amplitudes of θ_a and θ_b are found from Eq. 8.5 as

$$\theta_a = 2\,\sqrt{(c_1+1)^2+c_2^2}, \qquad \theta_b = 2\,\sqrt{c_1^2+c_2^2}\,. \tag{8.11}$$

The slow flow is also linearized about each fixed point, and eigenvalues of the linearized system are used to determine stability (as depicted in the figure). Equilibrium solution branches are numerically computed using an arclength-based branch following scheme (see, e.g, [184]), as Δ is varied in parameter space. Saddle-node bifurcations, jump phenomena, and hysteresis, familiar in nonlinear resonances, are all observed. The plot for θ_a appears to self-intersect in this view, but the underlying 3D curve ($\theta_a - \theta_b - \Delta$) does not self-intersect (see plot for θ_b).

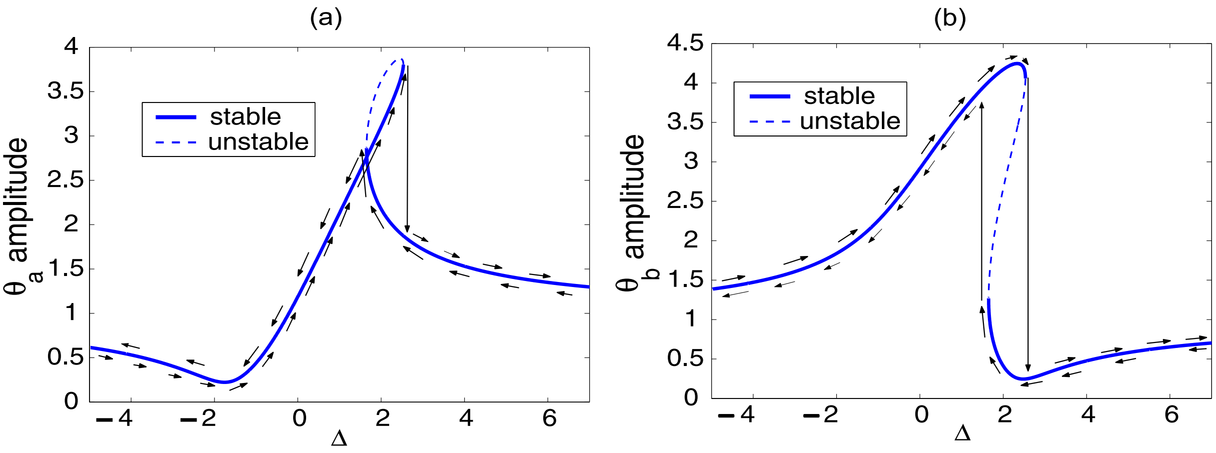

Figure 8.1: Multiple periodic solutions, both stable and unstable, can co-exist. Transitions from stable to unstable portions occur at points where tangents are vertical (at $\Delta \approx 2.53$ and $\Delta \approx 1.65$). Parameters: $\kappa = 7$, $\mu = 3$ and $J = 0.5$.

We present in Fig. 8.2 below a phase portrait for the first order slow flow, for $\Delta = 2$, $\kappa = 7$, $\mu = 3$ and $J = 0.5$, wherein three periodic solutions co-exist. The phase portrait shows one saddle and two stable foci, representing the one unstable and two stable periodic solutions respectively.

We now proceed to a more detailed investigation.

8.2.1 First *vs.* second order

To compare the first and second order slow flows, we consider two sets of parameter values. In each case, periodic solutions are computed in three ways: (a) by direct treatment of Eq. 8.2[1], (b) from the first order slow flow, Eqs. 8.9 and 8.10, and (c) from the second order slow flow (long equations, not presented here). Results are plotted in Fig. 8.3. For the first case (corresponding to plots (a) and (b) of the figure), first and second orders are both of acceptable accuracy; while for the second case (corresponding to plots (c) and (d)), first

---

[1] Periodic solutions of Eq. 8.2, or even the full equations Eqs. 7.4 and 7.5 (which we have done as well, but do not report here because they lead to no visible difference), are found iteratively through shooting methods and a numerical implementation of the Newton-Raphson method.

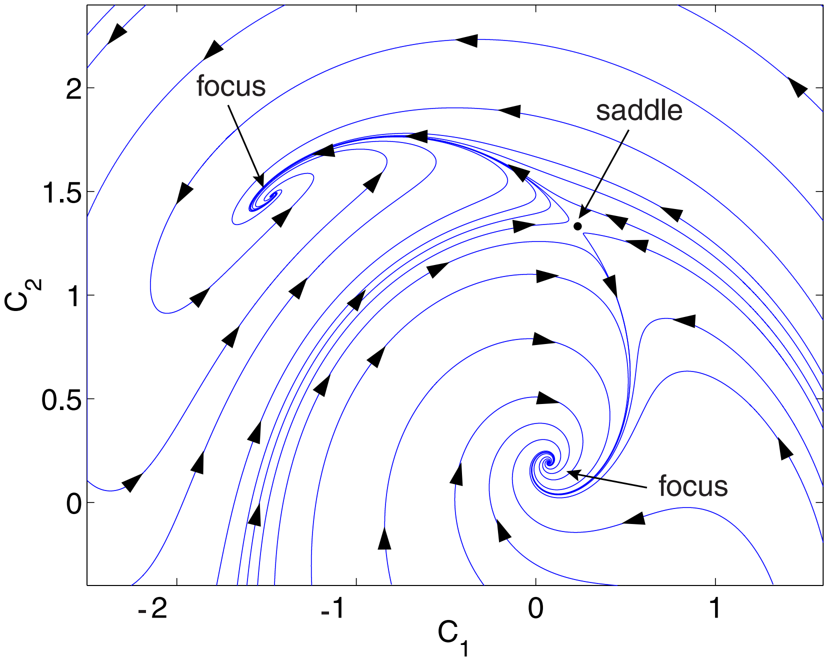

Figure 8.2: Phase portrait exhibiting multiple periodic solutions. Parameters: $\Delta = 2$, $\kappa = 7$, $\mu = 3$ and $J = 0.5$.

order has somewhat poor accuracy. In both cases, second order results are indistinguishable from full numerics within plotting accuracy. Henceforth, however, for computational ease and due to our primary interest in qualitative aspects of the dynamics, we will use the first order slow flow alone.

8.2.2 Some other observations

We summarize some other observations regarding the primary resonant solutions here.

Inertia asymmetry (δ) has no role in determination of gravity critical speed (see Eq. 7.9) and only a weak influence on amplitudes of resonant solutions [153], in that it drops out of the first order slow flow, Eqs. 8.9 and 8.10. However it does appear at second order.

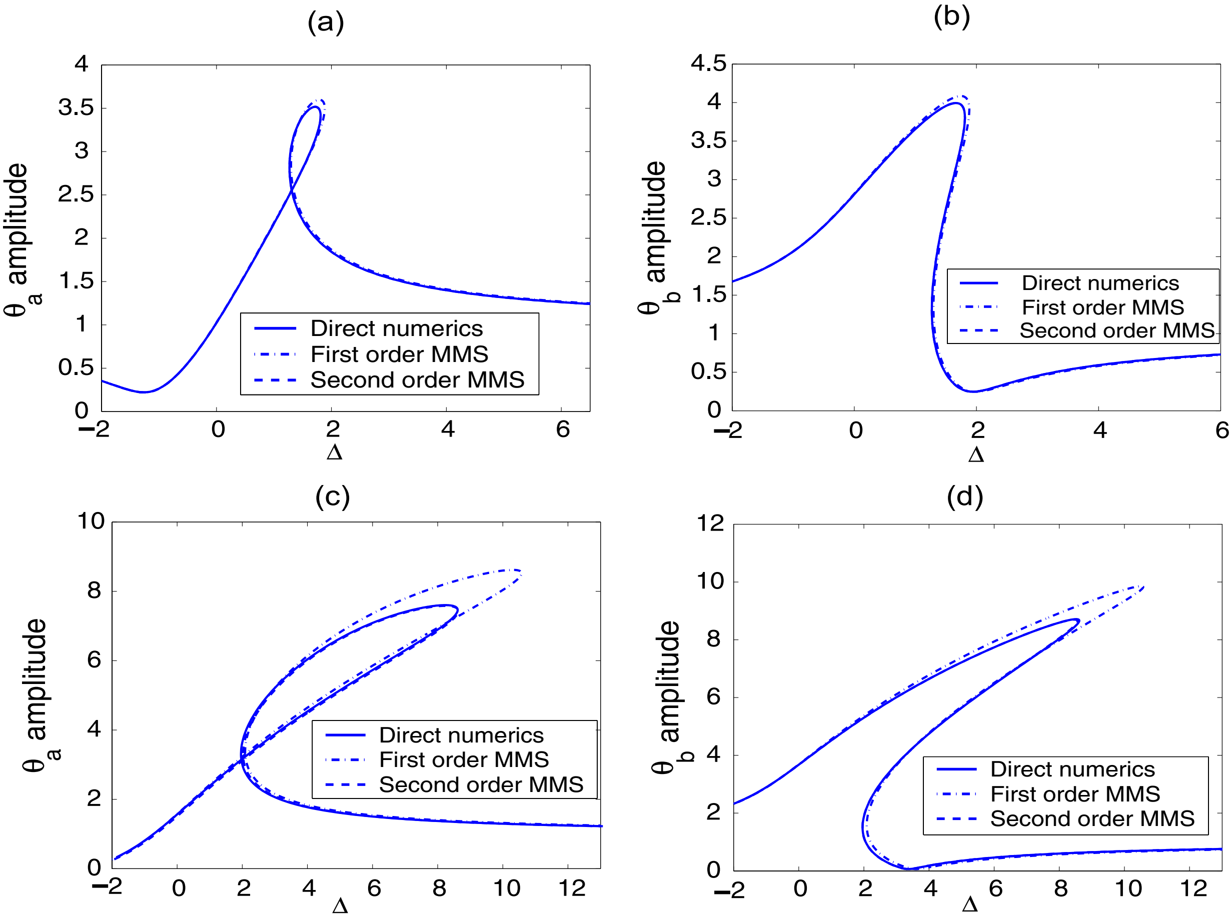

Figure 8.3: Comparison of first order and second order slow. (a) and (b): Parameters are $\nu = 0.002$, $\kappa = 5$, $\delta = 2$, $\mu = 2$, $\phi = \frac{\pi}{5}$ and $J = 0.7$; (c) and (d): Parameters are $\nu = 0.003$, $\kappa = 10$, $\delta = 2$, $\mu = 1$, $\phi = \frac{\pi}{5}$ and $J = 0.7$.

Gyroscopic effects, represented by J, have a significant role in the gravity induced resonant dynamics. Exploratory numerical results presented below suggest that, for light damping, decreasing J eventually raises the maximum amplitudes. Indirect analytical investigation of this issue, among others, is presented in Chapter 9, and constitutes one of the main contributions of this work. For a complementary view of the influence of the gyroscopic effect, through J, on the resonant amplitudes, we consider fixed points of the first order slow flow Eqs. 8.9 and 8.10, for three cases with $J = 0.3$, $J = 0.6$ and $J = 0.8$. Other parameters are held constant at $\kappa = 10$ and $\mu = 2$. Results are plotted in Fig. 8.4, and indicate that lower values of $J < 1$ leads to larger maximum amplitudes.

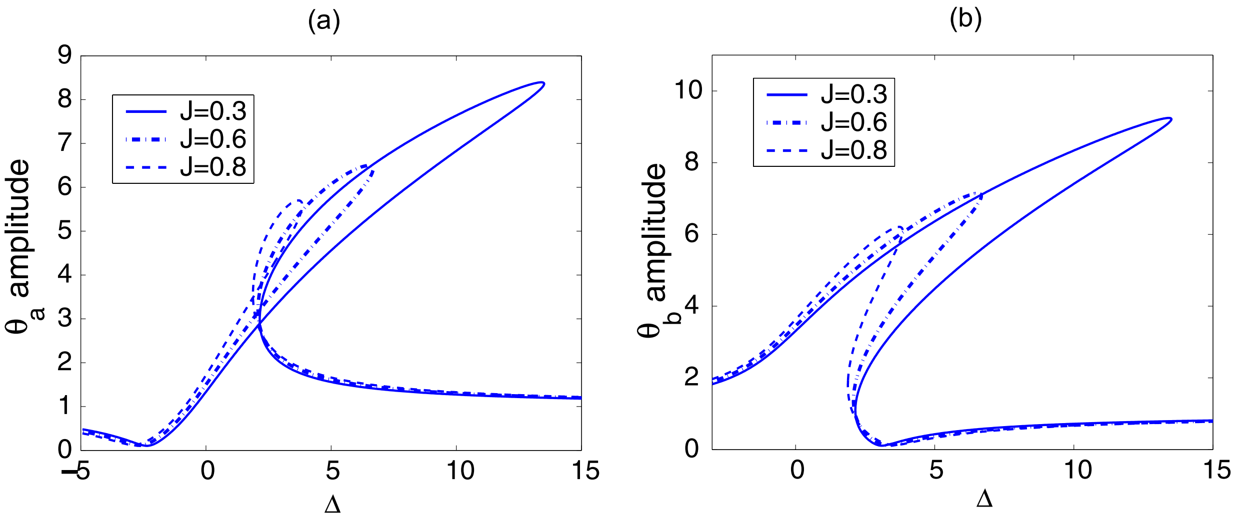

Figure 8.4: Effect of gyroscopic action on resonant solution amplitudes. Parameters: $\kappa = 10$ and $\mu = 2$.

Geometric nonlinearities, even in the absence of stiffness asymmetry, allow a somewhat weaker gravity-induced resonant response. The effect is attenuated by damping, and is in any case weaker than that of stiffness asymmetry.

Gravity induced secondary whirl is strong in the presence of stiffness asymmetry, and linear analyses demonstrating the former rely on the latter. However, with geometrical nonlinearities included, relatively weaker resonant effects exist even for a *symmetric* rotor, as we show next.

Mathematically, these weaker resonances exist because the potential energy expression Eq. 7.3 contains trigonometric nonlinearities which, during shaft rotation, give rise to higher order parametric forcing terms in Eq. 8.2 even for a symmetric shaft ($\kappa = 0$). However, these resonant responses are heavily attenuated by larger damping.

To demonstrate, we numerically examine the case of $\delta = 0$ and $\kappa = 0$, along with $J = 0.4$, $\mu = 0.3$ (a small value), and $\phi = \frac{\pi}{4}$. We use both Eq. 8.2 for $\nu = 0.0008$ (but with the ν^2 terms dropped), as well the first order slow flow. The near-identical results obtained from the two sets of equations are plotted in (a) and (b) of Fig. 8.5, where a significant whirl amplitude is observed. Upon increasing the damping to $\mu = 2$, however,

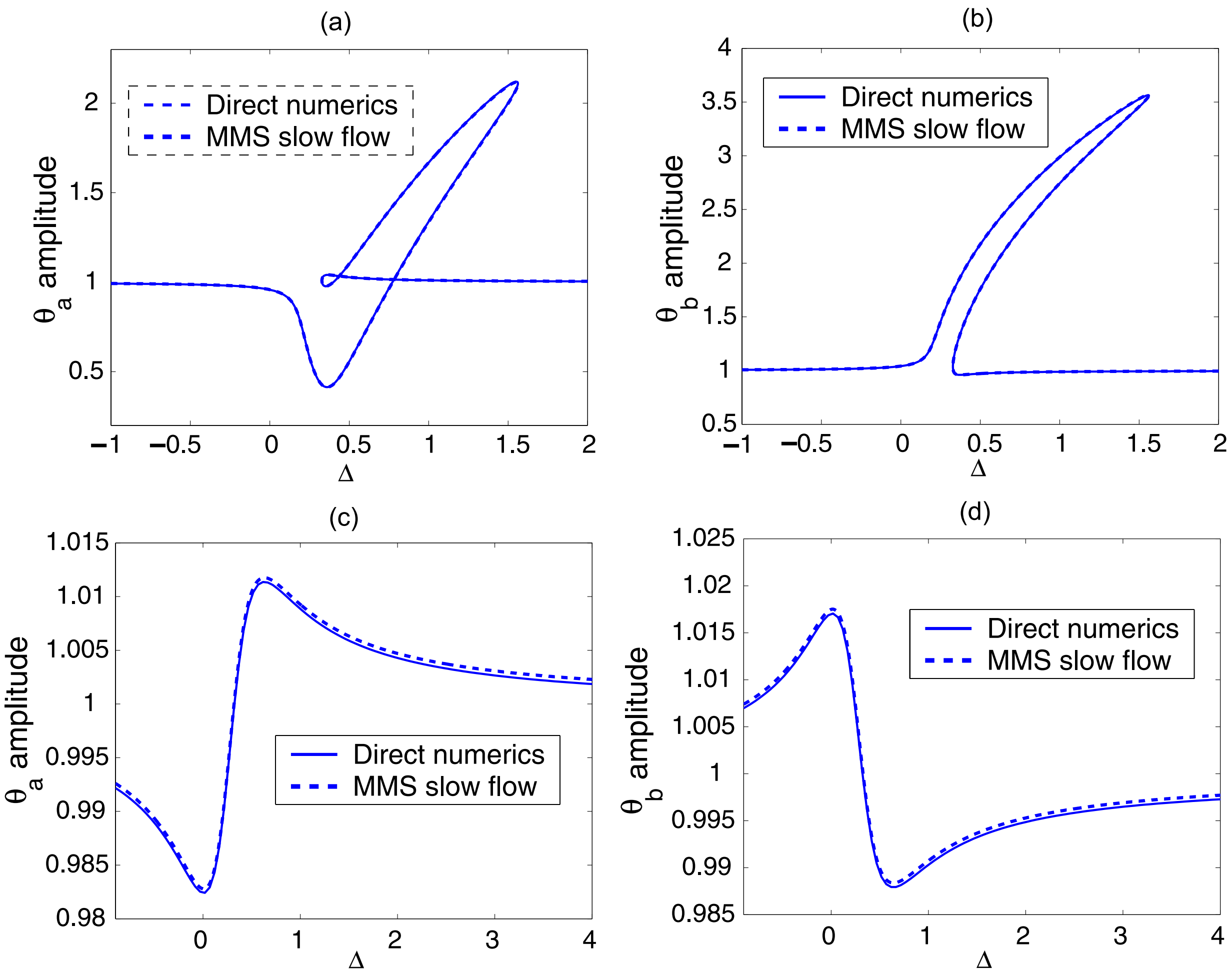

Figure 8.5: Weaker resonances for a *symmetric* rotor and their subsequent annihilation under increased damping. (a) and (b) - low damping with parameters $\nu = 0.0008$, $\delta = 0$, $\kappa = 0$, $\mu = 0.3$, $\phi = \frac{\pi}{4}$ and $J = 0.4$. (c) and (d) - increased damping with parameters $\nu = 0.0008$, $\delta = 0$, $\kappa = 0$, $\mu = 2$, $\phi = \frac{\pi}{4}$ and $J = 0.4$.

while keeping other parameters fixed, the response is attenuated as shown in (c) and (d) of Fig. 8.5.

8.3 Closing remarks

We conclude the MMS analysis of the *primary* resonant solutions of the overhung rotor.

In this chapter, we have used the MMS to derive the slow flow equations upto second order governing the gravity-induced whirl of the weakly asymmetric, weakly nonlinear, overhung rotor. The first order MMS slow flow verified the known unimportance of inertia asymmetry in gravity resonances; the second order slow flow, however, demonstrated a weak but nonzero role of the same. The role of gyroscopic effects on maximum resonant amplitudes was illustrated. Weakly resonant effects were found even in the absence of asymmetry, something that linear analyses do not capture.

All through this chapter, we have focused on the primary resonant solutions revealed by the slow flow. However, apart from this primary solution branch, the MMS slow flow also reveals other periodic solution branches. In the next chapter, we present a detailed numerical and analytical investigation of the bifurcation structure of the MMS slow flow to get a unified picture of the complete solution set.

Chapter 9

MMS slow flow: Analysis of auxiliary periodic solutions

In this chapter, we continue our study of the MMS slow flow of the rotor model of [32] developed in Chapters 7 and 8. In those chapters, we had focused on the primary resonant solutions yielded by the MMS slow flow. Apart from these solutions, we have observed the existence of another branch of nonlinearity-induced periodic solutions. In this chapter, we numerically and analytically investigate these auxiliary solutions. We also establish the bifurcation structure of the complete periodic solution set.

9.1 Other periodic solution branches

To motivate this section, let us consider the parameter values: $\nu = 0.001$, $J = 0.6$, $F = 1$, $\mu = 0.1$, $\delta = 0$, $\phi = \frac{\pi}{3}$ and $\kappa = 1$. Numerical results for this parameter set from the first order slow flow Eqs. 8.9 and 8.10 are plotted in Fig. 9.1. In Fig. 9.1, in addition to the usual stable-unstable-stable primary branches A-B-C, we see additional stable-unstable branches D-E. As a check, we have also computed these additional periodic solutions from the full nonlinear Eqs. 7.4 and 7.5 (i.e., with no series truncation at all, and incorporating ν, δ and ϕ as above) and plotted some of those using circles (o) in the same figure. Agreement is good enough that for subsequent studies, only the MMS first order slow flow is used.

A representative phase portrait at $\Delta = 2.5$, showing five co-existing solutions including three stable ones, is given in Fig. 9.2. It is clear that the primary stable solutions (marked 1 and 5) are foci in the portrait, while the primary unstable solution, marked 2, is a saddle. The secondary stable solution, marked 4, is also a focus while the secondary unstable solution, marked 3, is a saddle. The secondary focus possesses a significant basin of attraction, and the rotor could quite possibly settle on to that motion.

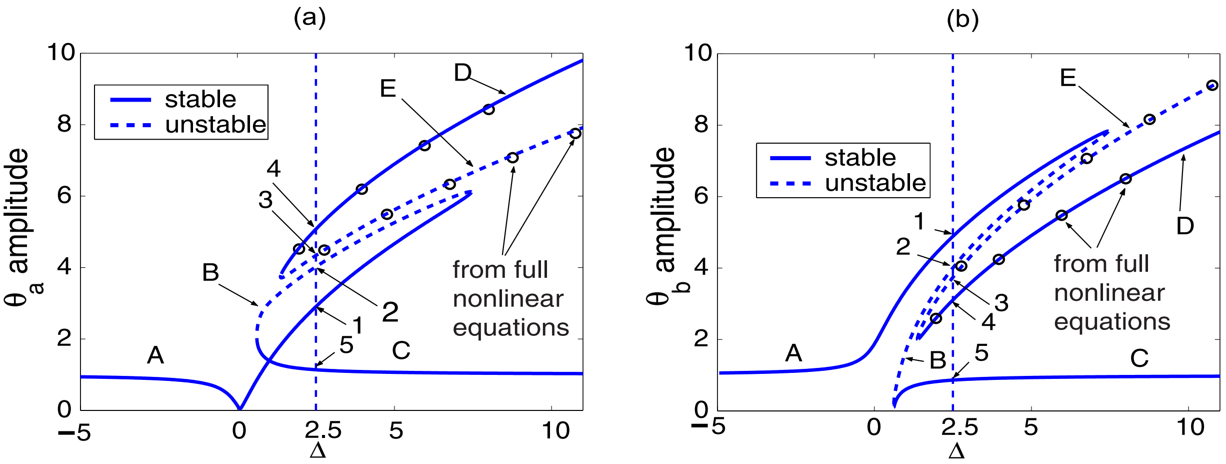

Figure 9.1: Additional periodic solution branches. Parameters: $\nu = 0.001$, $\delta = 0$, $\kappa = 1$, $\mu = 0.1$, $\phi = \frac{\pi}{3}$ and $J = 0.6$.

For higher damping, these additional solution branches recede from the primary branch. For sufficiently large damping, five coexisting periodic solutions are no longer possible. For the parameters considered above, viz., $J = 0.6$, $\mu = 0.1$ and $\kappa = 1$, we plot the various solution branches in the $c_1 - c_2 - \Delta$ space in Fig. 9.3. Marked in the figure, as heavy black dots numbered 1 to 5, are five co-existing solutions at $\Delta = 2.5$.

For larger damping, five coexisting periodic solutions are eventually impossible. This is seen in Fig. 9.4, which shows the primary and additional solution branches for $\mu = 0.4$. All other parameters are the same as for Fig. 9.3.

Conversely, for lower damping, we expect the additional solution branch to exist for values of Δ even closer to zero. To check this, we consider $\mu = 0.00001$ with all other parameters being the same as in Fig. 9.1. The resulting solution branches, this time in $c_1 - c_2 - \Delta$ space, are plotted in Fig. 9.5. For ease of identification, the various branches

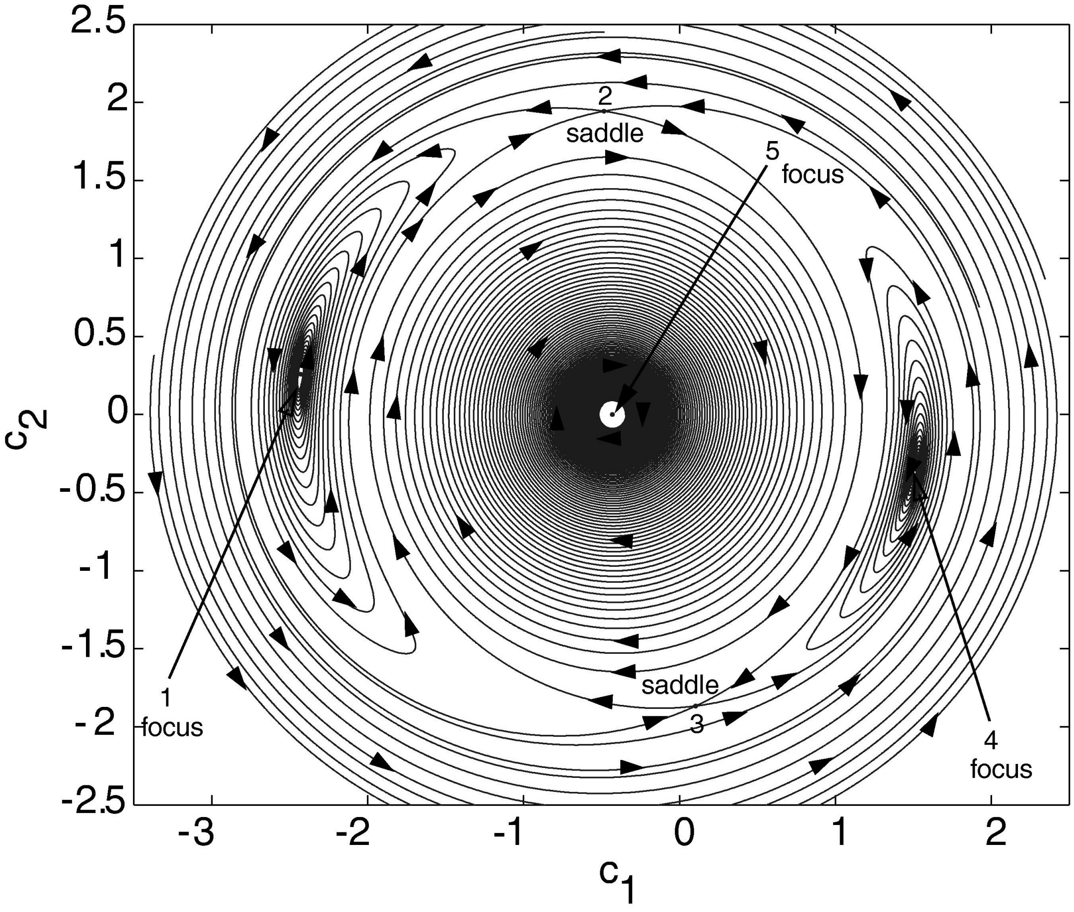

Figure 9.2: Phase portrait illustrating co-existence of 5 periodic solutions. Parameters: $\kappa = 1$, $\mu = 0.1$, $\Delta = 2.5$ and $J = 0.6$.

in Fig. 9.5 have been given the same labels as in Fig. 9.1.

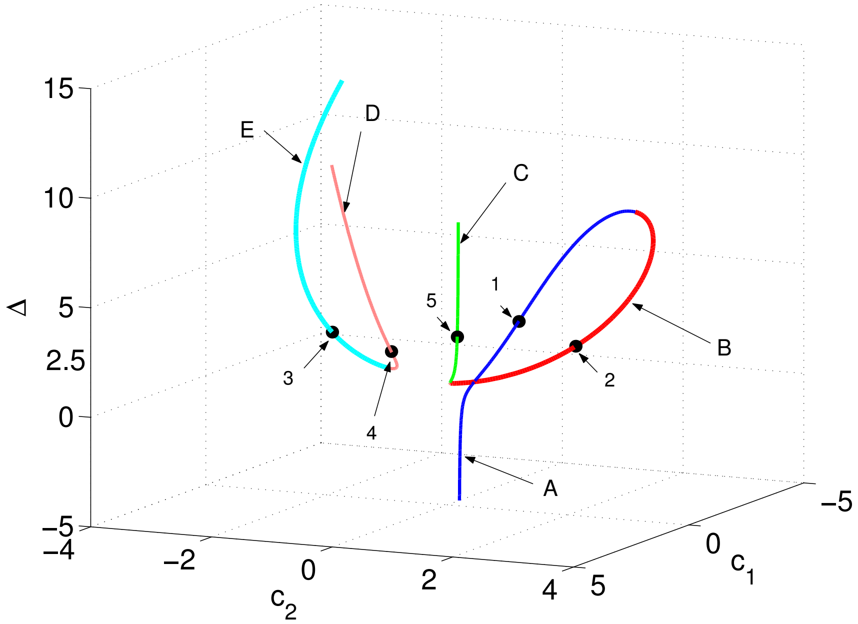

Figure 9.3: Additional periodic solutions. Parameters: $\kappa = 1$, $\mu = 0.1$ and $J = 0.6$.

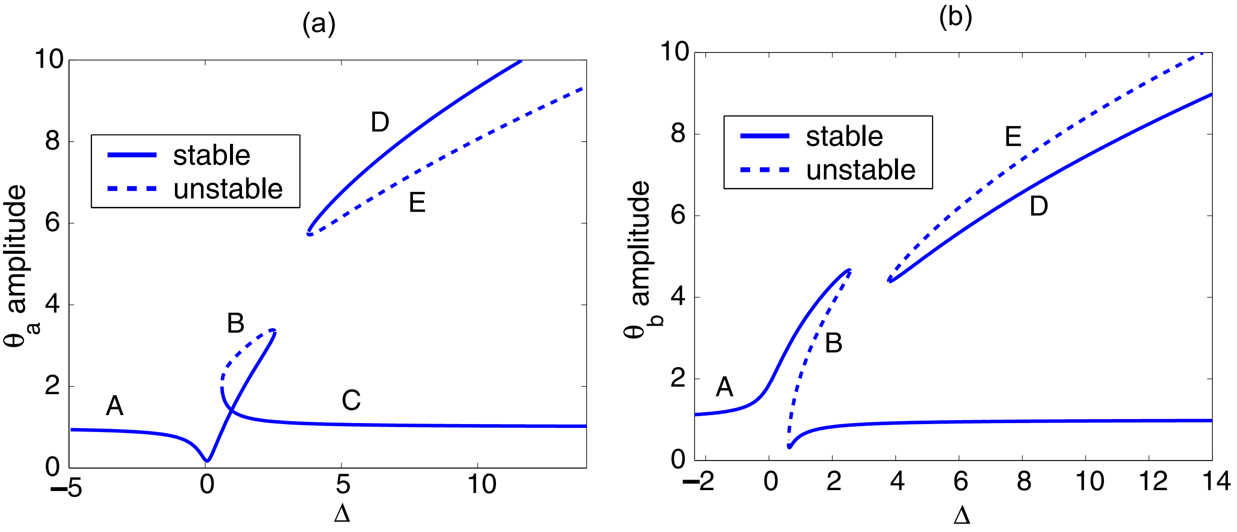

Figure 9.4: Increased damping causes additional solutions to recede. Parameters: $\kappa = 1$, $\mu = 0.4$ and $J = 0.6$.

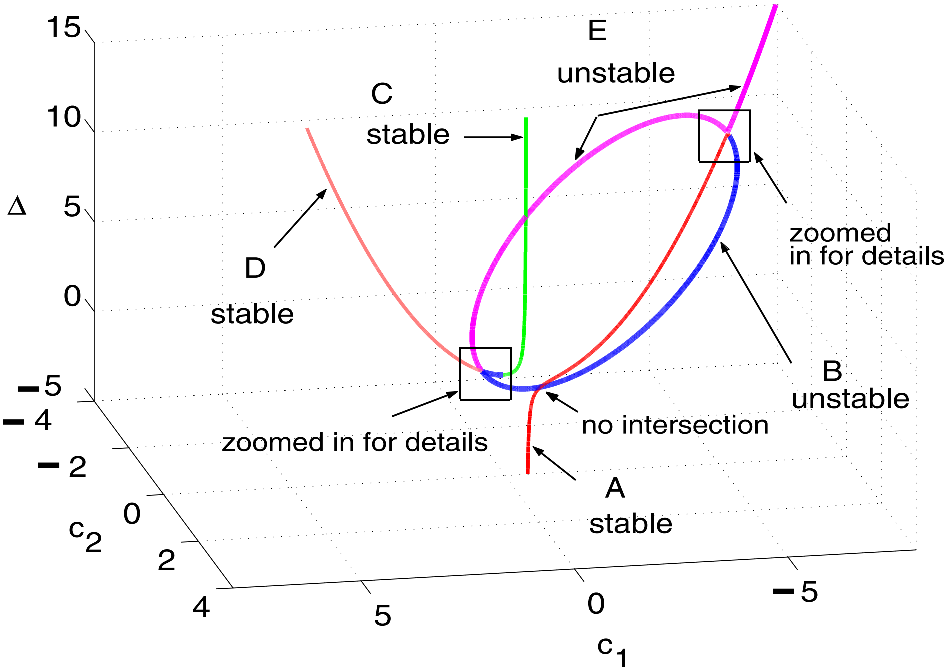

Figure 9.5: Solution branches at low damping showing the bifurcation structure. Parameters: $\kappa = 1$, $\mu = 0.00001$ and $J = 0.6$.

The rest of this chapter is essentially aimed at understanding Fig. 9.5. In the figure, for large negative values of Δ, we only have the solution branch A. For increasing Δ, A merges with branch B in a saddle node bifurcation (see zoomed view of the boxed portion, in Fig. 9.6, right). Following branch B, Δ now decreases until B merges with stable branch C in another saddle node bifurcation. Subsequently, Δ increases indefinitely along C. On the remaining branches shown, which form another single curve, starting along the additional stable branch D for large positive Δ, we encounter a saddle node bifurcation where D merges with unstable branch E (see zoomed view of the boxed portion, in Fig. 9.6, left). Continuing along E, Δ increases indefinitely.

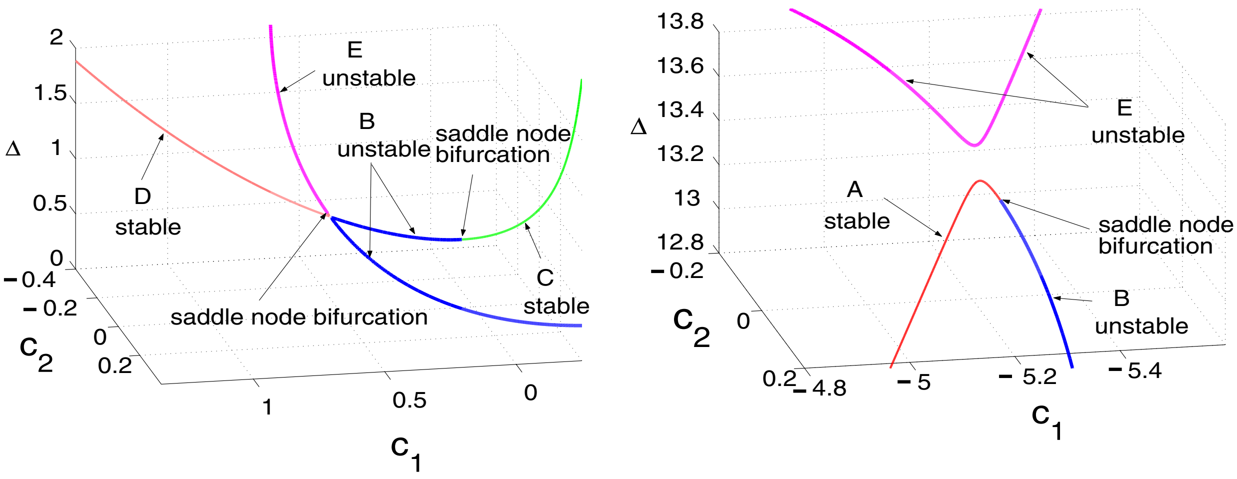

Figure 9.6: Zoomed portions of Fig. 9.5 near bifurcation points. Left: zoomed-in view near junction of branches D and E (left box in Fig. 9.5). Right: zoomed-in view near junction of branches A, B and E (right box in Fig. 9.5).

In Fig. 9.5, it seems that branches E and B are broken halves of an ellipse. We anticipate that with damping $\mu = 0$, these branches do form an ellipse. To verify this, we generate the solution branches for $\mu = 0$ and plot them in Fig. 9.7. In Fig. 9.7, we have used $\kappa = 0$ as well (but see the discussion later, following Eq. 9.5). All other parameters remain the same as for Fig. 9.1.

In Fig. 9.7, the stable branch A remains intact for large negative Δ. However, branch A now loses stability via a subcritical pitchfork bifurcation[1] and continues as branch G. At

---

[1] Note that, for $\mu = 0$, if (c_1, c_2) is a fixed point of Eqs. 8.9 and 8.10, then so is $(c_1, -c_2)$. Nonzero

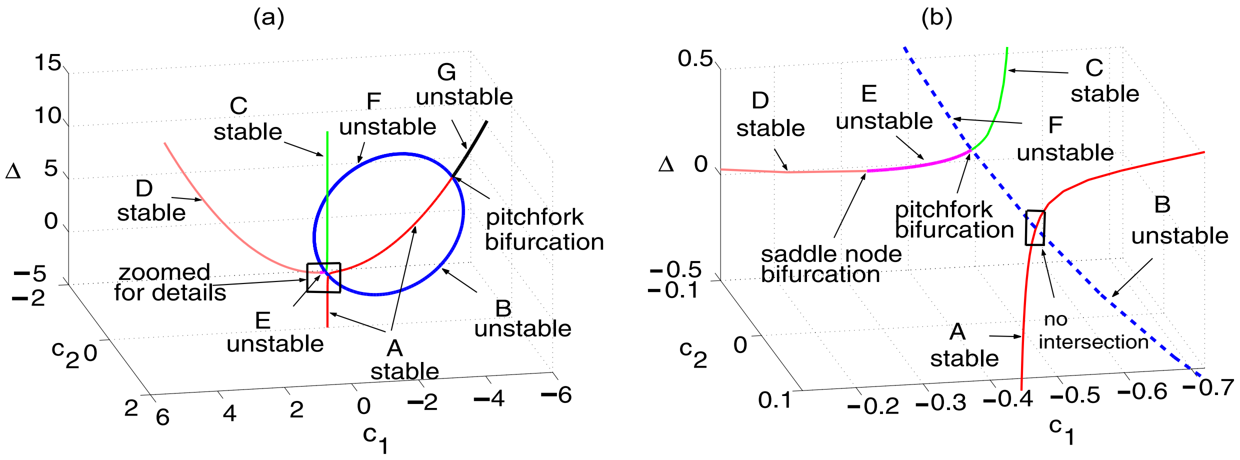

Figure 9.7: Bifurcation diagram for zero damping case. Parameters: $\kappa = 0$, $\mu = 0$ and $J = 0.6$. Left: overall picture. Right: zoomed portion of the overall picture showing bifurcation details.

the pitchfork point, two unstable branches, B and F, which now form a perfect ellipse (as will be demonstrated analytically later), meet branch A.

More interestingly, for large positive Δ, both branches C and D are stable. These branches meet, and also intersect the unstable branches B and F in what appears to be a pitchfork bifurcation. However, this suggests that either branch C or branch D must change stability prior to the pitchfork point, and this is indeed what happens. It is branch D which loses stability via yet another saddle-node bifurcation, changing to unstable branch E. Branch E, after a short distance, gains stability via a pitchfork bifurcation, meeting F and B. Post the pitchfork point, stable branch C emerges. These issues are more clearly seen in the zoomed plot on the right. Representative plots of whirl orbits corresponding to these branches are provided here below.

To graphically depict some whirl orbits, we choose several points as shown in Fig. 9.8. The periodic solutions corresponding to these points are found using the first order solution (see Eq. 8.5). We assume $\nu = 0.001$. Using $\bar{\theta} = \sqrt{\nu}\,\theta$, the physical angles are determined. Subsequently, using the rotation matrices, the coordinates of the center of the disc in the XYZ system are determined (wherein, again, we use length $l = 1$). The

---

damping breaks this symmetry, and breaks the pitchfork.

resulting trace of the whirl orbit on the $X - Y$ plane is plotted for each of the chosen periodic solutions in Fig. 9.9. It is interesting to see that though each orbit is close to circular, there is a large range in amplitudes. It may be noted that not all these solutions are at the same spin speed, because Δ varies from solution to solution. Both Δ, as well as the choice of branch, determine the observed amplitude.

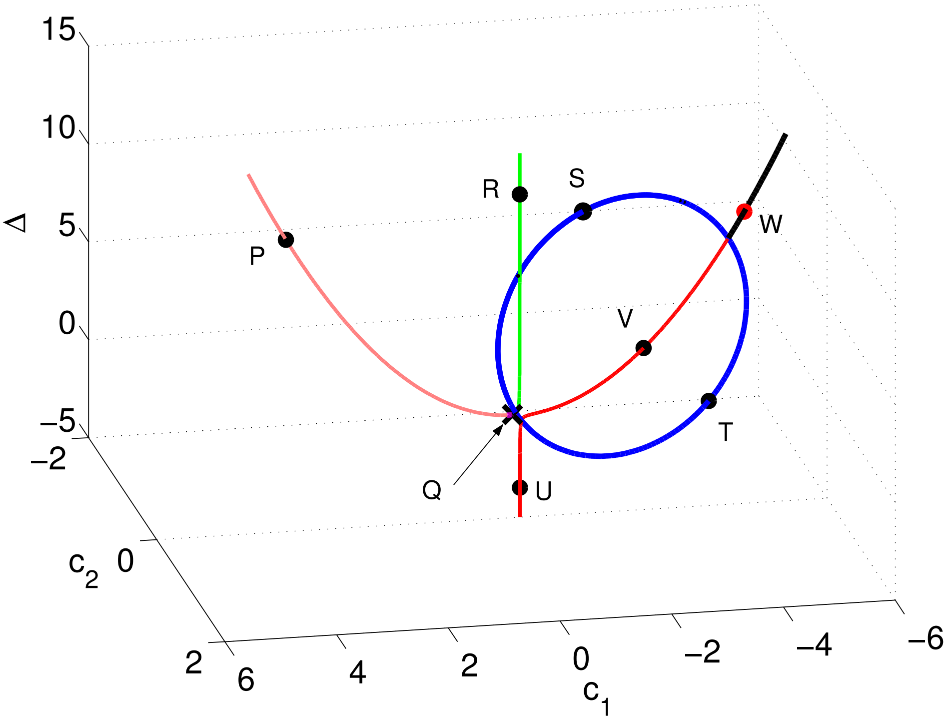

Figure 9.8: Chosen periodic solutions on various branches. Parameters: $\kappa = 0$, $\mu = 0$ and $J = 0.6$.

Finally, note that the branch A is separated from the pitchfork point, and does *not* intersect the ellipse in that region. This gap exists due to the nonzero *forcing* present in the system, and corresponds to the finite width near the base of a resonance peak for any oscillator forced near resonance; that width goes to zero as the damping goes to zero *and* the forcing amplitude goes to zero as well. So also, here, if we let damping *and* gravity go to zero, then the vertical part of A will merge with C (and both will shift sideways to merge with the Δ-axis, representing the trivial or zero solution). Simultaneously, the curved part of A, along with branches D, E and G, will make a perfect parabola (as we will demonstrate indirectly below) in the c_1-Δ plane, also passing through the origin. Finally, the ellipse will

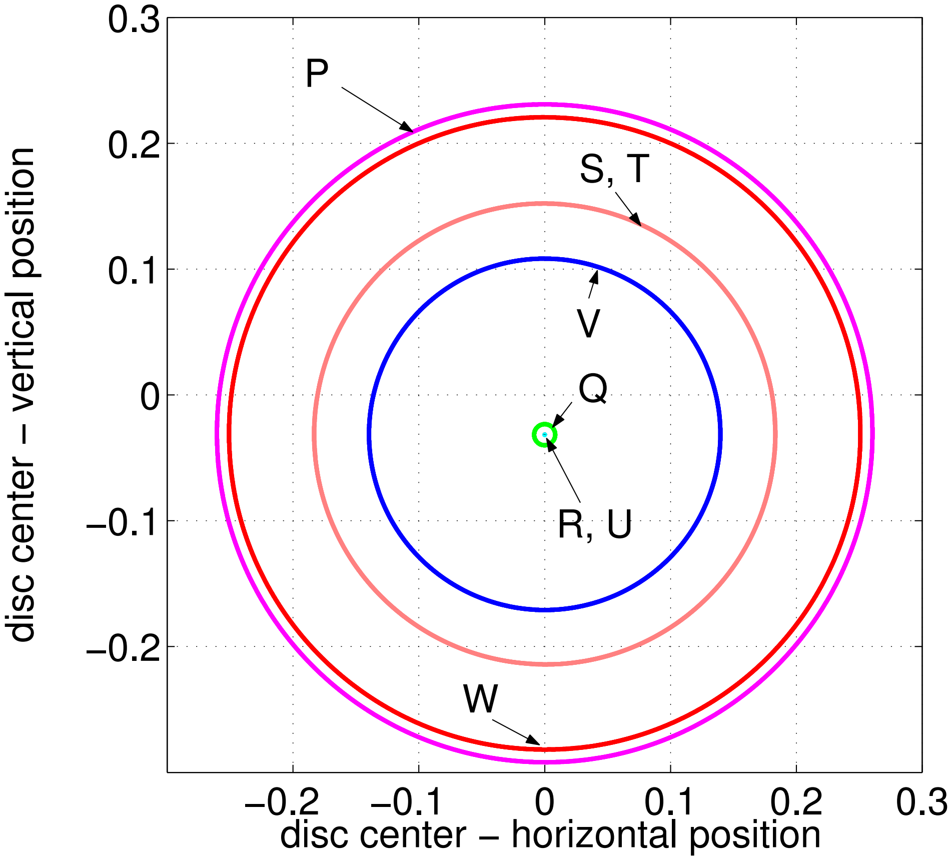

Figure 9.9: XY trace of whirl orbit of disc center corresponding to points P, Q, R, S, T, U, V and W of Fig. 9.8.

become indeterminate and turn into a paraboloid. In this sense, zero damping and small but nonzero gravity may be seen as leading to an imperfect version of three intersecting curves: a straight line, a parabola and an ellipse. Demonstration of the above features requires retaining a gravity forcing parameter F throughout the formulation, leading to longer expressions which we have avoided here (but verified separately). In this work, we have taken gravity as given, and used $F = 1$ after scaling in terms of the small parameter ν.

9.2 Analysis for zero damping

We now analytically consider the undamped case, using the first order slow flow Eqs. 8.9 and 8.10, whose fixed points were plotted for some choice of parameter values in Fig. 9.7. Our aim is to analytically establish the picture described above: that of an imperfect version of three mutually intersecting curves, viz., a straight line, a parabola and an ellipse.

9.2.1 Straight line and parabola ($c_2 = 0$)

We begin by setting $\mu = 0$ in the right hand sides of Eqs. 8.9 and 8.10 and then setting them to zero, obtaining

$$\begin{aligned}\frac{c_2}{2J-8}\Big(&16 + 24\,c_2^2 + 24\,c_1 + 8\,\sqrt{4-2\,J}\Delta\,J - 13\,J + 24\,c_1^2 - 22\,J\,c_2^2 - \\ &22\,J\,c_1^2 - 24\,J\,c_1 - 16\,\sqrt{4-2\,J}\Delta\Big) = 0,\end{aligned} \tag{9.1}$$

$$\begin{aligned}\frac{1}{2J-8}\big(&-6 - 4\,\kappa + 5\,J + 12\,J\,c_2^2 - 24\,c_2^2 c_1 + 23\,J\,c_1 + 36\,J\,c_1^2 + 22\,J\,c_2^2 c_1 + \\ &8\,\sqrt{4-2\,J}\Delta - 36\,c_1^2 - 12\,c_2^2 - 24\,c_1^3 + 22\,J\,c_1^3 - 24\,c_1 + 2\,\kappa\,J + \\ &16\,\sqrt{4-2\,J}\Delta\,c_1 - 4\,\sqrt{4-2\,J}\Delta\,J - 8\,\sqrt{4-2\,J}\Delta\,J\,c_1\Big) = 0.\end{aligned} \tag{9.2}$$

Since Eq. 9.1 is identically satisfied for $c_2 = 0$, Eq. 9.2 with $c_2 = 0$ gives a relation between c_1 and Δ which describes curves in the c_1-Δ plane:

$$\Delta = \frac{-36\,{c_1}^2 - 6 + 22\,J{c_1}^3 - 24\,{c_1}^3 + 23\,Jc_1 + 36\,J{c_1}^2 - 4\,\kappa - 24\,c_1 + 2\,\kappa\,J + 5\,J}{4\sqrt{4-2\,J}\,(J-2)\,(2\,c_1+1)}\,. \tag{9.3}$$

Equation 9.3 describes the curves D, E, A, G and C of Fig. 9.7. In Eq. 9.3, at $c_1 = -\frac{1}{2}$ there is an asymptote parallel to the Δ axis, giving the *straight line* portions of Fig. 9.7. Next, for large c_1, we replace $2c_1 + 1$ in the denominator with $2c_1$, and in the numerator retain only terms cubic in c_1. This gives the *parabola*

$$\Delta = \frac{1}{8}\,\frac{(22\,J - 24){c_1}^2}{\sqrt{4-2\,J}\,(-2+J)}\,. \tag{9.4}$$

As explained above, in the absence of gravity, we would have exactly a straight line and a parabola.

In Eq. 9.4, the coefficient of c_1^2 changes sign as J crosses 12/11, which is within the parameter range of interest ($0 < J < 2$). In Figs. 9.5 and 9.7, we had used $J = 0.6 < 12/11$. For $J > 12/11$, the parabola bends in the opposite direction, as we will illustrate at the end of this section.

9.2.2 Ellipse ($c_2 \neq 0$)

We now turn to the elliptical portion (branches B and F of Fig. 9.7). Here, $c_2 \neq 0$. Accordingly, we consider the expressions within parenthesis in Eqs. 9.1 and 9.2. Eliminating Δ, we find

$$4\,J^2\,c_1^2 + 4\,J^2\,c_2^2 + 8\,J\,(2-J)\,c_1 - 8\,\kappa\,J\,(2-J) + 8\,J - 6\,J^2 = 0\,. \tag{9.5}$$

The quadratic terms have identical positive coefficients, showing that it is in fact a circle (in the projection on to the $\Delta = 0$ plane). Note that κ here adjusts the size of the circle. With a little algebra, it can be shown that the radius of the circle remains positive for all $0 < J < 2$ and $\kappa \geq 0$ (as per our initial assumptions). Thus, the circle remains intact for all parameter values of interest. With some further algebra, c_2^2 can be eliminated between Eqs. 9.1 and 9.2, giving a *linear* relationship between Δ and c_1, showing that nonzero-c_2 solutions lie on some plane. Finally, projecting the above circle, of Eq. 9.5, along the Δ direction onto that plane gives exactly an ellipse (no approximation).

9.2.3 Other results

9.2.3.1 Maximum amplitudes

We can estimate the maximum amplitudes of the primary resonant solutions in the zero damping limit. The results will hold approximately for small damping. In the zero damping case, $c_2 = 0$ for any Δ on the primary resonant solution branch. Thus the corresponding solution amplitude become (see Eq. 8.11)

$$\theta_a = 2\,|c_1 + 1|\,, \qquad \theta_b = 2\,|c_1|\,. \tag{9.6}$$

Maximum amplitude on the primary branch A (see Fig. 9.7), as a function of Δ, is attained at the pitchfork point where the ellipse meets the branch A. The maximum amplitude point can thus be determined by setting $c_2 = 0$ in Eq. 9.5 and solving for c_1. We obtain two values for c_1 namely

$$c_1 = \left(1 - \frac{2}{J}\right) \pm \frac{1}{2\,J}\sqrt{\left(\sqrt{10}J - \frac{12}{\sqrt{10}}\right)^2 + \frac{8}{5} + 8\kappa J(2-J)} \tag{9.7}$$

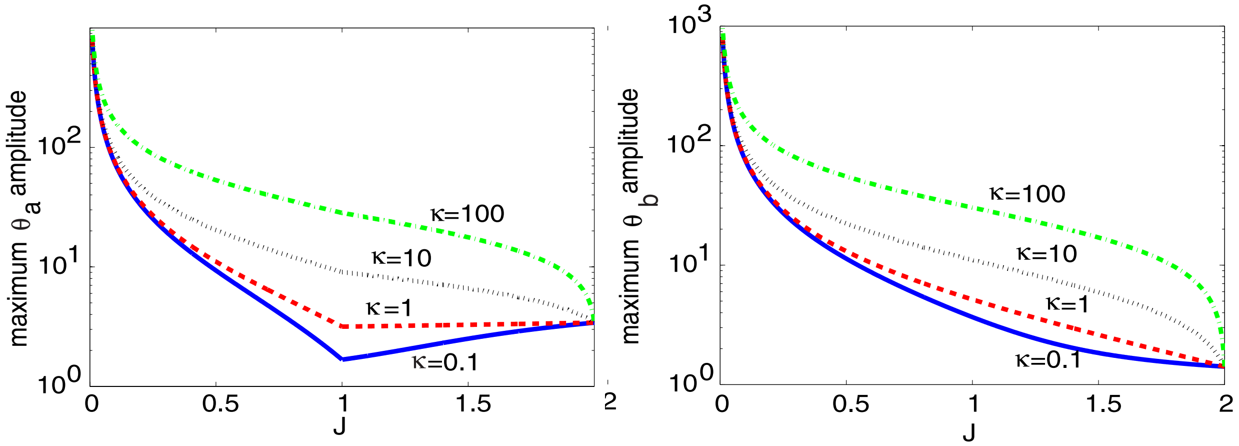

Figure 9.10: Influence of J on maximum amplitudes of θ_a and θ_b, on the primary branch, for zero-damping, and various values of κ. Values plotted should be multiplied by $\sqrt{\nu}$ to obtain actual values.

The first term in the right hand side of Eq. 9.7 is always negative for all permissible values of J. The radical is always clearly real for all $0 \leq J \leq 2$ and $\kappa \geq 0$. Now, it is straightforward to decide from Eq. 9.6 that the maximum amplitude for θ_b is obtained for the choice

$$c_1 = \left(1 - \frac{2}{J}\right) - \frac{1}{2\,J}\sqrt{\left(\sqrt{10}J - \frac{12}{\sqrt{10}}\right)^2 + \frac{8}{5} + 8\kappa J(2-J)}.$$

However, for the θ_a case, the choice of c_1 for the maximum amplitude will depend on J. For $J < 1$, it can be shown that the maximum occurs for

$$c_1 = \left(1 - \frac{2}{J}\right) - \frac{1}{2\,J}\sqrt{\left(\sqrt{10}J - \frac{12}{\sqrt{10}}\right)^2 + \frac{8}{5} + 8\kappa J(2-J)}\,,$$

while for $J > 1$, the maximum occurs for

$$c_1 = \left(1 - \frac{2}{J}\right) + \frac{1}{2\,J}\sqrt{\left(\sqrt{10}J - \frac{12}{\sqrt{10}}\right)^2 + \frac{8}{5} + 8\kappa J(2-J)}\,.$$

The maximum amplitude of θ_a and θ_b as a function of J for various fixed values of κ are plotted in Fig. 9.10 (note that the large values shown are scaled quantities, and actual amplitudes may be reasonable for small ν). It is seen from the figure that for a fixed J, the effect of increasing κ is to increase the maximum amplitudes. The role of J, however, is slightly more complicated. However, decreasing J eventually leads to increasing amplitudes.

9.2.3.2 Some results for $J > 12/11$

We close this section with some final numerical results for $J > 12/11$, so that the change in the bending direction of the parabola described above may be seen. We take $J = 1.25 > 12/11$, in the zero damping limit. Results are plotted in Fig. 9.11. In addition to the change in the parabola's bending direction, there is also movement of the saddle-node bifurcation point between branches D and E (see Fig. 9.7, right). As J approaches 12/11 from below, this bifurcation point moves off to the far left side, taking large positive c_1 values; as J crosses 12/11, this bifurcation point reappears on the far right, i.e., at large negative c_1. Further increases in J bring the saddle-node bifurcation point once again to the vicinity of the pitchfork bifurcation. The stability of major portions of the parabolic branch, as depicted in the figures, reflects this movement of the saddle-node point.

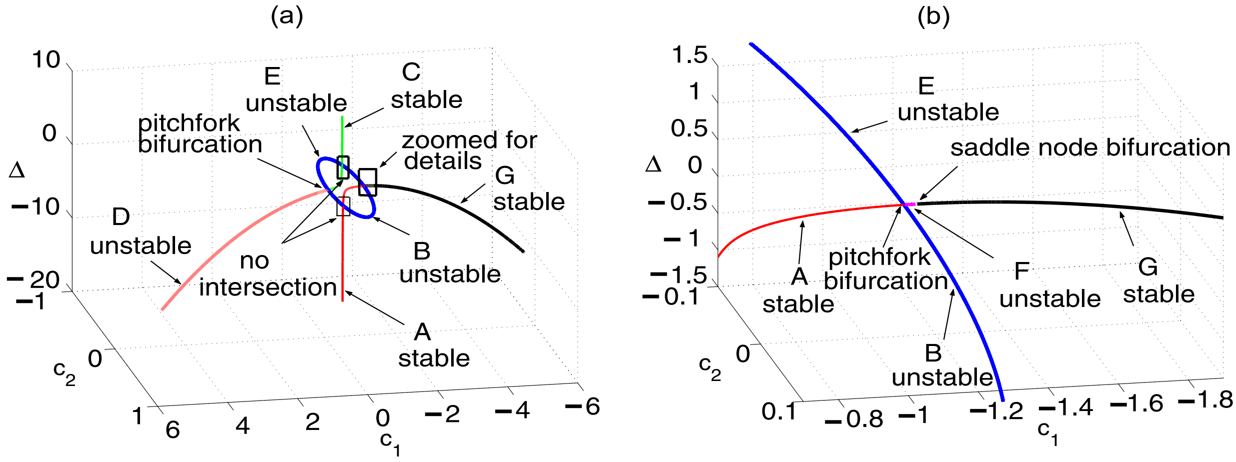

Figure 9.11: Bifurcation diagram for $J > 12/11$, with zero damping, showing the inversion of orientation of branches D, A and G. Parameters: $\kappa = 0$, $\mu = 0$, and $J = 1.25$. Left: overall picture. Right: zoomed portion of left.

9.3 Closing remarks

With this chapter, we conclude our presentation of the fourth problem studied in this thesis.

In this chapter, we have presented a detailed analytical and numerical investigation of the additional branch of periodic solutions based on first order slow flow. We have also established the bifurcation structure of the complete set of periodic solutions. In the three dimensional space of two modal coefficients and a detuning parameter, the full set of periodic solutions is found to be an imperfect version of three mutually intersecting curves: a straight line, a parabola, and an ellipse.

Before closing, we note that in the last problem of this thesis spanning Chapters 7 through 9, we have studied the simplest two degree of freedom system model of an overhung rotor. Future work in this direction may involve the next simplest nonlinear overhung rotor model, where the slender rotor portion is modeled as a beam. Such a model must include at least one more degree of freedom in each plane of bending, bringing in significant new complications.

Acknowledgements

I thank M. Pradeep for the detailed discussions he had with me on several aspects of rotordynamics. I thank him for pointing out this problem of gravity critical speeds and for providing initial directions to this work. I also thank him for providing several useful references.

Chapter 10

Conclusions and future work

The study of the four problems of this thesis is now complete. Conclusions specific to these problems have been presented as appropriate at the ends of the preceding chapters.

In this chapter, we present some general concluding remarks about the range of problems studied in this thesis and the versatility of the MMS in tackling these problems.

The Method of Multiple Scales is a very classical, asymptotic method as suggested by the number of textbooks dealing with the method as well as the huge volume of published papers that use the method. The textbooks on this subject, however, present a potentially misleading picture to the inexperienced reader, suggesting that the range of problems amenable to this method has been fully explored. The problems studied in this thesis serve to illustrate the contrary.

Although the procedural aspects of the method are clear for a vast majority of problems, there are still a variety of interesting applications where the method cannot be applied in a straightforward manner. Some of the relevant issues include dimensionality, scaling and ordering of terms.

Textbooks usually teach us the procedure to apply the MMS to toy problems and known systems. In such situations, the starting system for the MMS analysis, namely an unperturbed system along with small perturbing terms, is available or readily deducible. However, when we are faced with a situation of applying the method to a new physical problem, several decisions have to be taken before the system is at the starting point of application of the method. The major decisions involved might include identification of the small parameter, suitable scaling, ordering of terms, etc. A lot of these decisions are problem-specific. The study on rotors presented in this thesis illustrates many of these issues. A relevant discussion of these issues is also presented in [8].

Also, the MMS procedure is well developed for ODEs. Due to this reason, as well due to interest in lower dimensional dynamics, one often performs suitable lower dimensional projections on a given infinite dimensional system and then applies the MMS on the lower dimensional system. Although this procedure is quite well known for several problems, there do exist applications where it is not straightforward to perform the dimension reduction. The study of the fractional van der Pol oscillator is a case in point. The semi-analytical approach developed therein demonstrated the way to use the MMS on such infinite dimensional systems.

Even after casting the problem in the standard form, the procedure of MMS may be unclear for certain problems. For example, in the third problem of this thesis, studying tool vibrations, the perturbing terms contained large delays. Here, the development of the second order slow flow has novel aspects [31].

Finally, with fast computers, asymptotic methods such as the MMS may seem obsolete. Nevertheless, the MMS remains useful at least for two reasons:

1. Numerical integration of the MMS slow flow proceeds much faster than that of the full equations. Hence parameter studies can be conducted more extensively. The study of the large delay system in this thesis is a typical illustration of the ease of numerical integration provided by the MMS slow flow.
2. The MMS slow flow can be treated analytically in many cases. This gives us valuable insights into the physics of the problem in hand, and also serves as a check on the numerical results. The study on rotors serves to illustrate the usefulness of such analytical investigations.

We close by remarking that there still exists a wide variety of problems of engineering interest to be explored and understood with the aid of this classical method.

Appendix A

Second order slow flow expressions of Eq. 6.4

Amplitude slow flow

For brevity, we write $\gamma \equiv \phi + 2\,z - \phi_{2\,\tau}$. Then,

$$
\begin{aligned}
A_2 = {} & -\frac{1}{8}\,\beta^2 A_{2\,\tau} \sin(\gamma) + \frac{3}{8}\,\lambda\,{A_\tau}^2 \beta\, A_{2\,\tau} \sin(\gamma) + \frac{3}{128}\,\lambda^2 A A_\tau {A_{2\,\tau}}^3 \sin(-3\,\gamma + \psi) + \\
& \frac{3}{32}\,\beta\,\lambda\,{A_{2\,\tau}}^3 \sin(\gamma) - \frac{3}{8}\,\alpha\,\lambda\,A{A_\tau}^2 - \frac{3}{16}\,\alpha\,\lambda\,A^3 + \frac{27}{128}\,\lambda^2 A{A_\tau}^3 A_{2\,\tau} \sin(\gamma + \psi) - \\
& \frac{27}{128}\,\lambda^2 A^2 {A_\tau}^2 A_{2\,\tau} \sin(2\,\psi - \gamma) - \frac{9}{256}\,\lambda^2 A^2 A_\tau {A_{2\,\tau}}^2 \sin(\psi + 2\,\gamma) + \\
& \frac{9}{256}\,\lambda^2 A^2 {A_\tau}^2 A_{2\,\tau} \sin(\gamma + 2\,\psi) + \frac{3}{8}\,\lambda\,A{A_\tau}^2 \beta\, \sin(2\,\psi) - \frac{15}{32}\,\lambda\,A^2 A_\tau \sin(\psi)\beta - \\
& \frac{3}{16}\,\lambda\,A{A_\tau}^2 \cos(2\,\psi)\alpha - \frac{3}{16}\,\beta\, \sin(\psi)\lambda\,A_\tau {A_{2\,\tau}}^2 + \frac{9}{32}\,\lambda^2 A{A_\tau}^2 {A_{2\,\tau}}^2 \sin(-2\,\gamma + 2\,\psi) - \\
& \frac{9}{32}\,\lambda^2 A{A_\tau}^3 A_{2\,\tau} \sin(\psi - \gamma) + \frac{3}{32}\,\beta\,\lambda\,A_\tau {A_{2\,\tau}}^2 \sin(\psi - 2\,\gamma) - \frac{9}{32}\,\lambda^2 A{A_\tau}^2 \sin(2\,\psi) {A_{2\,\tau}}^2 - \\
& \frac{9}{32}\,\lambda^2 A A_\tau {A_{2\,\tau}}^3 \sin(\psi - \gamma) - \frac{27}{128}\,\lambda^2 A^2 A_\tau {A_{2\,\tau}}^2 \sin(\psi - 2\,\gamma) + \\
& \frac{9}{64}\,\lambda^2 A{A_\tau}^3 A_{2\,\tau} \sin(3\,\psi - \gamma) + \frac{9}{16}\,\lambda\,A^2 A_\tau \cos(\psi)\alpha - \frac{9}{128}\,\lambda^2 A{A_\tau}^2 {A_{2\,\tau}}^2 \sin(2\,\gamma) + \\
& \frac{27}{64}\,\lambda^2 A^2 A_\tau {A_{2\,\tau}}^2 \sin(\psi) - \frac{27}{64}\,\lambda^2 A^2 {A_\tau}^2 A_{2\,\tau} \sin(\gamma) + \frac{9}{64}\,\lambda^2 A A_\tau {A_{2\,\tau}}^3 \sin(\gamma + \psi) + \\
& \frac{3}{64}\,\lambda^2 A^2 {A_\tau}^3 \sin(3\,\psi) + \frac{1}{4}\,\beta^2 A_\tau \sin(\psi) + \frac{99}{256}\,\lambda^2 A^2 {A_\tau}^3 \sin(\psi) +
\end{aligned}
$$

$$
\begin{aligned}
&\frac{3}{8}\,\lambda\, A A_{\tau}\beta\, A_{2\,\tau}\sin(\psi-\gamma)+\frac{15}{128}\,\lambda^2 {A_{\tau}}^5\sin(\psi)+\frac{1}{3}\,\lambda^2 {A_{\tau}}^2 A_{2\,\tau}\sin(\gamma)+\\
&\frac{1}{6}\,\lambda^2 A A_{\tau} A_{2\,\tau}\sin(\gamma+\psi)+\frac{3}{256}\,\lambda^2 A^2 {A_{2\,\tau}}^3\sin(3\,\gamma)-\frac{3}{8}\,\beta\,\lambda\, {A_{\tau}}^3\sin(\psi)+\\
&\frac{9}{32}\,\lambda\, A^2\beta\, A_{2\,\tau}\sin(\gamma)+\frac{9}{128}\,\lambda^2 {A_{\tau}}^2 {A_{2\,\tau}}^3\sin(2\,\psi-\gamma)-\frac{1}{12}\,\lambda^2 A {A_{2\,\tau}}^2\sin(2\,\gamma)-\\
&\frac{1}{2}\,\lambda^2 {A_{\tau}}^2 A\sin(2\,\psi)-\frac{45}{256}\,\lambda^2 {A_{\tau}}^4 A_{2\,\tau}\sin(\gamma)-\frac{15}{64}\,\lambda^2 {A_{\tau}}^4 A\sin(2\,\psi)+\\
&\frac{1}{2}\,\lambda^2 {A_{\tau}}^2 A_{2\,\tau}\sin(2\,\psi-\gamma)+\frac{5}{12}\,\lambda^2 A^2 A_{\tau}\sin(\psi)-\frac{1}{12}\,\lambda^2 A_{\tau} {A_{2\,\tau}}^2\sin(\psi-2\,\gamma)-\\
&\frac{3}{256}\,\lambda^2 {A_{\tau}}^2 {A_{2\,\tau}}^3\sin(-3\,\gamma+2\,\psi)+\frac{15}{256}\,\lambda^2 A^4 A_{\tau}\sin(\psi)-\frac{9}{64}\,\lambda^2 {A_{\tau}}^2 {A_{2\,\tau}}^3\sin(\gamma)-\\
&\frac{27}{128}\,\lambda^2 A^2 {A_{2\,\tau}}^3\sin(\gamma)-\frac{1}{2}\,\lambda^2 A_{\tau} {A_{2\,\tau}}^2\sin(\psi)-\frac{15}{128}\,\lambda^2 {A_{\tau}}^2 A^3\sin(2\,\psi)+\\
&\frac{9}{64}\,\lambda^2 {A_{\tau}}^3\sin(\psi) {A_{2\,\tau}}^2-\frac{9}{128}\,\lambda^2 {A_{\tau}}^3 {A_{2\,\tau}}^2\sin(3\,\psi-2\,\gamma)+\frac{3}{16}\,\lambda\, {A_{\tau}}^3\cos(\psi)\alpha-\\
&\frac{27}{256}\,\lambda^2 {A_{\tau}}^3 {A_{2\,\tau}}^2\sin(\psi-2\,\gamma)-\frac{3}{16}\,\lambda\, A A_{\tau}\beta\, A_{2\,\tau}\sin(\gamma+\psi).
\end{aligned}
$$

Phase slow flow

Using γ as above,

$$
\begin{aligned}
\phi_2 = -\frac{1}{768\,A}\,(&-459\,\lambda^2 A^2 {A_\tau}^3 \cos(\psi) + 384\,\lambda^2 A {A_\tau}^2 \cos(2\,\psi) - 64\,\lambda^2 A_\tau {A_{2\tau}}^2 \cos(\psi - 2\,\gamma) + \\
&64\,\lambda^2 A {A_{2\tau}}^2 \cos(2\,\gamma) - 36\,\lambda^2 A^2 {A_\tau}^3 \cos(3\,\psi) + 54\,\lambda^2 A^2 {A_{2\tau}}^3 \cos(\gamma) + 180\,\lambda^2 A {A_\tau}^4 \cos(2\,\psi) + \\
&180\,\lambda^2 A^3 {A_\tau}^2 \cos(2\,\psi) - 9\,\lambda^2 A^2 {A_{2\tau}}^3 \cos(3\,\gamma) - 225\,\lambda^2 A^4 A_\tau \cos(\psi) + 288\,\lambda\, {A_\tau}^3 \cos(\psi)\beta - \\
&81\,\lambda^2 {A_\tau}^3 {A_{2\tau}}^2 \cos(\psi - 2\,\gamma) + 135\,\lambda^2 {A_\tau}^4 A_{2\tau} \cos(\gamma) + 54\,\lambda^2 {A_\tau}^3 {A_{2\tau}}^2 \cos(3\,\psi - 2\,\gamma) - \\
&9\,\lambda^2 {A_\tau}^2 {A_{2\tau}}^3 \cos(-3\,\gamma + 2\,\psi) - 108\,\lambda^2 {A_\tau}^3 \cos(\psi) {A_{2\tau}}^2 - 192\,\beta^2 A_\tau \cos(\psi) - \\
&72\,\beta\,\lambda\, {A_{2\tau}}^3 \cos(\gamma) + 45\,\lambda^2 A^5 + 320\,\lambda^2 A^3 + 96\,\alpha^2 A - 384\,\lambda^2 A {A_{2\tau}}^2 + \\
&384\,\lambda^2 A_\tau \cos(\psi) {A_{2\tau}}^2 + 108\,\lambda^2 {A_\tau}^2 {A_{2\tau}}^3 \cos(\gamma) + 144\,\lambda\, {A_\tau}^3 \sin(\psi)\alpha - \\
&\lambda^2 {A_\tau}^2 {A_{2\tau}}^3 \cos(2\,\psi - \gamma) + 96\,\beta^2 A_{2\tau} \cos(\gamma) + 108\,\lambda^2 A^2 {A_\tau}^2 A_{2\tau} \cos(\gamma) - \\
&108\,\lambda^2 A A_\tau {A_{2\tau}}^3 \cos(\gamma + \psi) - 162\,\lambda^2 A {A_\tau}^3 A_{2\tau} \cos(\gamma + \psi) - 90\,\lambda^2 {A_\tau}^5 \cos(\psi) - \\
&27\,\lambda^2 A^2 {A_\tau}^2 A_{2\tau} \cos(\gamma + 2\,\psi) + 54\,\lambda^2 A^2 {A_\tau}^2 A_{2\tau} \cos(2\,\psi - \gamma) - \\
&54\,\lambda^2 A^2 A_\tau {A_{2\tau}}^2 \cos(\psi - 2\,\gamma) + 54\,\lambda^2 A {A_\tau}^2 {A_{2\tau}}^2 \cos(2\,\gamma) - 288\,\lambda\, A {A_\tau}^2 \beta\, \cos(2\,\psi) - \\
&108\,\lambda^2 A {A_\tau}^3 A_{2\tau} \cos(3\,\psi - \gamma) + 27\,\lambda^2 A^2 A_\tau {A_{2\tau}}^2 \cos(\psi + 2\,\gamma) - 144\,\lambda\, A {A_\tau}^2 \sin(2\,\psi)\alpha - \\
&108\,\lambda^2 A^2 \cos(\psi) A_\tau {A_{2\tau}}^2 + 216\,\lambda^2 A {A_\tau}^2 \cos(2\,\psi) {A_{2\tau}}^2 + 768\, \cos(\psi - \gamma)\lambda^2 A A_\tau A_{2\tau} - \\
&72\,\lambda\, A^2 \beta\, A_{2\tau} \cos(\gamma) + 18\,\lambda^2 A A_\tau {A_{2\tau}}^3 \cos(-3\,\gamma + \psi) + 144\,\lambda\, A^2 \sin(\psi)\alpha\, A_\tau - \\
&128\,\lambda^2 A A_\tau A_{2\tau} \cos(\gamma + \psi) + 504\,\lambda\, A^2 A_\tau \cos(\psi)\beta + 144\,\beta\, \cos(\psi)\lambda\, A_\tau {A_{2\tau}}^2 + \\
&144\,\lambda\, A A_\tau \beta\, A_{2\tau} \cos(\gamma + \psi) + 72\,\beta\,\lambda\, A_\tau {A_{2\tau}}^2 \cos(\psi - 2\,\gamma) - 144\,\beta\, A^3 \lambda - \\
&960\,\lambda^2 A^2 A_\tau \cos(\psi) - 288\,\lambda\, A {A_\tau}^2 \beta + 270\,\lambda^2 A^3 {A_\tau}^2 + 256\,\lambda^2 A {A_\tau}^2 + 135\,\lambda^2 A {A_\tau}^4 + \\
&96\,\beta^2 A - 384\,\lambda^2 {A_\tau}^2 A_{2\tau} \cos(2\,\psi - \gamma) - 256\,\lambda^2 {A_\tau}^2 A_{2\tau} \cos(\gamma) - 288\,\lambda\, {A_\tau}^2 \beta\, A_{2\tau} \cos(\gamma)).
\end{aligned}
$$

Appendix B

System matrices A, B and c for $\alpha = \frac{1}{2}$ of section 5.2.2

$$\mathbf{A} = \left[\begin{array}{c|c} \mathbf{A}_1 & \mathbf{A}_2 \end{array} \right] ,$$

where the sub-matrices $\mathbf{A}_1$ and $\mathbf{A}_2$ are given by

$$\mathbf{A}_1 = \begin{bmatrix}
0.53332 & 0.13333 & 0 & 0 & 0 & 0 & 0 & 0 \\
0.13333 & 0.60601 & 0.16785 & 0 & 0 & 0 & 0 & 0 \\
0 & 0.16785 & 1.1134 & 0.34091 & 0 & 0 & 0 & 0 \\
0 & 0 & 0.34091 & 2.2586 & 0.69253 & 0 & 0 & 0 \\
0 & 0 & 0 & 0.69253 & 4.5653 & 1.4079 & 0 & 0 \\
0 & 0 & 0 & 0 & 1.4079 & 9.1036 & 2.8694 & 0 \\
0 & 0 & 0 & 0 & 0 & 2.8694 & 17.433 & 5.8635 \\
0 & 0 & 0 & 0 & 0 & 0 & 5.8635 & 31.714 \\
0 & 0 & 0 & 0 & 0 & 0 & 0 & 11.758 \\
0 & 0 & 0 & 0 & 0 & 0 & 0 & 0 \\
0 & 0 & 0 & 0 & 0 & 0 & 0 & 0 \\
0 & 0 & 0 & 0 & 0 & 0 & 0 & 0 \\
0 & 0 & 0 & 0 & 0 & 0 & 0 & 0 \\
0 & 0 & 0 & 0 & 0 & 0 & 0 & 0 \\
0 & 0 & 0 & 0 & 0 & 0 & 0 & 0
\end{bmatrix} \times 10^{-2} .$$

$$\mathbf{A}_2 = \begin{bmatrix} 0 & 0 & 0 & 0 & 0 & 0 & 0 \\ 0 & 0 & 0 & 0 & 0 & 0 & 0 \\ 0 & 0 & 0 & 0 & 0 & 0 & 0 \\ 0 & 0 & 0 & 0 & 0 & 0 & 0 \\ 0 & 0 & 0 & 0 & 0 & 0 & 0 \\ 0 & 0 & 0 & 0 & 0 & 0 & 0 \\ 0 & 0 & 0 & 0 & 0 & 0 & 0 \\ 11.758 & 0 & 0 & 0 & 0 & 0 & 0 \\ 60.798 & 22.788 & 0 & 0 & 0 & 0 & 0 \\ 22.788 & 126.73 & 44.709 & 0 & 0 & 0 & 0 \\ 0 & 44.709 & 263.64 & 89.701 & 0 & 0 & 0 \\ 0 & 0 & 89.701 & 539.84 & 181.58 & 0 & 0 \\ 0 & 0 & 0 & 181.58 & 1098.7 & 368.47 & 0 \\ 0 & 0 & 0 & 0 & 368.47 & 2232.6 & 748.19 \\ 0 & 0 & 0 & 0 & 0 & 748.19 & 5986.5 \end{bmatrix} \times 10^{-2}\,.$$

$$\mathbf{B} = \left[\begin{array}{c|c|c} \mathbf{B}_1 & \mathbf{B}_2 & \mathbf{B}_3 \end{array} \right] ,$$

where the sub-matrices $\mathbf{B}_1$, $\mathbf{B}_2$ and $\mathbf{B}_3$ are given by

$$\mathbf{B}_1 = \left[\begin{array}{ccccc}
0.76185e-7 & 0.57142e-7 & 0 & 0 & 0 \\
0.57142e-7 & 0.82838e-6 & 0.41270e-6 & 0 & 0 \\
0 & 0.41270e-6 & 0.66872e-5 & 0.34569e-5 & 0 \\
0 & 0 & 0.34569e-5 & 0.55913e-4 & 0.28950e-4 \\
0 & 0 & 0 & 0.28950e-4 & 0.46481e-3 \\
0 & 0 & 0 & 0 & 0.24225e-3 \\
0 & 0 & 0 & 0 & 0 \\
0 & 0 & 0 & 0 & 0 \\
0 & 0 & 0 & 0 & 0 \\
0 & 0 & 0 & 0 & 0 \\
0 & 0 & 0 & 0 & 0 \\
0 & 0 & 0 & 0 & 0 \\
0 & 0 & 0 & 0 & 0 \\
0 & 0 & 0 & 0 & 0 \\
0 & 0 & 0 & 0 & 0
\end{array} \right] ,$$

$$\mathbf{B}_2 = \begin{bmatrix} 0 & 0 & 0 & 0 & 0 \\ 0 & 0 & 0 & 0 & 0 \\ 0 & 0 & 0 & 0 & 0 \\ 0 & 0 & 0 & 0 & 0 \\ 0.24225e-3 & 0 & 0 & 0 & 0 \\ 0.37802e-2 & 0.20199e-2 & 0 & 0 & 0 \\ 0.20199e-2 & 0.28740e-1 & 0.16575e-1 & 0 & 0 \\ 0 & 0.16575e-1 & 0.19719 & 0.12953 & 0 \\ 0 & 0 & 0.12953 & 1.3903 & 0.97759 \\ 0 & 0 & 0 & 0.97759 & 11.068 \\ 0 & 0 & 0 & 0 & 7.6940 \\ 0 & 0 & 0 & 0 & 0 \\ 0 & 0 & 0 & 0 & 0 \\ 0 & 0 & 0 & 0 & 0 \\ 0 & 0 & 0 & 0 & 0 \end{bmatrix}.$$

$$\mathbf{B}_3 = \begin{bmatrix} 0 & 0 & 0 & 0 & 0 \\ 0 & 0 & 0 & 0 & 0 \\ 0 & 0 & 0 & 0 & 0 \\ 0 & 0 & 0 & 0 & 0 \\ 0 & 0 & 0 & 0 & 0 \\ 0 & 0 & 0 & 0 & 0 \\ 0 & 0 & 0 & 0 & 0 \\ 0 & 0 & 0 & 0 & 0 \\ 0 & 0 & 0 & 0 & 0 \\ 7.6940 & 0 & 0 & 0 & 0 \\ 92.149 & 63.128 & 0 & 0 & 0 \\ 63.128 & 771.56 & 525.92 & 0 & 0 \\ 0 & 525.92 & 6463.0 & 4399.5 & 0 \\ 0 & 4399.5 & 54139 & 36842 & 0 \\ 0 & 0 & 0 & 36842 & 0.11883e7 \end{bmatrix}.$$

$$\mathbf{c} = \begin{bmatrix} 0.66665e-2 \\ 0.90719e-2 \\ 0.16222e-1 \\ 0.32921e-1 \\ 0.66658e-1 \\ 0.13381 \\ 0.26166 \\ 0.49335 \\ 0.95344 \\ 1.9422 \\ 3.9805 \\ 8.1112 \\ 26.488 \\ 33.493 \\ 134.02 \end{bmatrix}$$

Appendix C

System matrices **A**, **B** and **c** for $\alpha = \frac{1}{3}$ of section 5.3.4

$$\mathbf{A} = \left[\begin{array}{c|c} \mathbf{A}_1 & \mathbf{A}_2 \end{array} \right],$$

where the sub-matrices $\mathbf{A}_1$ and $\mathbf{A}_2$ are given by

$$\mathbf{A}_1 = \begin{bmatrix}
2.9838 & 0.49732 & 0 & 0 & 0 & 0 & 0 & 0 \\
0.49732 & 1.8259 & 0.45093 & 0 & 0 & 0 & 0 & 0 \\
0 & 0.45093 & 2.6016 & 0.72323 & 0 & 0 & 0 & 0 \\
0 & 0 & 0.72323 & 4.1678 & 1.1603 & 0 & 0 & 0 \\
0 & 0 & 0 & 1.1603 & 6.6553 & 1.8634 & 0 & 0 \\
0 & 0 & 0 & 0 & 1.8634 & 10.498 & 3.0031 & 0 \\
0 & 0 & 0 & 0 & 0 & 3.0031 & 15.972 & 4.8685 \\
0 & 0 & 0 & 0 & 0 & 0 & 4.8685 & 23.279 \\
0 & 0 & 0 & 0 & 0 & 0 & 0 & 7.7851 \\
0 & 0 & 0 & 0 & 0 & 0 & 0 & 0 \\
0 & 0 & 0 & 0 & 0 & 0 & 0 & 0 \\
0 & 0 & 0 & 0 & 0 & 0 & 0 & 0 \\
0 & 0 & 0 & 0 & 0 & 0 & 0 & 0 \\
0 & 0 & 0 & 0 & 0 & 0 & 0 & 0 \\
0 & 0 & 0 & 0 & 0 & 0 & 0 & 0
\end{bmatrix} \times 10^{-2}\,.$$

$$\mathbf{A}_2 = \begin{bmatrix} 0 & 0 & 0 & 0 & 0 & 0 & 0 \\ 0 & 0 & 0 & 0 & 0 & 0 & 0 \\ 0 & 0 & 0 & 0 & 0 & 0 & 0 \\ 0 & 0 & 0 & 0 & 0 & 0 & 0 \\ 0 & 0 & 0 & 0 & 0 & 0 & 0 \\ 0 & 0 & 0 & 0 & 0 & 0 & 0 \\ 0 & 0 & 0 & 0 & 0 & 0 & 0 \\ 7.7851 & 0 & 0 & 0 & 0 & 0 & 0 \\ 35.924 & 12.033 & 0 & 0 & 0 & 0 & 0 \\ 12.033 & 59.934 & 18.732 & 0 & 0 & 0 & 0 \\ 0 & 18.732 & 99.000 & 29.720 & 0 & 0 & 0 \\ 0 & 0 & 29.720 & 160.33 & 47.525 & 0 & 0 \\ 0 & 0 & 0 & 47.525 & 257.78 & 76.162 & 0 \\ 0 & 0 & 0 & 0 & 76.162 & 413.67 & 122.12 \\ 0 & 0 & 0 & 0 & 0 & 122.12 & 675.85 \end{bmatrix} \times 10^{-2}\,.$$

$$\mathbf{B} = \left[\begin{array}{c|c|c} \mathbf{B}_1 & \mathbf{B}_2 & \mathbf{B}_3 \end{array} \right] ,$$

where the sub-matrices $\mathbf{B}_1$, $\mathbf{B}_2$ and $\mathbf{B}_3$ are given by

$$\mathbf{B}_1 = \begin{bmatrix} 0.29840e-6 & 0.19890e-6 & 0 & 0 & 0 \\ 0.19890e-6 & 0.23939e-5 & 0.10928e-5 & 0 & 0 \\ 0 & 0.10928e-5 & 0.15157e-4 & 0.72285e-5 & 0 \\ 0 & 0 & 0.72285e-5 & 0.10009e-3 & 0.47806e-4 \\ 0 & 0 & 0 & 0.47806e-4 & 0.65734e-3 \\ 0 & 0 & 0 & 0 & 0.31599e-3 \\ 0 & 0 & 0 & 0 & 0 \\ 0 & 0 & 0 & 0 & 0 \\ 0 & 0 & 0 & 0 & 0 \\ 0 & 0 & 0 & 0 & 0 \\ 0 & 0 & 0 & 0 & 0 \\ 0 & 0 & 0 & 0 & 0 \\ 0 & 0 & 0 & 0 & 0 \\ 0 & 0 & 0 & 0 & 0 \\ 0 & 0 & 0 & 0 & 0 \end{bmatrix} ,$$

$$\mathbf{B}_2 = \begin{bmatrix} 0 & 0 & 0 & 0 & 0 \\ 0 & 0 & 0 & 0 & 0 \\ 0 & 0 & 0 & 0 & 0 \\ 0 & 0 & 0 & 0 & 0 \\ 0.31599e-3 & 0 & 0 & 0 & 0 \\ 0.42296e-2 & 0.20832e-2 & 0 & 0 & 0 \\ 0.20832e-2 & 0.25558e-1 & 0.13557e-1 & 0 & 0 \\ 0 & 0.13557e-1 & 0.14058 & 0.84424e-1 & 0 \\ 0 & 0 & 0.84424e-1 & 0.79767 & 0.50780 \\ 0 & 0 & 0 & 0.50780 & 5.0766 \\ 0 & 0 & 0 & 0 & 3.1701 \\ 0 & 0 & 0 & 0 & 0 \\ 0 & 0 & 0 & 0 & 0 \\ 0 & 0 & 0 & 0 & 0 \\ 0 & 0 & 0 & 0 & 0 \end{bmatrix}.$$

$$\mathbf{B}_3 = \begin{bmatrix} 0 & 0 & 0 & 0 & 0 \\ 0 & 0 & 0 & 0 & 0 \\ 0 & 0 & 0 & 0 & 0 \\ 0 & 0 & 0 & 0 & 0 \\ 0 & 0 & 0 & 0 & 0 \\ 0 & 0 & 0 & 0 & 0 \\ 0 & 0 & 0 & 0 & 0 \\ 0 & 0 & 0 & 0 & 0 \\ 0 & 0 & 0 & 0 & 0 \\ 3.1701 & 0 & 0 & 0 & 0 \\ 33.533 & 20.568 & 0 & 0 & 0 \\ 20.568 & 222.01 & 135.35 & 0 & 0 \\ 0 & 135.35 & 1469.0 & 894.20 & 0 \\ 0 & 0 & 894.20 & 9717.6 & 5913.0 \\ 0 & 0 & 0 & 5913.0 & 71572 \end{bmatrix}.$$

$$\mathbf{c} = \begin{bmatrix} 0.34811e-1 \\ 0.27742e-1 \\ 0.37757e-1 \\ 0.60513e-1 \\ 0.96970e-1 \\ 0.15365 \\ 0.23843 \\ 0.35932 \\ 0.55743 \\ 0.90700 \\ 1.4745 \\ 2.3757 \\ 3.8147 \\ 6.1195 \\ 11.442 \end{bmatrix}$$

Appendix D

Eigenvalues of matrix R of section 5.4

S.no.	Eigenvalues
1	-15152
2	-1823.7
3	-436.38
4	-105.97
5	-25.911
6	-6.4124
7	-1.5669
8	-0.38985
9	-0.10726
10	-0.028716
11	-0.0073348
12	-0.0018231
13	-0.00010295
14	-0.00044621
15	-0.000010250
16	i
17	$-i$

Appendix E

Eigenvalues of M of section 5.3, and validity of the MMS

In this appendix we consider an important, but peripheral, question related to the second problem of the thesis, studied in Chapter 5.

In our van der Pol oscillator with fractional damping in Chapter 5, we observed that the MMS slow flow gives useful approximations to direct numerical simulations for relatively large deviations from the Hopf bifurcation, i.e., for relatively large values of ϵ (see, for e.g., Fig. 5.7). Now, because it is an asymptotic method, good MMS approximations are guaranteed only for sufficiently small values of the small parameter ϵ. In this light, the success of MMS, as seen in the results of Chapter 5, deserve some explanation which we attempt to provide here.

The fractional order operator has a continuous spectrum. Accordingly, its Galerkin approximation also introduces several long time scales represented by the small eigenvalues of the matrix **M** of Chapter 5. A list of the eigenvalues of **M** (see Eq. 5.17), for the case of $\alpha = 1/2$, at the Hopf point $(\bar{\mu}, \beta) = (0.60856, 1)$ is provided in Table E.1. We notice from Table E.1 that apart from the purely imaginary eigenvalues, we have 15 eigenvalues which are progressively decreasing in magnitude. These 15 eigenvalues arise from the internal degrees of freedom represented by Eq. 5.15. For an increased order of Galerkin approximation, as reflected in the sizes of the matrices **A**, **B** and **c**, we will get a similar hierarchy of eigenvalues starting from large negative ones to very small negative ones (close

Table E.1: List of eigenvalues of **M** at the Hopf point $(\bar{\mu}, \beta) = (0.60856, 1)$

S.no.	Eigenvalues
1	-20446
2	-2461.0
3	-588.86
4	-143.00
5	-34.965
6	-8.6531
7	-2.1144
8	-0.52607
9	-0.14473
10	-0.038750
11	-0.0098978
12	-0.0024601
13	-0.00060213
14	-0.00013892
15	-0.000013831
16	$1.3494\,i$
17	$-1.3494\,i$

to zero). The large negative eigenvalues represent very short time scales and affect the dynamics in the initial instants, whereas the very small eigenvalues may, perhaps, influence the dynamics at longer time scales. Now, for a fixed choice of matrices **A**, **B** and **c**, the minimum eigenvalue is a small, but technically $\mathcal{O}(1)$ quantity. Thus, for a given choice of approximation matrices, we could choose ϵ sufficiently small (much smaller than the smallest eigenvalue) in our numerical simulations to obtain good MMS approximations. However, in the simulations of Chapter 5, we obtained good results for relatively large values of the parameter ϵ. For example, in our simulations related to Fig. 5.3 we had used $\epsilon = 0.01$, while the smallest eigenvalue, as seen from Table E.1, is about 700 times smaller. A rigorous explanation of this observation may involve a deeper study of the properties of the fractional order operator. We avoid such a study in this work. However, in what follows, we give an informal, numerical explanation for the success of our MMS approximations.

Numerical justification of validity of the MMS

We consider the van der Pol oscillator with fractional damping studied in Chapter 5:

$$\ddot{x} + \frac{2}{\pi}\,\mathbf{c}^T\mathbf{a} + \mu\,\dot{x}\,(x^2 - 1) + x = 0\,, \tag{E.1}$$

$$\mathbf{A}\dot{\mathbf{a}} + \mathbf{B}\mathbf{a} = \mathbf{c}\dot{x}\,. \tag{E.2}$$

In Eq. E.1, x represents the primary dynamic quantity of interest; and **a**, whose dynamics is governed by Eq. E.2, represent internal degrees of freedom. These internal degrees of freedom are indirectly excited by the main dynamics. The response of these internal variables feeds back to the main system. This feedback is represented by the term $\frac{2}{\pi}\,\mathbf{c}^T\mathbf{a}$ of Eq. E.1, and constitutes the source of energy dissipation.

Now, the number of internal or hidden variables is equal to the size of the matrices **A**, **B** and **c**. We expect these internal variables to be excited to varied levels and in turn influence the main dynamics to varied extents.

To see this more explicitly, we introduce modal coordinates for the **a**-system and thus have $\mathbf{a} = \mathbf{E}\mathbf{z}$, where **E** is the modal matrix whose columns comprise unit norm eigenvectors of $-\mathbf{A}^{-1}\mathbf{B}$, and **z** is the vector of modal coordinates. The eigenvalues of $-\mathbf{A}^{-1}\mathbf{B}$ are listed in Table E.2. It is clear from Table E.2 that these eigenvalues are only slightly different from the first 15 eigenvalues of Table E.1. The successive columns of **E** are the unit norm eigenvectors of the corresponding eigenvalues in the sequence as presented in Table E.2.

Rewriting Eqs. E.1 and E.2 in terms of modal coordinates of **a**-subsystem, we get

$$\ddot{x} + \frac{2}{\pi}\,\mathbf{c}^T\mathbf{E}\mathbf{z} + \mu\,\dot{x}\,(x^2 - 1) + x = 0\,, \tag{E.3}$$

$$\dot{\mathbf{z}} = -\mathbf{E}^{-1}\mathbf{A}^{-1}\mathbf{B}\mathbf{E}\mathbf{z} + \mathbf{E}^{-1}\mathbf{A}^{-1}\mathbf{c}\dot{x}\,. \tag{E.4}$$

In Eq. E.4, $\mathbf{E}^{-1}\mathbf{A}^{-1}\mathbf{c}$ represents the typical modal forcing vector. For the choice of

Table E.2: List of eigenvalues of $-\mathbf{A}^{-1}\mathbf{B}$

S.no.	Eigenvalues
1	−20446
2	−2461.0
3	−588.88
4	−143.04
5	−35.039
6	−8.7900
7	−2.3906
8	−0.62843
9	−0.16698
10	−0.042151
11	−0.010344
12	−0.0025153
13	−0.00060882
14	−0.00013975
15	−0.000013897

matrices in this paper, this forcing vector is

$$\mathbf{E}^{-1}\mathbf{A}^{-1}\mathbf{c} = \begin{bmatrix} -2.3016 \\ -1.3680 \\ 1.3514 \\ -1.3552 \\ -1.3669 \\ -1.3934 \\ -1.4191 \\ -1.4024 \\ -1.3641 \\ -1.3457 \\ -1.3404 \\ 1.3378 \\ -1.1977 \\ -1.3130 \\ -1.3281 \end{bmatrix} \tag{E.5}$$

As seen from Eq. E.5, the forcing is of a similar magnitude for all degrees of freedom, and is $\mathcal{O}(1)$; hence, the nominal modal response is also expected to be $\mathcal{O}(1)$ (could be smaller).

Now, we compute the contribution of each of these modes to the fed-back component, represented $\mathbf{c}^T\mathbf{E}\mathbf{z}$, on the main system. We have

$$(\mathbf{c}^T\mathbf{E})^T = \begin{bmatrix} -118.99 \\ -26.805 \\ 12.718 \\ -6.2274 \\ -3.0261 \\ -1.4479 \\ -0.70176 \\ -0.36982 \\ -0.20301 \\ -0.10612 \\ -0.053282 \\ 0.026399 \\ -0.0062187 \\ -0.0071270 \\ -0.013160 \end{bmatrix}. \tag{E.6}$$

Thus we see that the contribution of the various modes to the fed-back component, causing dissipation, is progressively decreasing and becomes quite small for the small eigenvalues which could potentially influence the dynamics on large time scales. Thus the presence of very small eigenvalues do not influence the dynamics as much as the large eigenvalues. The large eigenvalues are anyway active over short time scales only and do not affect the dynamics on the long time scales over which we seek the MMS approximations.

We have thus presented a numerical justification for the MMS procedure implemented in this paper. However, our arguments are not rigorous and a satisfactory treatment of these issues is left for future work.

Appendix F

$\mathcal{O}(\nu)$ and $\mathcal{O}(\nu^2)$ terms of Eq. 8.1

$$
\begin{aligned}
N_{11} = {} & 4\,\sqrt{4-2\,J}\Delta\,\cos(\tau)J - 8\,\sqrt{4-2\,J}\Delta\,\cos(\tau) + 2\,\delta\,J\cos(-2\,\phi+\tau) - \\
& 4\,\delta\,\cos(-2\,\phi+\tau) + \delta\,\dot{\theta}_b\,J\cos(2\,\phi) + \delta\,J\dot{\theta}_a\,\sin(2\,\phi) - 2\,\delta\,\dot{\theta}_a\,\sin(2\,\phi) - \\
& 4\,\sqrt{4-2\,J}\Delta\,\theta_a\,J + \delta\,\theta_b\,J\sin(2\,\phi) + 2\,\kappa\,\theta_a\,J + \\
& 8\,\sqrt{4-2\,J}\Delta\,\theta_a - 2\,\delta\,\theta_b\,\sin(2\,\phi) - 2\,\delta\,\dot{\theta}_b\,\cos(2\,\phi) + 2\,\delta\,\theta_a\,\cos(2\,\phi) - \\
& \delta\,J\theta_a\,\cos(2\,\phi) - 4\,\kappa\,\theta_a.
\end{aligned}
$$

$$
\begin{aligned}
N_{12} = {} & -4\,\delta\,\sin(-2\,\phi+\tau) + 2\,\delta\,J\sin(-2\,\phi+\tau) + 8\,\sqrt{4-2\,J}\Delta\,\sin(\tau) - \\
& 4\,\sqrt{4-2\,J}\Delta\,\sin(\tau)J - 4\,\sqrt{4-2\,J}\Delta\,\theta_b\,J + \delta\,J\theta_a\,\sin(2\,\phi) + \delta\,\theta_b\,J\cos(2\,\phi) + \\
& 4\,\kappa\,\theta_b - \delta\,\dot{\theta}_b\,J\sin(2\,\phi) + \delta\,J\dot{\theta}_a\,\cos(2\,\phi) - 2\,\kappa\,\theta_b\,J + 8\,\sqrt{4-2\,J}\Delta\,\theta_b - \\
& 2\,\delta\,\theta_a\,\sin(2\,\phi) - 2\,\delta\,\theta_b\,\cos(2\,\phi) - 2\,\delta\,\dot{\theta}_a\,\cos(2\,\phi) + \\
& 2\,\delta\,\dot{\theta}_b\,\sin(2\,\phi).
\end{aligned}
$$

$$
\begin{aligned}
N_{21} = {} & -2\,\cos(\tau){\theta_a}^2 + 4\,\theta_b\,\sin(\tau)\theta_a - 2\,\theta_b\,\sin(\tau)\theta_a\,J + \cos(\tau){\theta_a}^2 J + \frac{1}{2}\,\dot{\theta}_b\,J{\theta_b}^2 - \\
& {\theta_b}^2\dot{\theta}_b + 2\,\dot{\theta}_b\,J{\theta_a}^2 + \dot{\theta}_b^2 J\theta_a - 2\,\dot{\theta}_b\,{\theta_a}^2 + \frac{2}{3}\,J{\theta_a}^3 + J\theta_a\,{\theta_b}^2 - \dot{\theta}_b^2\theta_a - \frac{2}{3}\,{\theta_a}^3 - \\
& \theta_a\,{\theta_b}^2.
\end{aligned}
$$

$$
\begin{aligned}
N_{22} = {} & -2\,{\theta_a}^2\sin(\tau) - 2\,{\theta_a}^2\sin(\tau)J^2 + 5\,{\theta_a}^2\sin(\tau)J - {\theta_b}^2\sin(\tau)J + 2\,{\theta_b}^2\sin(\tau) - \\
& \frac{2}{3}\,{\theta_b}^3 - 2\,\dot{\theta}_b\,J\theta_a\,\dot{\theta}_a + 2\,\dot{\theta}_b\,\theta_a\,\dot{\theta}_a - \frac{1}{2}\,J\dot{\theta}_a\,{\theta_b}^2 - {\theta_a}^2 J^2\dot{\theta}_a + \dot{\theta}_a\,{\theta_b}^2 + 5\,J\theta_b\,{\theta_a}^2 - \\
& {\theta_a}^2 J^2\theta_b + J\dot{\theta}_a\,{\theta_a}^2 - 4\,{\theta_a}^2\theta_b + \frac{2}{3}\,J{\theta_b}^3.
\end{aligned}
$$

$$
\begin{aligned}
N_{31} = {} & -\frac{1}{3}\, J\theta_a\, {\theta_b}^4 - \delta\, {\theta_b}^2 \cos(2\,\phi+\tau) + \delta\, {\theta_b}^2 \cos(2\,\phi-\tau) + \delta\, {\theta_a}^2 \cos(2\,\phi-\tau) - \\
& \frac{1}{12}\, \cos(\tau){\theta_a}^4 J + 48\,\Delta^2\theta_a\, J + \delta^2 J\theta_a + {\theta_b}^2\dot{\theta}_b\, {\theta_a}^2 - \dot{\theta}_b\, J\delta^2 - 12\,\Delta^2\theta_a\, J^2 - \\
& \frac{2}{3}\, \dot{\theta}_b^2 J{\theta_a}^3 - \frac{2}{3}\, {\theta_b}^3 \sin(\tau)\theta_a - \frac{4}{3}\, \delta\, {\theta_b}^3 \sin(2\,\phi) + 4\,\Delta\, \mu\, \dot{\theta}_a + 12\,\Delta^2 \cos(\tau) J^2 - \\
& 2\,\delta^2 \cos(\tau) J - 48\,\Delta^2 \cos(\tau) J - \frac{2}{3}\, \dot{\theta}_b\, J{\theta_a}^4 - \frac{2}{3}\, \theta_b\, \sin(\tau){\theta_a}^3 + \delta\, {\theta_a}^2 \cos(2\,\phi+\tau) \\
& + \frac{4}{3}\, \delta\, {\theta_a}^3 \cos(2\,\phi) - \frac{2}{3}\, J{\theta_a}^3{\theta_b}^2 - 4\,\sqrt{4-2\,J}\Delta\, \delta\, J \cos(2\,\phi-\tau) + \\
& 8\,\sqrt{4-2\,J}\Delta\, \delta\, \cos(2\,\phi-\tau) - {\theta_a}^2 J^2\theta_b\, \delta\, \sin(2\,\phi) - 2\,\delta\, \dot{\theta}_b\, \theta_b\, \theta_a\, \sin(2\,\phi) - \\
& 2\,\delta\, \dot{\theta}_b\, J\theta_a\, \dot{\theta}_a\, \sin(2\,\phi) + \frac{1}{2}\, J{\theta_a}^2\delta\, \dot{\theta}_a\, \sin(2\,\phi) - \frac{1}{2}\, \delta\, J\dot{\theta}_a\, {\theta_b}^2 \sin(2\,\phi) - \\
& \frac{1}{2}\, \delta\, \dot{\theta}_b\, J{\theta_b}^2 \cos(2\,\phi) - 2\,\delta\, \dot{\theta}_b\, J{\theta_a}^2 \cos(2\,\phi) - {\theta_a}^2 J^2\dot{\theta}_a\, \delta\, \sin(2\,\phi) - \\
& \dot{\theta}_b^2\delta\, J\theta_a\, \cos(2\,\phi) + \delta\, \dot{\theta}_a\, {\theta_b}^2 \sin(2\,\phi) - \frac{5}{2}\, \delta\, {\theta_a}^2 J \cos(2\,\phi+\tau) + \\
& 4\,\sqrt{4-2\,J}\Delta\, \theta_b\, \sin(\tau)\theta_a\, J + \frac{9}{2}\, \delta\, \theta_b\, J{\theta_a}^2 \sin(2\,\phi) - 4\,\sqrt{4-2\,J}\Delta\, \delta\, \theta_b\, J \sin(2\,\phi) \\
& - 2\,\delta\, \theta_b\, \kappa\, J \sin(2\,\phi) + 48\,\Delta^2 \cos(\tau) + 4\,\sqrt{4-2\,J}\Delta\, \delta\, \theta_a\, J \cos(2\,\phi) - \\
& 8\,\sqrt{4-2\,J}\Delta\, \delta\, \theta_a\, \cos(2\,\phi) + \delta\, \theta_b\, \theta_a\, J \sin(2\,\phi+\tau) + \delta\, J^2{\theta_a}^2 \cos(2\,\phi+\tau) + \\
& 2\,\dot{\theta}_b^2\delta\, \theta_a\, \cos(2\,\phi) + \delta\, \dot{\theta}_a\, {\theta_a}^2 \sin(2\,\phi) + 4\,\delta\, \dot{\theta}_b\, {\theta_a}^2 \cos(2\,\phi) - \dot{\theta}_b\, J{\theta_b}^2{\theta_a}^2 + \\
& \delta\, {\theta_b}^2\dot{\theta}_b\, \cos(2\,\phi) - \frac{1}{24}\, \dot{\theta}_b\, J{\theta_b}^4 - 2\,\delta\, \kappa\, \theta_a\, J \cos(2\,\phi) - 2\,\sqrt{4-2\,J}\Delta\, \cos(\tau){\theta_a}^2 J - \\
& 8\,\sqrt{4-2\,J}\Delta\, \theta_b\, \sin(\tau)\theta_a + 2\,\delta\, \dot{\theta}_b\, \theta_a\, \dot{\theta}_a\, \sin(2\,\phi) - \delta\, \theta_b\, \theta_a\, J \sin(2\,\phi-\tau) - \\
& \delta\, J\theta_a\, {\theta_b}^2 \cos(2\,\phi) + 8\,\sqrt{4-2\,J}\Delta\, \delta\, \theta_b\, \sin(2\,\phi) - 4\,\sqrt{4-2\,J}\Delta\, \kappa\, \theta_a\, J + \\
& \frac{3}{2}\, \delta\, {\theta_a}^2 J \cos(2\,\phi-\tau) + \frac{1}{3}\, \theta_b\, \sin(\tau){\theta_a}^3 J + \frac{1}{3}\, {\theta_b}^3 \sin(\tau)\theta_a\, J + \\
& 4\,\sqrt{4-2\,J}\Delta\, \cos(\tau){\theta_a}^2 + \frac{1}{2}\, \delta\, {\theta_b}^2 J \cos(2\,\phi+\tau) - 2\,\delta\, \theta_b\, \theta_a\, \sin(2\,\phi+\tau) - \\
& \frac{1}{2}\, \delta\, {\theta_b}^2 J \cos(2\,\phi-\tau) + \frac{2}{15}\, {\theta_a}^5 + \sqrt{4-2\,J}\delta\, \mu\, \dot{\theta}_a\, \cos(2\,\phi) - \\
& \sqrt{4-2\,J}\delta\, \mu\, \dot{\theta}_b\, \sin(2\,\phi) + 8\,\sqrt{4-2\,J}\Delta\, \kappa\, \theta_a + 4\,\delta\, \theta_b\, \kappa\, \sin(2\,\phi) + \\
& \frac{2}{3}\, \delta\, J{\theta_b}^3 \sin(2\,\phi) - 3\,\delta\, \theta_b\, {\theta_a}^2 \sin(2\,\phi) + 2\,\delta\, \theta_a\, {\theta_b}^2 \cos(2\,\phi) + \\
& 2\,\delta\, \theta_b\, \theta_a\, \sin(2\,\phi-\tau) - \delta\, J^2{\theta_a}^2 \cos(2\,\phi-\tau) - 2\,\Delta\, \mu\, \dot{\theta}_a\, J - \frac{2}{3}\, \delta\, J{\theta_a}^3 \cos(2\,\phi) + \\
& 4\,\delta\, \kappa\, \theta_a\, \cos(2\,\phi) + \frac{1}{6}\, \cos(\tau){\theta_a}^4 - 48\,\Delta^2\theta_a + \frac{2}{3}\, {\theta_a}^3{\theta_b}^2 - 2\,\delta^2\theta_a + \frac{1}{3}\, \theta_a\, {\theta_b}^4 - \\
& \frac{2}{15}\, J{\theta_a}^5 + \frac{2}{3}\, \dot{\theta}_b^2{\theta_a}^3 + \frac{2}{3}\, \dot{\theta}_b\, {\theta_a}^4 + \frac{1}{12}\, {\theta_b}^4\dot{\theta}_b + 2\,\delta^2\dot{\theta}_b + 4\,\delta^2 \cos(\tau).
\end{aligned}
$$

$$
\begin{aligned}
N_{32} = {} & -\frac{5}{3}\,{\theta_a}^4 J^2 \dot{\theta}_a + \frac{2}{3}\,\dot{\theta}_b\,{\theta_a}^3 \dot{\theta}_a + 4\,\Delta\,\mu\,\dot{\theta}_b + {\theta_b}^2 \sin(\tau) {\theta_a}^2 + \frac{61}{12}\,{\theta_a}^4 \sin(\tau) J + \\
& \delta\,{\theta_b}^2 \sin(-2\,\phi+\tau) + \delta^2 J \theta_b - \frac{17}{3}\,{\theta_a}^4 J^2 \theta_b + 2/3\,J {\theta_b}^3 {\theta_a}^2 + 48\,\Delta^2 \theta_b\,J + \\
& 4\,{\theta_a}^2 \kappa\,\theta_b + \delta^2 J \dot{\theta}_a + \frac{1}{12}\,{\theta_b}^4 \sin(\tau) J - \frac{4}{3}\,\delta\,{\theta_a}^3 \sin(2\,\phi) + \\
& 8\,\sqrt{4-2\,J}\Delta\,\delta\,\sin(-2\,\phi+\tau) - 4\,\sqrt{4-2\,J}\Delta\,\delta\,J \sin(-2\,\phi+\tau) + \\
& \delta\,J \theta_a\,{\theta_b}^2 \sin(2\,\phi) - \delta\,\theta_b\,\theta_a\,J \cos(-2\,\phi+\tau) - 4\,\sqrt{4-2\,J}\Delta\,\delta\,\theta_a\,J \sin(2\,\phi) + \\
& 8\,\sqrt{4-2\,J}\Delta\,\delta\,\theta_a\,\sin(2\,\phi) + \delta\,\theta_b\,\theta_a\,J \cos(2\,\phi+\tau) + \\
& 4\,\sqrt{4-2\,J}\Delta\,{\theta_a}^2 \sin(\tau) J^2 - {\theta_a}^2 J^2 \delta\,\sin(2\,\phi+\tau) + \delta\,\dot{\theta}\,{\theta_b}^2 \cos(2\,\phi) - \\
& \delta\,\dot{\theta}_a^2 \theta_a\,\sin(2\,\phi) - 2\,\delta\,\dot{\theta}_a\,{\theta_a}^2 \cos(2\,\phi) - \dot{\theta}_b^2 \delta\,\theta_a\,\sin(2\,\phi) - \frac{1}{2}\,\delta\,{\theta_b}^2 J \sin(2\,\phi+\tau) + \\
& \frac{2}{3}\,\delta\,J {\theta_b}^3 \cos(2\,\phi) - \delta\,J^2 {\theta_a}^3 \sin(2\,\phi) - 6\,{\theta_a}^2 \kappa\,\theta_b\,J - 8\,\sqrt{4-2\,J}\Delta\,\kappa\,\theta_b + \\
& 4\,\delta\,\theta_b\,\kappa\,\cos(2\,\phi) + \frac{5}{2}\,\delta\,J {\theta_a}^2 \sin(2\,\phi+\tau) + 8\,\sqrt{4-2\,J}\Delta\,\delta\,\theta_b\,\cos(2\,\phi) - \\
& 2\,{\theta_a}^2 J^2 \theta_b\,\delta\,\cos(2\,\phi) + \frac{2}{15}\,{\theta_b}^5 - 48\,\Delta^2 \theta_b + 7\,\delta\,\theta_b\,J {\theta_a}^2 \cos(2\,\phi) - \\
& 12\,\sqrt{4-2\,J}\Delta\,{\theta_a}^2 \theta_b\,J + 4\,\sqrt{4-2\,J}\Delta\,\kappa\,\theta_b\,J + 4\,\sqrt{4-2\,J}\Delta\,{\theta_a}^2 \sin(\tau) - \\
& 3\,{\theta_a}^2 J^2 \delta\,\sin(-2\,\phi+\tau) - \frac{1}{2}\,\delta\,{\theta_b}^2 J \sin(-2\,\phi+\tau) + {\theta_b}^2 \sin(\tau) {\theta_a}^2 J^2 - \\
& \delta\,{\theta_a}^2 \sin(-2\,\phi+\tau) + 2\,\delta\,\kappa\,\theta_a\,J \sin(2\,\phi) + 4\,\sqrt{4-2\,J}\Delta\,{\theta_a}^2 \theta_b\,J^2 - \\
& 2\,\delta\,\theta_b\,\kappa\,J \cos(2\,\phi) - 4\,\sqrt{4-2\,J}\Delta\,{\theta_b}^2 \sin(\tau) - \frac{5}{2}\,{\theta_b}^2 \sin(\tau) {\theta_a}^2 J - \\
& 4\,\delta\,\kappa\,\theta_a\,\sin(2\,\phi) + 2\,\delta\,\theta_b\,\theta_a\,\cos(-2\,\phi+\tau) - 2\,\delta\,\theta_b\,\theta_a\,\cos(2\,\phi+\tau) - \\
& \sqrt{4-2\,J}\delta\,\mu\,\dot{\theta}_a\,\sin(2\,\phi) - \sqrt{4-2\,J}\delta\,\mu\,\dot{\theta}_b\,\cos(2\,\phi) + \frac{1}{2}\,{\theta_a}^2 J^2 \dot{\theta}_a\,{\theta_b}^2 - \\
& \frac{8}{3}\,\dot{\theta}_b\,J {\theta_a}^3 \dot{\theta}_a + 2\,\dot{\theta}_b\,{\theta_a}^3 J^2 \dot{\theta}_a - \frac{1}{12}\,\dot{\theta}_a\,{\theta_b}^4 - \delta\,{\theta_b}^2 \dot{\theta}_b\,\sin(2\,\phi) - \frac{1}{6}\,{\theta_b}^4 \sin(\tau) + \\
& \frac{19}{6}\,\delta\,J {\theta_a}^3 \sin(2\,\phi) - 2\,\delta\,\theta_b\,{\theta_a}^2 \cos(2\,\phi) + 8\,\sqrt{4-2\,J}\Delta\,{\theta_a}^2 \theta_b + 2\,{\theta_a}^2 \kappa\,\theta_b\,J^2 - \\
& 3\,\delta\,\theta_a\,{\theta_b}^2 \sin(2\,\phi) - \delta\,\dot{\theta}_b\,{\theta_a}^2 \sin(2\,\phi) - \sqrt{4-2\,J}{\theta_a}^2 \mu\,\dot{\theta}_b - \frac{1}{2}\,J \dot{\theta}_a\,{\theta_b}^2 {\theta_a}^2 - \\
& \frac{2}{15}\,J {\theta_b}^5 - 2\,\delta^2 \theta_b - \frac{8}{3}\,{\theta_a}^4 \theta_b - \frac{1}{2}\,\delta\,\dot{\theta}_b\,J {\theta_a}^2 \sin(2\,\phi) - 2\,{\theta_a}^2 J^2 \dot{\theta}_a\,\delta\,\cos(2\,\phi) + \\
& 3\,J {\theta_a}^2 \delta\,\dot{\theta}_a\,\cos(2\,\phi) + \sqrt{4-2\,J}{\theta_a}^2 \mu\,\dot{\theta}_b\,J + \dot{\theta}_b^2 \delta\,J \theta_a\,\sin(2\,\phi) + \\
& \delta\,\dot{\theta}_b\,J^2 {\theta_a}^2 \sin(2\,\phi) + \frac{1}{2}\,\delta\,\dot{\theta}_b\,J {\theta_b}^2 \sin(2\,\phi) + 2\,\delta\,\dot{\theta}_a\,\theta_b\,\theta_a\,\sin(2\,\phi) - \\
& \frac{1}{2}\,\delta\,J \dot{\theta}_a\,{\theta_b}^2 \cos(2\,\phi) - 2\,\delta\,\dot{\theta}_b\,J \theta_a\,\dot{\theta}_a\,\cos(2\,\phi) - 4\,\sqrt{4-2\,J}\Delta\,\delta\,\theta_b\,J \cos(2\,\phi) -
\end{aligned}
$$

$$
\begin{aligned}
&10\sqrt{4-2J}\Delta\,{\theta_a}^2\sin(\tau)J + 2\sqrt{4-2J}\Delta\,{\theta_b}^2\sin(\tau)J + \\
&\frac{13}{2}\,\delta\,J{\theta_a}^2\sin(-2\,\phi+\tau) + 48\,\Delta^2\sin(\tau)J + 2\,\delta^2\sin(\tau)J - 12\,\Delta^2\sin(\tau)J^2 - \\
&12\,\Delta^2\theta_b\,J^2 + \frac{1}{24}\,J\dot{\theta}_a\,{\theta_b}^4 + 2\,{\theta_a}^4\sin(\tau)J^3 + {\theta_a}^4J^3\dot{\theta}_a + {\theta_a}^4J^3\theta_b + \frac{2}{3}\,J\dot{\theta}_a\,{\theta_a}^4 - \\
&4\,\delta^2\sin(\tau) - 2\,\delta^2\dot{\theta}_a + \delta\,{\theta_b}^2\sin(2\,\phi+\tau) - \delta\,{\theta_a}^2\sin(2\,\phi+\tau) - \frac{19}{3}\,{\theta_a}^4\sin(\tau)J^2 + \\
&\frac{22}{3}\,J\theta_b\,{\theta_a}^4 - 48\,\Delta^2\sin(\tau) - \frac{2}{3}\,{\theta_a}^2J^2{\theta_b}^3 - \frac{4}{3}\,\delta\,{\theta_b}^3\cos(2\,\phi) - \frac{5}{6}\,{\theta_a}^4\sin(\tau) - \\
&2\,\Delta\,\mu\,\dot{\theta}_b\,J.
\end{aligned}
$$

Appendix G

Second order MMS on Eq. 8.2

In Chapter 8, we developed the MMS slow flow for the study of the overhung rotor model near its gravity critical speed. We have actually proceeded to derive the slow flow equations upto second order in this thesis. In this appendix, we present the derivation of the second order slow flow equations for Eq. 8.2.

Let us first quickly recall the first order calculation. We have

$$\frac{\partial \mathbf{X}_0}{\partial T_0} = \mathbf{M}\mathbf{X}_0 + (2-J)\left\{\begin{array}{c} 0 \\ 1 \\ 0 \\ i \end{array}\right\} e^{iT_0} + (2-J)\left\{\begin{array}{c} 0 \\ 1 \\ 0 \\ -i \end{array}\right\} e^{-iT_0}, \tag{G.1}$$

where the matrix $\mathbf{M}$ is given in Chapter 8, and has eigenvalues $i, -i, i(J-3), -i(J-3)$. Further, at $\mathcal{O}(\nu)$ we have

$$\frac{\partial \mathbf{X}_1}{\partial T_0} - \mathbf{M}\mathbf{X}_1 = -\frac{\partial \mathbf{X}_0}{\partial T_1} + \mathbf{H}(\mathbf{X}_0, T_0), \tag{G.2}$$

where $\mathbf{H}$ is the same as in Eq. 8.2. After substitution of the assumed solution (see Eq. 8.5) at the first order, Eq. G.2 becomes

$$\frac{\partial \mathbf{X}_1}{\partial T_0} - \mathbf{M}\mathbf{X}_1 = \mathbf{U}(T_1,T_2)e^{iT_0} + \bar{\mathbf{U}}(T_1,T_2)e^{-iT_0} + \mathbf{V}(T_1,T_2)e^{3iT_0} + \bar{\mathbf{V}}(T_1,T_2)e^{-3iT_0}, \tag{G.3}$$

and the solvability conditions (explained in Chapter 8) yield the first order slow flow:

$$\begin{aligned}\frac{\partial c_1}{\partial T_1} &= \frac{1}{2J-8}\Big(16\,c_2+24\,c_2^3+24\,c_2c_1+8\,\sqrt{4-2\,J}\Delta\,J\,c_2-13\,J\,c_2+24\,c_1^2c_2- \\ &\qquad 22\,J\,c_1^2c_2-24\,J\,c_2c_1-16\,\sqrt{4-2\,J}\Delta\,c_2+2\,\sqrt{4-2\,J}\mu\,c_1+ \\ &\qquad \sqrt{4-2\,J}\mu\Big)\,, \end{aligned} \tag{G.4}$$

$$\begin{aligned}\frac{\partial c_2}{\partial T_1} &= \frac{1}{2J-8}\big(-6-4\,\kappa+5\,J+12\,J\,c_2^2-24\,c_2^2c_1+23\,J\,c_1+36\,J\,c_1^2+22\,J\,c_2^2c_1 \\ &\qquad +8\,\sqrt{4-2\,J}\Delta-36\,c_1^2-12\,c_2^2-24\,c_1^3+22\,J\,c_1^3-24\,c_1+2\,\kappa\,J \\ &\qquad 16\,\sqrt{4-2\,J}\Delta\,c_1-4\,\sqrt{4-2\,J}\Delta\,J+2\,\sqrt{4-2\,J}\mu\,c_2- \\ &\qquad 8\,\sqrt{4-2\,J}\Delta\,J\,c_1\Big)\,. \end{aligned} \tag{G.5}$$

To proceed to second order, we need to solve Eq. G.3 subject to the solvability conditions of Eqs. G.4 and G.5. To that end, substitution of Eqs. G.4 and G.5 into the right hand side of Eq. G.3 eliminates the secular-terms-causing portions of $\mathbf{U}e^{iT_0}$. Other, non-secular but resonant, terms remain. Thus Eq. G.3 takes the form

$$\frac{\partial \mathbf{X}_1}{\partial T_0}-\mathbf{M}\mathbf{X}_1=\mathbf{U}_1(T_1,T_2)e^{iT_0}+\bar{\mathbf{U}}_1(T_1,T_2)e^{-iT_0}+\mathbf{V}(T_1,T_2)e^{3iT_0}+\bar{\mathbf{V}}(T_1,T_2)e^{-3iT_0}\,, \tag{G.6}$$

where resonant forcing from the right hand side has now been eliminated by incorporating the first order slow flow. It may be emphasized, for those readers not familiar with the multidimensional version of the MMS, that in multidimensional cases $\mathbf{U}_1$ can indeed be nonzero without causing secular terms.

Thus Eq. G.6, like Eq. G.1, is resonantly forced yet has bounded responses. As before, the particular solution has a non-unique portion which can be absorbed into the complementary solution. Here, we will drop the complementary part and retain only a particular solution of the form

$$\mathbf{X}_1=\mathbf{u}(T_1,T_2)e^{iT_0}+\bar{\mathbf{u}}(T_1,T_2)e^{-iT_0}+\mathbf{v}(T_1,T_2)e^{3iT_0}+\bar{\mathbf{v}}(T_1,T_2)e^{-3iT_0}\,. \tag{G.7}$$

To that end, substituting the above into Eq. G.6, the unknown vectors $\mathbf{u}(T_1,T_2)$ and $\mathbf{v}(T_1,T_2)$ are solved for. The solution for $\mathbf{u}$ contains an arbitrary component along the right eigenvector corresponding to eigenvalue i; and here we simply take that arbitrary component to be zero (for justification see, e.g., page 53 of [3], page 121 of [185], and the discussion in [31]).

At $\mathcal{O}(\nu^2)$, we have long equations of the form

$$\frac{\partial \mathbf{X}_2}{\partial T_0} - \mathbf{M}\mathbf{X}_2 = -\frac{\partial \mathbf{X}_0}{\partial T_2} - \frac{\partial \mathbf{X}_1}{\partial T_1} + \frac{\partial \mathbf{H}(\mathbf{X}_0, T_0)}{\partial \mathbf{X}_0}\mathbf{X}_1 + \mathbf{W}(\mathbf{X}_0, T_0), \tag{G.8}$$

where $\mathbf{W}$ is the same as in Eq. 8.2. The above equation, after using Eq. G.4, G.5 and G.7, becomes

$$\begin{aligned}\frac{\partial \mathbf{X}_2}{\partial T_0} - \mathbf{M}\mathbf{X}_2 &= \mathbf{U}_2(T_1, T_2)e^{iT_0} + \bar{\mathbf{U}}_2(T_1, T_2)e^{-iT_0} + \\ &\quad \mathbf{V}_2(T_1, T_2)e^{3iT_0} + \bar{\mathbf{V}}_2(T_1, T_2)e^{-3iT_0} + \\ &\quad \mathbf{Z}(T_1, T_2)e^{5iT_0} + \bar{\mathbf{Z}}(T_1, T_2)e^{-5iT_0}. \end{aligned} \tag{G.9}$$

In Eq. G.9, we have resonant forcing from $\mathbf{U}_2(T_1, T_2)e^{iT_0}$. Eliminating secular terms as before, we get equations of the form

$$\frac{\partial c_1}{\partial T_2} = \frac{n_1}{d_1},$$

$$\frac{\partial c_2}{\partial T_2} = \frac{n_2}{d_2}.$$

The full expressions for the right sand sides above are:

$$
\begin{aligned}
n_1 = {} & 141312\,\mu\,\Delta\,J^2c_1 - 19200\,J^6{c_2}^3c_1 - 14688\,J^4c_1\,\sqrt{4-2\,J}\mu+\\
& 24\,\sqrt{4-2\,J}\mu\,\kappa\,J^5 + 129024\,J^4{c_1}^2\sqrt{4-2\,J}\Delta\,c_2 - 506880\,J^3c_1\,c_2\,\sqrt{4-2\,J}\Delta+\\
& 984\,J^5c_1\,{c_2}^2\sqrt{4-2\,J}\mu + 96\,\delta\,J^5{c_1}^2\sin(2\,\phi) - 27648\,J^5{c_1}^2\sqrt{4-2\,J}\Delta\,c_2-\\
& 10656\,J^4c_1\,{c_2}^2\sqrt{4-2\,J}\mu + 72528\,J^3{c_1}^2\sqrt{4-2\,J}\mu + 24576\,{c_1}^3c_2-\\
& 578560\,J^2{c_1}^4c_2 - 6912\,\mu^2c_2\,J - 2061312\,J^2{c_1}^3c_2 + 662016\,J{c_1}^2c_2+\\
& 220032\,J^4c_1\,c_2\,\sqrt{4-2\,J}\Delta + 167648\,J^5{c_1}^2{c_2}^3 - 279552\,J^3{c_1}^2\sqrt{4-2\,J}\Delta\,c_2-\\
& 5568\,\mu^2c_2\,J^3 + 568320\,\Delta^2J^3c_2 + 285696\,J^2{c_2}^3\sqrt{4-2\,J}\Delta+\\
& 1536\,\sqrt{4-2\,J}\Delta\,J^6c_2 - 10752\,\delta\,J^2c_1\,\sin(2\,\phi) + 1435520\,J^3{c_2}^3{c_1}^2-\\
& 73728\,\Delta\,\mu\,Jc_1 + 54816\,J^3c_1\,\sqrt{4-2\,J}\mu + 132096\,\mu\,\Delta\,J^2-\\
& 110592\,J{c_2}^3\sqrt{4-2\,J}\Delta + 48384\,J{c_1}^2\sqrt{4-2\,J}\mu + 156672\,c_1\,c_2\,\kappa\,J+\\
& 260352\,\kappa\,{c_2}^3J^3 + 184320\,\kappa\,J{c_2}^3 - 372880\,J^4{c_1}^4c_2 + 142336\,Jc_2\,{c_1}^4-\\
& 158976\,J^2c_2\,\kappa + 111936\,J^5{c_2}^3 - 362496\,\kappa\,J^2{c_2}^3 + 717760\,J^3{c_1}^4c_2-\\
& 39168\,\kappa^2J^3c_2 + 83824\,J^5{c_1}^4c_2 + 96\,\kappa^2J^6c_2 - 110592\,{c_1}^2c_2\,\sqrt{4-2\,J}\Delta\,J+\\
& 23040\,\sqrt{4-2\,J}\mu\,J{c_1}^3 + 2112\,J^6{c_1}^2\sqrt{4-2\,J}\Delta\,c_2 - 282624\,\sqrt{4-2\,J}\Delta\,J^3c_2+\\
& 381440\,Jc_1\,c_2 + 86016\,\delta\,J^2{c_1}^2c_2\,\cos(2\,\phi) - 1152\,\sqrt{4-2\,J}\mu\,\kappa\,J-\\
& 2197632\,J^2{c_1}^2c_2 + 622592\,Jc_2\,{c_1}^3 - 1728\,\kappa^2J^5c_2 + 70656\,\Delta^2J^5c_2+\\
& 622592\,J{c_2}^3c_1 + 34560\,J{c_2}^2\sqrt{4-2\,J}\mu - 2061312\,J^2{c_2}^3c_1 + 69120\,c_2\,\kappa\,J+\\
& 40320\,Jc_1\,\sqrt{4-2\,J}\mu - 110592\,\delta\,Jc_1\,c_2\,\cos(2\,\phi) - 81600\,J^2c_1\,\sqrt{4-2\,J}\mu+\\
& 184320\,\kappa\,Jc_2\,{c_1}^2 - 101088\,J^2{c_1}^2\sqrt{4-2\,J}\mu - 1224320\,J^2c_2\,c_1-\\
& 156672\,\sqrt{4-2\,J}\Delta\,Jc_2 + 2340224\,J^3c_2\,{c_1}^3 + 2526720\,J^3c_2\,{c_1}^2-\\
& 30768\,J^2\sqrt{4-2\,J}\mu + 24576\,{c_2}^3c_1 + 339456\,J^2\sqrt{4-2\,J}\Delta\,c_2 + 32196\,J^5c_2-\\
& 337152\,J^2c_1\,c_2\,\kappa - 6556\,J^6{c_1}^4c_2 + 63744\,Jc_2 - 362496\,\kappa\,J^2c_2\,{c_1}^2-\\
& 21504\,\delta\,J^2{c_1}^2\sin(2\,\phi) + 288\,\delta\,J^5{c_2}^2\sin(2\,\phi) + 48\,\delta\,J^5c_1\,\sin(2\,\phi)+\\
& 23040\,Jc_1\,{c_2}^2\sqrt{4-2\,J}\mu - 73728\,\delta\,J{c_1}^2c_2\,\cos(2\,\phi) + 548352\,J^2c_1\,c_2\,\sqrt{4-2\,J}\Delta-\\
& 21552\,J^6{c_1}^2c_2 - 52992\,\delta\,J^3c_2\,c_1\,\cos(2\,\phi) + 2340224\,J^3{c_2}^3c_1 + 123648\,J^3c_2\,\kappa+\\
& 260352\,\kappa\,c_2\,{c_1}^2J^3 + 1381376\,J^3c_2\,c_1 + 285696\,J^2{c_1}^2\sqrt{4-2\,J}\Delta\,c_2+\\
& 24576\,{c_2}^3{c_1}^2 - 578560\,J^2{c_2}^5 + 18432\,{c_2}^3 - 372880\,J^4{c_2}^5 + 717760\,J^3{c_2}^5-
\end{aligned}
$$

$$576\,\delta\,J^5 c_2\,c_1\,\cos(2\,\phi) - 61344\,J^2 {c_2}^2 \sqrt{4-2\,J}\mu + 253440\,J^3 c_2\,c_1\,\kappa +$$

$$9216\,\delta\,J c_1\,\sin(2\,\phi) - 240\,\sqrt{4-2\,J}\mu\,\kappa\,J^4 + 36336\,J^3 {c_2}^2 \sqrt{4-2\,J}\mu +$$

$$53760\,\delta\,J^2 c_2\,\cos(2\,\phi) + 83824\,J^5 {c_2}^5 - 11732\,J^6 c_2\,c_1 -$$

$$221184\,\sqrt{4-2\,J}\Delta\,J c_1\,c_2 - 336\,J^6 c_2\,\kappa + 1848\,J^5 {c_1}^2 \sqrt{4-2\,J}\mu +$$

$$984\,\sqrt{4-2\,J}\mu\,J^5 {c_1}^3 + 2112\,J^6 {c_2}^3 \sqrt{4-2\,J}\Delta + 342\,J^5 \sqrt{4-2\,J}\mu -$$

$$44544\,J^5 c_1\,c_2\,\sqrt{4-2\,J}\Delta + 3264\,J^6 c_1\,c_2\,\sqrt{4-2\,J}\Delta - 384\,\delta\,J^5 {c_2}^3 \cos(2\,\phi) +$$

$$142336\,J {c_2}^5 + 35808\,J^3 c_1\,{c_2}^2 \sqrt{4-2\,J}\mu - 64512\,\delta\,J^2 {c_2}^2 \sin(2\,\phi) + 336\,\Delta\,\mu\,J^6 -$$

$$768\,J^6 {c_1}^2 \kappa\,c_2 - 19200\,J^6 {c_1}^3 c_2 + 10368\,\mu^2 c_2\,J^2 + 86016\,\delta\,J^2 {c_2}^3 \cos(2\,\phi) +$$

$$4416\,\delta\,J^3 c_1\,\sin(2\,\phi) - 1153536\,J^4 {c_1}^3 c_2 - 41856\,J^4 c_2\,\kappa + 17856\,J \sqrt{4-2\,J}\mu +$$

$$250400\,J^5 {c_1}^3 c_2 + 250400\,J^5 {c_2}^3 c_1 - 10656\,\sqrt{4-2\,J}\mu\,J^4 {c_1}^3 + 6240\,J^5 c_2\,\kappa -$$

$$86016\,J^4 {c_1}^2 \kappa\,c_2 + 13248\,J^5 {c_1}^2 \kappa\,c_2 - 46080\,\delta\,J c_2\,\cos(2\,\phi) + 39552\,\Delta\,\mu\,J^4 c_1 -$$

$$7104\,\Delta\,\mu\,J^5 c_1 - 5280\,\Delta\,\mu\,J^5 - 35328\,\delta\,J^3 {c_1}^2 c_2\,\cos(2\,\phi) + 3072\,c_2 -$$

$$84288\,J^4 c_1\,c_2\,\kappa - 21696\,\sqrt{4-2\,J}\Delta\,J^5 c_2 + 129024\,J^4 {c_2}^3 \sqrt{4-2\,J}\Delta - 73728\,\Delta\,\mu\,J -$$

$$27648\,J^5 {c_2}^3 \sqrt{4-2\,J}\Delta - 36864\,\kappa^2 J c_2 - 494784\,J^4 {c_2}^3 - 1262688\,J^4 {c_1}^2 c_2 +$$

$$277632\,J^5 {c_1}^2 c_2 + 940800\,J^3 {c_2}^3 + 61440\,\kappa^2 J^2 c_2 - 4248\,J^4 \sqrt{4-2\,J}\mu +$$

$$17808\,J^3 \sqrt{4-2\,J}\mu - 47616\,\sqrt{4-2\,J}\mu\,J^2 {c_1}^3 + 35808\,\sqrt{4-2\,J}\mu\,J^3 {c_1}^3 -$$

$$267264\,\Delta^2 J^4 c_2 - 685424\,J^4 c_2\,c_1 + 150704\,J^5 c_2\,c_1 - 106752\,\Delta\,\mu\,J^3 c_1 -$$

$$1157120\,J^2 {c_1}^2 {c_2}^3 - 279552\,J^3 {c_2}^3 \sqrt{4-2\,J}\Delta + 294912\,\Delta^2 J c_2 +$$

$$480\,\Delta\,\mu\,J^6 c_1 + 129024\,\delta\,J^2 c_2\,c_1\,\cos(2\,\phi) - 92544\,\Delta\,\mu\,J^3 +$$

$$18432\,\delta\,J {c_1}^2 \sin(2\,\phi) + 6144\,\delta\,J^4 {c_2}^3 \cos(2\,\phi) - 8856\,J^6 {c_2}^3 + 18432\,{c_1}^2 c_2 -$$

$$144444\,J^4 c_2 + 1248\,\mu^2 c_2\,J^4 - 745760\,J^4 {c_1}^2 {c_2}^3 - 638976\,\Delta^2 J^2 c_2 +$$

$$285072\,J^3 c_2 - 13112\,J^6 {c_1}^2 {c_2}^3 + 13248\,J^5 {c_2}^3 \kappa - 768\,\delta\,J^4 c_1\,\sin(2\,\phi) -$$

$$86016\,J^4 {c_2}^3 \kappa + 6144\,c_2\,c_1 - 241152\,J^2 c_2 - 736896\,J^2 {c_2}^3 - 96\,\mu^2 c_2\,J^5 +$$

$$164352\,J {c_2}^3 + 11904\,\kappa^2 J^4 c_2 + 576\,\Delta^2 J^7 c_2 + 284672\,J {c_2}^3 {c_1}^2 - 9984\,\Delta^2 J^6 c_2 -$$

$$384\,\delta\,J^5 {c_1}^2 c_2\,\cos(2\,\phi) - 6556\,J^6 {c_2}^5 - 2529\,J^6 c_2 - 768\,J^6 {c_2}^3 \kappa + 12288\,c_2\,{c_1}^4 +$$

$$31680\,\mu\,\Delta\,J^4 + 576\,\sqrt{4-2\,J}\mu\,\kappa\,J^3 - 47616\,J^2 c_1\,{c_2}^2 \sqrt{4-2\,J}\mu +$$

$$113280\,J^4 \sqrt{4-2\,J}\Delta\,c_2 - 8976\,J^4 {c_2}^2 \sqrt{4-2\,J}\mu - 672\,J^6 c_1\,c_2\,\kappa +$$

$$1272\,J^5 c_1\,\sqrt{4-2\,J}\mu + 12480\,J^5 c_1\,c_2\,\kappa - 20592\,J^4 {c_1}^2 \sqrt{4-2\,J}\mu - 1153536\,J^4 {c_2}^3 c_1 +$$

$$
\begin{aligned}
&192\,\sqrt{4-2\,J}\mu\,\kappa\,J^2+744\,J^5{c_2}^2\sqrt{4-2\,J}\mu+12288\,{c_2}^5+3840\,\delta\,J^4c_2\,\cos(2\,\phi)-\\
&4608\,\delta\,J^4{c_2}^2\sin(2\,\phi)-73728\,\delta\,J{c_2}^3\cos(2\,\phi)+55296\,\delta\,J{c_2}^2\sin(2\,\phi)+\\
&6144\,\delta\,J^4{c_1}^2c_2\,\cos(2\,\phi)-22080\,\delta\,J^3c_2\,\cos(2\,\phi)-240\,\delta\,J^5c_2\,\cos(2\,\phi)+\\
&8832\,\delta\,J^3{c_1}^2\sin(2\,\phi)+26496\,\delta\,J^3{c_2}^2\sin(2\,\phi)+9216\,\delta\,J^4c_2\,c_1\,\cos(2\,\phi)-\\
&35328\,\delta\,J^3{c_2}^3\cos(2\,\phi)-1536\,\delta\,J^4{c_1}^2\sin(2\,\phi)\,,
\end{aligned}
$$

and

$$
d_1=-36864\,J+52224\,J^2+7488\,J^4-28416\,J^3-960\,J^5+48\,J^6\,.
$$

$$
\begin{aligned}
n_2 = {} & 10752\,\delta\,J^2c_2\,\sin(2\,\phi) - 48\,\delta\,J^5c_2\,\sin(2\,\phi) + 48576\,\delta\,J^3c_1\,\cos(2\,\phi) + \\
& 8001\,J^6c_1 + 3652224\,J^2{c_1}^3 + 35328\,\delta\,J^3{c_2}^2c_1\,\cos(2\,\phi) + 32712\,J^6{c_1}^3 + \\
& 163104\,J^2 - 83824\,J^5{c_1}^5 + 79488\,\delta\,J^3{c_1}^2\cos(2\,\phi) + 8832\,\delta\,J^3\cos(2\,\phi) - \\
& 30720\,{c_1}^4 - 717760\,J^3{c_1}^5 + 288\,\delta\,J^5{c_2}^2\cos(2\,\phi) + 165888\,\delta\,J{c_1}^2\cos(2\,\phi) + \\
& 768\,J^6{c_1}^3\kappa - 142336\,J{c_1}^5 + 43008\,\delta\,J^2c_1\,c_2\,\sin(2\,\phi) + 2740160\,J^2{c_1}^2 - \\
& 83824\,J^5{c_2}^4c_1 + 745760\,J^4{c_1}^3{c_2}^2 - 184320\,\kappa\,{c_1}^3J - 65320\,J^5{c_2}^2 + \\
& 24864\,J^4\kappa - 155648\,J{c_2}^4 + 22934\,J^6{c_1}^2 - 6144\,{c_2}^4 - 6144\,\delta\,J^4{c_1}^3\cos(2\,\phi) + \\
& 18432\,\delta\,J\cos(2\,\phi) - 284672\,J{c_1}^3{c_2}^2 + 362496\,\kappa\,{c_1}^3J^2 - 307288\,J^5{c_1}^4 + \\
& 1970688\,J^4{c_1}^3 + 8064\,\mu^2J + 36864\,\kappa^2J - 12288\,c_1\,{c_2}^4 - 147456\,\Delta^2J + \\
& 308824\,J^4{c_2}^2 - 199936\,J{c_2}^2 - 1435520\,J^3{c_1}^3{c_2}^2 + 49344\,J^2\kappa - 542048\,J^3{c_2}^4 + \\
& 4992\,\mu^2J^3 - 2882272\,J^3{c_1}^4 - 426048\,J^5{c_1}^3 + 1416672\,J^4{c_1}^4 - 299816\,J^5{c_1}^2 - \\
& 10560\,\mu^2J^2 - 11904\,\kappa^2J^4 - 294912\,\Delta^2Jc_1 + 39168\,\kappa^2J^3 + 6556\,J^6{c_2}^4c_1 + \\
& 638976\,\Delta^2J^2c_1 + 23568\,J^6{c_1}^4 + 133632\,\Delta^2J^4 + 3072\,c_1 - 142336\,Jc_1\,{c_2}^4 - \\
& 945920\,J{c_1}^2 - 10368\,\mu^2c_1\,J^2 + 6912\,\mu^2c_1\,J + 86016\,J^4{c_1}^3\kappa + 492288\,J^2{c_2}^4 - \\
& 1248\,\mu^2c_1\,J^4 - 18432\,c_1\,{c_2}^2 - 105396\,J^5c_1 - 96\,\kappa^2J^6 + 319488\,\Delta^2J^2 + \\
& 498588\,J^4c_1 + 267264\,\Delta^2J^4c_1 + 4992\,\Delta^2J^6 - 1178112\,J{c_1}^3 - 55200\,J^3\kappa + \\
& 604480\,J^2{c_2}^2 - 56888\,J^5{c_2}^4 + 35328\,\delta\,J^3{c_1}^3\cos(2\,\phi) + 1728\,\kappa^2J^5 - \\
& 11904\,\kappa^2J^4c_1 - 284160\,\Delta^2J^3 - 21504\,\delta\,J^2\cos(2\,\phi) + 101376\,\delta\,Jc_1\,\cos(2\,\phi) - \\
& 24576\,{c_1}^3{c_2}^2 - 4041984\,J^3{c_1}^3 + 1728\,\kappa^2J^5c_1 + 372880\,J^4{c_2}^4c_1 - \\
& 70656\,\Delta^2J^5c_1 + 263136\,J^4{c_2}^4 + 1157120\,J^2{c_1}^3{c_2}^2 + 528\,\delta\,J^5c_1\,\cos(2\,\phi) - \\
& 1536\,\delta\,J^4\cos(2\,\phi) + 6556\,J^6{c_1}^5 - 576\,\Delta^2J^7c_1 + 1028736\,J^2c_1 + 4954\,J^6{c_2}^2 + \\
& 578560\,J^2{c_1}^5 - 307776\,J^4{c_1}^2\sqrt{4-2\,J}\Delta - 4512\,\sqrt{4-2\,J}\Delta\,J^6{c_1}^2 + \\
& 1104\,J^5c_2\,c_1\,\sqrt{4-2\,J}\mu - 18432\,{c_1}^3 + 456\,J^5\sqrt{4-2\,J}\mu\,c_2 - 2926400\,J^3{c_1}^2 - \\
& 12288\,{c_1}^5 - 366336\,Jc_1 + 1400168\,J^4{c_1}^2 - 9216\,J\kappa + 13112\,J^6{c_1}^3{c_2}^2 - \\
& 1008\,\mu^2J^4 + 2553600\,J^2{c_1}^4 - 680448\,Jc_1\,{c_2}^2 + 1392\,{c_1}^2\kappa\,J^6 - 778240\,J{c_1}^4 - \\
& 167648\,J^5{c_1}^3{c_2}^2 - 717760\,J^3{c_2}^4c_1 - 36864\,{c_2}^2{c_1}^2 - 1064784\,J^3c_1 + \\
& 27648\,{c_2}^2\sqrt{4-2\,J}\Delta\,J^5c_1 + 42432\,\sqrt{4-2\,J}\Delta\,J^5c_1 - \\
& 129024\,{c_2}^2\sqrt{4-2\,J}\Delta\,J^4c_1 + 1536\,\sqrt{4-2\,J}\Delta\,\kappa\,J^5 + 17280\,\sqrt{4-2\,J}\Delta\,J^5{c_2}^2 +
\end{aligned}
$$

$$508416\sqrt{4-2J}\Delta J^3 c_1 + 27648\sqrt{4-2J}\Delta\kappa J - 4800 J^4\sqrt{4-2J}\mu c_2 -$$

$$3072\sqrt{4-2J}\Delta J^6 c_1 - 87744 J^4 {c_2}^2\sqrt{4-2J}\Delta - 2112 {c_2}^2\sqrt{4-2J}\Delta J^6 c_1 -$$

$$118272\delta J^2 c_1 \cos(2\phi) + 718848\sqrt{4-2J}\Delta J^3 {c_1}^2 + 29952\sqrt{4-2J}\Delta\kappa J^3 +$$

$$61824\sqrt{4-2J}\Delta J^5 {c_1}^2 + 3045888 J^2 {c_1}^2 {c_2}^2 + 2191488 J^2 {c_2}^2 c_1 -$$

$$166272 J^2\sqrt{4-2J}\Delta + 23040 J {c_2}^3\sqrt{4-2J}\mu + 470400 J^2 {c_1}^2\kappa +$$

$$141312\mu\Delta J^2 c_2 - 216576 {c_1}^2\kappa J + 72\mu^2 J^5 - 3424320 J^3 {c_1}^2 {c_2}^2 -$$

$$258048 J^3 c_1\kappa - 367872 J^3 {c_1}^2\kappa - 2456064 J^3 c_1 {c_2}^2 + 362496\kappa J^2 c_1 {c_2}^2 -$$

$$260352\kappa J^3 c_1 {c_2}^2 - 285696 J^2 {c_1}^3\sqrt{4-2J}\Delta + 295680 J^2 c_1\kappa -$$

$$46080\sqrt{4-2J}\Delta\kappa J^2 + 110592 {c_2}^2\sqrt{4-2J}\Delta J c_1 - 285696 J^2 {c_2}^2\sqrt{4-2J}\Delta c_1 -$$

$$246528 J^2 {c_2}^2\sqrt{4-2J}\Delta - 114432 J^3 {c_2}^2\kappa - 59904 {c_2}^2\kappa J +$$

$$110592 {c_1}^3\sqrt{4-2J}\Delta J - 115200 c_1\kappa J - 184320\kappa J c_1 {c_2}^2 - 9216\delta J c_2 \sin(2\phi) -$$

$$39744 J^2 c_1 c_2\sqrt{4-2J}\mu - 15936 J^2 c_2\sqrt{4-2J}\mu - 96\sqrt{4-2J}\Delta\kappa J^6 +$$

$$984 J^5 {c_1}^2\sqrt{4-2J}\mu c_2 - 1248\sqrt{4-2J}\Delta J^6 {c_2}^2 + 35808 J^3 {c_1}^2\sqrt{4-2J}\mu c_2 +$$

$$211968\sqrt{4-2J}\Delta J^3 {c_2}^2 - 64512\delta J^2 {c_2}^2\cos(2\phi) - 47616 J^2 {c_1}^2\sqrt{4-2J}\mu c_2 -$$

$$10656 J^4 {c_1}^2\sqrt{4-2J}\mu c_2 - 11616 J^4 c_2 c_1\sqrt{4-2J}\mu + 36192 J^3 c_2 c_1\sqrt{4-2J}\mu -$$

$$213888 J^4\sqrt{4-2J}\Delta c_1 - 9600\sqrt{4-2J}\Delta\kappa J^4 + 14880 J^3\sqrt{4-2J}\mu c_2 -$$

$$106752\Delta\mu J^3 c_2 + 768 J^6 {c_2}^2\kappa c_1 + 1200 c_1\kappa J^6 + 720 {c_2}^2\kappa J^6 + 27936 J^6 {c_2}^2 {c_1}^2 -$$

$$2112 {c_1}^3\sqrt{4-2J}\Delta J^6 + 20016 J^6 c_1 {c_2}^2 - 47616 J^2 {c_2}^3\sqrt{4-2J}\mu +$$

$$137280\sqrt{4-2J}\Delta J^3 + 96\delta J^5\cos(2\phi) - 744\sqrt{4-2J}\Delta J^6 +$$

$$331776\sqrt{4-2J}\Delta J {c_1}^2 + 248832\sqrt{4-2J}\Delta J c_1 + 110592\sqrt{4-2J}\Delta J {c_2}^2 -$$

$$36864\delta J c_2 c_1 \sin(2\phi) + 133248 J^2 {c_2}^2\kappa + 480\Delta\mu J^6 c_2 + 984 J^5 {c_2}^3\sqrt{4-2J}\mu -$$

$$794880 J^2 {c_1}^2\sqrt{4-2J}\Delta + 13824 J c_2 c_1\sqrt{4-2J}\mu - 576000 J^2\sqrt{4-2J}\Delta c_1 +$$

$$5760 J\sqrt{4-2J}\mu c_2 + 23040 J {c_1}^2\sqrt{4-2J}\mu c_2 - 73728\Delta\mu J c_2 -$$

$$129024 J^4 {c_1}^3\sqrt{4-2J}\Delta - 364176 J^5 {c_2}^2 {c_1}^2 + 78336\sqrt{4-2J}\Delta J -$$

$$933888 J {c_2}^2 {c_1}^2 + 578560 J^2 {c_2}^4 c_1 + 27648 {c_1}^3\sqrt{4-2J}\Delta J^5 + 100992 c_1\kappa J^4 -$$

$$260352 J^5 c_1 {c_2}^2 - 22176 {c_1}^2\kappa J^5 - 10656 J^4 {c_2}^3\sqrt{4-2J}\mu + 10512\sqrt{4-2J}\Delta J^5 -$$

$$9696 {c_2}^2\kappa J^5 + 1202784 J^4 {c_2}^2 c_1 - 18144 c_1\kappa J^5 + 132192 J^4 {c_1}^2\kappa -$$

$$7104\Delta\mu J^5 c_2 - 13248 J^5 {c_2}^2\kappa c_1 + 86016 J^4 {c_2}^2\kappa c_1 - 54912 J^4\sqrt{4-2J}\Delta +$$

$$\begin{gathered}
1679808\, J^4 {c_1}^2 {c_2}^2 + 39552\, \mu\, \Delta\, J^4 c_2 + 279552\, {c_1}^3 \sqrt{4-2\,J}\Delta\, J^3 + \\
35808\, J^3 {c_2}^3 \sqrt{4-2\,J}\mu + 47904\, {c_2}^2 \kappa\, J^4 - 86016\, \delta\, J^2 {c_2}^2 c_1\, \cos(2\,\phi) + \\
864\, \delta\, J^5 {c_1}^2 \cos(2\,\phi) + 372880\, J^4 {c_1}^5 - 15170\, J^5 + 73596\, J^4 - 4920\, J^5 \kappa + \\
384\, \delta\, J^5 {c_2}^2 c_1\, \cos(2\,\phi) + 96\, \mu^2 c_1\, J^5 + 5568\, \mu^2 c_1\, J^3 - 96\, \kappa^2 J^6 c_1 + \\
73728\, \delta\, J {c_1}^3 \cos(2\,\phi) - 288\, \Delta^2 J^7 + 36864\, \kappa^2 J c_1 - 61440\, \kappa^2 J^2 - 260352\, \kappa\, {c_1}^3 J^3 + \\
9984\, \Delta^2 J^6 c_1 - 162680\, J^3 + 1131\, J^6 + 4368\, J^6 {c_2}^4 - 193536\, \delta\, J^2 {c_1}^2 \cos(2\,\phi) - \\
35328\, \Delta^2 J^5 + 3072\, {c_1}^2 - 61440\, \kappa^2 J^2 c_1 - 649984\, J^3 {c_2}^2 - 13248\, J^5 {c_1}^3 \kappa - \\
568320\, \Delta^2 c_1\, J^3 + 348\, J^6 \kappa + 39168\, \kappa^2 J^3 c_1 - 58496\, J + \\
279552\, {c_2}^2 \sqrt{4-2\,J}\Delta\, J^3 c_1 - 86016\, \delta\, J^2 {c_1}^3 \cos(2\,\phi) + 26496\, \delta\, J^3 {c_2}^2 \cos(2\,\phi) - \\
4608\, \delta\, J^4 {c_2}^2 \cos(2\,\phi) - 6144\, \delta\, J^4 {c_2}^2 c_1\, \cos(2\,\phi) - 13824\, \delta\, J^4 {c_1}^2 \cos(2\,\phi) - \\
4416\, \delta\, J^3 c_2\, \sin(2\,\phi) - 192\, \delta\, J^5 c_1\, c_2\, \sin(2\,\phi) + 768\, \delta\, J^4 c_2\, \sin(2\,\phi) - 3072\, {c_2}^2 - \\
8448\, \delta\, J^4 c_1\, \cos(2\,\phi) + 3072\, \delta\, J^4 c_1\, c_2\, \sin(2\,\phi) - 17664\, \delta\, J^3 c_2\, c_1\, \sin(2\,\phi) + \\
384\, \delta\, J^5 {c_1}^3 \cos(2\,\phi) + 55296\, \delta\, J {c_2}^2 \cos(2\,\phi) + 73728\, \delta\, J {c_2}^2 c_1\, \cos(2\,\phi)\,,
\end{gathered}$$

and

$$d_2 = -36864\, J + 52224\, J^2 + 7488\, J^4 - 28416\, J^3 - 960\, J^5 + 48\, J^6\,.$$

References

[1] Nayfeh, A. H. *Perturbation methods.* John Wiley & Sons, Inc., 1973.

[2] Kevorkian, J. and Cole, J. D. *Multiple scale and singular perturbation methods.* Applied Mathematical Sciences, Vol. 114, Springer-Verlag, New York, 1996.

[3] Nayfeh, A. H. and Mook, D. T. *Nonlinear oscillations.* John Wiley & Sons, Inc., New York, 1979.

[4] Nayfeh, A. H. and Pai, F. P. *Linear and nonlinear structural mechanics.* John Wiley & Sons, Inc. Hoboke, New Jersey, 2004.

[5] Jordan, D. W. and Smith, P. *Nonlinear ordinary differential equations: An introduction for scientists and engineers.* Fourth edition, Oxford University Press Inc., New York, 2007.

[6] Thomsen, J. J. *Vibrations and stability: Order and chaos.* McGraw-Hill Publishing Company, England, 1997.

[7] Murdock, J. A. *Perturbations: Theory and methods.* John Wiley & Sons, Inc., U.S.A, 1991.

[8] Cartmell, M. P., Ziegler, S. W., Khanin, R. and Forehand, D.IM. Multiple scales analysis of the dynamics of weakly nonlinear mechanical systems. *Applied Mechanics Reviews*, **56**(5), 455-492 (2003).

[9] Nayfeh, A. H. Resolving controversies in the application of the method of multiple scales and the generalized method of averaging. *Nonlinear Dynamics*, **40**, 61-102 (2005).

[10] Rahman, Z. and Burton, T. D. Large amplitude primary and superharmonic resonances in the Duffing oscillator. *Journal of Sound and Vibration*, **110**, 363-380 (1986).

[11] Rahman, Z. and Burton, T. D. On higher order methods of multiple scales in nonlinear oscillations - periodic steady state response. *Journal of Sound and Vibration*, **133**(3), 369-379 (1989).

[12] Wang, H. and Hu, H. Remarks on the perturbation methods in solving the second-order delay differential equations. *Nonlinear Dynamics*, **33**, 379-398 (2003).

[13] Nayfeh, A. H. and Balachandran, B. Modal interactions in dynamical and structural systems. *Applied Mechanics Reviews*, **42**(11S), S175-S201 (1989).

[14] Nayfeh, A. H., Chin, C.-M. and Pratt, J. Perturbation methods in nonlinear dynamics - applications to machining dynamics. *ASME Journal of Manufacturing Science and Engineering*, **119**(4A), 485-493 (1997).

[15] Gordon, J. T. and Merchant, H. C. An asymptotic method for predicting amplitudes of nonlinear wheel shimmy. *Journal of Aircraft*, **15**(3), 155-159 (1978).

[16] Gordon, J. T. Perturbation analysis of nonlinear wheel shimmy. *Journal of Aircraft*, **39**(2), 305-317 (2002).

[17] Ganesan, R. Effects of bearing and shaft asymmetries on the instability of rotors operating at near-critical speeds. *Mechanism and Machine Theory*, **35**, 737-752 (2000).

[18] Ji, Z. and Zu, J. W. Method of multiple scales for vibration analysis of rotor-shaft systems with non-linear bearing pedestal model. *Journal of Sound and Vibration*, **218**(2), 293-305 (1998).

[19] Hu, H. Y. and Wang, Z. H. Singular perturbation methods for nonlinear dynamic systems with time delays. *Chaos, Solitons and Fractals*, **40**, 13-27 (2009).

[20] Das, S. L. and Chatterjee, A. Multiple scales without center manifold reductions for delay differential equations near Hopf bifurcations. *Nonlinear Dynamics*, **30**, 323-335 (2002).

[21] Rossikhin, Yu. A. and Shitikova, M. V. Application of fractional calculus for analysis of nonlinear damped vibrations of suspension bridges. *Journal of Engineering Mechanics*, **124**(9), 1029-1036 (1998).

[22] Das, S. L. and Chatterjee, A. Multiple scales via Galerkin projections: Approximate asymptotics for strongly nonlinear oscillations. *Nonlinear Dynamics*, **32**, 161-186 (2003).

[23] Chatterjee, A. and Chatterjee, D. Analytical investigation of hydrodynamic cavitation control by ultrasonics. *Nonlinear Dynamics*, **46**, 179-194 (2006).

[24] Okuizumi, N. and Kimura, K. Multiple time scale analysis of hysteretic systems subjected to harmonic excitation. *Journal of Sound and Vibration*, **272**, 675-701 (2004).

[25] Rajanbabu, N., Marathe, A., Chatterjee, A. and Menon, A. G. Multiple scales analysis of early and delayed boundary ejection in Paul traps. *International Journal of Mass Spectrometry*, **261**, 170-182 (2007).

[26] Fradkov, A. L. and Pogromsky, A. Yu. Speed gradient control of chaotic continuous-time systems. *IEEE Transactions on Circuits and Systems - I: Fundamental theory and Applications*, **43**(11), 907-913 (1996).

[27] Fradkov, A. L. Exploring nonlinearity by feedback. *Physica D*, **128**, 159-168 (1999).

[28] Dhooge, A., Govaerts, W. and Kuznetsov, Yu. A. MATCONT: A MATLAB package for numerical bifurcation analysis of ODEs. *ACM Transactions on Mathematical Software*, **29**(2), 141-164 (2003).

[29] Govaerts, W., Kuznetsov, Yu. A., De Feo, O., Dhooge, A., Govorukhin, V., Ghaziani, R. K., Meijer, H. G. E., Mestrom, W., Riet, A. and Sautois, B. *MATCONT, CL_MATCONT and CL_MATCONT_for_MAPS*, available via http://www.matcont.ugent.be/.

[30] Singh, S. J. and Chatterjee, A. Galerkin projections and finite elements for fractional order derivatives. *Nonlinear Dynamics*, **45**, 183-206 (2006).

[31] Das, S. L. and Chatterjee, A. Second order multiple scales for oscillators with large delay. *Nonlinear Dynamics*, **39**(4), 375-394 (2005).

[32] Crandall, S. H. and Brosens, P. J. On the stability of rotation of a rotor with rotationally unsymmetric inertia and stiffness properties. *Transactions of the ASME, Journal of Applied Mechanics*, **28**(4), 567-570 (1961).

[33] Nandakumar, K. and Chatterjee, A. Nonlinear secondary whirl of an overhung rotor. *Proceedings of the Royal Society of London, Series A*, **466**(2113), 283-301 (2010).

[34] Nandakumar, K. and Chatterjee, A. Continuation of limit cycles near saddle homoclinic points using splines in phase space. *Nonlinear Dynamics*, **57**(3), 383-399 (2009).

[35] Schecter, S. Numerical computation of saddle-node homoclinic bifurcation points. *SIAM Journal on Numerical Analysis*, **30**(4), 1155-1178 (1993).

[36] Doedel, E. J., Friedman, M. J. and Monteiro, A. C. On locating connecting orbits. *Applied Mathematics and Computation*, **65**, 231-239 (1994).

[37] Deng, B. Constructing homoclinic orbits and chaotic attractors. *International Journal of Bifurcation and Chaos*, **4**(4), 823-841 (1994).

[38] Beyn, W. -J., Champneys, A., Doedel, E., Govaerts, W., Kuznetsov, Yu. A. and Sandstede, B. Numerical continuation, and computation of normal forms. *Handbook of Dynamical Systems*, **2**, Chapter - 4, 149-219 (2002).

[39] Beyn, W. -J. The numerical computation of connecting orbits in dynamical systems. *IMA Journal of Numerical Analysis*, **9**, 379-405 (1990).

[40] Champneys, A. R., Kuznetsov, Yu. A. and Sandstede, B. A numerical toolbox for homoclinic bifurcation analysis. *International Journal of Bifurcation and Chaos*, **6**(5), 867-887 (1996).

[41] Lust, K. Improved numerical Floquet multipliers. *International Journal of Bifurcation and Chaos*, **11**(9), 2389-2410 (2001).

[42] Guckenheimer, J. and Meloon, B. Computing periodic orbits and their bifurcations with automatic differentiation. *SIAM Journal on Scientific Computing*, **22**(3), 951-985 (2000).

[43] Moore, G. Computation and parametrization of periodic and connecting orbits. *IMA Journal of Numerical Analysis*, **15**, 245-263 (1995).

[44] Moore, G. Computation and parametrisation of invariant curves and tori. *SIAM Journal on Numerical Analysis*, **33**(6), 2333-2358 (1996).

[45] Liu, L., Moore, G. and Russell, R. D. Computation and continuation of homoclinic and heteroclinic orbits with arclength parameterization. *SIAM Journal on Scientific Computing*, **18**(1), 69-93 (1997).

[46] Guckenheimer, J. and Holmes, P. *Nonlinear Oscillations, Dynamical Systems, and Bifurcation of Vector Fields.* Springer-Verlag, New York, 1983.

[47] Perko, L. *Differential Equations and Dynamical Systems.* Springer Texts in Applied Mathematics 7, Springer-Verlag, New York, 2001.

[48] Ott, E. *Chaos in dynamical systems.* Cambridge University Press, 1993.

[49] Khibnik, A. I., Kuznetsov, Yu. A., Levitin, V. V. and Nikolaev, E. V. Continuation techniques and interactive software for bifurcation analysis of ODEs and iterated maps. *Physica D*, **62**, 360-371 (1993).

[50] Doedel, E. J., Paffenroth, R. C., Champneys, A. R., Fairgrieve, T. F., Kuznetsov, Yu. A., Oldeman, B. E., Sandstede, B. and Wang, X. J. *AUTO2000: Continuation and bifurcation software for ordinary differential equations*, available via http://cmvl.cs.concordia.ca/auto/.

[51] Doedel, E. J., Keller, H. B. and Kernevez, J. -P. Numerical analysis and control of bifurcation problems(I): Bifurcation in finite dimensions. *International Journal of Bifurcation and Chaos*, **1**(3), 493-520 (1991).

[52] Doedel, E. J., Keller, H. B. and Kernevez, J. -P. Numerical analysis and control of bifurcation problems(II): Bifurcation in infinite dimensions. *International Journal of Bifurcation and Chaos*, **1**(4), 745-772 (1991).

[53] Doedel, E. J. Nonlinear numerics. *Journal of the Franklin Institute*, **334B**(5/6), 1049-1073 (1997).

[54] Freire, E., Pizarro, L. and Rodríguez-Luis, A. J. Numerical continuation of degenerate homoclinic orbits in planar systems. *IMA Journal of Numerical Analysis*, **19**, 51-75 (1999).

[55] Freire, E., Pizarro, L. and Rodríguez-Luis, A. J. Numerical continuation of homoclinic orbits to non-hyperbolic equilibria in planar systems. *Nonlinear Dynamics*, **23**, 353-375 (2000).

[56] Champneys, A. R. and Kuznetsov, Yu. A. Numerical detection and continuation of codimension-two homoclinic bifurcations. *International Journal of Bifurcation and Chaos*, **4**(4), 785-822 (1994).

[57] Kuznetsov, Yu. A. *Elements of Applied Bifurcation Theory.* Springer-Verlag, New York, 2004.

[58] Moore, G. Geometric methods for computing invariant manifolds. *Applied Numerical Mathematics*, **17**, 319-331 (1995).

[59] Doedel, E. J. *Lecture notes on Numerical analysis of nonlinear equations*, available via http://cmvl.cs.concordia.ca/publications.html.

[60] Piskunov, N. *Differential and Integral Calculus.* Mir Publishers, Moscow, 1974.

[61] Sparrow, C. *The Lorenz Equations: Bifurcations, Chaos, and Strange Attractors.* Springer Texts in Applied Mathematical Sciences 41, Springer-Verlag, New York, 1982.

[62] Doedel, E. J., Krauskopf, B. and Osinga, H. M. Global bifurcations of the Lorenz manifold. *Nonlinearity*, **19**, 2947-2972 (2006).

[63] Hastings, S. P. and Troy, W. C. A shooting approach to the Lorenz equations. *Bulletin (New Series) of the American Mathematical Society*, **27**(2), 298-303 (1992).

[64] Vakakis, A. F. and Azeez, M. F. A. Analytic approximation of the homoclinic orbits of the Lorenz system at $\sigma = 10$, $b = 8/3$ and $\rho = 13.926...$. *Nonlinear Dynamics*, **15**, 245-257 (1998).

[65] Khibnik, A. I., Roose, D. and Chua, L. O. On periodic orbits and homoclinic bifurcations in Chua's circuit with a smooth nonlinearity. *International Journal of Bifurcation and Chaos*, **3**(2), 363-384 (1993).

[66] Strogatz, S. H. *Nonlinear dynamics and chaos: with applications to physics, biology, chemistry, and engineering.* Addison-Wesley Publishing Company, 1994.

[67] Hlavacek, V. and Rompay, P. V. Calculation of parametric dependence and finite-difference methods *AIChE Journal*, **28**(6), 1033-1036 (1982).

[68] Seydel, R. *Practical bifurcation and stability analysis*, Second edition (1994), 129-140, Sringer-Verlag, New York, 1994.

[69] Nandakumar, K. and Chatterjee, A. Limit cycle continuation using splines in phase space. *Proceedings of the 9th International Conference on Vibration Problems*, IIT Kharagpur, Kharagpur, India, January 19 - 22 (2009).

[70] Gluck, H. Higher curvatures of curves in Euclidean space. *The American Mathematical Monthly*, **73**(7), 699-704 (1966).

[71] http://en.wikipedia.org/wiki/Frenet-Serret_formulas.

[72] Chakraborty, T. and Rand, R. H. The transition from phase locking to drift in a system of two weakly coupled van der Pol oscillators. *International Journal of Non-Linear Mechanics*, **23**(5/6), 369-376 (1988).

[73] Oldham, K. B. and Spanier, J. *The Fractional Calculus - Theory and applications of differentiation and integration to arbitrary order.* Academic Press, New York, 1974.

[74] Ichise, M., Nagayanagi Y. and Kojima, T. An analog simulation of non-integer order transfer functions for analysis of electrode processes. *Journal of Electroanalytical Chemistry*, **33**, 253-265 (1971).

[75] Sun, H. H. and Charef, A. Time domain analysis of the fractal system for electrode polarization phenomenon. *Annual International Conference of the IEEE Engineering in Medicine and Biology Society*, **12**(1), 0012-0013 (1990).

[76] Sun, H. H. and Charef, A. Fractal system - a time domain approach. *Annals of Biomedical Engineering*, **18**, 597-621 (1990).

[77] Laskin, N. Fractional market dynamics. *Physica A*, **287**, 482-492 (2000).

[78] Torvik, P. J. and Bagley, R. L. On the appearance of the fractional derivative in the behavior of real materials. *Transactions of the ASME, Journal of Applied Mechanics*, **51**, 294-298 (1984).

[79] Bagley, R. L. and Calico, R. A. Fractional order state equations for the control of viscoelastically damped structures. *Journal of Guidance, Control, and Dynamics*, **14**(2), 304-311 (1991).

[80] Bagley, R. L. and Torvik, P. J. Fractional calculus in the transient analysis of viscoelastically damped structures. *AIAA Journal*, **23**(6), 918-925 (1985).

[81] Chatterjee, A. Statistical origins of fractional derivatives in viscoelasticity. *Journal of Sound and Vibration*, **284**, 1239-1245 (2005).

[82] Jifeng, W. and Yuankai, L. Frequency domain analysis and applications for fractional-order control systems. *7th International Symposium on Measurement Technology and Intelligent Instruments*, Institute of Physics Publishing, Journal of Physics: Conference series **13**, 268-173 (2005).

[83] Ma, C. and Hori, Y. Fractional order control and its application of PI$^{\alpha}$D controller for robust two-inertia speed control. *The 4th International Power Electronics and Motion Control Conference*, IPEMC 2004, August 14-16 (2004), **3**, 1477-1482.

[84] Ge, Z.-M. and Jhuang, W.-R., Chaos, control and synchronization of a fractional order rotational mechanical system with a centrifugal governor. *Chaos, Solitons and Fractals*, **33**, 270-289 (2007).

[85] Arena, P., Caponetto, R., Fortuna, L. and Porto, D. Bifurcation and chaos in noninteger order cellular neural networks. *International Journal of Bifurcation and Chaos*, **8**(7), 1527-1539 (1998).

[86] Gao, X. and Yu, J. Chaos in the fractional order periodically forced complex Duffing's oscillators. *Chaos, Solitons and Fractals*, **24**, 1097-1104 (2005).

[87] Ge, Z.-M. and Yi, C.-Xi. Chaos in a nonlinear damped Mathieu system, in a nano resonator system and in its fractional order systems. *Chaos, Solitons and Fractals*, **32**, 42-61 (2007).

[88] Ge, Z.-M. and Hsu, M.-Y. Chaos in a generalized van der Pol system and in its fractional order system. *Chaos, Solitons and Fractals*, **33**, 1711-1745 (2007).

[89] Chen, J.-H. and Chen, W.-C. Chaotic dynamics of the fractionally damped van der Pol equation. *Chaos, Solitons and Fractals*, **35**, 188-198 (2008).

[90] Barbosa, R. S., Machado, J. A. T., Ferreira, I. M. and Tar, J. K. Dynamics of the fractional-order Van der Pol oscillator. *Proceedings of the IEEE International Conference on Computational Cybernetics (ICCC'04)*, Vienna, Austria, August 30 - September 1 (2004).

[91] Barbosa, R. S., Machado, J. A. T., Vinagre, B. M. and Claderón, A. J. Analysis of the Van der Pol oscillator containing derivatives of fractional order. *Journal of Vibration and Control*, **13**(9-10), 1291-1301 (2007).

[92] Gao, X. and Yu, J. Synchronization of two coupled fractional-order chaotic oscillators. *Chaos, Solitons and Fractals*, **26**, 141-145 (2005).

[93] Nickolay, K., Zaslavsky, G. M. and Tarasov, V. E. Coupled oscillators with power-law interaction and their fractional dynamics analogues. *Communications in nonlinear science and numerical simulation*, **12**, 1405-1417 (2007).

[94] Hartley, T. T., Lorenzo, C. F. and Qammer, H. K. Chaos in a fractional order Chua's system. *IEEE Transactions on Circuits and Systems-I: Fundamental Theory and Applications*, **42**(8), 485-490 (1995).

[95] Sun, H. H., Abdelwahab, A. A. and Onaral, B. Linear approximation of transfer function with a pole of fractional power *IEEE Transactions on Automatic Control*, **29**(5), 440-444 (1984).

[96] Charef, A., Sun, H. H., Tsao, Y. Y. and Onaral, B. Fractal system as represented by singularity function. *IEEE Transactions on Automatic Control*, **37**(9), 1465-1470 (1992).

[97] Oustaloup, A., Levron, F., Mathieu, B. and Nanot, F. M. Frequency-band complex noninteger differentiator: Characterization and synthesis. *IEEE Transactions on Circuits and Systems-I: Fundamental Theory and Applications*, **47**(1), 25-39 (2000).

[98] Vinagre, B. M., Podlubny, I., Hernández, A. and Feliu, V. Some approximations of fractional order operators used in control theory and applications. *Fractional Calculus and Applied Analysis*, **3**(3), 231-248 (2000).

[99] Singh, S. J. and Chatterjee, A. DAE-based solution of nonlinear multiterm fractional integrodifferential equations. *Journal Européen des Systèmes Automatisés, RS série JESA*, **42**(6-7-8), 677-688 (2008).

[100] Singh, S. J. and Chatterjee, A. Three classes of FDEs amenable to approximation using a Galerkin technique. *Advances in fractional calculus: Theoretical developments and applications in physics and engineering*, p. nos. 3-14, Springer, Dordrecht, Netherlands, 2007.

[101] Singh, S. J. and Chatterjee, A. Fractional damping: Stochastic origin and finite approximations. *Advances in fractional calculus: Theoretical developments and applications in physics and engineering*, p. nos. 389-402, Springer, Dordrecht, Netherlands, 2007.

[102] Li, G., Zhu, Z. and Cheng, C. Dynamic stability of viscoelastic column with fractional derivative constitutive relation. *Applied Mathematics and Mechanics*, **22**(3), 294-303 (2001).

[103] Wahi, P. and Chatterjee, A. Averaging oscillations with small fractional damping and delayed terms. *Nonlinear Dynamics*, **38**, 3-22 (2004).

[104] Rossikhin, Yu. A. and Shitikova, M. V. Nonlinear free damped vibrations of suspension bridges with uncertain fractional damping. *Journal Européen des Systèmes Automatisés, RS série JESA*, **42**(6-7-8), 879-894 (2008).

[105] Rossikhin, Yu. A. and Shitikova, M. V. Analysis of nonlinear vibrations of a two-degree-of-freedom mechanical system with damping modelled by a fractional derivative. *Journal of Engineering Mathematics*, **37**, 343-362 (2000).

[106] Rossikhin, Yu. A. and Shitikova, M. V. Analysis of free non-linear vibrations of a viscoelastic plate under the conditions of different internal resonances. *International Journal of Non-Linear Mechanics*, **41**, 313-325 (2006).

[107] Sugimoto, N., Masuda, M. and Hashiguchi, T. Frequency response of nonlinear oscillations of air column in a tube with an array of Helmholtz resonators. *Journal of Acoustical Society of America*, **114**(4), 1772-1784 (2003).

[108] Caputo, M. Linear models of dissipation where Q is almost frequency independent, Part II. *Geophysics Journal of Royal Astronomical Society*, **13**, 529-539 (1967).

[109] Deng, R., Davies, P. and Bajaj, A. K. Flexible polyurethane foam modelling and indentification of viscoelastic parameters for automotive seating applications. *Journal of Sound and Vibration*, **262**, 391-417 (2003).

[110] Thomsen, J. J. Chaotic dynamics of the partially follower-loaded elastic double pendulum. *Journal of Sound and Vibration*, **188**(3), 385-405 (1995).

[111] Rand, R. H. *Lecture notes on nonlinear vibrations.* Available online at http://audiophile.tam.cornell.edu/randdocs/nlvibe52.pdf.

[112] Chatterjee, A. *A brief introduction to nonlinear vibrations.* Available online at http://eprints.iisc.ernet.in/15716/.

[113] Plaut, R. H. and Hseih, J. C., Nonlinear structural vibrations involving a time delay in damping. *Journal of Sound and Vibration*, **117**(3), 497-510 (1987).

[114] Hu, H., Dowell, E. H. and Virgin, L. N. Resonances of a harmonically forced Duffing oscillator with time delay state feedback. *Nonlinear Dynamics*, **15**(4), 311-327 (1998).

[115] Maccari, A. The response of a parametrically excited van der Pol oscillator to a time delay state feedback. *Nonlinear Dynamics*, **26**(2), 105-119 (2001).

[116] Pieroux, D., Erneux, T., Gavrielides, A. and Kovanis, V. Hopf bifurcation subject to a large delay in a laser system. *SIAM Journal of Applied Mathematics*, **61**(3), 966-982 (2000).

[117] Erneux, T. Multiple time scale analysis of delay differential equations modeling mechanical systems. *Proceedings of IDETC/CIE 2005, ASME 2005 International Design Engineering Technical Conferences & Computers and Information in Engineering Conference*, Long Beach, California, USA, DETC2005-85028, September 24-28 (2005).

[118] Yanchuk, S. and Wolfrum, M. Instabilities of equilibria of delay-differential equations with large delay. ENOC2005, Eindhoven, Netherlands, August 7-12 (2005).

[119] Fowler, A. C. Asymptotic methods for delay equations. *Journal of Engineering Mathematics*, **53**, 271-290 (2005).

[120] Nandakumar, K., Wahi, P. and Chatterjee, A. Infinite dimensional slow modulations in a delayed model for orthogonal cutting vibrations. *Proceedings of the 9th Biennial ASME Conference on Engineering Systems Design and Analysis*, Haifa, Israel, ESDA2008-59339, July 7-9 (2008).

[121] Gopalsamy, K. Stability and oscillations in delay differential equations of popular dynamics. *Kluwer Academic Publishers*, Dordrecht, 1992.

[122] Stépán, G. and Haller, G. Quasiperiodic oscillations in robot dynamics. *Nonlinear Dynamics*, **8**, 513-528 (1995).

[123] Bélair, J., Campbell, S. A. and Van Den Driessche, P. Frustration, stability, and delay-induced oscillations in a neural network model. *SIAM Journal of Applied Mathematics*, **56**(1), 245-255 (1996).

[124] Heil, T., Fischer, I., Elsaßer, W., Krauskopf, B., Green, K. and Gavrielides, A. Delay dynamics of semiconductor lasers with short external cavities: Bifurcation scenarios and mechanisms. *Physical Review E*, **67**(066214), 2003.

[125] Alhazza, K. A., Daqaq, M. F., Nayfeh, A. H. and Inman, D. J. Non-linear vibrations of parametrically excited cantilever beams subjected to non-linear delayed-feedback control. *International Journal of Non-Linear Mechanics*, **43**, 801-812 (2008).

[126] Daqaq, M. F., Alhazza, K. A. and Arafat, H. N. Non-linear vibrations of cantilever beams with feedback delays. *International Journal of Non-Linear Mechanics*, **43**, 962-978 (2008).

[127] Tobias, S. A. *Machine-tool vibration.* Blackie and Sons Ltd., London, 1965.

[128] Stépán, G., Insperger, T. and Szalai, R. Delay, parametric excitation, and the nonlinear dynamics of cutting processes. *International Journal of Bifurcation and Chaos*, **15**(9), 2783-2798 (2005).

[129] Wiercigroch, M. and Budak, E. Sources of nonlinearities, chatter generation and suppression in metal cutting. *Philosophical Transactions of the Royal Society of London, Series A*, **359**(1781), 663-693 (2001).

[130] *Dynamics and chaos in manufacturing processes.* (ed. F. C. Moon), Wiley, 1997.

[131] Kalmár-Nagy, T., Stépán, G. and Moon, F. C. Subcritical Hopf bifurcation in the delay equation model for machine tool vibrations. *Nonlinear Dynamics*, **26**, 121-142 (2001).

[132] Hanna, N. H. and Tobias, S. A. A theory of nonlinear regenerative chatter. *Transactions of the ASME - Journal of Engineering for Industry*, **96**, 247-255 (1974).

[133] Moon, F. C. and Kalmár-Nagy, T. Nonlinear models for complex dynamics in cutting materials. *Philosophical Transactions of the Royal Society of London, Series A*, **359**, 695-711 (2001).

[134] Johnson, M. A. and Moon, F. C. Experimental characterization of quasiperiodicity and chaos in a mechanical system with delay. *International Journal of Bifurcation and Chaos*, **9**(1), 49-65 (1999).

[135] Johnson, M. A. and Moon, F. C. Nonlinear techniques to characterize prechatter and chatter vibrations in machining of metals. *International Journal of Bifurcation and Chaos*, **11**(2), 449-467 (2001).

[136] Stépán, G. *Retarded dynamical systems: stability and characteristic functions.* Longman Scientific & Technical, Longman Group UK Limited (1989), Pitman research notes in mathematics series, **210**.

[137] Warmiński, J., Litak, G., Cartmell, M. P., Khanin, R. and Wiercigroch, M. Approximate analytical solutions for primary chatter in the non-linear metal cutting model. *Journal of Sound and Vibration*, **259**(4), 917-933 (2003).

[138] Chandiramani, N. K. and Pothala, T. Dynamics of 2-dof regenerative chatter during turning. *Journal of Sound and Vibration*, **290**, 448-464 (2006).

[139] Grabec, I. Chaotic dynamics of the cutting process. *International Journal of Machine Tools and Manufacture*, **28**(1), 19-32 (1988).

[140] Wiercigroch, M. and Cheng, A. H-D. Chaotic and stochastic dynamics of orthogonal metal cutting. *Chaos, Solitons and Fractals* **8**(4), 715-726 (1997).

[141] Fofana, M. S. Delay dynamical systems and applications to nonlinear machine-tool chatter. *Chaos, Solitons and Fractals*, **17**, 731-747 (2003).

[142] Gilsinn, D. E. Estimating critical Hopf bifurcation parameters for a second-order delay differential equation with application to machine tool chatter. *Nonlinear Dynamics*, **30**, 103-154 (2002).

[143] Wahi, P. and Chatterjee, A. Regenerative tool chatter near a codimension 2 Hopf point using multiple scales. *Nonlinear Dynamics*, **40**, 323-338 (2005).

[144] Nayfeh, A. H. Order reduction of retarded nonlinear systems - the method of multiple scales versus center-manifold reduction. *Nonlinear Dynamics*, **51** 483-500 (2008).

[145] Chatterjee, S. and Singha, T. K. Controlling chaotic instability of cutting process by high-frequency excitation: a numerical investigation. *Journal of Sound and Vibration*, **267**, 1184-1192 (2003).

[146] Litak, G., Kasperek, R. and Zaleski, K. Effect of high-frequency excitation in regenerative turning of metals and brittle materials. *Chaos, Solitons and Fractals*, Article in press, *doi:10.1016/j.chaos.2007.09.090.*

[147] Brandt, S. F., Pelster, A. and Wessel, R. Variational calculation of the limit cycle and its frequency in a two-neuron model with delay. *Physical Review E*, **74**(036201), 2006.

[148] Rand, R. and Verdugo, A. Hopf bifurcation in a DDE model of gene expression. *Communications in Nonlinear Science and Numerical Simulation*, **13**, 235-242 (2008).

[149] Ariaratnam, S. T. and Fofana, M. S. The effects of nonlinearity in turning operation. *Journal of Engineering Mathematics*, **42**, 143-156 (2002).

[150] Engelborghs, K., Luzyanina, T. and Roose, D. Numerical bifurcation analysis of delay differential equations using DDE-BIFTOOL. *ACM Transactions on Mathematical Software*, **28**(1), 1-21 (2002).

[151] Nayfeh, A., Chin, C. and Pratt, J. Applications of perturbation methods to tool chatter dynamics. *Dynamics and chaos in manufacturing processes*(ed. F. C. Moon), Wiley, 193-213 (1997).

[152] Wahi, P. and Chatterjee, A. Self-interrupted regenerative metal cutting in turning. *International Journal of Non-Linear Mechanics*, **43**, 111-123 (2008).

[153] Smith, D. M. The motion of a rotor carried by a flexible shaft in flexible bearings. *Proceedings of the Royal Society of London, Series A*, **142**, 92-118 (1933).

[154] Yamamoto, T. and Ōta, H. On the vibrations of the shaft carrying an asymmetrical rotating body. *Bulletin of the Japanese society of mechanical engineers*, **6**(21), 29-36 (1963).

[155] Yamamoto, T. and Ōta, H. On the unstable vibrations of a shaft carrying an unsymmetrical rotor. *Transactions of the ASME, Journal of Applied Mechanics*, **31**(3), 515-522 (1964).

[156] Yamamoto, T., Ōta, H. and Kōno, K. On the unstable vibrations of a shaft with unsymmetrical stiffness carrying an unsymmmetrical rotor. *Transactions of the ASME, Journal of Applied Mechanics*, **35**(2), 313-321 (1968).

[157] Genta, G. *Dynamics of Rotating Systems.* Springer, New York, 2005.

[158] Den Hartog, J. P. *Mechanical Vibrations.* Fourth edition, McGraw-Hill, New York, 1956.

[159] Rao, J. S. *Rotor Dynamics.* New Age International Publishers, New Delhi, 1983.

[160] Yamamoto, T., Ishida, Y., Ikeda, T. and Yamamoto, M. Nonlinear forced oscillations of a rotating shaft carrying an unsymmetrical rotor at the major critical speed. *Bulletin of the Japanese Society of Mechanical Engineers*, **25**(210), 1969-1976 (1982).

[161] Ishida, Y., Liu, J., Inoue, T. and Suzuki, A. Vibrations of an asymmetrical shaft with gravity and nonlinear spring characteristics (isolated resonances and internal resonances). *ASME Journal of Vibration and Acoustics*, **130**, 041004-1 to 041004-8 (2008).

[162] Yamamoto, T., Ishida, Y., Ikeda, T. and Yamada, M. Subharmonic and summed-and-differential harmonic oscillations of an unsymmetrical rotor. *Bulletin of the Japanese Society of Mechanical Engineers*, **24**(187), 192-199 (1981).

[163] Yamamoto, T., Ishida, Y. and Ikeda, T. Vibrations of a rotating shaft with rotating nonlinear restoring forces at the major critical speed. *Bulletin of the Japanese Society of Mechanical Engineers*, **27**(230), 1728-1736 (1984).

[164] Ishida, Y., Ikeda, T., Yamamoto, T. and Hiei, M. Effects of nonlinear spring characteristics on the dynamic unstable region of an unsymmetrical rotor. *Bulletin of the Japanese Society of Mechanical Engineers*, **29**(247), 200-207 (1986).

[165] Ikeda, T., Ishida, Y., Yamamoto, T. and Suzuki, T. Nonlinear forced oscillations of an unsymmetrical shaft and unsymmetrical rotor with quartic nonlinearity (Variations of resonance curves of subharmonic and ultra-subharmonic oscillations and

the occurence of unstable vibrations). *JSME International Journal*, **31**(3), 530-538 (1988).

[166] Foote, W. R., Poritsky, H. and Slade, J. J. Jr. Critical speeds of a rotor with unequal shaft flexibilities, mounted in bearings of unequal flexibility - I. *Transactions of the ASME, Journal of Applied Mechanics*, **10**(2), A77-A84 (1943).

[167] Brosens, P. J. and Crandall, S. H. Whirling of unsymmetrical rotors. *Transactions of the ASME, Journal of Applied Mechanics*, **28**(3), 355-362 (1961).

[168] Iwatsubo, T., Tomita, A. and Kawai, R. Vibrations of asymmetric rotors supported by asymmetric bearings. *Ingenieur-Archiv*, **42**, 416-432 (1973).

[169] Messal, E. E. and Bonthron, R. J. Subharmonic rotor instability due to elastic asymmetry. *Transactions of the ASME, Journal of Engineering for Industry*, **94**(1), 185-192 (1972).

[170] Ishida, Y. Nonlinear vibrations and chaos in rotordynamics. *JSME International Series C - Dynamics, Control, Robotics, Design and Manufacturing*, **37**(2), 237-245 (1994).

[171] Childs, D. *Turbomachinery rotordynamics: Phenomena, modeling and analysis.* Wiley-Interscience, New York, 1993.

[172] Coleman, R. P. and Feingold, A. M. Theory of self-excited mechanical oscillations of helicopter rotors with hinged blades. *NACA report* **1351**, chapters 2 and 3, Langley Field, VA, 1958.

[173] Taylor, H. D. Critical-speed behavior of unsymmetrical shafts. *Transactions of the ASME, Journal of Applied Mechanics*, **7**(2), A71-A79 (1940).

[174] Rajalingham, C., Bhat, R. B. and Xistris, G. D. Influence of external damping on the stability and response of a horizontal rotor with anisotropic bending stiffness. *Tribology Transactions*, **36**(3), 393-398 (1993).

[175] Kondo, Y. and Kimura, H. Study on the vibration of an asymmetrically elastic rotating shaft - some considerations on the phase response and whirling. *Memoirs of Shonan Institute of Technology*, **25**(1), 29-39 (1991).

[176] Bishop, R. E. D. and Parkinson, A. G. Second order vibration of flexible shafts. *Philosophical Transactions of the Royal Society of London, Series A*, **259**, 1-31 (1965).

[177] Sakata, M., Endo, M. and Kishimoto, K. Secondary critical speed of flexible rotors with inertia slots. *Journal of Sound and Vibration*, **87**(1), 61-70 (1983).

[178] Rao, J. S. and Sreenivas, R. Dynamics of asymmetric rotors using solid models. *Proceedings of the International Gas Turbine Congress 2003*, Tokyo, November 2-7, 2003.

[179] Hull, E. H. Shaft whirling as influenced by stiffness asymmetry. *Transactions of the ASME, Journal of Engineering for Industry, Series B*, **83**(2), 219-226 (1961).

[180] Bishop, R. E. D. and Mahalingam, S. Some experiments in the vibration of a rotating shaft. *Proceedings of the Royal Society of London, Series A*, **292**, 537-561 (1965).

[181] Nagasaka, I., Ishida, Y. and Liu, J. Forced oscillations of a continuous asymmetrical rotor with geometrical nonlinearity (major critical speed and secondary critical speed). *ASME Journal of Vibration and Acoustics*, **130**, 031012-1 to 031012-7 (2008).

[182] Basu-Mandal, P., Chatterjee, A. and Papadopoulos, J. M. Hands-free circular motions of a benchmark bicycle. *Proceedings of the Royal Society of London, Series A*, **463**(2084), 1983-2003 (2007).

[183] Mahadevan, P., Jog, C. S. and Chatterjee, A. Modal projections for synchronous rotor whirl. *Proceedings of the Royal Society of London, Series A*, **464**(2095), 1739-1760 (2008).

[184] Nandakumar, K. and Chatterjee, A. Resonance, parameter estimation, and modal interactions in a strongly nonlinear benchtop oscillator. *Nonlinear Dynamics*, **40**, 149-167 (2005).

[185] Hinch, E. J. *Perturbation methods.* Cambridge University Press, 1991.